

THESIS

WASTE HEAT RECOVERY FROM A HIGH TEMPERATURE DIESEL ENGINE

Submitted by

Jonas E. Adler

Department of Mechanical Engineering

In partial fulfillment of the requirements

For the Degree of Master of Science

Colorado State University

Fort Collins, Colorado

Fall 2017

Master's Committee:

Advisor: Todd M. Bandhauer

Daniel B. Olsen
Sybil E. Sharvelle

Copyright by Jonas E. Adler 2017

All Rights Reserved

ABSTRACT

WASTE HEAT RECOVERY FROM A HIGH TEMPERATURE DIESEL ENGINE

Government-mandated improvements in fuel economy and emissions from internal combustion engines (ICEs) are driving innovation in engine efficiency. Though incremental efficiency gains have been achieved, most combustion engines are still only 30-40% efficient at best, with most of the remaining fuel energy being rejected to the environment as waste heat through engine coolant and exhaust gases. Attempts have been made to harness this waste heat and use it to drive a Rankine cycle and produce additional work to improve efficiency. Research on waste heat recovery (WHR) demonstrates that it is possible to improve overall efficiency by converting wasted heat into usable work, but relative gains in overall efficiency are typically minimal (~5-8%) and often do not justify the cost and space requirements of a WHR system. The primary limitation of the current state-of-the-art in WHR is the low temperature of the engine coolant (~90°C), which minimizes the WHR from a heat source that represents between 20% and 30% of the fuel energy.

The current research proposes increasing the engine coolant temperature to improve the utilization of coolant waste heat as one possible path to achieving greater WHR system effectiveness. An experiment was performed to evaluate the effects of running a diesel engine at elevated coolant temperatures and to estimate the efficiency benefits. An energy balance was performed on a modified 3-cylinder diesel engine at six different coolant temperatures (90°C, 100°C, 125°C, 150°C, 175°C, and 200°C) to determine the change in quantity and quality of waste heat as the coolant temperature increased. The waste heat was measured using the flow rates and temperature differences of the coolant, engine oil, and exhaust flow streams into and out of the

engine. Custom cooling and engine oil systems were fabricated to provide adequate adjustment to achieve target coolant and oil temperatures and large enough temperature differences across the engine to reduce uncertainty. Changes to exhaust emissions were recorded using a 5-gas analyzer. The engine condition was also monitored throughout the tests by engine compression testing, oil analysis, and a complete teardown and inspection after testing was completed. The integrity of the head gasket seal proved to be a significant problem and leakage of engine coolant into the combustion chamber was detected when testing ended. The post-test teardown revealed problems with oil breakdown at locations where temperatures were highest, with accompanying component wear.

The results from the experiment were then used as inputs for a WHR system model using ethanol as the working fluid, which provided estimates of system output and improvement in efficiency. Thermodynamic models were created for eight different WHR systems with coolant temperatures of 90°C, 150°C, 175°C, and 200°C and condenser temperatures of 60°C and 90°C at a single operating point of 3100 rpm and 24 N-m of torque. The models estimated that WHR output for both condenser temperatures would increase by over 100% when the coolant temperature was increased from 90°C to 200°C. This increased WHR output translated to relative efficiency gains as high as 31.0% for the 60°C condenser temperature and 24.2% for the 90°C condenser temperature over the baseline engine efficiency at 90°C. Individual heat exchanger models were created to estimate the footprint for a WHR system for each of the eight systems. When the coolant temperature increased from 90°C to 200°C, the total heat exchanger volume increased from $16.6 \times 10^3 \text{ cm}^3$ to $17.1 \times 10^3 \text{ cm}^3$ with a 60°C condenser temperature, but decreased from $15.1 \times 10^3 \text{ cm}^3$ to $14.2 \times 10^3 \text{ cm}^3$ with a 90°C condenser temperature. For all cases, increasing the coolant temperature resulted in an improvement in the efficiency gain for each cubic meter of heat

exchanger volume required. Additionally, the engine oil coolers represented a significant portion of the required heat exchanger volume due to abnormally low engine oil temperatures during the experiment ($\sim 80^{\circ}\text{C}$). Future studies should focus on allowing the engine oil to reach higher operating temperatures which would decrease the heat rejected to the engine oil and reduce the heat duty for the oil coolers resulting in reduced oil cooler volume.

ACKNOWLEDGEMENTS

First and foremost, I would like to thank my advisor, Dr. Todd Bandhauer, for giving me the opportunity to work on this fascinating and fulfilling project, and for guiding and encouraging me along the way. The lessons and confidence I gained in my time working with him will serve me throughout my career. In addition, I would like to thank the members of the Interdisciplinary Thermal Science Lab for their assistance with many of the details of this endeavor. Specifically, I want to thank Torben Grumstrup, Taylor Bevis, and Kevin Westhoff. I would also like to thank the staff of the Engines and Energy Conversion Lab for sharing their knowledge and expertise. I am also thankful for the advice, technical help, and coffee provided by my friend, Arun Lakshminarayanan. I would also like to thank Kelsey Bilsback for advice on data analysis and general moral support. Finally, I would like to thank my family and my fiancé, Pia Martiny, for their endless encouragement and support throughout this process.

TABLE OF CONTENTS

LIST OF TABLES	viii
LIST OF FIGURES	x
NOMENCLATURE	xv
CHAPTER 1. INTRODUCTION	1
1.1 Background	1
1.2 Research Objectives	5
1.3 Thesis Organization.....	6
CHAPTER 2. LITERATURE REVIEW	7
2.1 WHR Using Exhaust Gases.....	7
2.2 WHR Using Engine Coolant.....	19
2.3 Need for Further Research	30
CHAPTER 3. EXPERIMENTAL METHODS	32
3.1 Engine Modifications	32
3.2 Test Facility Overview	41
3.3 Test Matrix and Procedure	50
CHAPTER 4. DATA REDUCTION	56
4.1 Energy Balance	56
4.2 Waste Heat Availability	64
4.3 Correlations and Statistical Significance.....	66
CHAPTER 5. MODELING EFFORT	68
5.1 WHR System Design	68
5.2 Thermodynamic Analysis	71
5.3 Detailed System Modeling.....	84
CHAPTER 6. RESULTS AND DISCUSSION.....	134
6.1 Energy Balance	134
6.2 Engine Efficiency and Emissions.....	142
6.3 Engine Condition Monitoring	147
6.4 Modeling Results.....	158
CHAPTER 7. CONCLUSIONS AND RECOMMENDATIONS	185

7.1 Recommendations for Future Work	188
REFERENCES	190
APPENDIX A: INSTRUMENT CALIBRATION	194
A.1 Uncertainty in Measurements	194
A.2 Dynamometer	195
A.3 Thermocouples	196
A.4 Pressure Transducers	197
APPENDIX B: Uncertainty in Energy Balance Calculations.....	199
APPENDIX C: Engine component measurements	212

LIST OF TABLES

Table 2-1.	Summary of WHR studies (NA = not applicable, NR = not reported).	8
Table 3-1.	Test engine specifications [37]......	33
Table 3-2.	Measured piston ring end gaps.....	37
Table 3-3.	List of test facility equipment used for experiment.....	44
Table 3-4.	Instrumentation and property accuracy.	50
Table 3-5.	Test matrix for high-temperature diesel engine experiment.	52
Table 4-1.	Data for representative test point of 3100 rpm engine speed and 18 N-m of torque at 150°C coolant temperature.	57
Table 4-2.	Source and assumed uncertainty for fluid properties.	58
Table 4-3.	Energy balance results for representative point 3100 rpm, 18 N-m torque and 150°C coolant temperature.....	64
Table 5-1.	Thermodynamic analysis assumptions.....	72
Table 5-2.	Inputs for thermodynamic analysis.	73
Table 5-3.	Matrix of WHR operating points modeled.....	74
Table 5-4.	System pressure values for each of the modeled system configurations.	76
Table 5-5.	Thermodynamic model inputs for representative point of 3100 rpm, 24 N-m, 90°C coolant temperature, and 90°C condenser temperature with WHR from exhaust only.....	77
Table 5-6.	Thermodynamic model inputs for the representative point of 3100 rpm, 24 N-m, 150°C coolant temperature, and 90°C condenser temperature. This system utilizes both engine coolant and exhaust for WHR.	83
Table 5-7.	Detailed heat exchanger model assumptions.....	85
Table 5-8.	Heat exchanger model inputs.	85
Table 5-9.	Condenser model design and dimensions.	88
Table 5-10.	Condenser model inputs for the representative point of 3100 rpm, 24 N-m, 150°C coolant temperature, and 90°C condenser temperature.....	89
Table 5-11.	Evaporator model design and dimensions.....	103
Table 5-12.	Evaporator model inputs for the representative point of 3100 rpm, 24 N-m, 150°C coolant temperature, and 90°C condenser temperature.....	104
Table 5-13.	Superheater model design and dimensions.	114
Table 5-14.	Superheater model inputs for the representative point of 3100 rpm, 24 N-m, 150°C coolant temperature, and 90°C condenser temperature.....	114
Table 5-15.	Recuperator model design and dimensions.	120

Table 5-16.	Recuperator model inputs for the representative point of 3100 rpm, 24 N-m, 150°C coolant temperature, and 90°C condenser temperature.....	120
Table 5-17.	Oil cooler model design and dimensions.	124
Table 5-18.	Oil cooler model inputs for the representative point of 3100 rpm, 24 N-m, 150°C coolant temperature, and 90°C condenser temperature.....	125
Table 5-19.	Radiator model design and dimensions.....	132
Table 5-20.	Radiator model inputs for the representative point of 3100 rpm, 24 N-m, 90°C coolant temperature.	133
Table 6-1.	Relative efficiency gain for eight WHR system models	172
Table A-1.	Summary of dynamometer calibration results.....	196
Table A-2.	Summary of thermocouple calibration results.	197
Table A-3.	Summary of pressure transducer calibration results.	198
Table B-1.	Measurement and uncertainty data for orifice and pipe diameters.	207
Table B-2.	Uncertainty results for exhaust gas enthalpy calculations.	208
Table C-1.	Engine component measurements.	213

LIST OF FIGURES

Figure 1-1.	Energy balance for a typical diesel engine at high load [1-5].	1
Figure 1-2.	Rankine cycle waste heat recovery system components and T-S diagram [13].	3
Figure 2-1.	Combined evaporator and catalyst design (left) and resulting efficiency (right) [32].	9
Figure 2-2.	WHR system diagram showing the typical configuration and components [15].	12
Figure 2-3.	Configuration of WHR systems for EGR only and EGR and exhaust combined [34].	16
Figure 2-4.	Diagram of cylinder head modified specifically for WHR with the goal of increasing working fluid temperatures [32]. Modifications include special cooling passages around exhaust valves to recover waste heat at high temperatures (~190°C).	26
Figure 2-5.	Redesigned coolant passages used to recover heat from the top of the cylinders at 190°C [32].	27
Figure 3-1.	Custom copper cylinder head gasket.	34
Figure 3-2.	Engine block with stainless steel combustion chamber O-ring seals installed.	35
Figure 3-3.	Piston ring in cylinder bore with arrowing pointing to ring gap.	36
Figure 3-4.	Front (left) and rear (right) crankshaft seals that were replaced with high temperature Viton alternative.	38
Figure 3-5.	Heat shield for high pressure fuel pump.	39
Figure 3-6.	Engine timing gears with arrows showing crankshaft gear, idler gear, and oil pump gear.	40
Figure 3-7.	Removing oil pump drive shaft and pinion (left). Bolt used to plug oil pump shaft bore (right).	40
Figure 3-8.	Completed test facility including dynamometer controller in the bottom of the image.	42
Figure 3-9.	Diagram of test facility showing cooling and oil systems and all instrumentation.	43
Figure 3-10.	Internal gear pump used to pressurize cooling system.	45
Figure 3-11.	Brazed flat plate heat exchanger used to reject heat from primary coolant to secondary coolant.	46
Figure 3-12.	Adapter used to connect to custom cooling system installed in original water pump location.	47
Figure 3-13.	Locations of thermocouples used to monitor air temperature.	49

Figure 4-1.	Regression analysis results for 3100 rpm and 18 N-m of torque used to determine correlations between parameters and coolant temperature and their significance using a 95% confidence interval.	67
Figure 5-1.	Diagram for state-of-the-art WHR system.	69
Figure 5-2.	Diagram for high-temperature coolant WHR systems.	70
Figure 5-3.	Flow chart for thermodynamic analysis.	71
Figure 5-4.	Graphic representation of WHR system optimization strategy. WHR system output is maximized through increasing superheat (up to 375°C maximum) while maintaining at least a 5° CAT in the exhaust evaporator.	75
Figure 5-5.	Diagram showing the cross-flow condenser configuration as well as single-phase and two-phase sections.	86
Figure 5-6.	Diagram showing condenser construction with two rows of horizontal tubes separated by louvered fins.	87
Figure 5-7.	Condenser tube configuration and dimensions in mm.	90
Figure 5-8.	Left: Cross-section of condenser fin showing louver angle and pitch. Right: Side view of condenser assembly showing louver length and fin pitch.	90
Figure 5-9.	Plot of ethanol heat transfer coefficient in the condenser vs. the cumulative heat duty. The plot starts with the single-phase section (first point) and proceeds through the two-phase section as the cumulative heat duty increases. The representative point is the first point in the two-phase section.	100
Figure 5-10.	Cumulative condenser length vs. cumulative heat duty starting with vapor inlet and ending with 100% liquid ethanol.	101
Figure 5-11.	Diagram showing the counter-flow evaporator configuration.	102
Figure 5-12.	Diagram showing evaporator construction with ethanol channels on the outside and exhaust channels running in the center.	105
Figure 5-13.	Left: Cross-section of ethanol channels in evaporator. Right: Cross-section of exhaust channels in exhaust evaporator.	106
Figure 5-14.	Plot of ethanol heat transfer coefficient in the evaporator vs. the cumulative heat duty. The plot starts with the single-phase section (first point) and proceeds through the two-phase section as the cumulative heat duty increases.	110
Figure 5-15.	Cumulative evaporator length vs. cumulative heat duty starting with liquid inlet and ending with 100% ethanol vapor.	112
Figure 5-16.	Diagram showing cross-flow superheater configuration.	115
Figure 5-17.	Diagram showing superheater construction with ethanol channels on the outside and exhaust channels running in the center.	115
Figure 5-18.	Left: Cross-section of ethanol channels in superheater. Right: Cross-section of exhaust channels in superheater.	116
Figure 5-19.	Diagram showing counter-flow recuperator configuration.	119

Figure 5-20. Diagram showing recuperator construction with liquid channels on the outside and vapor channels running in the center.....	121
Figure 5-21. Left: Cross-section of liquid channels in recuperator. Right: Cross-section of vapor channels in recuperator.....	122
Figure 5-22. Diagram showing cross-flow engine oil cooler configuration.	126
Figure 5-23. Diagram showing oil cooler construction with one row of tubes separated by louvered fins.....	126
Figure 5-24. Oil cooler tube configuration and dimensions in mm.	126
Figure 5-25. Diagram showing cross-flow radiator configuration.	129
Figure 5-26. Diagram showing radiator construction with one row of tubes separated by louvered fins.....	130
Figure 5-27. Radiator tube configuration and dimensions in mm.	131
Figure 6-1. Results of energy balance on the test engine at 3100 rpm and 18 N-m of torque showing absolute values (top) and values as a percentage of fuel energy entering the engine (bottom).	136
Figure 6-2. Comparison of leakage rates for engine oil and HTF with fuel flow and engine brake efficiency for 3100 rpm and 18 N-m of torque.	138
Figure 6-3. Waste heat from engine coolant and exhaust with the corresponding exergy for each source at 3100 rpm and 18 N-m of torque (top), and 3100 rpm and 24 N-m of torque (bottom).....	140
Figure 6-4. Exhaust temperatures for five load points over the measured coolant temperature range at an engine speed of 3100 rpm.	141
Figure 6-5. Engine efficiency for 3100 rpm at five load points over the measured coolant temperature range.....	142
Figure 6-6. Exhaust emissions data with mass air flow rate at 3100 rpm and 18 N-m of torque.	145
Figure 6-7. Cylinder compression test results over the course of testing. Compression tests were performed with the engine cold after completion of testing for the given temperature.....	149
Figure 6-8. Image of engine block to head gasket mating surface with coolant passages and signs of leakage noted.	150
Figure 6-9. Image of copper head gasket after testing was completed. Arrows indicate coolant passages and discoloration from HTF leaking into combustion chamber.....	151
Figure 6-10. Image of copper cylinder head gasket showing pressurized oil passage and external leakage path.	151
Figure 6-11. Cylinder head surface above the combustion chamber for each of the three cylinders. The liquid present on the combustion chamber surfaces suggests HTF leakage was most severe in cylinder 2 and negligible in cylinder 3.	152

Figure 6-12. Oil analysis results including metal content in parts per million per hour and oxidation in spectral absorbance units.	152
Figure 6-13. Documentation of piston condition showing piston from cylinder 1 before (top) and after (bottom) testing.	154
Figure 6-14. Example of scuffing of cylinder surface on thrust side of cylinder 1 bore.	155
Figure 6-15. Photos of a) piston pin bore, b) piston pin, c) connecting rod pin bushing before testing, and d) connecting rod pin bushing after testing.....	156
Figure 6-16. Photos cylinder 2 exhaust valve lifter, a) before testing and b) after testing.	157
Figure 6-17. Photos of camshaft before (a) and after (b) testing with arrow indicating slight wear from insufficient lubrication at sliding contact between lobe and lifter.....	158
Figure 6-18. WHR system diagram for 90°C coolant and 60°C condenser temperature with results from the thermodynamic analysis. Note that underlined temperatures are predetermined values entered into the model as constants.	160
Figure 6-19. T-s diagram for 90°C coolant and 60°C condenser temperature WHR system. The exhaust temperature is shown in red and the working fluid shown in blue.	160
Figure 6-20. WHR system diagram for 90°C coolant and 90°C condenser temperature with results from the thermodynamic analysis.....	162
Figure 6-21. T-s diagram for 90°C coolant and 90°C condenser temperature WHR system. The exhaust temperature is shown in red and the working fluid shown in blue.	162
Figure 6-22. WHR system diagram for 150°C coolant and 60°C condenser temperature with results from the thermodynamic analysis.....	164
Figure 6-23. T-s diagram for 150°C coolant and 60°C condenser temperature WHR system. The exhaust temperature is shown in red and the working fluid shown in blue.	164
Figure 6-24. WHR system diagram for 150°C coolant and 90°C condenser temperature with results from the thermodynamic analysis.....	166
Figure 6-25. T-s diagram for 150°C coolant and 90°C condenser temperature WHR system. The exhaust temperature is shown in red and the working fluid shown in blue.	166
Figure 6-26. WHR system diagram for 175°C coolant and 60°C condenser temperature with results from the thermodynamic analysis.....	167
Figure 6-27. T-s diagram for 175°C coolant and 60°C condenser temperature WHR system. The exhaust temperature is shown in red and the working fluid shown in blue.	167
Figure 6-28. WHR system diagram for 175°C coolant and 90°C condenser temperature with results from the thermodynamic analysis.....	169
Figure 6-29. T-s diagram for 175°C coolant and 90°C condenser temperature WHR system. The exhaust temperature is shown in red and the working fluid shown in blue.	169
Figure 6-30. WHR system diagram for 200°C coolant and 60°C condenser temperature with results from the thermodynamic analysis.....	170

Figure 6-31. T-s diagram for 200°C coolant and 60°C condenser temperature WHR system. The exhaust temperature is shown in red and the working fluid shown in blue.	170
Figure 6-32. WHR system diagram for 200°C coolant and 90°C condenser temperature with results from the thermodynamic analysis.	171
Figure 6-33. T-s diagram for 200°C coolant and 90°C condenser temperature WHR system. The exhaust temperature is shown in red and the working fluid shown in blue.	171
Figure 6-34. Waste heat recovery model power output results for 3100 rpm and 24 N-m of torque.	173
Figure 6-35. Relative efficiency gain of WHR system over 90°C engine efficiency for each temperature at 3100 rpm and 24 N-m of torque.	174
Figure 6-36. Footprint of heat exchangers for 60°C condenser temperature and 90°C coolant temperature WHR system (dimensions in mm).	176
Figure 6-37. Footprint of heat exchangers for 90° condenser temperature and 90°C coolant temperature WHR system (dimensions in mm).	176
Figure 6-38. Footprint of heat exchangers for 60°C condenser temperature and 150°C coolant temperature WHR system (dimensions in mm).	177
Figure 6-39. Footprint of heat exchangers for 90°C condenser temperature and 150°C coolant temperature WHR system (dimensions in mm).	177
Figure 6-40. Footprint of heat exchangers for 60°C condenser temperature and 175°C coolant temperature WHR system (dimensions in mm).	178
Figure 6-41. Footprint of heat exchangers for 90°C condenser temperature and 175°C coolant temperature WHR system (dimensions in mm).	178
Figure 6-42. Footprint of heat exchangers for 60°C condenser temperature and 200°C coolant temperature WHR system (dimensions in mm).	179
Figure 6-43. Footprint of heat exchangers for 90°C condenser temperature and 200°C coolant temperature WHR system (dimensions in mm).	179
Figure 6-44. Total heat exchanger volume for all modeled system.	180
Figure 6-45. Volume of each heat exchanger for 60°C condenser temperature systems.	181
Figure 6-46. Volume of each heat exchanger for 90°C condenser temperature systems.	181
Figure 6-47. Total heat exchanger volume and efficiency increase for 60°C condenser temperature systems.	182
Figure 6-48. Total heat exchanger volume and efficiency increase for 90°C condenser temperature systems.	183
Figure 6-49. Efficiency benefit per total heat exchanger volume for condenser temperatures of 60°C and 90°C.	184

NOMENCLATURE

Symbol	Description	Units	Dimensionless Number Expression
A	Area	m^2	
\dot{B}	Exergy exchange rate	kW	
BTE	Brake thermal efficiency	-	
c_p	Specific heat capacity	$kJ\ kg^{-1}\ K^{-1}$	
C	Heat capacity rate	$kJ\ K^{-1}\ s^{-1}$	
C_{CO}	Concentration of carbon monoxide in exhaust	-	
C_{CO_2}	Concentration of carbon dioxide in exhaust	-	
C_{THC}	Concentration of hydrocarbons in exhaust	-	
C_r	Heat capacity ratio	-	C_{min}/C_{max}
CAT	Closest approach temperature	$^{\circ}C$	
Ch	Chisolm parameter	-	
Co	Confinement number	-	$(\sigma/(g(\rho_l-\rho_g)D_h^2))^{1/2}$
CSU	Colorado State University	-	
d	Distance	m	
D	Diameter	m	
e	Absolute roughness	m	
\dot{E}	Energy flow rate	kW	
$EECL$	Engines and Energy Conversion Laboratory	-	
f	Darcy friction factor	-	

Fr	Froude number	-	$G/(gD\rho)$
g	Acceleration due to gravity	$m\ s^{-2}$	
G	Mass velocity	$kg\ m^{-2}\ s^{-1}$	
h	Heat transfer coefficient	$kW\ m^{-2}\ K^{-1}$	
h_{ch}	Channel height	mm	
$h_{wf,i}$	Enthalpy of working fluid at point i	$kJ\ kg^{-1}$	
$h_{wf,i,s}$	Isentropic enthalpy of working fluid at point i	$kJ\ kg^{-1}$	
$h_{wf,i,j}$	Enthalpy of working fluid with temperature at point i and pressure at point j	$kJ\ kg^{-1}$	
j	Colburn j factor	-	$StPr^{2/3}$
k	Thermal conductivity	$kW\ m^{-1}\ K^{-1}$	
k_p	Coverage factor	-	
L	Length	m	
La	Laplace number	-	$[\sigma/(g(\rho_l-\rho_g))]^{0.5}/D_h$
LHV	Lower heating value	$kJ\ kg^{-1}$	
m	Mass	kg	
\dot{m}	Mass flow rate	$kg\ s^{-1}$	
MF	Mass fraction	-	
MW	Molecular weight	$kg\ kmol^{-1}$	
n	Number of samples	-	
\dot{n}	Molar flow rate	$kmol\ s^{-1}$	
N	Engine speed	rpm	
N_{ch}	Number of channels in a tube	-	

N_f	Fin count	-	
N_{row}	Number of rows in heat exchanger	-	
N_t	Number of tubes in a row	-	
NTU	Number of transfer units	-	UA/C_{min}
p	Pitch	m	
P	Pressure	kPa	
P_c	Critical pressure	kPa	
Pe	Perimeter	m	
Pr	Prandtl number	-	ν/α
P_r	Reduced pressure	-	P/P_{crit}
q''	Heat flux	$W\ m^{-2}$	
Q	Heat transfer	kJ	
\dot{Q}	Heat transfer rate	kW	
r	Resolution	-	
R	Thermal resistance	$K\ kW^{-1}$	
R_{air}	Specific gas constant for air	$kJ\ kg^{-1}\ K^{-1}$	
R_{cor}	Correlation coefficient	-	
R_p	Surface roughness parameter	μm	
Re	Reynold's number	-	$\nu L/\nu$
Re_L	Reynold's number assuming all flow is liquid	-	GD/μ_1
SEE	Sum of Experimental Error	-	
St	Stanton number	-	h/Gc_p

t	Thickness	m	
t -value	Test statistic	-	
t_{test}	Recorded test duration	s	
T	Temperature	K	
\bar{T}	Average temperature	K	
u	Standard uncertainty	-	
u_c	Combined uncertainty	-	
U	Overall heat transfer coefficient	$\text{W m}^{-2} \text{K}^{-1}$	
v	Velocity	m s^{-1}	
V	Volume	m^3	
\dot{V}	Volumetric flow rate	$\text{m}^3 \text{s}^{-1}$	
w	Width	mm	
\dot{W}_{out}	Engine power output	kW	
x	Quality	-	
x_c	Number of carbon atoms in fuel molecule	-	
y_{H}	Number of hydrogen atoms in fuel molecule	-	
Greek Symbols			
α_r	Channel aspect ratio	-	$w_{\text{ch}}/h_{\text{ch}}$
ε	Heat exchanger effectiveness	-	
η_{Carnot}	Carnot efficiency	-	$1 - T_{\text{L}}/\bar{T}_{\text{H}}$
$\eta_{\text{pump,s}}$	Isentropic pump efficiency	-	
$\eta_{\text{turb,s}}$	Isentropic turbine efficiency	-	

η_f	Fin efficiency	-	
η_o	Fin array efficiency	-	
θ	Louver angle	degrees	
μ	Dynamic viscosity for liquid flow	Pa-s	
ρ	Density	kg m ⁻³	
τ	Torque	N-m	
Φ	Two-phase multiplier	-	
χ	Martinelli parameter	-	
Subscripts			
air	Air		
abs	Absolute		
avg	Average		
b	Brake		
c	Corrected		
ch	Channel		
comb	Combined		
cond	Condenser		
conv	Convection		
cool	Coolant		
cyl	Cylinder		
d	Displacement		
eng	Engine		

eth	Ethanol		
exh	Exhaust		
evap	Evaporator		
f	Fin		
FB	Flow boiling		
g	Gas phase		
go	Gas phase only		
h	Hydraulic		
ht	Heat transfer		
H	High		
HC	Hydrocarbon		
HTF	Heat transfer fluid		
i	Inlet		
in	Inner		
int	Intake		
l	Liquid phase		
lo	Liquid phase only		
lv	Louver		
L	Low		
m	Major		
max	Maximum		
min	Minimum		

NB	Nucleate boiling		
oc	Oil cooler		
oth	Other		
out	Outer		
r	Ratio		
rad	Radiation		
ran	Random		
rec	Recuperator		
s	Surface		
sh	Superheater		
sp	Single-phase		
st	Start		
sys	Systematic		
t	Tube		
tot	Total		
tp	Two-phase		
turb	Turbine		
v	Volumetric		
w	Wall		
wet	Wetted		

CHAPTER 1. INTRODUCTION

1.1 Background

Government-mandated improvements in fuel economy and emissions from internal combustion engines (ICEs) are driving innovation in engine efficiency [6-11]. ICEs convert chemical energy contained in fuels into mechanical work via the combustion of the fuel mixed with air. The resulting thermal expansion of gases due to heat released from the ignition of the fuel and air mixture does work on a piston which in turn acts on a crankshaft to create torque. The ratio of the work output at the crankshaft to the fuel energy input is known as the brake efficiency of an ICE. An energy balance for a typical diesel engine is shown in Figure 1-1. The figure shows that only 30-40% of the fuel energy is converted into mechanical work, with the rest of the energy wasted through various losses. In Figure 1-1, these losses are broken up into heat loss to the exhaust gases, heat loss to the engine coolant, and all other losses. Other losses include incomplete combustion, pumping losses, friction, and heat loss to the environment through the engine oil and

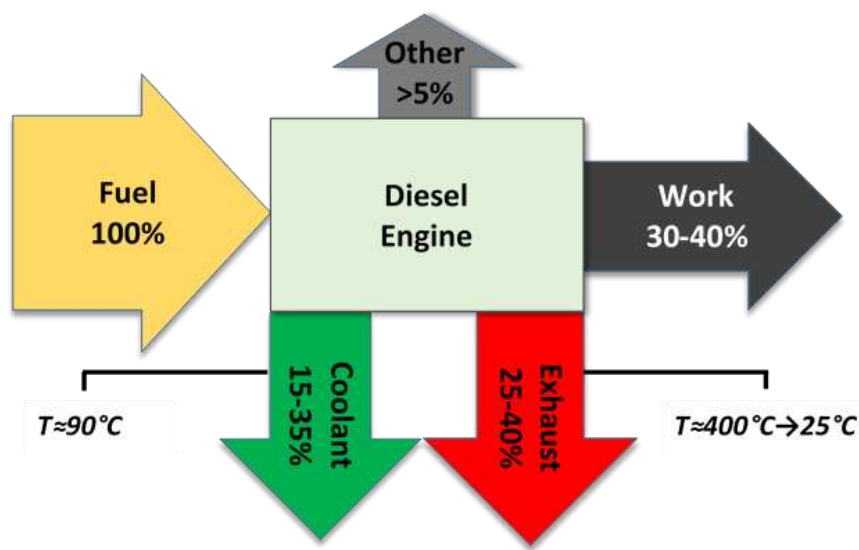


Figure 1-1. Energy balance for a typical diesel engine at high load [1-5].

engine structure, and many of the incremental gains in modern engine efficiency were realized through reductions in the losses from this category. The combustion efficiency of modern ICEs has been improved through high energy ignition systems, advanced combustion chamber designs, and high-pressure direct fuel injection. Combustion efficiency typically exceeds 97% in typical applications, leaving little room for improvement [12]. Pumping losses arise from the restrictions between the ambient air supply and the cylinder, namely throttles, intake plumbing, and intake valves. Pumping losses in diesel engine tend to be lower than spark ignited engines since they do not usually require throttles to regulate engine output, but instead regulate fuel injection to attain the target output. Figure 1-1 demonstrates that the sum of these ‘other’ losses is a relatively small fraction of the fuel energy flowing into the engine, and that the heat rejected to the ambient surroundings via the engine coolant and exhaust gases accounts for the vast majority of losses in an ICE.

With between 50 and 60 percent of the fuel energy being lost as waste heat, it is no wonder that research on harnessing this energy and converting it to additional work has been plentiful. This is typically accomplished by using a heat engine such as a Rankine cycle to recover the waste heat and produce additional output. The basic waste heat recovery (WHR) system components and the Rankine cycle represented on a T-S diagram are shown in Figure 1-2. Four primary components are required to complete the cycle: a pump, a boiler, an expander, and a condenser. The pump pressurizes the working fluid, shown by the increase in temperature from point 1 to point 2 in the T-S diagram. The boiler transfers heat from the waste heat source to the working fluid and acts as the high-temperature reservoir for the heat engine. As heat is added to the working fluid, the temperature increases up to the saturation point, where evaporation occurs at constant temperature under the vapor dome. As the diagram shows, additional heat may be added after the working fluid

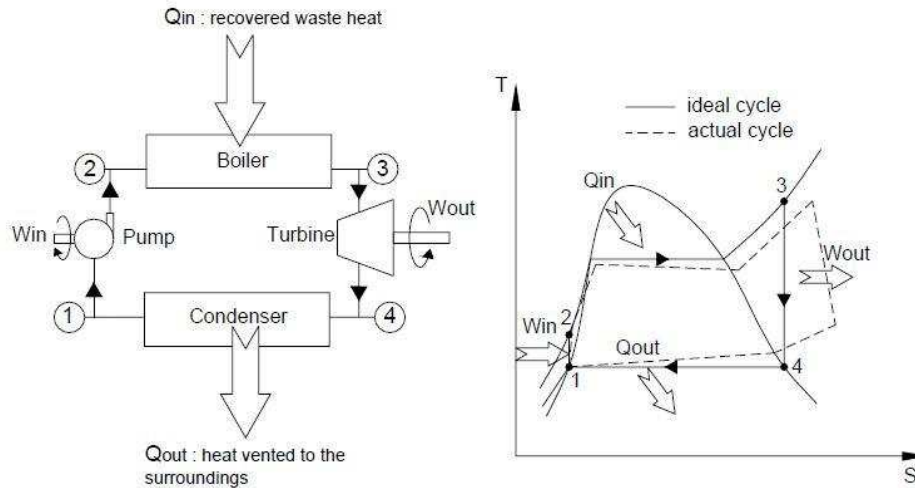


Figure 1-2. Rankine cycle waste heat recovery system components and T-S diagram [13].

has been converted entirely to vapor, resulting in superheating of the working fluid up to point 3. In addition to increasing enthalpy, superheating can be beneficial by preventing droplet formation inside of the expander as volume increases and temperature drops from point 3 to point 4. Finally, heat must be transferred from the working fluid to the environment via the condenser acting as the heat sink, returning the working fluid to a liquid state at point 1.

As shown in Figure 1-1, the exhaust waste heat represents a large percentage of the energy loss in the engine. This fact, coupled with the high gas temperatures, make exhaust the preferred source for WHR in most prior investigations. However, the exhaust gases are somewhat limited as a heat source due to their relatively low heat capacity rate, which is the product of the mass flow rate and its specific heat. Because these values are low for the exhaust gas, it must be cooled significantly to extract enough available energy to provide meaningful mechanical work. For example, in some configurations, the exhaust gas is cooled by 160-350°C and increases the relative brake power by at most 14.3% [2, 14-19]. In contrast, the engine coolant recirculates through the engine and the radiator at a high mass flow rate and has a higher specific heat than the exhaust gas

(i.e., 3-4 kJ kg⁻¹ K⁻¹ vs. 1-2 kJ kg⁻¹ K⁻¹ [18, 20, 21]). As a result, rejecting coolant heat requires a minimal temperature change, whereas the exhaust requires a large temperature change to reject the same amount of heat. However, the major limitation of WHR from engine coolant is its low temperature (~90°C), which greatly decreases the amount of coolant waste heat that can be utilized. If the temperature of the engine coolant is increased, the potential for heat rejected from the coolant to produce work increases. The Carnot efficiency is the maximum possible efficiency of a heat engine and is defined as follows:

$$\eta_{\text{Carnot}} = 1 - \frac{T_L}{T_H} \quad (1.1)$$

The Carnot efficiency depends on the average temperature of the heat source (\bar{T}_H) and the temperature of the heat sink (T_L), both in absolute units. Although no real WHR system can achieve the Carnot efficiency limit, it is useful to consider for demonstrating the potential to improve WHR by increasing the coolant temperature. For example, the heat sink for a Rankine cycle WHR system is the condenser, which is assumed to be 50°C (i.e., 323.15 K). With engine coolant as the heat source at a typical temperature of 90°C, the Carnot efficiency is 11%. If 30% of the incoming fuel energy is rejected to the coolant, this means that the maximum possible relative efficiency improvement is 11% for a 30% efficient engine (i.e., 11% × 30% ÷ 30%). However, if the coolant temperature is increased to 200°C, the Carnot efficiency jumps to 32%, which increases the maximum possible relative efficiency improvement by the same amount, which is well above any prior WHR engine studies using exhaust as the only heat source.

Packaging and cost are also important factors in the feasibility of using WHR to increase ICE efficiency. The heat exchanger footprints have the greatest effect on overall package size, and their design must balance size with ability to effectively transfer heat. For equivalent designs, greater heat transfer rates will require larger heat exchangers, which means recovering the

additional waste heat from high-temperature coolant can significantly increase the WHR system size and cost. One way to minimize this effect is to use the engine block as an evaporator and utilize the WHR working fluid as the engine coolant. This design eliminates the need for a second evaporator and thereby reduces the size and cost impact of the WHR system. In addition, the thermal resistance between the engine and the working fluid is decreased, which further improves the utilization of the waste heat from the engine. Using the engine cooling passages as an evaporator means that heat is removed from the engine via phase change rather than temperature change of the coolant. Phase change cooling has a number of advantages over traditional cooling systems in automotive applications. First, since boiling occurs at a constant temperature, the temperature of the engine structure tends to be more uniform which increases engine longevity [22]. Additionally, the high heat transfer coefficients during boiling allow for a reduction in coolant mass flow rate, thus lowering the coolant pump power requirements. Finally, phase change cooling allows for faster warm-up times which can lower fuel consumption and emissions [23].

1.2 Research Objectives

The main objective of the current research is to investigate the benefits and feasibility of WHR from a high-temperature diesel engine as a means to dramatically increase overall system efficiency. The state-of-the-art WHR systems offer relative efficiency gains of approximately 5 to 8%. Though no specific efficiency goal was set for this work, initial calculations suggested efficiency gains of 3X the state of the art are possible. The target of the current research is to understand how operation at elevated temperatures effects engine performance and longevity. An energy balance was performed on a modified 3-cylinder diesel engine at coolant temperatures of 90°C, 100°C, 125°C, 150°C, 175°C, and 200°C. The condition of the engine was monitored throughout testing and the engine was disassembled after the experiment was complete to inspect

for any damage. The results from the experiment were then used to estimate the output from a theoretical WHR system as well as estimate the required footprint at various coolant temperatures.

1.3 Thesis Organization

This thesis is organized into the following chapters. A review of the available literature on WHR from ICEs is presented in Chapter two, followed by an in-depth description of the experimental setup in Chapter three. Chapter four covers the data analysis methods used to reduce the data and includes sample calculations. The modeling effort is detailed in Chapter five, where descriptions of each model and the correlations used are presented. Chapter six presents the results of the experiment and modeling effort, as well as a discussion of these results. Chapter seven contains the conclusions drawn from the project, and recommendations for future work. The references for sources cited in the work are listed in Chapter eight. The appendices contain information on instrument calibration (Appendix A), uncertainty calculations (Appendix B), and engine component measurements taken before and after testing (Appendix C).

CHAPTER 2. LITERATURE REVIEW

Researchers have been investigating the potential of WHR systems to improve ICE efficiency for over 20 years. This literature review will provide an overview of the relevant work in this field and concentrate specifically on the recovery of waste heat from ICEs using a Rankine cycle. The Rankine cycle is the primary method of WHR in the literature due to its efficiency using low to medium grade heat sources and its relative simplicity [24]. Inspection of prior research reveals that investigators have successfully implemented WHR systems and shown efficiency gains. However, the improvements in overall efficiency have been minimal compared to the additional cost and space required for a WHR system. The existing body of work on the subject of WHR shows that there are inherent difficulties in recovering waste heat from ICEs, and that these obstacles have yet to be overcome.

This literature review will be presented in two sections: WHR using exhaust gases and WHR using engine coolant. The section on exhaust gases includes recovery from the primary exhaust stream, as well as recovery from the exhaust gas recirculation (EGR) system. The section on coolant as a heat source will cover WHR at a typical coolant temperature of 90°C as well as WHR at elevated coolant temperatures. The objective of the following literature survey is to understand the current state of the art and provide a context for the work in the present study.

2.1 WHR Using Exhaust Gases

A summary of relevant literature on previous WHR studies is presented in Table 2-1, with details on the WHR sources, exhaust temperature, coolant temperature, working fluid, and efficiency gains. The vast majority of studies on WHR from ICEs use the exhaust gas heat as the primary heat source. The exhaust gases from combustion represent the highest temperature waste

Table 2-1. Summary of WHR studies (NA = not applicable, NR = not reported).

Author	WHR Source(s)	Exhaust Temp	Coolant Temp	Conditions	Working Fluid	Model/Exp	Efficiency Increase
Delgado and Lutsey Daimler[25]	Exhaust	Unknown	Normal	Steady State	Ethanol	Experiment	2.8% Max.
Teng et al. [21]	Exhaust, EGR	688°C	NA	Steady State	Dry Organic Fluid	Model	4.2% Max.
Fu et al. [26]	Exhaust	674-923°C	NA	Steady State	Water	Model	5.3-6.8%
Kadota and Yamamoto [27]	Exhaust	Unknown	NA	Drive Cycle	Water	Model/Exp	6.1% Avg.
Katta et al. [22]	Exhaust, Coolant	400°C	110°C	Steady State	Water	Model/Exp	4.3-6.2%
Boretti [28]	Exhaust, Coolant	Unknown	Normal	Steady State	Water	Model/Exp	6.4%
Srinivasan et al. [18]	Exhaust	279°C	NA	Steady State	R113	Model	7% Avg.
Fu et al. [29]	Exhaust	627°C	NA	Steady State	Water	Model	7.2%
Delgado and Lutsey Cummins [25]	Exhaust, EGR	Unknown	Normal	Steady State	Unknown	Experiment	7.6% Max.
Edwards and Wagner [30]	Exhaust, EGR	355°C	Normal	Steady State	R245fa	Model	8.6% Max.
Schmid [19]	Exhaust	320°C	85°C	Steady State	Water	Model	8.76-9.60%
Ringler [31]	Exhaust, Coolant	500-800°C	115°C	Steady State	Ethanol	Model/Exp	10% Avg.
Wenzhi et al. [15]	Exhaust	533°C	Normal	Steady State	Water	Model	12% Max.
Vaja and Gambarotta [17]	Exhaust, Coolant	477°C	Normal	Steady State	Benzene, R11, R134a	Model	12.6% max.
Arias et al. [1]	Exhaust	~600°C	NA	Steady State	Water	Model	10.1% Max.
Arias et al. [1]	Exhaust, Coolant	~600°C	80-120°C	Steady State	Water	Model	10.2% Max.
Endo et al. [32]	Exhaust	~650°C	Normal	Steady State	Water	Experiment	13.2%
Endo et al. [32]	Exhaust, Coolant	NR	189°C	NR	Water	Experiment	NR
Arias et al. [1]	Exhaust, Coolant	~400°C	300°C	Drive Cycle	Water	Model	22% Max.
Arias et al. [1]	Exhaust, Coolant	~600°C	300°C	Steady State	Water	Model	32% Max.

heat source available from an ICE, and, therefore, offer the greatest recovery potential. In addition to using post-catalyst exhaust gases, some researchers evaluated WHR from EGR systems as well. Even when using the same heat source, WHR system design and implementation vary from study to study so direct comparison is difficult. However, the primary purpose of this section is to provide a representative sample of the efficiency gains possible when exhaust gases are the exclusive WHR source.

The addition of an exhaust heat exchanger creates packaging issues in light-duty automotive applications. Endo et al. [32] (Honda R&D) attempted to overcome this limitation by combining the heat exchanger and catalyst into a single unit as shown on the left in Figure 2-1. The resulting evaporator/catalyst was only 1.8 times the size of a traditional catalyst. Additionally, the heat from the catalyst reaction could be utilized to supplement the exhaust heat, allowing an effective evaporator efficiency of over 90% despite the small size of the heat exchanger. Since the evaporator efficiency is simply the steam energy leaving the evaporator divided by the heat energy in the entering exhaust gases, any additional heat generated by the catalyst reaction and transferred

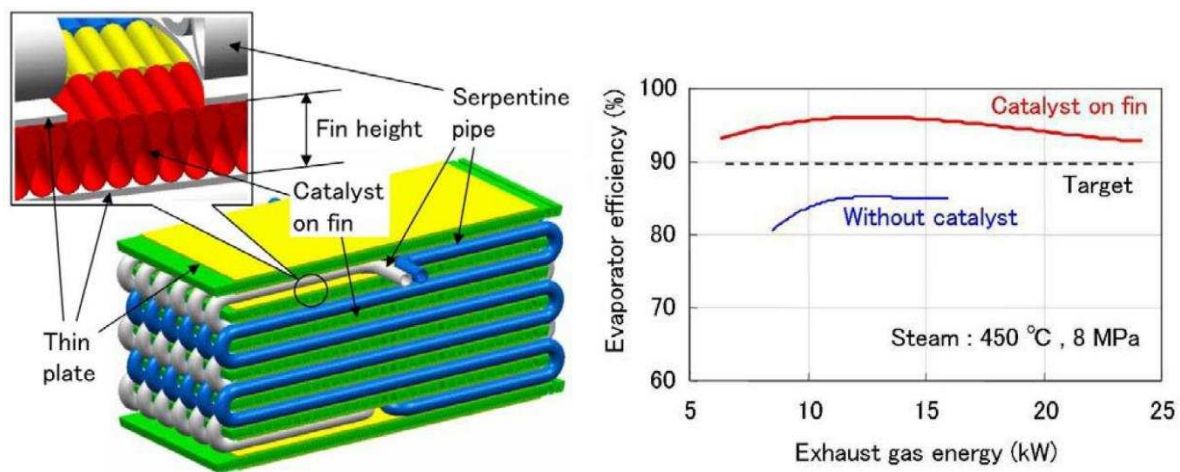


Figure 2-1. Combined evaporator and catalyst design (left) and resulting efficiency (right) [32].

to the working fluid results in an apparent efficiency increase. This can be compared to the efficiency of the design without the catalyst incorporated, which was roughly 10% lower as shown on the right in Figure 2-1. The authors installed a WHR system using this evaporator design in a Honda Civic Hybrid, with a generator driven by a swash plate axial expander producing electricity, which was fed into the hybrid drive system. At 100 km/h steady state operation, Endo et al. estimated that the thermal efficiency increased from 28.9% to 32.7%, or a 13.2% relative increase. This is an impressive result, but average efficiency gains over a typical drive cycle are not reported and would be more meaningful since an automobile only spends a fraction of the time at steady state. However, these results do highlight the potential for WHR systems to complement hybrid powertrains by producing power when charging of the hybrid battery is at a minimum (i.e., highway driving). The location and design of the evaporator may be a large factor contributing to the relatively large efficiency increase. Typical systems would have to recover heat from the exhaust post-catalyst, resulting in decreased exhaust temperatures. Additionally, the cost and durability of such a unit is unknown.

Kadota and Yamamoto [27], also at Honda R&D, did simulate the transient behavior of a WHR equipped Honda Civic Hybrid using a sophisticated test bench with a combination of real and modeled components that communicate and interact much like on a real vehicle. Real components consisted of the engine and WHR system, while the simulated components included the hybrid electric motor, hybrid battery, transmission, vehicle, and the driver. The engine, exhaust, steam, and expander output were simulated over the Japanese 10-15 drive cycle, which mimics a typical driving pattern for urban Japan [33]. Modeled components were validated using data from an actual vehicle operated over the same drive cycle, and fuel economy was found to be within $\pm 1\%$. The validated model predicted that average thermal efficiency would increase from

29.5% to 31.3%, giving a 6.1% relative increase. The authors noted that peak steam generation experienced a five second delay after peak engine output, which may translate to drivability issues. Few details are presented on the actual WHR system used for the model. The system diagram indicates that it is a basic Rankine system using the heat from the exhaust gases only. However, there is no mention of the exhaust gas temperatures during the simulation.

Through financial support from the National Basic Research Program of China, Wenzhi et al. [15] attempted to improve WHR system performance by optimizing the running conditions for a reciprocating piston expander. Extensive modeling was performed on a Rankine cycle WHR system using water as the working fluid and recovering waste heat from the exhaust gases of a 3.9L 4-cyl turbo diesel via a separate preheater and super heater as shown in Figure 2-2. The authors used REFPROP 7.0 to determine the thermodynamic conditions of the working fluid, with steam modeled as a real gas. The WHR system was evaluated with power output, expander efficiency, and global efficiency as a function of expander speed, mass flow rate, and expander intake pressure. Wenzhi et al. estimated that a maximum increase in overall power output of 12% would occur at 4 MPa of intake pressure, 0.018 kg/s mass flow rate, and an expander speed of 2000 rpm. This translates into a 12% relative increase in thermal efficiency of the combined system. However, the authors failed to achieve these conditions with the experimental setup they designed to validate the model. The maximum expander inlet pressure was limited to 0.35 MPa, which is only a fraction of the target pressure. The authors attribute this low intake pressure to heat exchangers that did not meet the design parameters set in the model. It is unclear why the heat exchangers did not adhere to the design specifications, but Wenzhi et al. reran the model under the experimental conditions and found the calculated output to be 10% higher than the experimental value. The authors cite expander friction, leakage loss, and generator loss as the causes of the

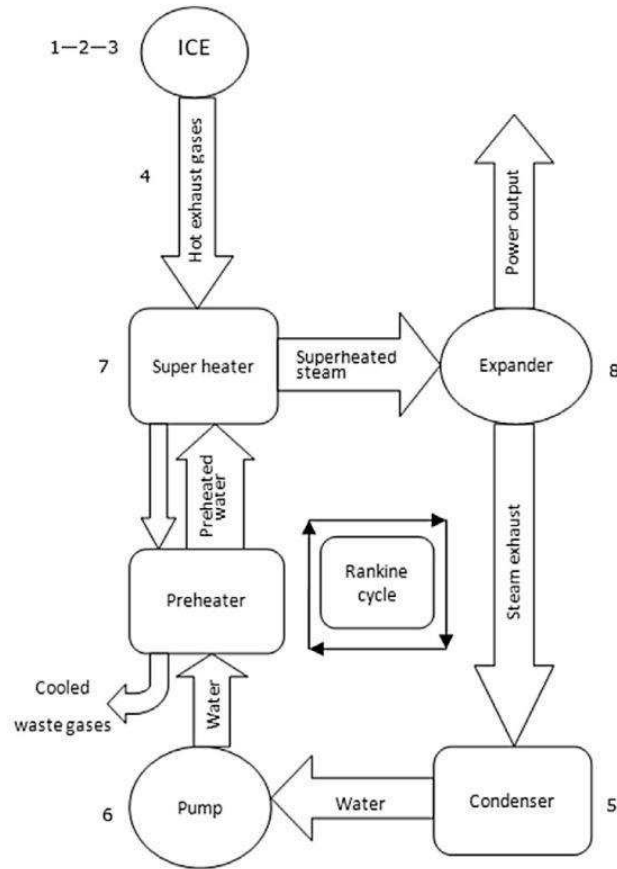


Figure 2-2. WHR system diagram showing the typical configuration and components [15].

discrepancy. The model clearly overestimates the WHR system output and further experimental validation would be needed to determine the validity of the model at target conditions.

WHR is an important part of current research to improve the efficiency of long-haul Class 8 diesel trucks. High diesel prices greatly impact the costs of goods transported by these trucks and there is significant interest in technology that can reduce fuel consumption. In 2014, Delgado and Lutsey [25] reported the results to date of the joint-funded SuperTruck program, which aims to drive new technologies that could increase diesel truck efficiency and reduce emissions. One of the major goals of the program is to reach an engine brake thermal efficiency (BTE) of 50%. An additional goal is to describe an approach to eventually reach 55% BTE using modeling and analysis. Each manufacturer selected their own baseline vehicle with the guideline of using their

“best-in-class” 2009 model truck. This means that the BTE for each manufacturer’s baseline truck was different, and only the average values for the four manufacturers were included in the report. Therefore, the authors assumed a baseline BTE of 42% for all manufacturers when calculating efficiency improvements. Four major manufacturers participated in the program including: Cummins, Daimler, Navistar, and Volvo. Of the four participants, all but Navistar chose to use some form of organic Rankine cycle (ORC) WHR as part of their approach. According to the report, Volvo has performed some initial testing with WHR, but has not completed installation in a test vehicle, and, therefore, no data was available. The results from Cummins and Daimler will now be covered.

At the time of the report, only Cummins had achieved the 50% BTE goal, and they accomplished it by utilizing a combination of optimized combustion, reductions in friction and pumping losses, and WHR. The optimized combustion and reductions in friction and pumping losses helped increase BTE to 47.5% before WHR was added. Cummins’ WHR system utilized an unnamed low-global warming potential working fluid and recovered heat from the engine exhaust as well as the EGR system. Output from the WHR system was mechanically coupled to the engine output to increase the total power delivered to the wheels resulting in a 3.6% absolute increase in thermal efficiency, or a 7.6% relative increase (compared to 47.5% enhanced BTE). The SuperTruck report mentions that Cummins also recovered waste heat from the engine coolant and oil for the engine demonstration. However, it is unclear if the reported gains include waste heat recovery from these additional sources or not. The report notes that the system weighs approximately 300 lbs., and, despite the relatively impressive results, Cummins has not demonstrated the cost-effectiveness of these upgrades.

Daimler also included a WHR system in their efficiency improvement strategy, with additional gains coming from directly improving engine efficiency. Gains from improved combustion via a predictive engine controller, as well as reductions in friction and pumping losses, increased BTE up to 47% before WHR. For their WHR system, Daimler chose an ORC with ethanol as the working fluid. Energy was recovered from the exhaust stream only and the system accounted for 1.3% of the absolute BTE gain, or a 2.8% relative improvement (compared with the 47% enhanced BTE). The WHR system drove an electrical generator which fed a hybrid electric drive system. Daimler's next step will be to recover waste heat from the engine coolant and charge air cooler in addition to the engine exhaust. They estimate an additional 0.7% absolute gain in BTE, for a total of 2.0% absolute and 4.3% relative improvement in BTE. These results are significantly lower than what Cummins has achieved. Cummins does utilize the EGR system to recover heat from the higher temperature exhaust gases and may be further ahead in the development phase. Also, as mentioned before, Cummins may be recovering waste heat from additional sources such as engine coolant. One issue with these results is that each manufacturer participating in the SuperTruck program was allowed to choose the drive cycle over which they evaluated engine efficiency, and these drive cycles were not specified in the report. Therefore, it is difficult to compare the individual results without knowing what the conditions for evaluation were. However, the results are still useful in providing an indication of the current state of the art.

The majority of the research on WHR systems focuses on applications for conventional gasoline or diesel engines. Srinivasan et al. [18] set out to model the potential of a WHR system applied to a diesel engine operating on Advanced Low Pilot Ignited Natural Gas (ALPING) combustion. The authors explain that ALPING injects pilot sprays of diesel early in the compression stroke to ignite a lean natural gas mixture. This method produces low temperature

combustion, which reduces NO_x and particulate emissions. A one-cylinder diesel engine running ALPING was used to provide data for a WHR model. Hot exhaust gas recirculation was evaluated for hydrocarbon and carbon monoxide emission reduction (both of which are typically high in low temperature combustion) as well as efficiency improvement. Turbocharging and exhaust backpressure were simulated using compressed air and surge tanks. Measurements included engine power output, intake, exhaust, coolant, and oil temperatures, air and gas flow rates, and exhaust emissions. Data was collected at 1700 rpm for both quarter and half engine loads. The theoretical WHR system used R113 as the working fluid and the exhaust stream as the sole source of waste heat. A single heat exchanger was used to evaporate the R113 and produce 179°C vapor at 2.0 MPa. The authors estimated that a maximum thermal efficiency increase of 14% was possible, with a 7% average thermal efficiency increase over the range of tested injection timings and loads.

EGR systems recirculate exhaust gases back into the combustion chamber to reduce NO_x emissions under certain running conditions. EGR coolers are often used to lower exhaust gas temperatures before the gases are added to the intake air and pulled into the combustion chamber. The excess heat is typically transferred to the engine cooling system and subsequently rejected to the atmosphere as waste heat. The benefit of capturing heat from the EGR system is that the gases are diverted from the exhaust system before travelling through turbochargers and catalysts, and, therefore, are recovered at the highest possible temperature. Two journal articles based on a project undertaken by AVL Powertrain Engineering provide some insight into the realistic gains from using waste heat from the EGR system. Teng [34] and Park et al. [2] provide results from an experiment comparing the output of an ORC powered by EGR heat, exhaust heat, and both EGR and exhaust heat combined. The experiment was conducted on a 10.8L Cummins ISM engine and each WHR system setup was tested at four Heavy-Duty Supplemental Emissions Test (SET) mode

points: B50, B75, B100, and C100. The letter in the mode point denotes the engine speed during testing, and the number represents the fraction of maximum torque, with B equating to an engine speed of 1615 rpm and C equating to an engine speed of 1900 rpm [35]. Ethanol was chosen as the working fluid for the WHR system due to lower system pressure and a reduction in the required recuperator size. The authors used a Garret GT25 turbo as an air brake to load the WHR system. The WHR system output was calculated using the mass air flow, pressure ratio, and shaft speed of the GT25 turbo. The EGR flow rate as a percentage of total intake flow was calculated using intake CO₂ measurements. Teng and Park et al. estimated the fuel consumption benefit by dividing the WHR output by the engine output. The rationale for this method provided by the authors is that the engine output could be reduced by the amount of the WHR output. However, it can be shown that this percentage increase is equivalent to the relative increase in thermal efficiency if the WHR output is simply added to engine output.

The WHR system tested by Teng and Park et al. consisted of an evaporator and a super-heater using different combinations of EGR and exhaust heat. The authors first investigated the

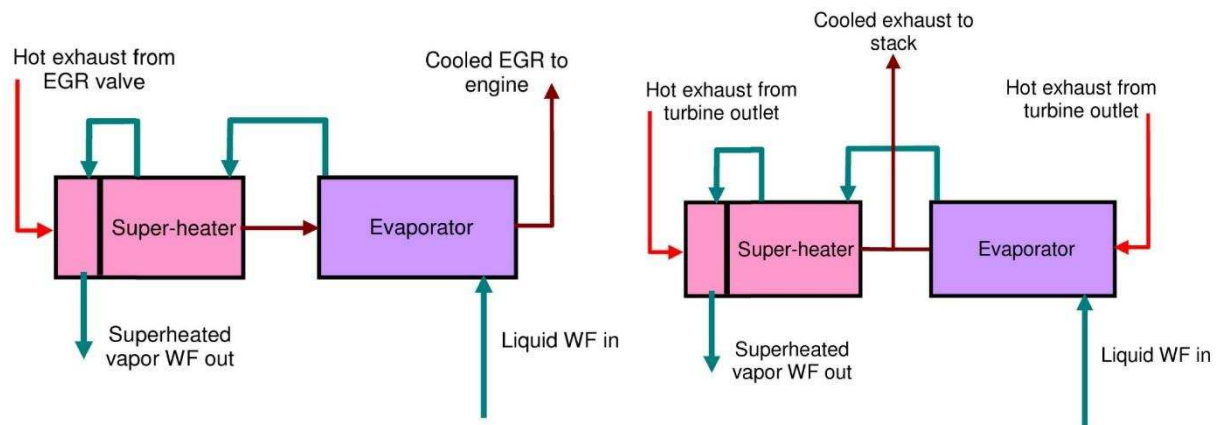


Figure 2-3. Configuration of WHR systems for EGR only and EGR and exhaust combined [34].

output from the WHR using only the EGR system heat for both the evaporator and super-heater (diagram on the left in Figure 2-3). They initially planned to be able to use EGR rates up to 35% and had estimated a 3% gain in efficiency using EGR alone. However, testing quickly showed that any EGR rates over 10% produced large amounts of smoke. Therefore, with the EGR rate limited to 10%, the authors reported a minimum of 1.3% relative increase in thermal efficiency for the B100 point and a maximum of 2.1% at the C100 point. For the second test, the EGR flow was channeled through the evaporator and the engine exhaust from the turbo outlet provided superheating in the second heat exchanger (diagram on the right in Figure 2-3). The results improved to a minimum gain of 1.6% at B75 to a maximum gain of 3.0% at C100. However, Teng noted that the results were still hampered by the low EGR rate. For the final test, the exhaust heat was the sole source for the WHR system and the best results were obtained with this system. A minimum relative efficiency increase of 3.4% at B50 and a maximum of 4.2% at C100 were reported. Although the EGR flow represents the highest temperature waste heat, the results suggest that the EGR flow rate tends to be too low to offer significant benefits in WHR.

Edwards and Wagner [30] modeled an ORC WHR system using both the post turbo exhaust stream and the EGR stream from a GM 1.9L turbodiesel using GT-Suite. R245fa was chosen as the working fluid due to its low saturation pressure and its positive saturation vapor curve slope in the T-s diagram. The positive slope of the saturation curve makes R245fa a ‘dry working fluid’ which ensures superheat after vapor expansion and prevents condensation within the turbine which can cause severe damage. The authors evaluated two designs: one with working fluid heated by EGR gases first and exhaust second, and one with the working fluid heated by exhaust first and EGR gases second. A recuperator was present in both systems to improve WHR system efficiency. The analysis showed that the design using the exhaust for the initial heating and the EGR gases

for the secondary heating resulted in 27% higher WHR power output than the alternate design. The authors chose to investigate this design for the remainder of the analysis. Edwards and Wagner pointed out that, although the EGR gases were hotter than the exhaust gases, the majority of the energy transfer came from the exhaust. Even though the EGR gases were taken before the turbocharger and were at higher temperature and pressure, the mass flow rate of the post-turbo exhaust stream was still significantly higher. The WHR system performance was analyzed at steady state for the peak efficiency point of 2250 rpm and 18-bar brake mean effective pressure (BMEP) and road-load point of 1500 rpm and 2-bar BMEP. BMEP is a volume normalized measurement of engine output that is not dependent on the specific size and displacement of the engine. For a four stroke engine, BMEP is defined as [36]:

$$BMEP = \frac{\dot{W}_{out,b}}{V_d N / 2} \quad (2.1)$$

Here, $\dot{W}_{out,b}$ is the brake power output of the engine, V_d is the displacement volume of the engine, and N is the engine speed. At peak efficiency, the model showed an increase from 43.9% to 47.1% thermal efficiency, giving a 7.3% relative increase. At the road-load point, the model showed an increase from 24.4% to 26.5% thermal efficiency, representing an 8.6% relative increase. One important point presented by the authors is the need to maintain exhaust temperature for after-treatment in on-road applications. This necessity limits the amount of heat that can be recovered from the post-turbo exhaust stream. In addition, Edwards and Wagner note that EGR temperatures in their study remained above 190°C after waste heat recovery, which means that an additional EGR cooler would be required to minimize volumetric efficiency losses. The volumetric efficiency is the measure of how fully the cylinders fill with air during the intake stroke and is defined as follows for diesel engines [36]:

$$\eta_v = \frac{2\dot{m}_{\text{air}}}{\rho_{\text{int}} V_d N / 2} \quad (2.2)$$

Here, \dot{m}_{air} is the mass flow rate of air entering the engine and ρ_{int} is the density of the air in the intake. Hotter EGR gasses would increase temperatures in the combustion chamber and reduce the density (and therefore mass flow) of the incoming air, thereby lowering the volumetric efficiency. An additional EGR cooler would require additional package space and it is unclear why the EGR gases were not cooled further even when the EGR cooler was placed before the exhaust cooler.

This section provided a sample of the results from the current state-of-the-art WHR systems utilizing only exhaust gases as a heat source. The results show that significant investment has been made by manufacturers, such as Honda, Cummins, and Daimler, as well as governments, to investigate the benefits of WHR. The majority of this research focuses on recovery from exhaust gases alone and the resulting relative efficiency gains (from experiment and modeling) range from 2.4% to 14% at steady state conditions. Though the gains are not trivial, a significant portion of waste heat is left untapped. The next section will review the past work on WHR using engine coolant in addition to exhaust gases.

2.2 WHR Using Engine Coolant

Exhaust gases from combustion may be the highest temperature source for waste heat, but the engine coolant has a large heat capacity rate and still carries a large portion of the fuel energy. Therefore, despite the relatively low temperature ($\sim 90^\circ\text{C}$) of the heat source, many researchers have attempted to recover waste heat from the engine coolant stream. Typically, the standard engine coolant (ethylene glycol (EG)/water mix) is channeled through a pre-heater which warms the working fluid before it is evaporated by the exhaust gases in an evaporator. A few researchers have analyzed the possibility of altered coolant passages to increase coolant temperature or using

the engine block cooling passages as a method of heating the working fluid directly. To facilitate discussion, this section is divided into two subsections: WHR at a 90°C Coolant Temperature, and WHR at Elevated Coolant Temperatures.

2.2.1 WHR at a 90°C Coolant Temperature

Despite the limitations on waste heat utilization using 90°C engine coolant, a significant amount of research exists on WHR from ICEs where the engine coolant heat is captured. The most informative investigations are those where systems with and without engine coolant as a waste heat source are directly compared. Two such systems were modeled by Vaja and Gambarotta [17] using a thermodynamic analysis to evaluate the performance of each system. Benzene, R11, and R134a were evaluated as working fluids for each system in terms of cycle efficiency and operating conditions. The ICE used for the analysis was a 12 cylinder supercharged natural gas engine with a baseline efficiency of 41.8%. The two WHR systems resemble systems described previously, except for the addition of a heat exchanger that uses the engine coolant to pre-heat the working fluid before it travels to the evaporator, which then solely uses the engine exhaust gases. The authors made the following assumptions for their model: isentropic turbine efficiency of 70%, isentropic pump efficiency of 80%, condenser temperature of 35°C, no losses in piping and heat exchangers, and dry expansion for the working fluid. For benzene, the combined system efficiency of the ICE plus the WHR system increased from 46.6% to 47.1% when waste heat from the engine coolant was utilized, representing a 1.1% relative increase. With R11 as the working fluid, the combined efficiency increased from 45.8% for the system using only exhaust gases to 46.3% for the system using both coolant and exhaust, giving a relative efficiency gain of 1.1% with coolant utilization. Finally, R134a produced efficiencies of 43.8% and 44.5% for WHR with exhaust and WHR with exhaust and coolant, respectively. The system using R134a showed the greatest

improvement in efficiency when using the engine coolant with a 1.5% relative increase. With the baseline efficiency of 41.8%, the exhaust only systems increase efficiency between 4.8% and 11.5%. In comparison with the gains from exhaust WHR alone (4.8-11.5%), the addition of WHR from the engine coolant contributed little to total efficiency gains. Additionally, the reported gains may not be realistic because the stated condenser temperature of 35°C is quite low and may not be realistic if condenser size is a consideration.

Boretti [28] modeled the transient operation of a Rankine cycle system used as a bottoming cycle for a 1.6 L, ethanol-fueled, turbocharged, spark ignition engine. The WHR system used water as the working fluid, with the engine cooling system used as a pre-heater and the engine exhaust used for evaporation. A recuperator was used to increase system efficiency. The output of the WHR system powered a generator which fed power into a hybrid electric drivetrain. The additional efficiency improvements of the hybrid drivetrain were not considered in this work. A one-dimensional engine simulation software (WAVE) was utilized to predict the amount of fuel energy converted to mechanical energy and lost as waste heat in the engine exhaust. Boretti assumed that heat lost to the surroundings via convection and radiation from the engine surfaces was 10% of fuel energy, with the remainder of the fuel energy rejected to the engine coolant. The author claims that the 10% figure is an overestimate and that the energy rejected to the engine coolant was therefore underestimated. Ultimately, the WAVE simulations produced engine-only and engine-plus-WHR performance maps for use in a full vehicle simulation.

Boretti used the Lotus Vehicle Simulation (LVS) software to model the performance of this system in a full-size passenger car over the New European Driving Cycle (NEDC), as well as under 120 km/h cruise conditions. The vehicle simulation was based on a passenger car with a 4.0 L gasoline engine and a 5-speed automatic transmission weighing 1,819 kg. The mass of the

simulated vehicle was not adjusted to account for the difference in weight between the 4.0 L engine and the 1.6 L engine from the WAVE simulation, but 50 kg of additional weight was added to account for the mass of the WHR components. The 4.0 L transmission and final drive ratios were also retained. The author used experimental data from the 4.0 L engine taken over the NEDC to estimate engine coolant and oil warm-up times. The 4.0 L engine coolant reached full temperature after 800 seconds, but the author assumes a 600 second warm-up time for the 1.6 L due to its higher power density. The first 600 seconds of the NEDC were therefore modeled using the warmed-up engine maps (engine-only) from the WAVE simulation with an additional fuel penalty for cold operation of 10.5%. After the 600 second warm-up period, the model switched to an output map that included the Rankine cycle power. The LVS model predicted a relative fuel efficiency improvement of 4.2% for the NEDC with the addition of the WHR system. The model also predicted a 6.7% relative fuel efficiency increase at a steady 120 km/h.

In 2009, Ringler et al. [31] analyzed the potential of an automotive WHR system for the BMW Group Research and Technology division. The goal of the analysis was to evaluate two different Rankine cycle configurations on a four-cylinder ICE and to study the effectiveness of different working fluids. The first configuration (System A) captured waste heat from the exhaust gases alone, where the second configuration (System B) utilized both the exhaust and engine coolant. Like other reviewed systems, System B used the engine coolant to pre-heat the working fluid and the exhaust gas for evaporation. The authors first modeled both systems as ideal Rankine cycles and placed the following constraints on the Rankine cycle systems to maintain economic feasibility. The minimum condensation temperature was set to 70°C and the overall maximum system temperature was limited to 300°C. The minimum and maximum system pressures were 0.7 and 10 bar, respectively. Finally, the evaporation temperature was held to 110°C to keep it below

the engine coolant temperature (115°C). They evaluated water, toluene, and ethanol under these constraints and analyzed the resulting temperature difference between the condensation temperature and the evaporation temperature. Toluene had the greatest temperature difference for System A (~120°C), but was not considered further due to its low heat of vaporization. The authors selected water for System A by virtue of its high heat of vaporization and relatively large temperature difference (~90°C). System B was limited further by the coolant temperature, giving ethanol the temperature difference advantage (~40°C) over water (~20°C) even with its smaller heat of vaporization. Ringler et al. then compared the simulated heat flows to the exhaust and engine coolant over varying exhaust gas temperatures and the ratio of the engine coolant to exhaust gas heat (waste heat ratio). System A performed better than System B with increasing exhaust temperatures and decreasing waste heat ratio. The authors note that this condition occurs when vehicle speeds exceed 70 mph. System B produced more power than System A in the speed range of 45-70 mph, which corresponds to more typical cruising speeds. Therefore, System B was the chosen configuration for the experimental portion of the investigation.

In Ringler et al. investigation, the test bench consisted of a four-cylinder engine with a dual-loop WHR system that is configurable for either System A or System B with slight modifications. As mentioned before, the authors configured the test bench for System B for this experiment. Losses to the ambient air were minimized by insulating system components such as the exhaust pipe, tubing, heat exchangers, and expander. At loads following the road resistance curve, expander output was found to vary from 0.7 kW at 45 mph to 2.0 kW at 90 mph, which was between 50 and 65% of the ideal output from the simulation. The authors state that this represents roughly 10% of the engine output at these loads, or equivalently, a potential 10% relative increase in thermal efficiency. At higher loads this value was seen to decrease to approximately 8%, while

at lower loads 15% increases were seen. Though these results give some indication of the WHR system performance, testing over a drive cycle would be much more informative when it comes to real-world efficiency improvements. Also, Ringler et al. present very few details about the WHR components used on the test bench to achieve this level of performance (heat exchanger size, etc). This raises the question of how realistic the reported efficiency improvements are for an actual automotive installation.

Large diesel power plants are some of the most efficient engines in use, with thermal efficiencies approaching 50%. Nonetheless, half of the fuel energy is still being wasted in various heat paths to the environment. Wartsila, a Finnish company that manufactures large bore engines for use in marine applications, evaluated the ability of a WHR system to improve the efficiency of a large, low-speed marine engine with a maximum continuous output of 68,640 kW [19]. Wartsila first optimized the engine for WHR by channeling in outside air for the intake stream. They assume the maximum intake air temperature can be decreased from 45°C to 35°C using this method. Reducing intake air temperature will increase air density and, with the addition of more fuel, power output will increase along with exhaust temperature and flow rate. If the turbocharger is downsized to return power output to previous levels, there will be excess exhaust energy (~10%) which can be recovered before the turbocharger and used to power an additional turbine (power turbine). This power turbine is one part of what Wartsila refers to as a Total Heat Recovery Plant (THRP). In the THRP, the engine cooling water (~90°C) was used to pre-heat the working fluid for the steam cycle. Next, the water was evaporated and superheated using the exhaust gases collected after the turbocharger using a dual-pressure evaporator which provided ship service steam (high pressure) and steam for powering a steam turbine (low pressure). The steam turbine, along with the power turbine, were coupled to an alternator and generated the ship service power. The alternator could

also act as a motor under conditions where excess electrical power is generated, providing additional shaft power to the propeller. Simulations were performed to estimate the increase in overall system efficiency from the THRP concept. At 85% of maximum engine load, the WHR system should produce 6,650 kW which would increase overall system efficiency from 49.3% to 54.9%, giving a 12% relative increase. Since the THRP is the only WHR system reviewed that uses a power turbine as well as a Rankine cycle, it may be helpful to consider the output of the individual components for comparison. Per the report, the steam turbine power output accounts for between 73% and 80% of the total WHR output, with the power turbine providing the remainder. Therefore, the Rankine cycle portion of the system is responsible for between 8.76% and 9.6% of the relative efficiency gains. Wartsila demonstrated that a significant amount of waste heat can be recovered from large diesel marine engines, but it is still a relatively small portion of the total thermal losses and the engine coolant is still vastly underutilized. The next subsection provides a sample of the studies that investigated WHR from engines with elevated coolant temperatures.

2.2.2 WHR at Elevated Coolant Temperatures

Examples of research on WHR using elevated coolant temperatures are scarce in the existing literature. WHR with coolant temperature significantly higher than 90°C is usually achieved by using the Rankine cycle working fluid as the engine coolant and using the engine cooling passages to directly heat (and evaporate) the working fluid rather than having an additional heat exchanger. This saves space and reduces cost over a system that attempts to recover heat from 90°C coolant. It also reduces the thermal resistance between the engine structure and the working fluid of the WHR system, resulting in greater utilization of this waste heat. This subsection will

cover the few examples of WHR using engine coolant at temperatures over 90°C that are found in the literature.

One method to increase the temperature of engine coolant for WHR is to redesign the cylinder head so that coolant flowing through the hottest area of the engine can be recovered separately from the rest of the cooling system. This strategy was employed by Endo et al [32] in addition to the work mentioned in the previous section. The authors redesigned a cylinder head and created special passages for the working fluid to flow near the exhaust valves to produce additional steam. This steam was then combined with the steam output from the exhaust powered evaporator. Heat transfer was enhanced by using many small diameter passages that encircle the exhaust ports as shown in Figure 2-4. The cylinder head was also modified to create three-layered coolant passages at the top of the combustion chamber. The 3 mm diameter passages were placed

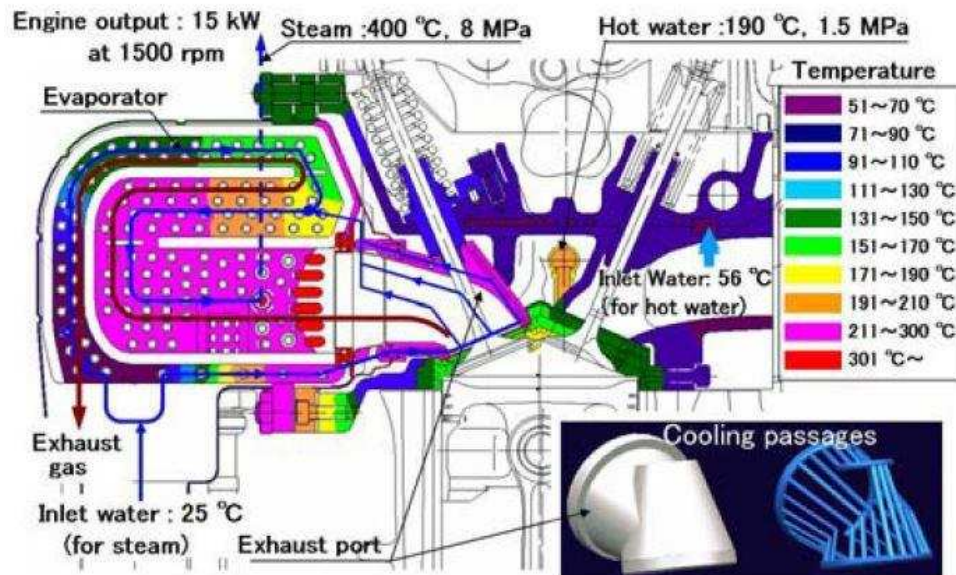


Figure 2-4. Diagram of cylinder head modified specifically for WHR with the goal of increasing working fluid temperatures [32]. Modifications include special cooling passages around exhaust valves to recover waste heat at high temperatures (~190°C).

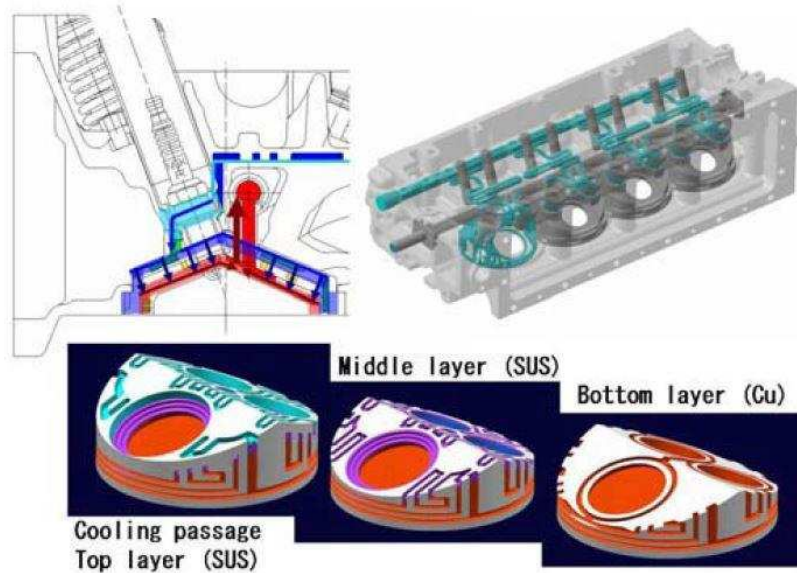


Figure 2-5. Redesigned coolant passages used to recover heat from the top of the cylinders at 190°C [32].

at the top of the combustion chamber as shown in Figure 2-5. This design produced pressurized pure water at 189°C (saturation temperature) and 1.22 MPa, while maintaining normal surface temperatures in the combustion chamber. Though not tested with a full WHR system and no efficiency gain was estimated, the modified design (including an integrated evaporator) was shown to produce between 1.34 and 1.78 times the steam mass flow as a standard engine with a traditional exhaust evaporator.

The work done by Arias et al. [1] on modeling three different WHR system designs for use in a spark ignited engine hybrid vehicle helps to clarify the magnitude of the individual contributions from engine exhaust and engine coolant. Initial simulations were conducted on a 2.0 L engine running at 2000 rpm with water as the working fluid for the WHR system. All heat exchangers were counter-flow designs and were modeled using the effectiveness-NTU method. The authors first investigated the performance of a WHR system recovering heat from the exhaust stream only, referred to as System 1. The simulation estimated that System 1 would produce 2.12

kW of power which translated to a thermal efficiency increase from 25.0% to 27.5%, or a 10.1% relative increase. System 2 added a heat exchanger to preheat the water using the engine coolant before the working fluid traveled to the evaporator. The authors only observed a 20 W increase in estimated system output with this modification. Arias et al. blame the low coolant temperature (80-120°C) for the poor results. The third and final system was the same as System 2, except that the working fluid recovered heat directly from the engine coolant passages rather than a separate heat exchanger. Therefore, the working fluid acted as the engine coolant and no radiator was used. The authors maintained an intermediate quality for the working fluid inside the engine block to prevent complete boiling and potential hot spots. The saturation temperature was 300°C with a saturation pressure of approximately 8.6 MPa. The water was then superheated to 600°C by the exhaust gases. Arias et al. predicted a WHR system power output of 6.8 kW, representing an increase in thermal efficiency from 25% to 33%. This translates to a 32% relative increase in thermal efficiency.

Arias et al. chose to explore System 3 in more detail due to the impressive results of the initial simulations. Data from a 2004 Toyota Prius hybrid was gathered at Argonne National Laboratory over a city-type drive cycle, including fuel mass flow rate, exhaust temperature, and engine speed. The authors estimated an absolute thermal efficiency gain of 5.5% using the Prius data, but it should be noted that this efficiency gain appears to be the maximum gain over the cycle and not an average value. The relative thermal efficiency increase is unknown since the thermal efficiency of the engine itself at the point of maximum efficiency gain is not reported, but would be 22% assuming the 25% baseline efficiency from the original simulation. This thermal efficiency increase is over 30% lower than predicted by the initial simulation. One reason for this discrepancy is that the average measured exhaust temperature of 400°C was much lower than estimated in the

original model ($>700^{\circ}\text{C}$). Consequently, the simulations using the test data showed a reduction in average power output from 6.8 kW down to roughly 3.0 kW. Graphs of the engine speed over the drive cycle indicate that the engine cycled on and off frequently throughout testing. The exhaust gas temperature is correlated with the frequency and duration of engine on time, which is low throughout much of the drive cycle. Therefore, the WHR output might have been significantly higher if coupled to a non-hybrid engine. Arias et al. established the potential for gains using high temperature coolant, but experiments to fully validate the concept appear to be non-existent in the current literature.

Though experimental results for WHR using high-temperature coolant are not found, experimental research on using phase change cooling in ICEs does exist. In 2008, Katta et al. [22] tested the feasibility of phase change cooling for use with WHR in heavy duty engines. A Perkins 4.154 2.5L 4-cylinder diesel engine was instrumented and operated with a conventional single-phase cooling system as well as a two-phase cooling system. The engine was operated at speeds of 1500 and 2000 rpm and torque of 52 N-m and 110.5 N-m at each speed. At each load condition, the engine was run with single phase cooling ($\sim 70\text{-}80^{\circ}\text{C}$ coolant temperatures), two phase cooling at atmospheric pressure ($\sim 95^{\circ}\text{C}$ coolant temperature), and two-phase cooling at 69 kPa system pressure ($\sim 110^{\circ}\text{C}$ coolant temperature). The cylinder head temperature was measured at four locations to determine the effect of two phase cooling on magnitude and uniformity of the engine structure temperature. The experiment showed that two phase cooling resulted in a very even temperature distribution in the engine compared to single phase cooling. For example, at 1500 rpm and 52 N-m or torque, the cylinder head temperature variation was approximately 12°C with single phase cooling. With two phase cooling, the cylinder head temperature variation was approximately 4°C at both atmospheric and 69 kPa system pressure. The authors used the results from the

experiment to estimate the WHR system output for each of the four operating conditions. Steam generation from the cooling system was found from the rate of water consumption during the test (as the steam was exhausted after exiting the engine cooling system). The WHR turbine expander efficiency was assumed to be 70% and the exhaust temperature drop in the evaporator was set at 100°C. No other details of the theoretical WHR system are given and the calculations are vague. The WHR system model estimated that relative efficiency gains using this system would be between 4.3% and 6.2% over the tested operating conditions.

2.3 Need for Further Research

Relevant prior research summarized in Table 2-1 and discussed above demonstrates that the experimentally validated state-of-the-art WHR systems underutilize the available waste heat from ICEs, even when the engine coolant waste heat is harnessed. The literature shows that a 13.2% relative efficiency increase is the maximum gain realized through experimental testing, and that this was accomplished at steady state without the use of the engine coolant waste heat. As detailed in the previous section, great lengths were required to attain this 13.2% increase and has yet to be put into production. Ultimately, the disappointing results stem from the inherent limitations on WHR due to the characteristics of the two primary waste heat sources. The exhaust gases from an ICE are a high-temperature heat source, but the heat capacity rate of these gases is low, which limits the amount of heat that can be recovered. The additional use of the engine coolant to pre-heat the working fluid of a Rankine cycle has been shown to provide marginal gains at best. The engine coolant temperature is too low for efficient energy conversion. The few studies that model WHR systems with elevated coolant temperatures reported significant improvements in WHR system output and combined efficiency gains as high as 32%.

The present work is aimed at providing an accurate measurement of the availability of waste heat from a diesel engine with increased coolant temperature since no such study can be found in the current literature. Throughout these tests, the condition of the engine at each temperature was monitored to provide qualitative data on wear and other potential engine issues resulting from the increased coolant temperature. In addition, thermodynamic models of theoretical WHR systems are used to predict the efficiency gain possible by incrementally increasing coolant temperature. Individual heat exchanger models are then used to estimate the footprint required for each system configuration. The next section will describe the details of the test facility and experimental setup.

CHAPTER 3. EXPERIMENTAL METHODS

The literature review in the previous chapter highlighted the lack of experimental work on combustion engines running at raised coolant temperatures for waste heat recovery purposes. A large portion of the effort for the current work was focused on running such an experiment, and the details are presented in this chapter. An experimental facility was commissioned to perform a complete energy balance on a small diesel engine, provide inputs for WHR system modeling, and to allow monitoring of the engine condition as coolant temperature was increased from 90°C to 200°C. This chapter begins with a description of the engine modifications performed to increased durability under the test conditions. Next, an overview of the experimental facility and its individual components is given. Finally, the test matrix is presented followed by a description of the system operation and test procedure.

3.1 Engine Modifications

The test engine is a 0.7L 3-cylinder normally aspirated diesel engine. It is an indirect injection diesel using pre-combustion chambers to increase swirl for better fuel atomization and mixing. The block and cylinder head are made from cast iron. Table 3-1 provides the key specifications for the engine, which was manufactured by Daihatsu but sold by Briggs and Stratton under their Vanguard line. Net power output from this engine under continuous operation is approximately 10.5 kW, with a maximum 12 kW intermittent output. The test engine is not designed to operate above the standard coolant temperature of 90°C, so modifications were performed to increase the engine's durability under the test conditions. The modifications fall into six main categories: cylinder head sealing, clearances, engine seals, injection pump, oil pump, and oil pan. This section will cover each of these six categories in detail.

Table 3-1. Test engine specifications [37].

Engine Specifications	
Model	DM 700D
Number of Cylinders	3
Bore x Stroke [mm]	68 x 64
Displacement [cc]	697
Compression Ratio	25:1
Net Power [kW] @ 3600 rpm	10.44
Torque [N-m] @ 2400 rpm	35.25
Fuel System	
Injector Pump	Bosch VE (distributor type)
Injector Nozzle Type	Throttle
Injector Pressure [bar]	140

3.1.1 Cylinder Head Sealing

One of the primary concerns when increasing the coolant temperature of the engine was maintaining the cylinder head to engine block seal. As engine temperature increases, the cylinder head expands against the cylinder head bolts, and, at high enough temperatures, it will crush a traditional composite cylinder head gasket. The result would be a loss of seal between the cylinders and the coolant passages or between the cylinders themselves. Either failure would result in a loss of compression in one or more cylinders or leakage of oil or coolant into the combustion chambers. The following three modifications were made to prevent the failure of the cylinder head to block seal.

First, the traditional composite cylinder head gasket was replaced with a solid copper gasket made from dead soft 99.9% pure copper (Figure 3-1). It was essential that the copper be sufficiently soft to properly conform to the engine block and cylinder head surfaces. The copper gasket was designed in SolidWorks® and cut out on the waterjet at the CSU EECL. The original gasket was scanned in and the image, along with measurements of the original gasket, was used to create an accurate sketch. The sketch was then converted to the necessary files for the waterjet.



Figure 3-1. Custom copper cylinder head gasket.

The engine block and head were resurfaced at a local machine shop by removing 0.08 mm of material from each surface to ensure trueness and even clamping force.

The second step taken to improve combustion chamber seal was to install stainless steel combustion chamber O-rings around each cylinder in the engine block (Figure 3-2). The machine shop cut a 0.89 mm deep groove around each cylinder to allow a 1.04 mm diameter stainless steel wire to be installed. The wire protruded 0.15 mm above the engine block deck and was pressed into the copper gasket when the cylinder head was fastened to the engine block. The contact between the stainless steel O-ring and the copper head gasket created a high pressure seal to prevent combustion chamber gases from escaping. However, the copper gasket alone was not sufficient to seal the coolant and oil passages between the engine block and cylinder head. Sealants such as Hylomar® and Permatex® High-Temp Red RTV Gasket Maker were initially used to try and seal fluid passages through the head gasket. Unfortunately, neither sealant was successful and oil and coolant leaks both externally and into the combustion chamber were found. Eventually,



Figure 3-2. Engine block with stainless steel combustion chamber O-ring seals installed.

K&W Copper Coat® gasket compound was recommended for this purpose. The Copper Coat® was sprayed on both sides of the gasket and allowed to tack up before the cylinder head was bolted in place. Copper Coat® is a high temperature sealant specifically made for sealing cylinder head gaskets, and was found to work better than other available sealants in this application. Minor external oil seepage was still visible, but it was deemed acceptable and oil and coolant levels were closely monitored during testing.

The final modification to improve the durability of the head gasket seal was to replace the factory cylinder head bolts with high strength studs and nuts from Automotive Racing Products (ARP). ARP head studs are stronger than the factory head bolts, and studs do not experience the torsional forces that a cylinder head bolt would. The result is more accurate and even clamping force between the cylinder head and engine block. The cylinder head nut tightening torque was

also increased from 34 N-m to 41 N-m after initial testing showed signs of poor head gasket crush in some areas.

3.1.2 Clearances

The test engine was set from the factory with certain component clearances to account for thermal expansion. These clearances were modified for this experiment to account for the increased temperatures and subsequent expansion that was expected during testing. The two main clearances of concern were the piston ring end gaps and the valve clearances. Piston rings provide a seal between the piston and cylinder wall to prevent combustion gases from escaping into the crankcase and to prevent excessive oil from entering the combustion chamber. Installation onto the piston is made possible by a break in the ring which leaves a small gap once the piston is placed in the cylinder bore (see Figure 3-3). Since the combustion chamber temperatures were expected to increase significantly as coolant temperature was raised, there was concern that the piston ring end gaps might close and cause the piston rings to seize in the cylinders and cause significant

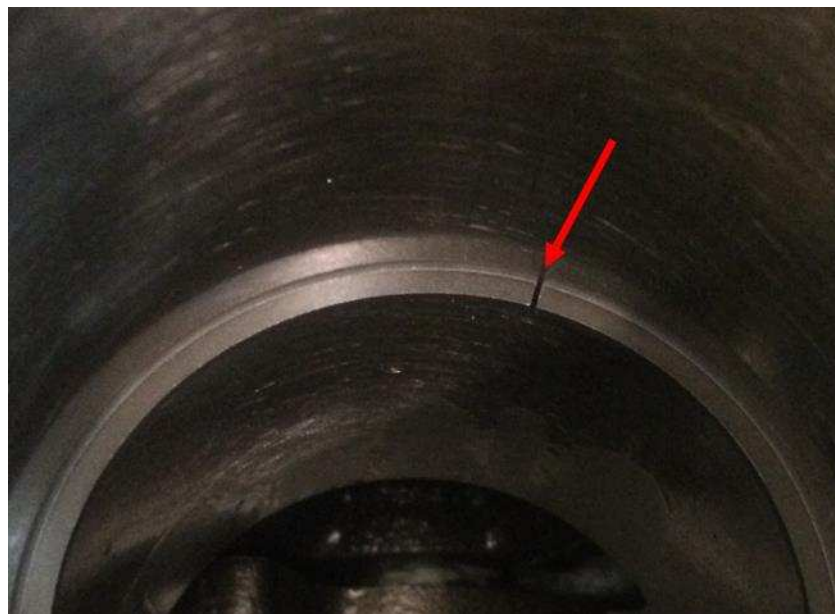


Figure 3-3. Piston ring in cylinder bore with arrowing pointing to ring gap.

damage to the cylinder surface. The original piston ring end gaps were measured for each cylinder and the results are shown in Table 3-2. Each piston ring was hand filed to enlarge the end gaps to match the recommendations for piston rings on extreme performance applications. The final piston ring end gaps shown in Table 3-2 are still within the tolerance for the maximum allowed end gap stated by the manufacturer so no significant performance loss was expected while testing at normal operating temperatures.

Table 3-2. Measured piston ring end gaps.

Piston Ring	Initial End Gaps [mm]			Final End Gaps [mm]
	Cyl. 1	Cyl. 2	Cyl. 3	All Cylinders
Top Compression Ring	0.20	0.33	0.30	0.46
Middle Compression Ring	0.23	0.46	0.46	0.51
Oil Control Ring	0.25	0.38	0.36	0.38

The Daihatsu 3-cylinder diesel engine uses a cam in block design with solid lifters and pushrods actuating the valves. This type of valve train requires clearance to allow for thermal expansion, which is set using adjustable rockers at the valve tip. Engine valve clearances are set by the factory for the expected operating temperature range to ensure there is always clearance when the camshaft is on the base circle. The additional expansion from the elevated temperatures for this experiment could have reduced the valve clearance to zero, preventing the valves from closing entirely once the engine reached temperature. The result would have been a loss of compression and poor engine performance. The specified valve clearance for this engine is 0.20 mm for both intake and exhaust valves, set with the engine at room temperature. The valve clearances were increased to the conservative values of 0.25 mm and 0.28 mm for the intake and exhaust valves, respectively.

3.1.3 Engine Seals

The factory rubber engine seals were not intended to see temperature greater than 100°C for extended periods of time. Engine seal failure could have resulted in rapid oil loss and potential engine damage from a loss of lubrication in key areas. Therefore, the front and rear crankshaft seal dimensions were measured and high temperature Viton replacements were used (Figure 3-4). The valve stem seals were also replaced with Viton seals since the factory valve stem seal material was unknown. It was critical to retain valve stem sealing as any unwanted oil entering the combustion chamber would be unmeted fuel and would adversely affect the fuel flow measurements for the energy balance.

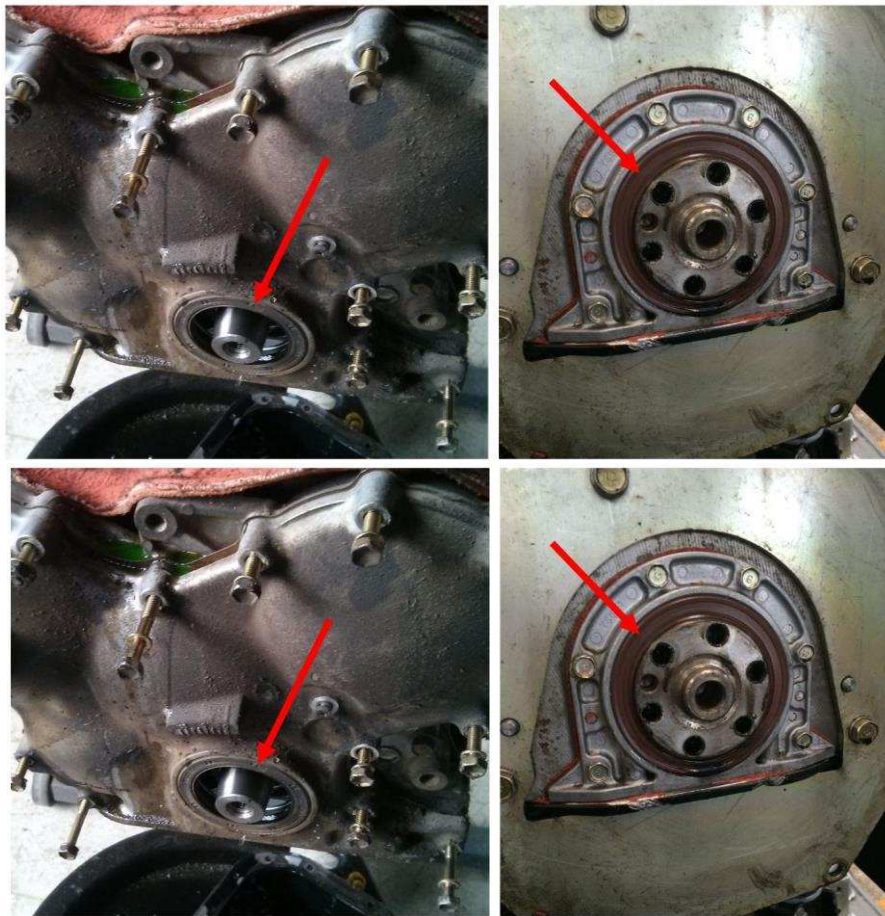


Figure 3-4. Front (left) and rear (right) crankshaft seals that were replaced with high temperature Viton alternative.

3.1.4 Injection Pump

The fuel pressure for the test engine is provided by a Bosch distributor type fuel injection pump that is gear driven off the crankshaft. The pump had close tolerances to supply diesel fuel at 137.9 MPa to the pre-combustion chambers. Since the injection pump was fixed to the engine, there were concerns that additional heat from the high-temperature engine would overheat the fuel inside the pump and create deposits that could damage the unit. Unfortunately, the conduction heat path was unavoidable due to the injection pump mounting points. However, radiation from the high temperature engine block was minimized with the addition of a heat shield. The heat shield was fabricated out of aluminum sheet metal and mounted to existing threaded holes in the engine block (Figure 3-5).

3.1.5 Oil Pump and Oil Pan Modifications

The use of an external oil pump required several modifications to the engine. The two primary modifications were to remove the stock oil pump internals and to fabricate connections



Figure 3-5. Heat shield for high pressure fuel pump.

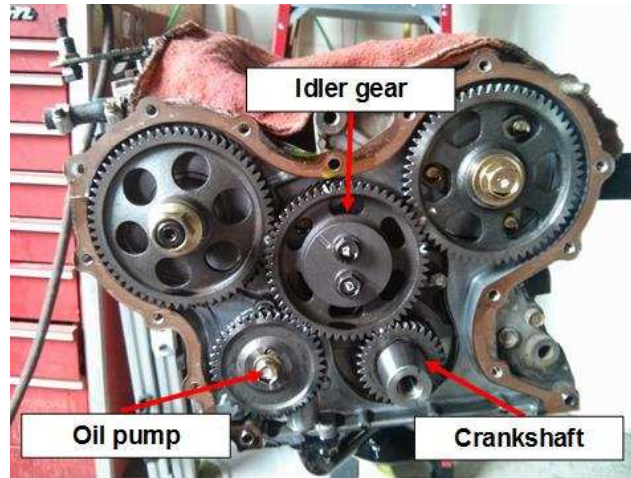


Figure 3-6. Engine timing gears with arrows showing crankshaft gear, idler gear, and oil pump gear.

from the external oil system to the engine. The factory oil pump was driven off the front of the crankshaft via an idler gear (Figure 3-6). The new oil system bypassed the stock pump, preventing any lubrication from reaching the pump rotor and pinion. Without lubrication, the friction would eventually cause the pump to get hot and seize and potentially damage the rest of the engine. Therefore, the pump components were removed from the timing cover including the drive gear, the pump pinion, and the pump rotor (left side of Figure 3-7). However, with the pump components



Figure 3-7. Removing oil pump drive shaft and pinion (left). Bolt used to plug oil pump shaft bore (right).

removed, an opening remained in the rear timing cover leading to the oil passage that originally supplied oil to the oil filter (which was relocated). Oil sprayed onto the timing gears could potentially have travelled this path and resulted in an external oil leak since the passage was not sealed at the original oil filter mounting location. To prevent any oil leakage, the opening in the timing cover was sealed using a bolt, a nut, and two large washers (right side of Figure 3-7).

To connect the external oil system to the engine, a new oil pump pickup and tube were required. An aftermarket external oil pump pickup kit from Moroso® was selected to fit the oil pan. The oil pan was drilled to allow the oil pump pickup tube and pressure relief tube to pass through the side of the pan. The pickup and tubes were MIG welded into place and a 19 mm diameter tubing to 19 mm female NPT fitting was welded to the outside of the pan to allow connection of the oil pump pickup tube to the inlet side of the oil pump. The test facility is described in the next section.

3.2 Test Facility Overview

The test facility was designed to allow measurement of the key data required to calculate each portion of the energy balance (Figure 3-8). Additional considerations were made to provide exhaust emissions data as well as measurements for monitoring engine condition. The test facility diagram shown in Figure 3-9 provides an overview of the equipment and instrumentation used in the experiment. The test facility includes an engine, a coolant loop, an oil lubrication loop, a fuel system, an air intake, an exhaust system, and a dynamometer. Details of the equipment used in the experiment are provided in Table 3-3.

The cooling system can be seen in the lower half of the diagram in Figure 3-9. A high temperature heat transfer fluid (HTF) (Duratherm G) is used in place of ethylene glycol as the primary engine coolant to prevent evaporation at temperatures above 200°C. Duratherm G is a



Figure 3-8. Completed test facility including dynamometer controller in the bottom of the image.

polyalkylene glycol based heat transfer fluid that contains a blend of additives to fight oxidation and corrosion and ensure compatibility with a wide range of metals and seal materials. Oxidation occurs when the fluid is in contact with air while at elevated temperatures ($>100^{\circ}\text{C}$) and leads to the generation of carboxylic acids and sludge formation [38-40]. Sludge can clog passages and the increased acidity of the fluid can also promote corrosion. Oxidation was a concern in this experiment since the primary coolant was in contact with oxygen in the reservoir and would be raised to temperatures well over 100°C .

The primary coolant is pressurized by a high temperature internal gear pump (Haight Pumps, 10U-CW) driven by a 208V, 3-phase electric motor providing 0.75 kW of power (Figure

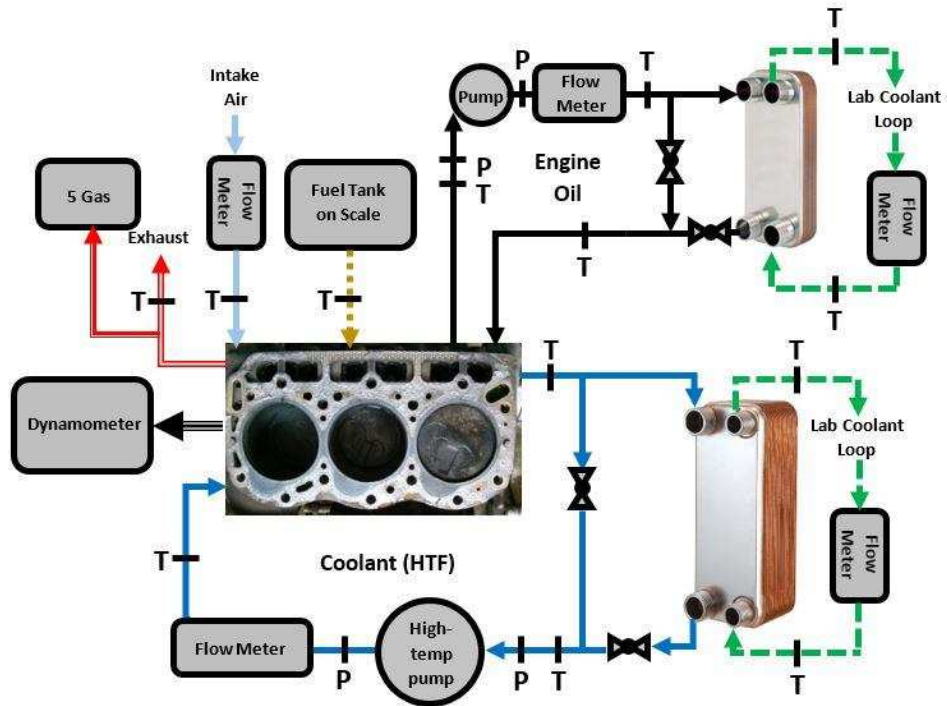


Figure 3-9. Diagram of test facility showing cooling and oil systems and all instrumentation.

3-10). A variable frequency drive (VFD; ABB, ACS310) provides pump speed adjustment and allows for control of the system pressure and flow rate. Pump inlet and outlet pressure is monitored using high-temperature Perma-Cal® pressure gauges. After the pump, the HTF travels through a volumetric flow meter (FLO-CORP, PDSG1-S2-03-TT) before entering the engine. The primary coolant then exits the engine and flows to the flat plate heat exchanger (GEA, FP5X12-12) where heat is rejected to the secondary cooling loop (Figure 3-11). The HTF is filtered before the heat exchanger inlet using a y-strainer with the 40-micron screen recommended by the pump manufacturer. Primary coolant temperature is monitored throughout the system, with the average coolant temperature and temperature rise across the engine measured by two type-T thermocouples (Omega, TQIN-18U-6) which were calibrated to ensure the highest possible accuracy. The details of the calibration procedures for all instrumentation are provided in Appendix A.

Table 3-3. List of test facility equipment used for experiment.

Items	Description	Manufacturer	Supplier	Part Number
Primary coolant pump	Series DIU square flange internal gear pump, 37.85 L/min max, 1.7 MPa max, 204°C max	Haight Pumps	Kaman Industrial Tech	10U-CW
Oil pump	Series GA flange mount external gear pump, 18.9 L/min max, 115°C max, 880 cp max	Flowserve	McMaster	1GAFM1DO
AC Drive for Pumps	3-phase AC drive, 200 to 240 V, 0.75 kW	ABB	Kaman Industrial Tech	ACS310-03U-05A2-2
Heat Exchangers	Copper-brazed 12 plate liquid-to-liquid	GEA	Gustave A. Larson	FP5X12-12
	Copper-brazed 6 plate liquid-to-liquid	GEA	Gustave A. Larson	FP5X12-6
Thermocouples	Type T: 13 mm length; pipe plug	Omega		TC-T-NPT-G-72
	Type T: 150 mm length; quick disconnect; 304 SS	Omega		TQSS-18E-6
	Type T: 150 mm length; quick disconnect; Inconel	Omega		TQIN-18U-6
	Type T: 13 mm length; pipe plug	Omega		TC-T-1/8NPT-G-72
	Type T: ready-made insulated	Omega		5TC-GG-T-20-72
	Type T: self-adhesive surface	Omega		SA1XL-T-72
	Type K: 300 mm length; quick disconnect	Omega		KQIN-18E-12
Viscometer	Rotational type; dynamic viscosity 0.2 to 10,000 mPa-s; density 0.65 to 2 g/cm ²	Anton Paar		SVM 3000
Flow Meters	Gear type; 0.2 to 75.7 L/min	FLO-Corp		PDSG1-S2-03-TT
	Gear type; 0.1 to 26.5 L/min	FLO-Corp		PDSG1-S1-02-TT
	4-20 mA; 3-wire transmitter	FLO-Corp		PDTX3-04-S
	Variable area; 0.8 to 26.5 L/min	FLO-Corp		MFTV-LSU-0706-TXB-MFT2-01-N4
	4-20 mA; 2-wire transmitter	FLO-Corp		MFT2
	0.8" orifice; for 1.5" pipe flange	Dwyer		PE-E-2
Pressure Transducers	Absolute, 0-15 psi	Omega		PX305-015AI
	Differential; 0-5 psi	Omega		MMDDU005-C1P1C2T2A4
Data Acquisition System	CompactRIO 8-slot chassis	National Instruments		9074
	Thermocouple module; 16ch	National Instruments		9213
	Analog current +/-20 mA; 8ch	National Instruments		9203



Figure 3-10. Internal gear pump used to pressurize cooling system.

The secondary cooling loop is filled with a 50/50 mix of ethylene glycol and water and is pressurized by a dedicated centrifugal pump powered by a 2.24 kW electric motor. The secondary coolant flows to a radiator located in the basement of the building. A heat exchanger bypass is installed on the primary coolant side to assist in temperature control. Two type-T thermocouples (Omega, TQIN-18U-6) are used to monitor the secondary coolant temperature. The secondary coolant temperature difference across the heat exchanger, along with a volumetric flow meter, provides a check on the heat rejection calculation on the primary coolant side.

The cooling system components were connected with 19.05 mm outside diameter, 1.65 mm wall, 316 stainless steel tubing and compression fittings from Swagelok®. The exceptions were the connections to the engine itself which were made with 19.05 mm inside diameter high-temperature hoses to reduce the transmission of engine vibrations to the cooling system. The tubing was wrapped with 12.70 mm thick ceramic fiber insulation (FiberFrax® Durablanket® S) to minimize heat loss. The insulation had a density of 128 kg m^{-3} and a thermal conductivity of $0.12 \text{ W m}^{-1} \text{ K}^{-1}$ at 600°C , with thermal conductivity decreasing with decreasing temperature. The Durablanket® was also used to insulate cooling system components such as the heat exchanger



Figure 3-11. Brazed flat plate heat exchanger used to reject heat from primary coolant to secondary coolant.

and flow meter. The connections to the engine were made using an adapter fabricated from 38.10 mm thick steel and drilled and tapped for 19.05 mm NPT fittings. As seen in Figure 3-12, the adapter was bolted in place where the original water pump interfaced with the cylinder head.

In the upper right hand corner of Figure 3-9, the engine lubrication system is shown. Red Line® 40WT Race Oil is used for engine lubrication. Red Line® engine oils formulated for racing applications are made from polyol ester base stocks with high viscosity indexes. Polyol ester based oils are known for having lower volatility resulting in less evaporation at high temperatures [41]. A high viscosity index translates to a reduction in the loss of viscosity as temperature is increased, which was especially critical for this experiment. The engine oil is pressurized by an external gear pump (Flowserve, 1GAFM1DO) designed specifically for high-viscosity fluids. The pump is driven by a 0.37 kW 3-phase electric motor with a VFD (ABB, ACS310) for speed control. A Perma-Cal® pressure gauge measures the oil pressure at the pump outlet. The oil then passes through a gear type flow meter (FLO-Corp, PDSG1-S1-02-TT) that measures the volumetric flow rate of the oil. The oil then enters a flat plate heat exchanger (GEA, FP5X12-6) where the engine



Figure 3-12. Adapter used to connect to custom cooling system installed in original water pump location.

oil heat is transferred to the secondary coolant loop before returning to the engine. The oil is filtered before entering the engine using an oversized engine oil filter (NAPA Gold, 1516) selected for the extra filtering surface area over the original filter. As with the cooling system, the average oil temperature and temperature rise across the engine are measured by two calibrated type-T thermocouples (Omega, TQIN-18U-6).

The diagram in Figure 3-9 also shows the additional instrumentation used in the experiment. On the left, the engine dynamometer (Mid-West Inductor, 1014A) is used to load the engine and measure then engine output. The dyno is controlled through a DyneSystems, Inc. DYN-LOC IV digital dynamometer controller. Directly above the dynamometer is the engine exhaust where three type-K thermocouples (Omega, KQIN-18E-12) measure exhaust gas temperature

exiting each of the three cylinders. A 5-gas analyzer samples the exhaust gases to measure the presence of O₂, CO₂, CO, total hydrocarbons (THC), and oxides of nitrogen (NO_x). The exhaust gases are sampled using a probe placed transverse to the flow direction inside the exhaust pipe. The probe is made from 9.5 mm diameter tubing with the end welded closed. Holes are placed at locations 6.7%, 25.0%, 75%, and 93.3% of the probe length as per the Code of Federal Regulations [42]. To the right of the exhaust, the intake air path is shown flowing through an orifice flow meter (Dwyer, PE-E-2) with a type-T thermocouple (Omega, TQSS-18E-6) measuring the air temperature. Finally, the fuel tank and the scale used to measure fuel flow are seen to the right of the intake. The pressure and return paths are shown, with type-T thermocouples (Omega, TC-T-1/8NPT-G-72) to measure the temperature of the fuel entering and leaving the high-pressure fuel pump.

Though not displayed in the diagram, the engine surface temperatures are also monitored using surface mount type-T thermocouples (Omega, SA1XL-T-72) with self-adhesive backing. The thermocouples are permanently secured using thermally conductive high-temperature epoxy (Omega, OB-200-2) and high-temperature cement (Omega, CC Filler and CC Binder). Each thermocouple is epoxied in place and strain relief is accomplished by cementing the thermocouple wire to a nearby location. The ambient air temperature is also measured in various locations around the facility using bare type-T thermocouples (Omega, 5TC-GG-T-20-72). The air temperature is monitored at the inlet of the intake system, above the engine, below the oil pan, and near the cooling system heat exchanger (Figure 3-13).

Displaying and logging data from the data acquisition system (NI, 9074) is accomplished with LabVIEW programs. The system is used to record process flow temperatures, engine surface temperatures, ambient air temperatures, intake air pressure, and exhaust emissions. Table 3-4

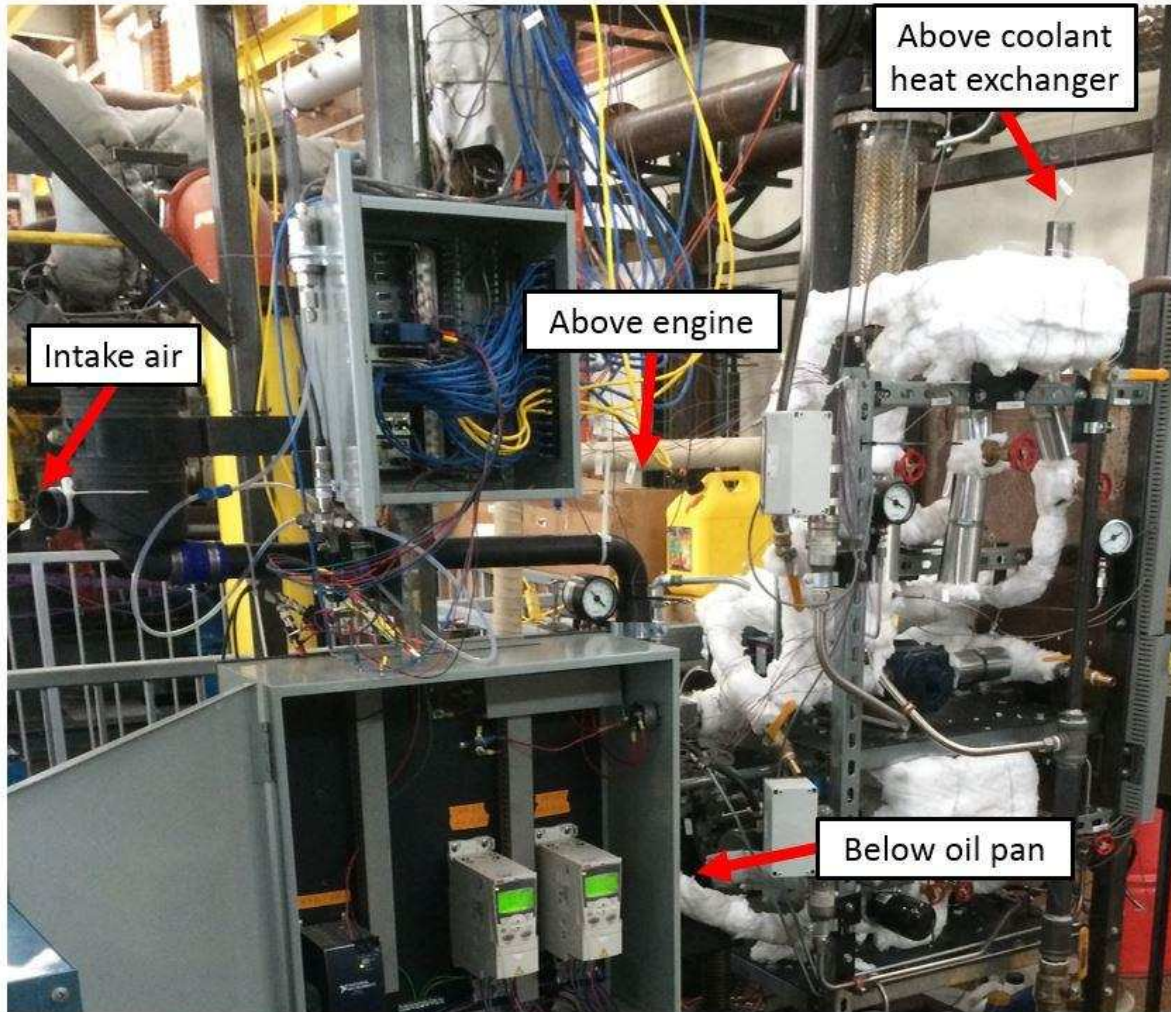


Figure 3-13. Locations of thermocouples used to monitor air temperature.

contains a list of instrumentation and the associated uncertainty for each component. In addition to reading instrument data, LabVIEW is used to control components via an existing NI cRIO installed on the engine skid. Network shared variables are used to start and stop the secondary coolant pump and radiator fan as well as to adjust the secondary coolant radiator bypass control valve. The cooling water flow for the dynamometer is also enabled from the host VI. The test matrix for the experiment is described in the next section.

Table 3-4. Instrumentation and property accuracy.

Temperature Measurements	Medium	Brand	Model #	Calibrated Uncertainty
Oil Pump Inlet	Engine Oil	Omega	TC-T-NPT-G-72	±0.15°C
Oil Pump Outlet	Engine Oil	Omega	TC-T-NPT-G-72	±0.13°C
Oil Cooler Outlet	Engine Oil	Omega	TC-T-NPT-G-72	±0.11°C
HTF Cooler Inlet	HTF	Omega	TC-T-NPT-G-72	±0.06°C
HTF Pump Inlet	HTF	Omega	TC-T-NPT-G-72	±0.12°C
HTF Pump Outlet	HTF	Omega	TC-T-NPT-G-72	±0.10°C
Ambient Air Intake	Air	Omega	TQSS-18E-6	±0.5°C
Exhaust Manifold Cyl. 1	Exhaust	Omega	KQIN-18E-12	±1.33°C
Exhaust Manifold Cyl. 2	Exhaust	Omega	KQIN-18E-12	±0.78°C
Exhaust Manifold Cyl. 3	Exhaust	Omega	KQIN-18E-12	±1.45°C
Pressure Measurements				
Intake Flow Orifice	Air	Omega	PX305-015AI	±0.18 kPa
Intake Flow Orifice – Diff.	Air	Omega	MMDDU005-C1P1C2T2A4	±0.14 kPa
Flow Measurements				
Oil Pump Outlet	Engine Oil	FlowCorp	PDSG1-S1-02-TT	±0.5%
HTF Pump Outlet	HTF	FloCorp	PDSG1-S2-03-TT	±0.5%
	HTF	Hedland	H701A-005-HT	±2.8-5.5%
Oil Cooler Inlet	EG	FloCorp	MFTV-LSU-0706-TXB-MFT2-01-N4	±1%
HTF Cooler Inlet	EG	FloCorp	MFTV-LSU-0706-TXB-MFT2-01-N4	±1%
Air Flow Orifice	Air	Dwyer	PE-E-2	±3.5%-6.0%
Lab Equipment				
Dynamometer/ Controller	Engine Output/Speed	Mid-West DynSystems	1014A DYN-LOC IV	±0.77 N-m 0.5%
Scale 1	Fuel Weight	Ohaus	SD35	±0.02 kg
Scale 2	Fuel Weight	Mettler Toledo	31000L	±0.005 kg
LabVIEW Data Logging	Time Capture	National Instruments	N/A	±1 sec
5 gas: CO/CO2	Exhaust Gas	Siemens	Ultramat 6	0.5% FS
5 gas: NOx	Exhaust Gas	Siemens	NOXMAT 600	0.5% FS
5 gas: O2/THC	Exhaust Gas	Emerson	NGA 2000	1.0% FS

3.3 Test Matrix and Procedure

The goal of the experiment is to evaluate the energy balance of the engine over a wide range of steady-state operating conditions. The test parameters were engine speed, engine torque, and coolant temperature. Table 3-5 shows the full test matrix with an “X” denoting a completed

test run. Three engine speeds were chosen between the idle speed of 1200 rpm and the maximum engine speed of 3600 rpm. For each engine speed, the engine was subject to a load requiring engine torque of 12, 15, 18, 21, and 24 N-m. Since power output is the product of torque and speed, the result was 15 different load points between 3.48 kW and 8.43 kW (34-81% of maximum load). The 15 load points were repeated for six engine coolant temperature set points from 90°C up to 200°C, with the inlet and outlet temperatures at the engine set to approximately 5°C below and 5°C above the target value, respectively. Therefore, the average coolant temperature inside the engine block was extremely close to the target temperature, except for the 12, 15, and 18 N-m data points at 2800 rpm and 90°C coolant temperature. For these data points, the outlet coolant temperature was set near the target temperature and the inlet temperature was much lower. The average coolant temperature for these three data points was between 75°C and 80°C. Also, note that tests were limited to 3100 rpm above 150°C coolant temperature due to issues with excessive driveline vibration.

The testing began with the 90°C coolant temperature test points and proceeded by incrementally increasing the coolant temperature after all points shown in the text matrix for the given temperature were completed. Tests were typically run in order of lowest engine speed up to highest, with torque increasing or decreasing to minimize adjustments. For example, the first test point would be for 90°C, 2800 rpm, and 12 N-m of torque. The torque would then be increased to 15, 18, 21, and 24 N-m before increasing the engine speed to 3100 rpm. The 3100 rpm points would be run with decreasing engine torque from 24 N-m back down to 12 N-m.

Before testing began, and in between each temperature, the engine compression was checked and recorded, and the engine oil was sampled and sent out for analysis for oxidation levels and metal particle content. The cylinder compression was checked in the following manner. With

Table 3-5. Test matrix for high-temperature diesel engine experiment.

Speed [rpm]	Torque [N-m]	% of Max Load	Coolant Temperature [°C]					
			90	100	125	150	175	200
			Operating Hours					
			42	49	73	38	21	11
2800	12	34%	X	X	X	X		
	15	42%	X	X	X	X		
	18	50%	X	X	X	X		
	21	59%	X	X	X	X		
	24	67%	X	X	X	X		
3100	12	37%	X	X	X	X	X	X
	15	46%	X	X	X	X	X	X
	18	56%	X	X	X	X	X	X
	21	65%	X	X	X	X	X	X
	24	74%	X	X	X	X	X	X
3400	12	41%	X	X	X	X		
	15	51%	X	X	X	X		
	18	61%	X	X	X	X		
	21	71%	X	X	X	X		
	24	81%	X	X	X	X		

the engine at room temperature, the fuel system was disabled and all three glow plugs were removed from the engine. The compression test adapter was then threaded into the glow plug hole (Briggs and Stratton part# 19443) and the diesel compression gauge (OTC, 5021) was then connected to the adapter. The pressure relief valve was pressed to zero the gauge. The engine was then cranked for 10 cycles and the compression value was recorded. The relief valve was opened and the test was performed two more times for a total of three data points. These values were then averaged to arrive at the compression for the given cylinder. The process was then repeated for each additional cylinder.

The engine oil was sampled by removing the engine oil drain plug and holding the sample container (provided by Wagner Equipment Co.) under the draining oil until the container was sufficiently full (a fill line is provided on the container). The container was then sealed in the provided plastic bag and shipped to Wagner for analysis. Wagner measured the sample then sent

an analysis report for the oil sample detailing the levels of wear metals and oil oxidation. A clean oil sample was analyzed before the experiment to provide baseline values for accurate comparison.

Much of the facility described in the previous sections is manually controlled and this section will describe the procedures used to start and operate the system as well as the actual test procedures. Before startup, a series of system checks were performed to ensure readiness for operation. First, all fluid levels were checked, including engine oil, HTF, EG, and diesel fuel. The quantity of engine oil and HTF added was recorded to monitor usage. After fluid levels were verified, the HTF pump was started using the VFD and set to a frequency that resulted in a flow rate of at least 3.8 L min^{-1} . The oil pump was then started via the VFD and set to provide between 310.3 and 344.7 kPa of pressure. Before cranking the engine, the key was turned to the ON position and the glow plug switch was energized for approximately 15 seconds to warm the pre-chambers. The engine was then cranked until engine firing was confirmed. The engine was allowed to idle until the oil temperature was above 40°C , after which the engine speed was increased in steps to the desired value (2800-3400 rpm). Once the oil temperature was above 50°C , a load was applied via the dynamometer in 2 N-m increments up to the target torque allowing time between each step for the engine oil temperature to stabilize.

The test engine was operated over a wide range of loads as well as coolant temperatures. The procedure for reaching a set point is as follows. First, the engine speed was adjusted to the rough target using the cable operated speed control on the high-pressure fuel pump. Following speed adjustment, engine load was set using tumblers on the front face of the dyno controller. Engine speed was then readjusted after the target load was reached to achieve the target engine speed within ± 10 rpm. Initially, the secondary cooling system pump remained off to allow the HTF temperature to increase more rapidly. Once the HTF temperature approached 75% of the target

value, the secondary coolant pump was turned on to allow the secondary cooling system temperature to rise. As the HTF temperature reached within 10°C of the target temperature, the secondary cooling system fan was activated. Finally, the HTF target temperature was achieved by adjusting the HTF flow rate, secondary coolant flow rate, and the heat exchanger bypass. These adjustments were also used to fine tune the temperature difference across the engine to approximately 10°C. The oil system took significantly longer to reach operating temperature than the cooling system. Rather than adjusting the oil system to reach a set temperature, adjustments were made to ensure 275.8 kPa of oil pressure and a minimum temperature increase across the engine of at least 10°C.

The logging of experimental data was initiated only after the relevant temperatures had stabilized to steady state. To assist in the determination of steady state, two minute averages of the key temperatures were displayed on the host VI. The real-time temperatures were compared to these values, and steady state was assumed when the differences between the real time and average temperatures were sufficiently small ($< 0.1^{\circ}\text{C}$). Once steady state was reached, occasional adjustments to the cooling system were required to prevent the HTF temperature from drifting more than 1°C from the target temperature. These small adjustments were typically made using the heat exchanger bypass valve.

Data logging was activated after steady state was reached and adequate temperature differences across the engine were verified. Data was logged at a rate of 2 Hz for the period of time in minutes that was entered into the VI. The length of the data logging period was determined from the estimated fuel usage at the given load condition. Accurate fuel flow calculations using the starting and ending fuel weights required a long enough run to reduce the error in the difference of the weights to approximately 1%. Initially, a scale with an accuracy of ± 0.02 kg was used to

weigh the fuel before and after the test. Due to the small engine and relatively low output, logging times between one and two hours were necessary to reach the desired uncertainty. However, in the latter portion of the experiment, a high accuracy scale was acquired (accuracy of ± 0.002 kg) which greatly reduced the test duration.

Once all tests were completed, the engine was disassembled and carefully inspected for signs of wear. Photos were taken of internal engine components such as pistons, connecting rods, crankshaft, camshaft, lifters, and the key surfaces of the engine block itself. The aforementioned components were also measured using precision instruments for comparison with measurements taken before testing began. The measurements included the cylinder bores diameters, connecting rod bearing clearances, piston pin clearances, crankshaft main bearing clearances, and lifter to lifter bore clearances. The measurements and photos are further described in section 6.3 (Engine Condition Monitoring) and the measurement data is provided in Appendix C. The methods used to reduce the data collected in the experiment are covered in the next chapter.

CHAPTER 4. DATA REDUCTION

The experiment described in the previous chapter was performed to understand the effect of running an engine at elevated coolant temperatures and to measure the available waste heat. This chapter will provide detailed descriptions of the calculations required for each component of the energy balance, the engine thermal efficiency, and the availability of the waste heat from the test engine. Sample calculations are performed and will be based on one of the 70 data points from the test matrix described previously. The details of the representative data point are given in Table 4-1. Table 4-2 lists the fuel, oil, and HTF properties used in the calculations and their sources and assumed uncertainty. This chapter will be covered in the following three sections: Energy Balance, Waste Heat Availability, and Correlations and Statistical Significance.

4.1 Energy Balance

The primary goal of the experiment described in the previous chapter was to perform an energy balance on the small diesel engine at increasing coolant temperatures. The energy balance for a diesel engine can be represented by the following equation:

$$\dot{E}_{\text{fuel}} = \dot{W}_{\text{out}} + \dot{Q}_{\text{exh}} + \dot{Q}_{\text{cool}} + \dot{Q}_{\text{oil}} + \dot{E}_{\text{HC}} + \dot{E}_{\text{oth}} \quad (4.1)$$

In the present work, the following components of the energy balance were measured: the fuel energy input (\dot{E}_{fuel}), engine output (\dot{W}_{out}), heat lost to the exhaust (\dot{Q}_{exh}), coolant (\dot{Q}_{cool}), and engine oil (\dot{Q}_{oil}), and lost energy due to unburned hydrocarbons (\dot{E}_{HC}). Despite efforts to obtain a complete energy balance, some losses were not captured and will fall into the ‘other’ category. Such losses include heat loss from the engine structure in the form of convection and radiation, soot present in the exhaust, and pumping losses. The losses that were not measured are estimated by solving

equation (4.1). This section will cover each of the components measured and describe in detail how the values were calculated.

Table 4-1. Data for representative test point of 3100 rpm engine speed and 18 N-m of torque at 150°C coolant temperature.

Parameter	Value	Units
Coolant Temperature	150	°C
Avg. Engine Speed	3101.5	rpm
Avg. Engine Torque	17.8	N-m
Fuel Mass Start	22.12	kg
Fuel Mass End	19.08	kg
Test Duration	6000.00	s
LHV	43.2	MJ kg ⁻¹
HTF Temperature In	144.77	°C
HTF Temperature Out	155.67	°C
HTF Density	860.29	kg m ⁻³
HTF Heat Capacity	2.194	kJ kg ⁻¹ K ⁻¹
HTF Volumetric Flow Rate	210	cm ³ s ⁻¹
Oil Temperature In	70.30	°C
Oil Temperature Out	83.40	°C
Oil Density	838.41	kg m ⁻³
Oil Heat Capacity	2.183	kJ kg ⁻¹ K ⁻¹
Oil Volumetric Flow Rate	100	cm ³ s ⁻¹
Avg. HTF Vol. Flow Rate	0.000206	m ³ s ⁻¹
Avg. Oil Vol. Flow Rate	0.000101	m ³ s ⁻¹
Air Mass Flow Rate	0.0149	kg s ⁻¹
Air Temperature	34.34	°C
Air Viscosity	1.972x10 ⁻⁵	Pa-s
MW of Air	28.97	kg kmole ⁻¹
MW of Fuel	167.31	kg kmole ⁻¹
MW of N ₂	28.01	kg kmole ⁻¹
MW of O ₂	32.00	kg kmole ⁻¹
MW of H ₂ O	18.02	kg kmole ⁻¹
MW of CO ₂	44.01	kg kmole ⁻¹
Exhaust Temperature	429.22	°C
C _{CO}	385.2	ppm
C _{CO₂}	68700	ppm
C _{THC}	73.17	ppm

4.1.1 Fuel Energy

Before an energy balance can be performed, the rate of energy flow into the engine must be accurately known. This task was complicated by the small size of the engine and the corresponding low rate of fuel flow. Care was taken to ensure that the test durations were sufficiently long to decrease the uncertainty in the fuel mass difference to an acceptable level of $\pm 1\%$. Initially, this level of accuracy required test durations between one and two hours per data point, depending on the engine load. This length of time was necessary due to the relatively low accuracy of the scale (Scale 1 in Table 3-4). Before the 175°C data points were recorded, a higher accuracy scale was acquired which allowed test durations to be reduced to between 10 and 25 minutes while maintaining the same accuracy (Scale 2 in Table 3-4).

Table 4-2. Source and assumed uncertainty for fluid properties.

Property	Source	Assumed Uncertainty
Lower Heating Value of Off-Road Diesel Fuel	Literature [43]	$\pm 800 \text{ kJ kg}^{-1}$
Oil Density	Anton Paar SVM 3000 – curve fit	5%
Oil Heat Capacity	Dynalene Lab Services – curve fit	5%
HTF Density	Duratherm Literature – curve fit	5%
HTF Heat Capacity	Duratherm Literature – curve fit	5%

The energy flow into the engine is in the form of off-road diesel fuel entering the combustion chamber, which is subsequently mixed with air and burned to produce the heat necessary to expand the inert gases and push the piston down. The energy flow from the diesel fuel is found as follows:

$$\dot{E}_{\text{fuel}} = \dot{m}_{\text{fuel}} \cdot LHV_{\text{fuel}} \quad (4.2)$$

$$\dot{m}_{\text{fuel}} = \frac{\Delta m_{\text{fuel}}}{t_{\text{test}}} \quad (4.3)$$

The change in mass of the diesel fuel is found by placing the fuel tank on a scale and taking one measurement immediately after data acquisition is begun, and one measurement immediately after data acquisition is complete. The difference between the two measurements is then divided by the test duration as recorded by the data acquisition system, giving the average mass flow rate of the fuel. The fuel mass flow rate is then multiplied by the lower heating value (LHV) of diesel fuel to arrive at the energy flow entering the engine. The LHV is defined as the heat energy released from combustion per kg of fuel, assuming all combustion products are returned to initial conditions of 298°C and 101 kPa, and that all water present is in vapor form [36]. For this calculation, the LHV of diesel fuel was taken to be 43.2 MJ kg⁻¹ [43]. For the representative test point, the change in fuel mass is 3.04 kg and the test duration is 6000 s, giving a fuel mass flow rate of 0.507 g s⁻¹. Using equations (4.2) and (4.3), the fuel energy flow is found to be 21.89 kW.

4.1.2 Engine Power Output and Thermal Efficiency

As previously mentioned, the engine power output was controlled and measured via an eddy current dynamometer and controller. The controller provides 0-5V outputs for torque and engine speed for data acquisition purposes. However, the 0-5V signals from the outputs on the back of the controller were found to be inconsistent and unreliable and the decision was made to manually record the engine speed and torque from the digital display of the controller. Engine speed was displayed in rpm and engine torque was set to display in N-m. The values were recorded once every five minutes during the longer tests with the original scale and once every minute with the higher accuracy scale.

Using the engine speed and torque recorded from the dynamometer controller, the engine power is calculated as follows:

$$\dot{W}_{\text{out}} = N\tau \left(\frac{2\pi}{\text{rev}} \right) \left(\frac{1 \cdot \text{kN}}{1,000 \cdot \text{N}} \right) \left(\frac{1 \cdot \text{min}}{60 \cdot \text{s}} \right) \quad (4.4)$$

Here, the engine speed (N) is multiplied by the engine torque (τ), as well as conversion factors to reach the desired units of kW. Using the torque value of 17.8 N-m and the engine speed of 3101.5 rpm from Table 4-1, the engine power for the representative data point is 5.78 kW.

Engine BTE provides the baseline system efficiency used to evaluate the WHR modeling results discussed in the next chapter. BTE is also good indicator of the health of the engine, and was monitored closely for changes as the coolant temperature was increased. As discussed in the literature review, the engine brake thermal efficiency is essentially the engine output normalized by the fuel input:

$$BTE = \frac{\dot{W}_{\text{out}}}{\dot{E}_{\text{fuel}}} \quad (4.5)$$

From the previously calculated values for the engine output and fuel energy flow input, the BTE for the representative test point is 26.40%.

4.1.3 Engine Coolant and Oil Waste Heat

The heat rejected to the engine coolant and engine oil were calculated in the same manner. Heat rejection to the coolant and engine oil were of primary importance for this work, not only for the contribution to the energy balance, but as important inputs for the WHR modeling discussed in the next chapter. The heat loss from the engine to both fluids was found using the measured volumetric flow rate and the temperature difference across the engine:

$$\dot{Q} = \dot{V} \cdot \rho \cdot c_p (T_{\text{out}} - T_{\text{in}}) \quad (4.6)$$

The inlet and outlet temperatures were corrected using the fit obtained from calibration of the thermocouples against a highly accurate reference. From the values in Table 4-1, the HTF temperatures in and out of the engine are 144.77°C and 155.67°C, respectively. The density and

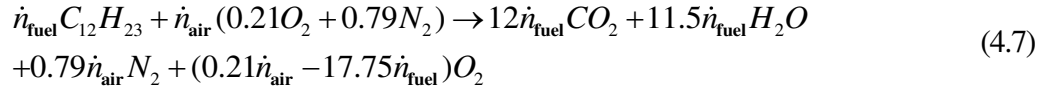
heat capacity for the Duratherm G were supplied by the manufacturer over a wide temperature range. A linear fit was applied to the density and heat capacity data to arrive at linear equations to determine the values at a given temperature. From the table, the HTF density is 860.29 kg m^{-3} and the HTF heat capacity is $2.19 \text{ kJ kg}^{-1} \text{ K}^{-1}$. Using the values above along with the volumetric flow rate for HTF of $210 \text{ cm}^3 \text{ s}^{-1}$ from Table 4-1, the heat rejection to the HTF for the representative point is 4.22 kW.

A similar procedure is used to calculate the heat rejection rate to the engine oil. The corrected values for the oil temperature are given in Table 4-1. The inlet and outlet oil temperatures are found to be 70.30°C and 83.40°C , respectively. The density of the engine oil was measured using an Anton Paar SVM 3000 viscometer at the CSU EECL. An oil sample was also analyzed by Dynalene to provide heat capacity data over a range of temperatures. A linear fit was performed on the engine oil properties and the resulting fit was used to calculate the values for each test condition. For the average oil temperature of 76.85°C for the representative point, the oil density is 838.41 kg m^{-3} and the oil heat capacity is $2.18 \text{ kJ kg}^{-1} \text{ K}^{-1}$. From these values and the volumetric flow rate of $100 \text{ cm}^3 \text{ s}^{-1}$, the heat rejection rate to the engine oil is 2.42 kW.

4.1.4 Exhaust Waste Heat

The quantity of waste heat present in the exhaust gases is another main component of the energy balance for the test engine. Like the coolant and engine oil heat rejection, the exhaust waste heat is also a key input to the WHR models. The heat loss to the exhaust gases was found by assuming lean combustion products and calculating the difference in enthalpy for each gas as it cools from the exhaust temperature to a standard ambient temperature of 25°C . The lean combustion products were assumed to be N_2 , O_2 , CO_2 , and H_2O . These four products were taken

to be gases at ambient temperature. The chemical reaction for combustion was balanced to determine the molar flow rates for each product as follows:



Here, \dot{n}_{fuel} is the molar flow rate of the diesel fuel and \dot{n}_{air} is the molar flow rate of the intake air, both found by dividing the measured mass flow rates by the molecular weights. For the representative point, \dot{n}_{fuel} is found by dividing the fuel mass flow rate of 30.42 g min⁻¹ by the molecular weight of 167.31 kg kmol⁻¹ with the result of 0.18 mol min⁻¹. The air molar flow rate is found by dividing the air mass flow rate of 14.91 g s⁻¹ by the molecular weight of 28.97 kg kmol⁻¹ to reach 0.51 mol s⁻¹. Using equation (4.7), the molar flow rates for CO₂, H₂O, N₂, and O₂ are 2.18 mol min⁻¹, 2.09 mol min⁻¹, 24.60 mol min⁻¹, and 3.31 mol min⁻¹, respectively. The mass fraction for each gas is then found using the molar flow rates of the products as well as the molar mass for each species:

$$MF = \frac{\dot{n} \cdot MW}{\dot{m}_{\text{fuel}} + \dot{m}_{\text{air}}} \quad (4.8)$$

From the molar flow rates calculated above and the molecular weights given in Table 4-1, the mass fractions for CO₂, H₂O, N₂, and O₂ are 0.104, 0.041, 0.745, and 0.115, respectively. The mass fractions for the products were then used to weight the respective enthalpy change for the four gases when cooled from the exhaust temperature to room temperature. The enthalpy changes were found using the JANAF tables provided by the National Institute of Standards and Technology [44]. The data for each gas was narrowed down to the temperature range of interest (130°C – 730°C) and a second order polynomial fit was performed to ensure high levels of accuracy. The following formulas represent the fits for each of the four gases, with temperature in units of °C:

$$\Delta h_{\text{CO}_2} = 0.0002T_{\text{exh}}^2 + 0.9118T_{\text{exh}} - 29.472 \quad (4.9)$$

$$\Delta h_{\text{H}_2\text{O}} = 0.0003T_{\text{exh}}^2 + 1.8038T_{\text{exh}} - 42.152 \quad (4.10)$$

$$\Delta h_{\text{N}_2} = 0.0001T_{\text{exh}}^2 + 1.0048T_{\text{exh}} - 22.907 \quad (4.11)$$

$$\Delta h_{\text{O}_2} = 0.0001T_{\text{exh}}^2 + 0.918T_{\text{exh}} - 24.316 \quad (4.12)$$

Using equations (4.9-4.12) and the exhaust temperature from Table 4-1 of 429.22°C, the change in enthalpy for CO₂, H₂O, N₂, and O₂ are 398.74 kJ kg⁻¹, 787.34 kJ kg⁻¹, 427.39 kJ kg⁻¹, and 388.13 kJ kg⁻¹, respectively. The total exhaust heat transfer was then found as follows:

$$\dot{Q}_{\text{exh}} = (\dot{m}_{\text{fuel}} + \dot{m}_{\text{air}}) \cdot (MF_{\text{CO}_2} \cdot \Delta h_{\text{CO}_2} + MF_{\text{H}_2\text{O}} \cdot \Delta h_{\text{H}_2\text{O}} + MF_{\text{N}_2} \cdot \Delta h_{\text{N}_2} + MF_{\text{O}_2} \cdot \Delta h_{\text{O}_2}) \quad (4.13)$$

Using the values calculated previously, the total exhaust heat loss for the representative point is 6.73 kW.

4.1.5 Unburned Hydrocarbons

Combustion is never 100% efficient in an engine and some fuel energy is always lost through unburned fuel exiting the exhaust. This unburned fuel can be measured using a 5-gas analyzer with the result reported as total hydrocarbon (THC) present. The THC measurement is dependent on the hydrocarbon used to calibrate the equipment. The 5-gas analyzer at the EECL was calibrated using methane (CH₄), so the reported quantity of hydrocarbons present in the exhaust must be converted to the appropriate fuel to accurately calculate the energy lost. The rate of energy loss in the exhaust due to uncombusted fuel is calculated as follows:

$$\dot{E}_{\text{THC}} = \frac{12 \cdot \dot{m}_{\text{fuel}} \cdot LHV_{\text{fuel}} \cdot C_{\text{THC}}}{C_{\text{THC}} + C_{\text{CO}} + C_{\text{CO}_2}} \quad (4.14)$$

The 12 in the numerator refers to the number of carbon atoms in typical a diesel fuel molecule, \dot{m}_{fuel} is the mass flow rate of diesel fuel, LHV_{fuel} is the lower heating value of diesel fuel (43.2 MJ kg⁻¹), MW_{fuel} is the molecular weight of diesel fuel (167.31 kg kmol⁻¹), C_{CO} is the CO

concentration in the exhaust, C_{CO_2} is the CO_2 concentration in the exhaust, and C_{THC} is the concentration of THC in the exhaust (assuming methane). For the representative point, the fuel mass flow rate is 0.507 g s^{-1} and the LHV of diesel fuel is 43.2 MJ kg^{-1} . The emissions concentrations are: 73.17 ppm for C_{THC} , 385.2 ppm for C_{CO} , and 68,700 ppm for C_{CO_2} . From these values, equation (4.14) yields a loss of 0.28 kW from the unburned hydrocarbons measured in the exhaust.

The energy balance results for the representative point are summarized in Table 4-3. The fuel input of 21.89 kW and the total measured output of 19.43 kW leaves 2.46 kW of additional fuel energy. As mentioned earlier, this energy is lost to the environment, soot in the exhaust, and pumping losses.

Table 4-3. Energy balance results for representative point 3100 rpm, 18 N-m torque and 150°C coolant temperature.

<i>Input</i>	Value	Units
Fuel Energy	21.89	kW
Outputs		
Engine Power Output	5.78	kW
Coolant Waste Heat	4.22	kW
Oil Waste Heat	2.42	kW
Exhaust Waste Heat	6.73	kW
Unburned Hydrocarbons	0.28	kW
Total	19.43	kW
Other Losses	2.46	kW

4.2 Waste Heat Availability

Prior work shows that the quality of waste heat is as important as the quantity of that waste heat. The First Law of Thermodynamics is useful for evaluating energy balances, but is not sufficient to analyze a Rankine cycle and determine the possible efficiency gain for a given heat source. Here, the Second Law of Thermodynamics can be used to analyze a cycle and shed light

on the possible efficiency of that cycle. The Kelvin-Planck formulation of the Second Law of Thermodynamics states that it is impossible for a cycle to accept a certain quantity of heat from a reservoir and produce the same quantity as work with no other effects [45]. For a cycle such as a heat engine, some of the heat received by the cycle must be rejected to a lower temperature reservoir. Carnot's theorem (see equation (1.1)) stems from this formulation of the Second Law and provides a method for estimating the maximum efficiency of a cycle based on the absolute temperatures of the hot and cold reservoirs. This concept can be extended to allow the estimation of the usable portion (or availability) of a waste heat source. The quantity representing the availability of a waste heat source is known as exergy.

For heat transfer, the rate of exergy exchanged is defined as follows:

$$\dot{B} = \dot{Q} \left(1 - \frac{T_L}{T_H} \right) \quad (4.15)$$

The rate of exergy exchanged is based on the Carnot efficiency given in equation (1.1) and therefore gives the upper limit of usable energy. From equation (4.15) it can be deduced that, to increase the output of a heat engine such as a WHR system for a fixed cold temperature reservoir, either the heat input can be increased or the temperature of the source can be raised. The availability of each waste heat stream was evaluated to estimate the quantity of usable heat through the calculation of the rate of exergy exchanged in the heat transfer process. For this analysis, the temperature of the sink was set to 25°C (298.15K) for all points to ensure consistency in the evaluation of exergy. The temperature of the heat source was taken to be the average temperature of the coolant inside the engine or the average exhaust temperature in the manifold. The exergy exchange rate for the exhaust and engine coolant can be found for the representative test point using the heat flow rates calculated previously and the temperatures from Table 4-1. For the exhaust gases, the heat flow rate is 6.73 kW and the temperature is 429.22°C (702.37K), giving an

exergy rate of 3.87 kW. The engine coolant heat flow rate was found to be 4.22 kW and the average coolant temperature is 150.10°C (423.25 K), which gives an exergy flow rate of 1.25 kW. Finally, the engine oil heat flow rate is 2.42 kW with an average oil temperature of 76.74°C (349.89 K), which returns an exergy flow rate of 0.36 kW. The uncertainty calculations for the values presented in this chapter can be found in Appendix B.

4.3 Correlations and Statistical Significance

Correlations between measured engine parameters and the coolant temperature were evaluated using a linear regression analysis. A least squares fit was performed for each parameter to determine the correlation coefficient R_{cor} , which was then used to perform a t -test. The t distribution was used to test the hypothesis of the correlation due to the sample size being below 30. The null hypothesis occurs when no correlation exists between the measured parameter and the engine coolant temperature, and corresponds to a t -value below the critical t -value. The critical t -value is found by taking the two-tailed inverse of the t distribution using the desired probability and the number of degrees of freedom. The null hypothesis was taken to be the case where either no correlation exists, or the correlation with the opposite sign from the one found during the regression analysis exists. The t -value for the regression is found using the following formula [46]:

$$t - \text{value} = R_{\text{cor}} \cdot \sqrt{\frac{n-2}{1-R_{\text{cor}}^2}} \quad (4.16)$$

Here, n represents the number of samples and $n-2$ is the number of degrees of freedom. The t -value was then compared with the one-sided critical t -value for a 95% confidence interval and the number of degrees of freedom for the given measurement. If the calculated t -value was greater than the critical t -value, the correlation was taken to be significant. Otherwise, it was assumed that not enough data points were available to determine whether the correlation was significant. To

provide additional information on the significance of the correlations, the p -value was also calculated. The p -value was found by subtracting the cumulative distribution function evaluated at the t -value from 1 [47]. The p -value represents the probability that the given t -value (or a more extreme t -value) would be found given that the null hypothesis is true. The results of the regression and statistical significance analysis are shown in Figure 4-1, which presents the probability that each correlation shown is statistically significant. The specific correlations will be discussed further in the Chapter 6: Results and Discussion. In the next chapter, the methods used to estimate the efficiency gains from utilizing engine coolant waste to drive a hypothetical Rankine WHR system, and the associated space requirements for adding this system.

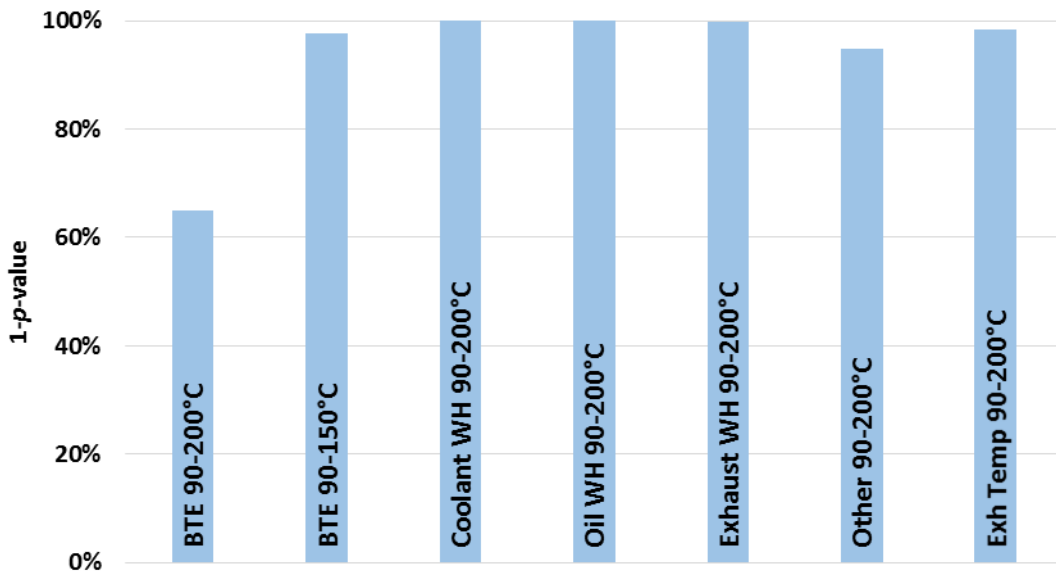


Figure 4-1. Regression analysis results for 3100 rpm and 18 N-m of torque used to determine correlations between parameters and coolant temperature and their significance using a 95% confidence interval.

CHAPTER 5. MODELING EFFORT

The previous chapter covered the data reduction techniques used to provide meaningful results from the experiments. In addition to this analysis, modeling was performed to estimate the efficiency gains of the high temperature diesel engine using WHR, as well as estimate the footprint required for each system. Both thermodynamic system level models and individual heat exchanger models were created for a selection of coolant temperatures. All models were created in Engineering Equation Solver (EES) [48], which is a simultaneous equation solver that also has a large database of thermodynamic properties for many fluids and solids. The EES property database was used for all fluid and solid material properties unless otherwise noted. The difficulty of simultaneous equation solving is that it becomes burdensome to step through and describe the calculations in a logical progression. With that in mind, this chapter will present the equations used to perform the thermodynamic analysis along with sample data needed to solve the equations. The first section of this chapter will give an overview of the WHR system design. Next, the thermodynamic models for the system will be described in detail. Finally, the last section will cover the heat exchanger models that were used to estimate the footprint of the system at varying coolant temperatures.

5.1 WHR System Design

Two different WHR system configurations were modeled, one for the state-of-the-art WHR system with 90°C coolant, and one for the high-temperature coolant systems. Figure 5-1 shows the state-of-the-art system, which only recovers waste heat from the exhaust gases. The numbers shown throughout the system will be used to reference the working fluid and exhaust properties at each location. Starting in the lower left-hand corner, the pump pressurizes the working fluid, which

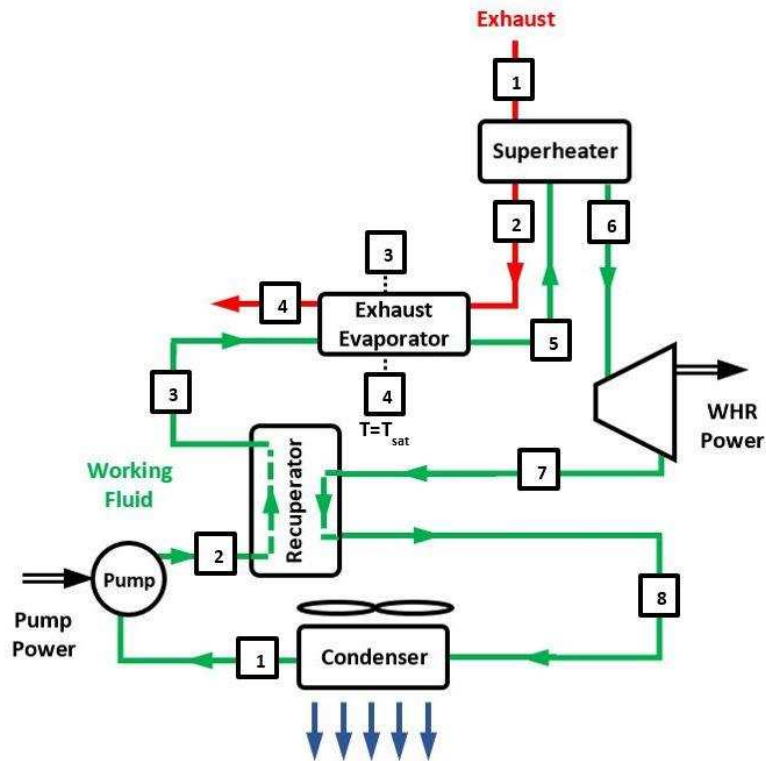


Figure 5-1. Diagram for state-of-the-art WHR system.

then travels through the low-temperature side of the recuperator for pre-heating. The working fluid then passes through the exhaust evaporator and superheater. Note that an additional point inside the exhaust evaporator is labeled for both the exhaust and working fluid streams. This point denotes where the working fluid reaches the saturation temperature and signifies the end of the single-phase portion and the beginning of the two-phase portion of the evaporator. The superheated vapor then flows into the turbine where it expands and creates mechanical output. The lower pressure vapor from the outlet of the turbine then travels through the hot side of the recuperator. Finally, the vapor is condensed back to the liquid state before entering the pump. The configuration for the high-temperature coolant WHR systems is shown in Figure 5-2 and is like the first configuration with one primary difference. Unlike the first configuration, the working fluid path splits after the

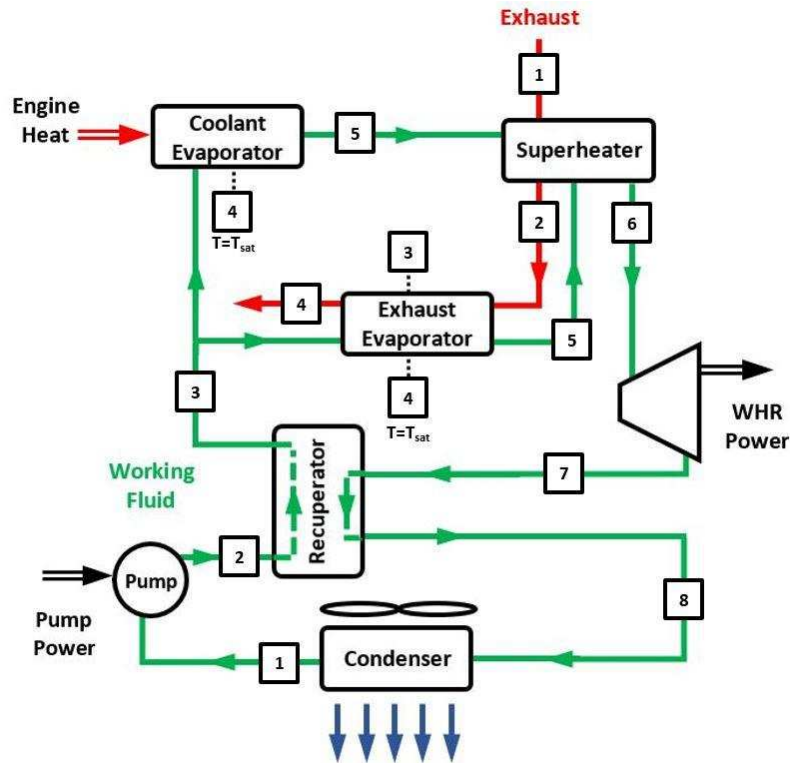


Figure 5-2. Diagram for high-temperature coolant WHR systems.

recuperator, with one path flowing through the coolant evaporator, which is the engine coolant passages, and the other through an exhaust evaporator. Both streams are fully evaporated and then combine before the superheater, where the high temperature exhaust gases raise the working fluid vapor temperature beyond the saturation temperature. Ethanol was chosen as the working fluid for this theoretical WHR system. However, this does not imply that ethanol is the optimum choice for this system. A working fluid comparison was beyond the scope of this work and further optimization may result in additional gains.

5.2 Thermodynamic Analysis

A flow chart for the thermodynamic analysis is shown in Figure 5-3. The thermodynamic models were built using a number of assumptions listed in Table 5-1. The experiment was performed at approximately 1,500 m above sea level, so the ambient air pressure was found to be near 85 kPa. Therefore, it was assumed that the exhaust pressure was 100 kPa which represents a gauge pressure of approximately 15 kPa. The evaporator and recuperator effectiveness were set at 80% for all models. Isentropic pump and turbine efficiency were assumed to be 50% and 60%, respectively. The quality of the ethanol at the evaporator outlet was assumed to be exactly 1, and the quality of the ethanol at the condenser outlet was assumed to be exactly 0. A target closest approach temperature (CAT) for the evaporator was set at 5°C for all cases. Finally, a maximum superheat temperature was set at 375°C, though the superheat temperature was often lower than the maximum in order to meet the CAT requirements. Next, inputs from the experiment were entered into the model (Table 5-2). The inputs included the exhaust temperature, air/fuel ratio, fuel mass flow rate, exhaust and coolant heat flow rates, and exhaust mass fraction for the lean combustion products of CO₂, H₂O, N₂, and O₂. The exhaust temperature was used as an input for

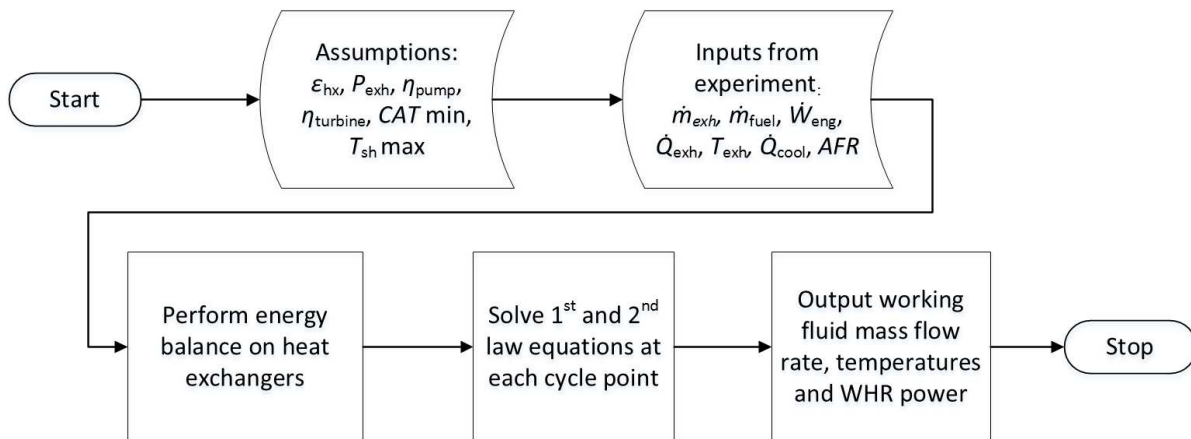


Figure 5-3. Flow chart for thermodynamic analysis.

Table 5-1. Thermodynamic analysis assumptions.

Assumption	Value	Units
Exhaust Pressure	100	kPa
Evaporator Effectiveness	80	%
Recuperator Effectiveness	80	%
Isentropic Pump Efficiency	50	%
Isentropic Turbine Efficiency	60	%
Minimum Closest Approach Temperature	5	°C
Quality at Evaporator Outlet	1	-
Quality at Condenser Outlet	0	-
Maximum Superheat	375	°C

the energy balance of the superheater (exhaust temperature at point 1). The air/fuel ratio was needed to calculate the exhaust enthalpy and entropy as a function of the combustion product enthalpies and entropies. The exhaust heat flow provided an input for the energy balance on the evaporator and superheater. The coolant heat flow was necessary to solve the energy balance on the engine block evaporator. Finally, the mass fractions of the lean combustion products were used to calculate the specific heat capacity for the exhaust. The inputs from the experiment and model assumptions were used to perform energy balances on each heat exchanger and solve 1st and 2nd laws of thermodynamic equations to arrive at the working fluid state at each point in the Rankine cycle. The thermodynamic modeling also provided an estimate of the WHR system output, which was then used to determine the efficiency gain.

The matrix of WHR system operating points that were modeled is shown in Table 5-3. The operating point of 3100 rpm and 24 N-m of torque was chosen for this analysis, and coolant temperatures of 90°C, 150°C, 175°C, and 200°C were investigated. The analysis was performed using condenser temperatures of 60°C and 90°C to provide insight into the trade-off between system performance and condenser footprint, which will be discussed further in the next section. The 90°C coolant temperature point represents the state of the art and uses only the exhaust gases for WHR since the coolant temperature is too low for utilization. This speed and load point resulted

Table 5-2. Inputs for thermodynamic analysis.

Experimental Data Inputs	90°C	150°C	175°C	200°C
Engine Power Output [kW]	7.70	7.65	7.64	7.64
Exhaust Temp [°C]	500.6	566.0	539.1	597.3
Air/Fuel Ratio	24.97	22.14	24.06	23.46
Fuel Mass Flow Rate [g s ⁻¹]	0.6264	0.6666	0.6125	0.6487
Exhaust Mass Flow [kg/s]	0.01627	0.01543	0.1535	0.01587
Exhaust Heat Flow [kW]	8.45	9.23	8.66	10.05
Coolant Heat Flow [kW]	N/A	6.47	4.96	5.05
CO ₂ Exhaust Mass Fraction	0.1215	0.1364	0.1260	0.1290
H ₂ O Exhaust Mass Fraction	0.0477	0.0535	0.0494	0.0506
N ₂ Exhaust Mass Fraction	0.7374	0.7338	0.7362	0.7375
O ₂ Exhaust Mass Fraction	0.0930	0.0759	0.0874	0.0934
User Defined Inputs				
Evaporator Saturation Temp [°C]	200	150	175	200
Max Superheat Temp [°C] (60°C Condenser Temp)	375	290	350	375
Max Superheat Temp [°C] (90°C Condenser Temp)	375	240	300	375

in an engine power output of approximately 7.65 kW. At 90°C coolant temperature, the engine efficiency was found to be 28.47%. The total increase in efficiency due to the WHR system configurations considered here will be compared to this baseline engine efficiency value, even though the actual engine efficiency may differ at each operating temperature. This will ensure that the relative efficiency increase from WHR at higher temperatures will not be underestimated due to issues with the engine efficiency measurement that will be discussed in Chapter 6. Therefore, the reported relative efficiency increase is calculated as follows:

$$\eta_{\Delta\text{rel}} = \frac{\eta_{\text{comb}} - \eta_{\text{base}}}{\eta_{\text{base}}} = \frac{\left(\frac{\dot{W}_{\text{eng}} + \dot{W}_{\text{WHR}}}{\dot{E}_{\text{fuel}}} \right)_{\text{actual}} - \eta_{\text{base}}}{\eta_{\text{base}}} \quad (5.1)$$

Here, the combined efficiency for a given WHR system is found by using the actual measured engine power output and fuel energy input for the given coolant temperature. This combined

Table 5-3. Matrix of WHR operating points modeled.

Engine Speed [rpm]	Torque [N-m]	% of Max Load	Coolant Temp [°C]	Condenser Temp [°C]	
				60	90
3100	24	74%	90	X	X
			150	X	X
			175	X	X
			200	X	X

efficiency is then compared to the baseline efficiency of the 90°C coolant temperature for consistency.

The inputs for the thermodynamic analysis are shown in detail in Table 5-2 for each coolant temperature modeled. The first section of the table lists the inputs pulled directly from the experiment data for the temperatures, flow rates, and measured heat transfer rates to the exhaust and coolant. The second section of the table shows the values that were inputs for the model, such as the evaporator saturation temperature and the maximum superheat temperature. Note that the values may differ between the two condenser temperatures that were modeled. Each model was optimized to produce the maximum output and still maintain a minimum CAT of approximately 5°C for each heat exchanger. The CAT was allowed to occur at any location, including the inlet of the heat exchanger. Optimization was accomplished by adjusting the maximum superheat temperature (see Figure 5-4). The superheat temperatures were kept under a maximum of 375°C for all configurations.

The thermodynamic models were created using several assumptions and simplifications. Table 5-1 summarizes the assumptions for values such as the heat exchanger effectiveness and isentropic efficiency of the pump and turbine. In addition to these assumptions, it was also assumed that no exhaust aftertreatment would be used since the test engine is a Tier 0 diesel engine with minimal emission standards. Therefore, no effort was made to ensure that exhaust temperatures would be sufficiently high after the exhaust evaporator for adequate operation of an aftertreatment

system. In an application where emissions would be a concern, the heat transfer from the exhaust to the working fluid might have to be reduced to maintain sufficient exhaust temperature, which would negatively impact the WHR system performance and reduce the efficiency gains from the values reported here. Assumptions were also made regarding the working fluid pressure throughout the WHR systems. The thermodynamic analysis assumed that there are no pressure drops throughout the system except for the turbine expander. However, the pressure drops were calculated in the individual heat exchanger models and it was determined that the effect of pressure drop on the saturation temperature was insignificant. The high side system pressure (point 2 to point 6) is determined using the saturation temperature in the evaporator. The low side system

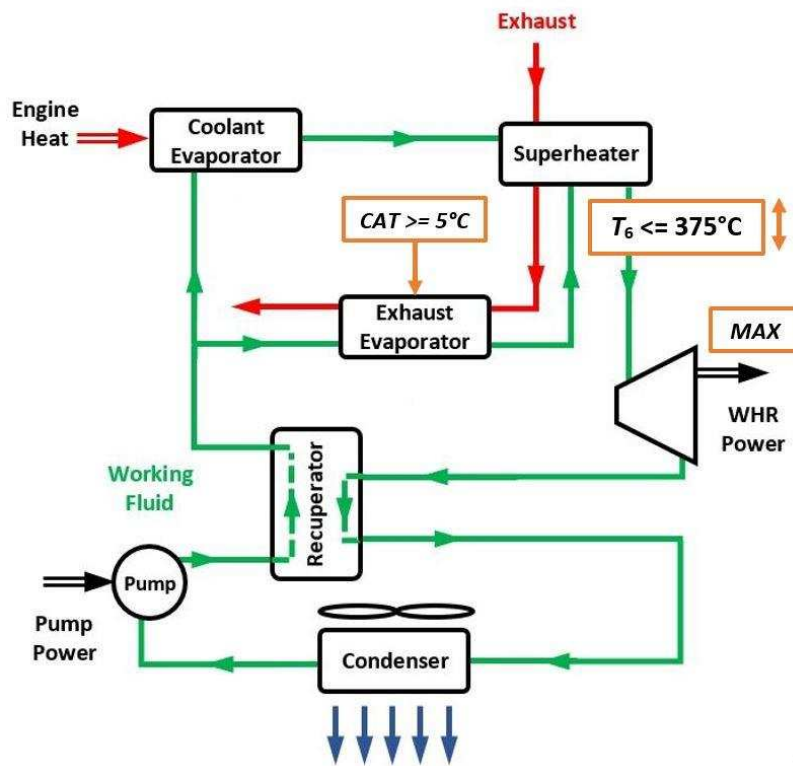


Figure 5-4. Graphic representation of WHR system optimization strategy. WHR system output is maximized through increasing superheat (up to 375°C maximum) while maintaining at least a 5° CAT in the exhaust evaporator.

pressure (point 7 to point 1) is found using the saturation temperature and quality at the condenser outlet. The pressures for each system configuration are listed in Table 5-4.

The WHR systems modeled here require four primary heat exchangers (condenser, evaporator, superheater, and recuperator) and an oil cooler for the engine to ensure the increased engine temperature does not have a negative impact on oil temperature. The condenser is modeled as an aluminum compact heat exchanger with a cross-flow design, much like an automotive radiator. The evaporator is modeled as a counter-flow heat exchanger with rectangular tubes and the cooler fluid (ethanol) flowing in the outer tubes to reduce heat loss. The superheater also uses rectangular tubes, but is a cross-flow design. The recuperator is of similar construction as the evaporator, with a counter-flow design and the cooler fluid running in the outside tubes. Finally, the oil cooler is another compact heat exchanger with cross-flow design much like the condenser. More detail on the construction of the individual heat exchangers is provided in section 5.3, Detailed System Modeling.

Table 5-4. System pressure values for each of the modeled system configurations.

Condenser Temperature [°C]	Coolant Temperature [°C]	High Side Pressure [kPa]	Low Side Pressure [kPa]
60	90	2,959.30	46.77
	150	981.61	46.77
	175	1,767.04	46.77
	200	2,959.30	46.77
90	90	2,959.30	157.59
	150	981.61	157.59
	175	1,767.04	157.59
	200	2,959.30	157.59

A thermodynamic model description and sample calculation are provided for each of the two basic WHR system designs. The state-of-the-art 90°C coolant temperature system shown in Figure 5-1 does not utilize engine coolant waste heat and will be presented first. The high-

temperature WHR systems (Figure 5-2) build upon the state-of-the-art system by adding the engine coolant passages as a second evaporator that runs in parallel with the exhaust evaporator. The differences between the state-of-the-art and the high-temperature WHR system models will follow, including a second sample calculation for clarity. The model for the 90°C WHR system will be described first using a thermodynamic analysis for a closed system. Sample calculations will be presented using the representative point data provided in Table 5-5. At point 1 for the working fluid, the state is defined by the condenser temperature (either 60°C or 90°C) and the working fluid quality of one, since we assume that the working fluid is 100% liquid at the outlet of the condenser.

Table 5-5. Thermodynamic model inputs for representative point of 3100 rpm, 24 N-m, 90°C coolant temperature, and 90°C condenser temperature with WHR from exhaust only.

Parameter	Value	Units
Ethanol		
Ethanol mass flow rate	5.25	g s ⁻¹
Isentropic ethanol enthalpy at point 2	440	kJ kg ⁻¹
Ethanol temperature at point 3	180	°C
Ethanol enthalpy at point 4	850	kJ kg ⁻¹
Ethanol temperature at point 5	200	°C
Ethanol enthalpy at point 6	1,846	kJ kg ⁻¹
Ethanol enthalpy at point 7	1,667	kJ kg ⁻¹
Isentropic ethanol enthalpy at point 7	1,548	kJ kg ⁻¹
Ethanol enthalpy at point 8	1,349	kJ kg ⁻¹
Theoretical ethanol enthalpy at T_7 and P_3	1,621	kJ kg ⁻¹
Theoretical ethanol enthalpy at T_2 and P_8	1,269	kJ kg ⁻¹
Exhaust		
Exhaust mass flow rate	16.3	g s ⁻¹
Exhaust specific heat capacity rate in single-phase evaporator	1.08	kJ kg ⁻¹ K ⁻¹
Exhaust temperature at point 1	500.6	°C
Exhaust enthalpy at point 4	170	kJ kg ⁻¹
Other		
Minimum heat capacity rate for evaporator (single-phase)	17.6	W K ⁻¹
Minimum heat capacity rate for superheater	13.9	W K ⁻¹

Since the ethanol state at this point is completely defined by the temperature and the quality, the low side pressure, enthalpy, and entropy at this point are also known. For the representative conditions at point 1, the condenser temperature of 90°C and a quality of one result in a low side ethanol pressure of 158 kPa, an ethanol enthalpy of 436 kJ kg⁻¹, and an ethanol entropy of 1.74 kJ kg⁻¹ K⁻¹. The ethanol state at point 2 can be found by considering the isentropic efficiency of the fluid pump, which is defined as follows:

$$\eta_{\text{pump,s}} = \frac{h_{\text{wf},2,s} - h_{\text{wf},1}}{h_{\text{wf},2} - h_{\text{wf},1}} \quad (5.2)$$

The isentropic efficiency of the fluid pump is set as 50%, and the enthalpy at point 1 along with the isentropic enthalpy at point 2 are known. Therefore, the actual enthalpy at point 2 can be found using equation (5.2). For the representative point, the isentropic enthalpy at point 2 is 440 kJ kg⁻¹, giving an enthalpy of 444 kJ kg⁻¹ at point 2. To find the ethanol state at point 3, the energy balance on the recuperator is used:

$$Q_{\text{rec}} = h_{\text{wf},3} - h_{\text{wf},2} = h_{\text{wf},7} - h_{\text{wf},8} \quad (5.3)$$

$$Q_{\text{rec}} = \varepsilon_{\text{rec}} Q_{\text{rec,max}} \quad (5.4)$$

From the values in Table 5-5, the ethanol enthalpy at point 7 is 1,667 kJ kg⁻¹ and the enthalpy at point 8 is 1,349 kJ kg⁻¹, giving an enthalpy of 762 kJ kg⁻¹ at point 3 for the representative point. The effectiveness of the recuperator is set to 80%. The maximum recuperator heat transfer is defined as follows:

$$Q_{\text{rec,max}} = \min \left[(h_{\text{wf},7/3} - h_{\text{wf},2}), (h_{\text{wf},7} - h_{\text{wf},2/8}) \right] \quad (5.5)$$

Here, the maximum heat transfer is the smaller of the two possible enthalpy difference bounds. The first is the difference between the theoretical enthalpy of ethanol at T_7 and P_3 and the actual enthalpy at point 2, and the second is the difference between the actual enthalpy at point 6 and the theoretical enthalpy of ethanol at T_2 and P_8 . The theoretical enthalpy of ethanol at T_7 and P_3 is

1,621 kJ kg⁻¹ and the actual ethanol enthalpy at point 2 is 444 kJ kg⁻¹, giving a difference of 1,177 kJ kg⁻¹. The actual ethanol enthalpy at point 7 is 1,667 kJ kg⁻¹ and the theoretical enthalpy at T_2 and P_8 is 1,269 kJ kg⁻¹, giving a difference of 398 kJ kg⁻¹. The second difference is the smaller of the two values, so the maximum recuperator heat transfer is 398 kJ kg⁻¹. The ethanol state at the outlet of the evaporator (point 5) is defined by the evaporation temperature set point from Table 5-3 and the assumed vapor quality of one. Therefore, the state at point 5 is fully defined and the enthalpy and entropy are readily found. For the representative point, the evaporator temperature is 200°C giving an ethanol enthalpy of 1,354 kJ kg⁻¹ and an entropy of 3.8 kJ kg⁻¹ K⁻¹ at point 5.

Further analysis of the heat transfer inside the evaporator is split into two parts: single-phase and two-phase. This split is necessary since the application of heat exchanger effectiveness is different for the single-phase and two-phase portions. The single-phase heat transfer in the evaporator is found using the following equations:

$$\dot{Q}_{\text{evap,sp}} = \dot{m}_{\text{wf,evap}} (h_{\text{wf,4}} - h_{\text{wf,3}}) \quad (5.6)$$

$$\dot{Q}_{\text{evap,sp}} = \dot{m}_{\text{exh}} (h_{\text{exh,3}} - h_{\text{exh,4}}) \quad (5.7)$$

$$\dot{Q}_{\text{evap,sp}} = \varepsilon_{\text{evap,sp}} \dot{Q}_{\text{evap,sp,max}} \quad (5.8)$$

$$\dot{Q}_{\text{evap,sp,max}} = C_{\text{evap,sp,min}} (T_{\text{exh,3}} - T_{\text{wf,3}}) \quad (5.9)$$

$$\dot{Q}_{\text{evap,sp}} = \dot{m}_{\text{exh}} c_{\text{p,exh,sp}} (T_{\text{exh,3}} - T_{\text{exh,4}}) \quad (5.10)$$

Starting with equation (5.6), the mass flow rate of ethanol is 5.25 g s⁻¹ and the enthalpies for points 3 and 4 are 762 kJ kg⁻¹ and 850 kJ kg⁻¹ giving a single-phase evaporator heat transfer rate of 0.46 kW. From equation (5.7), the single-phase evaporator heat transfer rate of 0.46 kW, exhaust mass flow rate of 16.3 g s⁻¹, and exhaust enthalpy of 170 kJ kg⁻¹ at point 4, the exhaust enthalpy at point 3 is found to be 198 kJ kg⁻¹. The single-phase evaporator effectiveness is set at 80% (see Table 5-3) for all models, which results in a maximum single-phase evaporator heat transfer of 0.58 kW

(equation (5.8)). Using equation (5.9), the minimum heat capacity rate of 17.6 W K^{-1} and the ethanol temperature at point 3 of 180°C , the exhaust temperature at point 3 is 213°C . Finally, the exhaust temperature at point 4 is found using equation (5.10). With a single-phase evaporator heat transfer rate of 0.46 kW , and exhaust mass flow rate of 16.3 g s^{-1} , an exhaust heat capacity of $1.08 \text{ kJ kg}^{-1} \text{ K}^{-1}$, and the exhaust temperature of 213.1°C at point 3, the exhaust temperature at point 4 is 187.0°C . The heat transfer in the two-phase portion of the evaporator is determined in a similar manner:

$$\dot{Q}_{\text{evap,tp}} = \dot{m}_{\text{wf,evap}} (h_{\text{wf,5}} - h_{\text{wf,4}}) \quad (5.11)$$

$$\dot{Q}_{\text{evap,tp}} = \dot{m}_{\text{exh}} (h_{\text{exh,2}} - h_{\text{exh,3}}) \quad (5.12)$$

Using the ethanol mass flow rate of 5.25 g s^{-1} , the ethanol enthalpy of 850 kJ kg^{-1} at point 4, and the ethanol enthalpy of $1,354 \text{ kJ kg}^{-1}$ at point 5, the two-phase evaporator heat flow rate is 2.65 kW . With the two-phase heat flow rate, exhaust mass flow rate of 16.3 g s^{-1} , and exhaust enthalpy of 198 kJ kg^{-1} at point 3, the exhaust enthalpy at point 2 is 361 kJ kg^{-1} .

The working fluid state at the superheater outlet is defined by setting the maximum superheat temperature as listed in Table 5-2, coupled with the high-side system pressure. The enthalpy and entropy are calculated using the known temperature and pressure at point 6. The superheater heat transfer rate and effectiveness are found as follows:

$$\dot{Q}_{\text{sh}} = \dot{m}_{\text{wf}} (h_{\text{wf,6}} - h_{\text{wf,5}}) \quad (5.13)$$

$$\dot{Q}_{\text{sh}} = \dot{m}_{\text{exh}} (h_{\text{exh,1}} - h_{\text{exh,2}}) \quad (5.14)$$

$$\dot{Q}_{\text{sh,max}} = C_{\text{sh,min}} (T_{\text{exh,1}} - T_{\text{wf,5}}) \quad (5.15)$$

$$\dot{Q}_{\text{sh}} = \varepsilon_{\text{sh}} \dot{Q}_{\text{sh,max}} \quad (5.16)$$

For the representative point, equation (5.13) can be used along with the ethanol mass flow of 5.25 g s^{-1} , the ethanol enthalpy of $1,354 \text{ kJ kg}^{-1}$ at point 5, and the ethanol enthalpy of $1,846 \text{ kJ kg}^{-1}$ at

point 6 (Table 5-5) to arrive at a superheater heat transfer rate of 2.58 kW. Equation (5.14) is then solved for the exhaust enthalpy at point 1 using the superheater heat transfer rate of 2.58 kW, the exhaust mass flow rate of 16.3 g s⁻¹, and the exhaust enthalpy of 361 kJ kg⁻¹ at point 2. The result is an exhaust enthalpy of 519 kJ kg⁻¹ at point 1 for the representative test point. The maximum heat transfer rate in the superheater is then found using equation (5.15). From Table 5-5, the minimum heat capacity rate for the superheater is 13.9 W K⁻¹, the exhaust temperature at point 1 is 500.6°C, and the ethanol temperature at point 5 is 200°C. The result is a maximum superheater heat transfer rate of 4.18 kW, which is then used to find the heat exchanger effectiveness (equation (5.16)) of 62%.

The key result of the thermodynamic models is the power output from the turbine expander. The power output is found using the isentropic efficiency of the turbine, which is defined as follows:

$$\eta_{\text{turb},s} = \frac{h_{\text{wf},6} - h_{\text{wf},7}}{h_{\text{wf},6} - h_{\text{wf},7,s}} \quad (5.17)$$

Using the isentropic efficiency for the turbine of 60% (given in Table 5-2), and the theoretical isentropic enthalpy of the ethanol at point 7 of 1,548 kJ kg⁻¹, and the ethanol enthalpy of 1,846 kJ kg⁻¹ at point 6, the enthalpy at point 7 is found to be 1,667 kJ kg⁻¹. The enthalpy difference across the turbine is then used to determine the power output:

$$\dot{W}_{\text{turb}} = \dot{m}_{\text{wf}} (h_{\text{wf},6} - h_{\text{wf},7}) \quad (5.18)$$

From the previous calculations, the ethanol enthalpy at point 6 and 7 for the representative operating condition are 1,846 kJ kg⁻¹ and 1,667 kJ kg⁻¹, respectively. From Table 5-5, the ethanol mass flow rate is 5.25 g s⁻¹, yielding a turbine power output of 0.94 kW.

The working fluid state at point 8 is determined using the previously discussed energy balance on the recuperator. The enthalpy and entropy for point 8 are known and the heat transfer in the condenser is calculated as:

$$\dot{Q}_{\text{cond}} = \dot{m}_{\text{wf}} (h_{\text{wf},8} - h_{\text{wf},1}) \quad (5.19)$$

The working fluid state at the outlet of the condenser was defined at the start of the analysis as a saturated liquid at 90°C, completing the definition of the closed thermodynamic system. For the representative point, the ethanol enthalpy at point 1 is 436 kJ kg⁻¹, the ethanol enthalpy at point 8 is 1,349 kJ kg⁻¹, and the ethanol mass flow rate is 5.25 g s⁻¹, yielding a condenser heat transfer rate of 4.79 kW.

The thermodynamic models for the WHR systems at elevated coolant temperatures were similar to the analysis outlined for the 90°C coolant systems, with a few important differences. Therefore, only the differences will be highlighted and covered in detail. As previously mentioned, the high-temperature WHR systems differ from the 90°C systems in that the working fluid path splits after the low-temperature side of the recuperator, with one path flowing through the engine as coolant and one path flowing through an exhaust evaporator like the one described in the 90°C case. The heat transfer to the working fluid inside the engine structure is known from the experimental data, where the heat transfer in the exhaust evaporator is found using the same method outlined for the 90°C case. The sample calculations for the high-temperature coolant models will use the representative operating point of 3100 rpm, 24 N-m, 150°C coolant temperature, and 90°C condenser temperature (Table 5-6). The mass flow rate of the ethanol through each evaporator can vary with the following constraints:

$$\dot{m}_{\text{wf,tot}} = \dot{m}_{\text{wf,eng}} + \dot{m}_{\text{wf,evap}} \quad (5.20)$$

Conservation of mass dictates that the sum of the mass flow rates in the two legs must equal the total working fluid mass flow rate for the system. From Table 5-6, the mass flow rate through the engine is 8.45 g s^{-1} and the mass flow rate through the evaporator is 5.89 g s^{-1} , giving a total ethanol mass flow rate of 14.34 g s^{-1} . Additionally, the heat transfer in the engine and exhaust evaporator were then defined in terms of these individual mass flow rates:

$$\dot{Q}_{\text{engine}} = \dot{m}_{\text{wf,eng}} (h_{\text{wf,5}} - h_{\text{wf,3}}) \quad (5.21)$$

$$\dot{Q}_{\text{evap}} = \dot{m}_{\text{wf,evap}} (h_{\text{wf,5}} - h_{\text{wf,3}}) \quad (5.22)$$

Table 5-6. Thermodynamic model inputs for the representative point of 3100 rpm, 24 N-m, 150°C coolant temperature, and 90°C condenser temperature. This system utilizes both engine coolant and exhaust for WHR.

Parameter	Value	Units
Ethanol		
Ethanol mass flow rate through engine	8.45	g s^{-1}
Ethanol mass flow rate through evaporator	5.89	g s^{-1}
Isentropic ethanol enthalpy at point 2	437	kJ kg^{-1}
Ethanol temperature at point 3	135	$^{\circ}\text{C}$
Ethanol enthalpy at point 3	585	kJ kg^{-1}
Ethanol enthalpy at point 4	642	kJ kg^{-1}
Ethanol temperature at point 5	150	$^{\circ}\text{C}$
Ethanol enthalpy at point 5	1,331	kJ kg^{-1}
Ethanol enthalpy at point 6	1540	kJ kg^{-1}
Ethanol enthalpy at point 7	1450	kJ kg^{-1}
Isentropic ethanol enthalpy at point 7	1390	kJ kg^{-1}
Ethanol enthalpy at point 8	1303	kJ kg^{-1}
Theoretical ethanol enthalpy at T_7 and P_3	1420	kJ kg^{-1}
Theoretical ethanol enthalpy at T_2 and P_8	1267	kJ kg^{-1}
Exhaust		
Exhaust mass flow rate	15.4	kg s^{-1}
Exhaust specific heat capacity rate in single-phase evaporator	1.07	$\text{kJ kg}^{-1} \text{K}^{-1}$
Exhaust temperature at point 1	566	$^{\circ}\text{C}$
Exhaust enthalpy at point 4	121	kJ kg^{-1}
Other		
Minimum heat capacity rate for evaporator (single-phase)	16.6	W K^{-1}
Minimum heat capacity rate for superheater	18.0	W K^{-1}

From Table 5-6, the ethanol enthalpy at point 3 is 585 kJ kg^{-1} and the ethanol enthalpy at point 5 is $1,330.7 \text{ kJ kg}^{-1}$. Using equation (5.21) and the mass flow rate through the engine of 8.45 g s^{-1} , the heat transfer rate in the engine is found to be 6.30 kW . Using equation (5.22) and the mass flow rate of ethanol through the evaporator of 5.89 g s^{-1} , the heat transfer rate in the evaporator is found to be 4.39 kW . Note that the ethanol mass flow rate through the exhaust evaporator is larger in the high-temperature WHR system than in the state-of-the-art system. The extra waste heat recovered in the engine block results in a much larger combined ethanol mass flow rate through the superheater in the high-temperature system. Therefore, the superheat temperature is much lower at 240°C than the 375°C superheat temperature in the low-temperature example. The lower maximum ethanol temperature in the system results in a smaller ethanol inlet temperature at the exhaust evaporator. This lower inlet temperature, along with the lower saturation temperature, results in a smaller ethanol temperature difference across the exhaust evaporator than seen in the 90°C system. To fully utilize the remaining exhaust waste heat, the ethanol mass flow through the exhaust evaporator had to be increased. The remainder of the thermodynamic analysis for the high-temperature WHR systems is identical to that described for the 90°C systems. The next section will describe the modeling of the individual heat exchangers for the WHR systems.

5.3 Detailed System Modeling

The thermodynamic analysis described in the previous section provided estimates of the WHR power output and overall efficiency gain for each of eight WHR system configurations with varying coolant and condenser temperatures. However, one of the drawbacks of WHR is the additional space required for the additional components. Of the required components, the heat exchangers take up the most space and, therefore, further analysis was performed to understand how the space required changes for each WHR system and what tradeoffs may exist between

performance and packaging. The four heat exchangers shown in the WHR system diagrams from the previous section were modeled and will be described in detail in this section. First, the condenser model will be covered, followed by the evaporator, superheater, and recuperator models. Next, the oil cooler models for each system are described since higher engine temperature leads to increased heat rejection to the engine oil, which may require a larger oil cooler. Finally, the radiator models for the 90°C systems are covered. The 90°C WHR systems do not utilize the waste heat from the engine coolant and therefore a radiator is needed to reject this heat to the environment. The assumptions and inputs for the models are listed in Table 5-7 and Table 5-8, respectively. The models neglect contact resistances as well as fouling resistances for simplicity.

Table 5-7. Detailed heat exchanger model assumptions.

Assumption	Value	Units
Ambient air temperature	25	°C
Ambient air pressure	85	kPa
Air speed over condenser	3	m s ⁻¹
Air speed over oil cooler/radiator	2.2	m s ⁻¹
Exhaust inlet pressure (superheater)	101	kPa
Contact resistance	None	-

Table 5-8. Heat exchanger model inputs.

Input	90°C	150°C	175°C	200°C
Exhaust inlet temperature (superheater) [°C]	500.6	566.0	539.1	597.3
Exhaust inlet temperature (evaporator, 60°C condenser) [°C]	379.2	319.7	290.1	314.2
Exhaust inlet temperature (evaporator, 90°C condenser) [°C]	374.7	398.1	334.7	293.3
Exhaust mass flow rate [g s ⁻¹]	16.27	15.43	15.35	15.87
Coolant mass flow rate (60°C condenser, total) [g s ⁻¹]	5.28	12.64	9.75	10.48
Coolant mass flow rate (90°C condenser, total) [g s ⁻¹]	5.47	14.34	11.17	11.23
Fuel flow rate [g s ⁻¹]	0.626	0.667	0.613	0.649

Like the previous chapter describing the data analysis from the experimental results, this chapter will use a representative point to provide sample results for the heat exchanger model calculations. The representative data points for each heat exchanger will be based on the 3100 rpm, 24 N-m, 150°C coolant temperature engine operating point, modeled with a 90°C condenser temperature. The heat exchanger model equations were solved simultaneously, so some of the values for the representative point that are necessary to complete the sample calculations were outputs of the iterative solver in EES.

5.3.1 Condenser Model

The WHR system condensers were modeled as compact aluminum cross-flow heat exchangers with micro channels and louvered fins (Figure 5-5). This design results in maximum heat transfer with minimal air-side pressure drop in a relatively small package despite the small temperature difference between the ethanol and ambient air. The ethanol vapor enters and undergoes a temperature drop in the single-phase section of the condenser. The ethanol begins to condense in the two-phase section and becomes 100% ethanol vapor at the exit of the condenser. The configuration of microchannel tubes and louvered fins is shown in detail in Figure 5-6. The

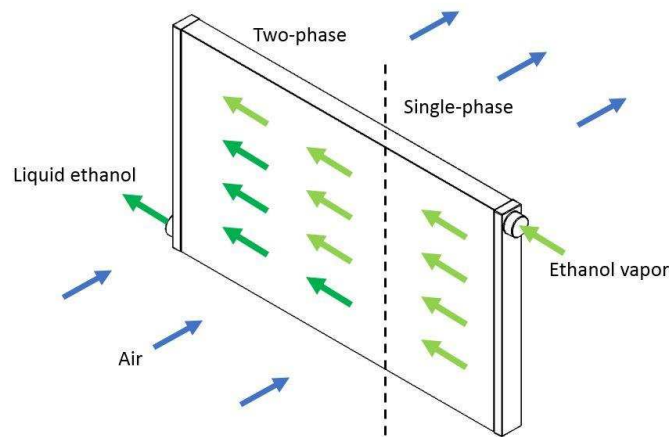


Figure 5-5. Diagram showing the cross-flow condenser configuration as well as single-phase and two-phase sections.

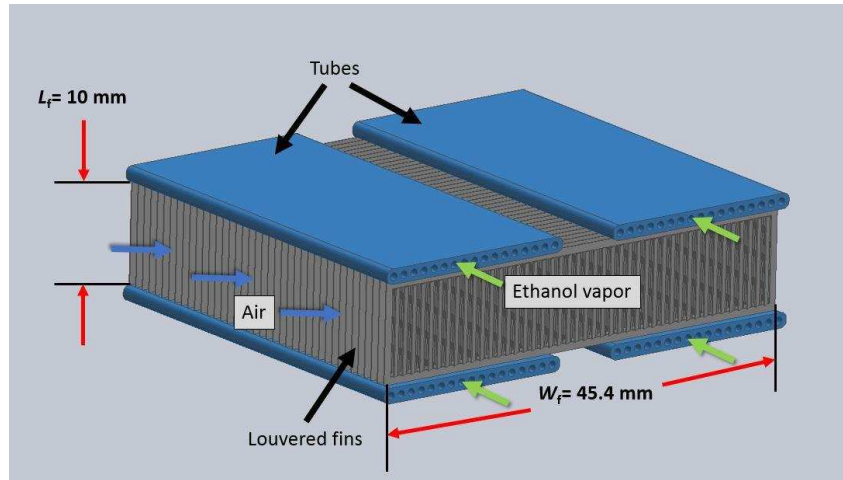


Figure 5-6. Diagram showing condenser construction with two rows of horizontal tubes separated by louvered fins.

basic dimensions of the condenser design are listed in Table 5-9 and the inputs for the representative point are shown in Table 5-10. Each tube is 1.5 mm thick, 20.4 mm deep, and contains 17 channels each with a diameter of 0.761 mm (Figure 5-7). The condenser has two rows of tubes with 30 tubes per row. The cooling fins have a 1 mm pitch with 8.5 mm long 27° louvers that are spaced at 1 mm intervals as shown in Figure 5-8. All condensers have a width of 45.4 mm, with the heat exchanger length varying to meet required the heat duty for each WHR system. The condenser models are broken into two sections: single-phase and two-phase. In the first section of the condenser, the liquid ethanol is cooled to the saturation temperature using the corresponding heat transfer correlations. The phase change takes place in the second section of the condenser, which uses the appropriate heat transfer correlations for the two-phase working fluid. The air velocity through the condenser was set at 3 m s^{-1} for each condenser model, with the assumption that the condenser fan would be sized to provide the required air flow depending on the condenser length.

The results show that the estimated maximum pressure drop for airflow through the condenser is 95.71 Pa and the greatest airflow requirement is $1,630 \text{ m}^3 \text{ h}^{-1}$. To verify that this is a

Table 5-9. Condenser model design and dimensions.

Parameter	Value	Units
Material	Aluminum	-
HX design	Cross-flow compact	-
Rows (N_{row})	2	-
Tubes per row (N_t)	30	-
Tube width (w_t)	20.4	mm
Tube thickness (t_t)	1.5	mm
Tube pitch (p_t)	11.5	mm
Channels per tube (N_{ch})	17	-
Channel diameter (D_h)	0.761	mm
Channel pitch (p_{ch})	1.17	mm
Channel shape	Round	-
HX width (w_{hx})	45.4	mm
Fin style	Louvered	-
Louver angle (θ)	27	°
Louver length (L_{lv})	8.5	mm
Louver pitch (p_{lv})	1	mm
Fin pitch (p_f)	1	mm
Fin thickness (t_f)	0.1	mm
Fin width (w_f)	45.4	mm
Fin length (L_f)	10	mm
Corrected fin length (L_c)	5	mm
Absolute roughness (e)	1.5	μm

realistic demand of an electric fan, the SPAL catalog was consulted for fans that meet these requirements. SPAL sells a 385 mm 12V blowing axial fan (SPAL, VA18-AP51/C-41S) that meets these criteria, providing $1640 \text{ m}^3 \text{ h}^{-1}$ at a static pressure of 99 Pa. Therefore, the assumption of achieving 3 m s^{-1} air velocity through each condenser is sufficient.

The condenser model is based on the Number of Transfer Units (NTU) Effectiveness method, which uses the inlet temperatures of the two fluids (hot and cold) to define the maximum possible heat transfer rate for the given heat exchanger. This maximum heat transfer rate is defined as follows:

$$\dot{Q}_{\max} = C_{\min} (T_{\text{in,hot}} - T_{\text{in,cold}}) \quad (5.23)$$

Table 5-10. Condenser model inputs for the representative point of 3100 rpm, 24 N-m, 150°C coolant temperature, and 90°C condenser temperature.

All Phases:	Value	Units
Air inlet temperature ($T_{in,cold}$)	25	°C
Air dynamic viscosity (μ_{air})	0.019	mPa-s
Air density (ρ_{air})	0.994	kg m ⁻³
Air heat capacity ($c_{p,air}$)	1.01	kJ kg ⁻¹ K ⁻¹
Ethanol mass flux (G_{eth})	30.9	kg m ⁻² s ⁻¹
Single-phase:		
Minimum heat capacity rate ($C_{min}=C_{eth}$)	26.0	W K ⁻¹
Maximum heat capacity rate ($C_{max}=C_{air}$)	29.6	W K ⁻¹
Ethanol inlet temperature ($T_{in,hot}$)	110.8	°C
Actual heat transfer rate (\dot{Q})	0.54	kW
Tube wall thermal conductivity (k_w)	240	W m ⁻¹ K ⁻¹
Ethanol thermal conductivity (k_{eth})	0.023	W m ⁻¹ K ⁻¹
Ethanol dynamic viscosity (μ_{eth})	0.011	mPa-s
Ethanol density (ρ_{eth})	2.43	kg m ⁻³
Two-phase:		
Average ethanol quality (x_{avg})	0.975	-
Minimum heat capacity rate ($C_{min}=C_{air}$)	10.4	W K ⁻¹
Ethanol inlet temperature ($T_{in,hot}$)	90	°C
Actual heat transfer rate (\dot{Q})	0.60	kW
Liquid ethanol heat capacity ($c_{p,eth,l}$)	3.06	kJ kg ⁻¹ K ⁻¹
Liquid ethanol dynamic viscosity ($\mu_{eth,l}$)	0.381	mPa-s
Liquid ethanol thermal conductivity ($k_{eth,l}$)	0.150	W m ⁻¹ K ⁻¹
Liquid ethanol density ($\rho_{eth,l}$)	724.7	kg m ⁻³
Vapor ethanol density ($\rho_{eth,g}$)	2.50	kg m ⁻³
Ethanol inlet pressure ($P_{eth,in}$)	157.3	kPa
Ethanol critical pressure (P_{crit})	6,268	kPa
Ethanol surface tension (σ)	0.017	N m ⁻¹

The term C_{min} is the minimum heat capacity rate of the two fluids. Note that the total mass flow rate of the air flowing across the condenser is found iteratively due to the cross-flow design. The actual heat transfer is some fraction of the maximum, and this fraction is known as the effectiveness ε :

$$\dot{Q} = \varepsilon \dot{Q}_{max} \quad (5.24)$$

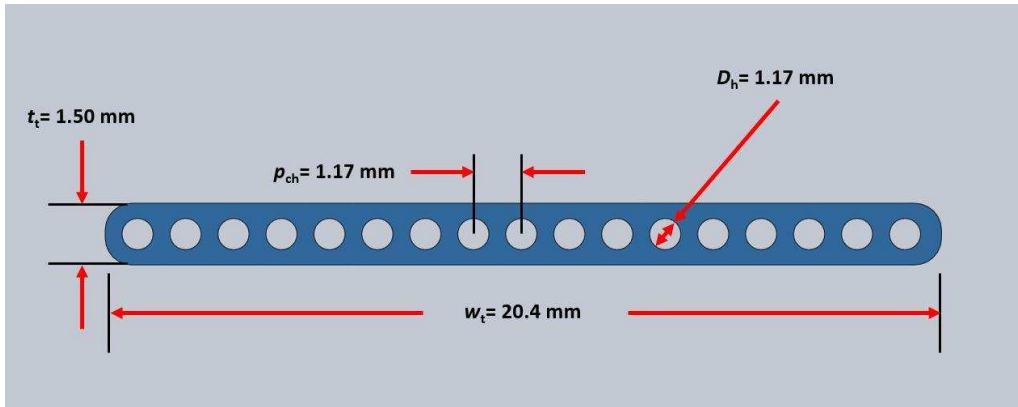


Figure 5-7. Condenser tube configuration and dimensions in mm.

For the single-phase portion of the condenser model for the representative data point, the minimum heat capacity rate ($C_{\min} = C_{\text{eth}}$ for the single-phase section) is $26.0 \text{ J s}^{-1} \text{ K}^{-1}$, the hot side inlet temperature ($T_{\text{in,hot}}$) is 110.8°C , and the cold side inlet temperature ($T_{\text{in,cold}}$) is assumed to be 25°C , giving a maximum heat transfer rate of 2.23 kW . With an actual heat transfer rate of 0.54 kW from the thermodynamic model, the heat exchanger effectiveness for the single-phase portion of the condenser is 24.2% .

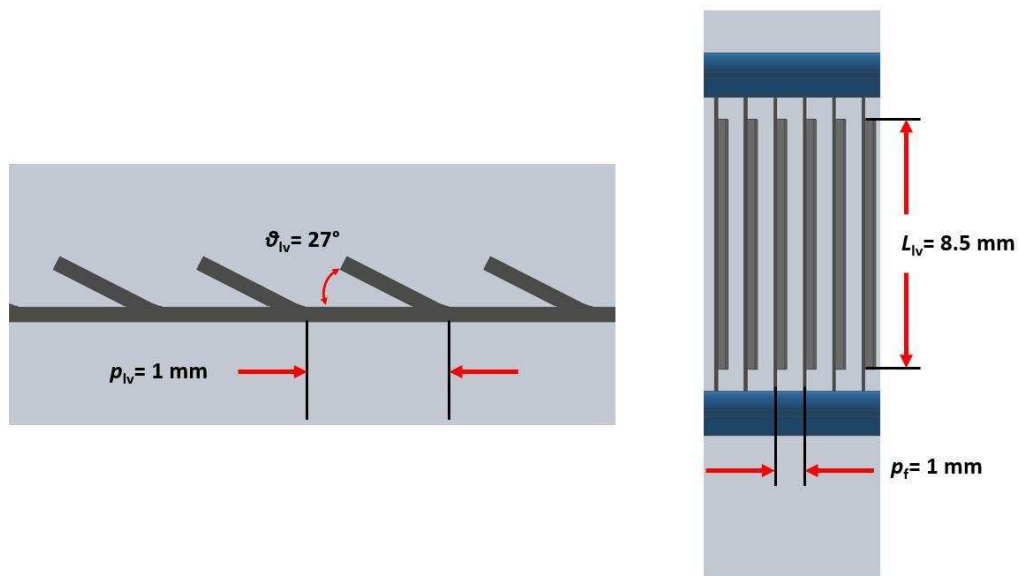


Figure 5-8. Left: Cross-section of condenser fin showing louver angle and pitch. Right: Side view of condenser assembly showing louver length and fin pitch.

In the condenser models, the actual heat transfer is known from the thermodynamic analysis, and the NTU method is used to solve for the heat exchanger length required to accomplish the necessary heat transfer with the calculated effectiveness. For the single-phase section of the condensers, the model uses the NTU- ε relation for unmixed fluids in a single-pass cross-flow design, defined as [49]:

$$\varepsilon_{sp} = 1 - \exp \left[\left(\frac{1}{C_r} \right) (NTU)^{0.22} \left\{ \exp \left[-C_r (NTU)^{0.78} \right] - 1 \right\} \right] \quad (5.25)$$

The term C_r is the ratio of heat capacity rates:

$$C_r = \frac{C_{min}}{C_{max}} \quad (5.26)$$

For the representative point, the minimum heat capacity rate ($C_{min} = C_{eth}$) is $26.0 \text{ J s}^{-1} \text{ K}^{-1}$ and the maximum heat capacity rate ($C_{max} = C_{air}$) is $29.6 \text{ J s}^{-1} \text{ K}^{-1}$, giving a heat capacity ratio (C_r) of 0.88. Entering the heat capacity ratio and the heat exchanger effectiveness into equation (5.25) yields an NTU value of 0.33. The NTU is defined as:

$$NTU = \frac{UA_{ht}}{C_{min}} \quad (5.27)$$

Using the values for the minimum heat capacity rate and NTU value from above, the UA value for the representative point is 8.6 W K^{-1} . The product of the overall heat transfer coefficient, U , and the heat transfer area, A , is found by summing the thermal resistances across the condenser:

$$\begin{aligned} R_{cond,tot} &= \frac{1}{UA_{ht,cond}} = R_{conv,eth} + R_{cond,w} + R_{conv,air} \\ &= \frac{1}{h_{cond,eth} A_{s,in}} + \frac{t_{w,cond}}{k_{w,cond} A_{s,tube}} + \frac{1}{\eta_o h_{cond,air} A_{s,out}} \end{aligned} \quad (5.28)$$

The thermal resistances for the convection of the two fluids and the conduction through the tube wall are added in series. For the air convection term, the resistance is multiplied by the overall fin array efficiency, η_o , which compensates for the lack of uniform temperature over the surface area of the fins [49]. The overall fin array efficiency is defined as:

$$\eta_o = 1 - \frac{N_f A_f}{A_{s,out}} (1 - \eta_f) \quad (5.29)$$

The fin area (A_f) is the surface area of a single fin:

$$A_f = 2L_f w_f \quad (5.30)$$

The surface area of the exterior of all of the tubes and fins for the entire heat exchanger ($A_{s,out}$) is given by:

$$A_{s,out} = A_{f,tot} + A_{ch,tot} = N_{row} N_{ch} A_f + A_{s,b} \quad (5.31)$$

$$A_{s,b} = 2N_{row} N_{tube} (w_t + t_t) L_t \quad (5.32)$$

The individual fin efficiency is:

$$\eta_f = \frac{\tanh(mL_c)}{mL_c} \quad (5.33)$$

Here, m represents the following expression:

$$m \approx \left(\frac{2h}{k_w t_f} \right)^{1/2} \quad (5.34)$$

The approximation for m is appropriate where fin width is much greater than the fin thickness. Here, the fin thickness of 0.1 mm is 0.22% of the fin width of 45.4 mm so the approximation is assumed to be valid. Note that the contact resistance between the fins and tubes has been neglected.

The air side heat transfer coefficient was found using the Colburn j factor correlation proposed by Chang and Wang [50, 51] for louvered fins. The correlation is valid for corrugated fin geometries with louver pitch Reynolds numbers in the range of 100 to 3,000. The following

equation was used to find the louver pitch Reynolds number ($Re_{p,lv}$), which was determined to be 162 at and air speed ($v_{air,max}$) of 3 m s^{-1} for all cases:

$$Re_{plv} = \frac{v_{air,max} p_{lv} \rho_{air}}{\mu_{air}} \quad (5.35)$$

The Chang and Wang correlation for the dimensionless heat transfer coefficient j is of the following form:

$$j = Re_{plv}^{-0.49} \left(\frac{\theta}{90} \right)^{0.27} \left(\frac{p_f}{p_{lv}} \right)^{-0.14} \left(\frac{L_f}{p_{lv}} \right)^{-0.29} \left(\frac{w_t}{p_{lv}} \right)^{-0.23} \left(\frac{L_{lv}}{p_{lv}} \right)^{0.68} \left(\frac{p_t}{p_{lv}} \right)^{-0.28} \left(\frac{t_f}{p_{lv}} \right)^{-0.05} \quad (5.36)$$

From the values in Table 5-10 for the representative point, the Colburn j factor is found to be 0.037. The heat transfer coefficient was then found using the following set of equations [49]:

$$j = St \cdot Pr^{2/3} \quad (5.37)$$

$$St = \frac{h_{air}}{G_{air} c_{p,air}} \quad (5.38)$$

$$Pr = \frac{\mu_{air}}{\alpha_{air} \rho_{air}} \quad (5.39)$$

$$G_{air} = \rho_{air} v_{air,max} \quad (5.40)$$

Substituting equations (5.38) through (5.40) into equation (5.37) and solving for the air side heat transfer coefficient yields:

$$h_{air} = \frac{j}{G_{air} c_{p,air}} \left(\frac{\alpha_{air} \rho_{air}}{\mu_{air}} \right)^{2/3} \quad (5.41)$$

Therefore, using the values in Table 5-10, the air side heat transfer coefficient (h_{air}) is found to be $141 \text{ W m}^{-2} \text{ K}^{-1}$. The air side heat transfer coefficient (h_{air}) along with the tube material thermal conductivity (k_w) of $240 \text{ W m}^{-1} \text{ K}^{-1}$ and the fin thickness (t_f) of 0.1 mm can then be used to solve equation (5.34) which produces an m value of 108. The resulting fin efficiency (η_f) for the representative model is 91.3%. From equation (5.29), the efficiency for the entire fin array is

92.6%. All properties for air, as well as other fluids, were found using EES's built-in library of thermophysical properties. EES provides air properties either assuming air is an ideal gas or that it acts as a real fluid. For the current models, air properties assume real fluid behavior.

Air side pressure drop across the condenser was estimated using the Darcy friction factor and the following general relation [49]:

$$\frac{dP}{dL} = \frac{fG^2}{2D_h\rho} \quad (5.42)$$

The correlation for the Darcy friction factor (f_{air}) for louver fin geometry put forth by Chang et al. [51] is as follows:

$$f_{\text{air}} = 4f_1f_2f_3 \quad (5.43)$$

$$f_1 = \begin{cases} 14.39Re_{p,\text{lv}}^{(-0.805 p_f/L_f)} \left(\ln(1.0 + (p_f/p_{\text{lv}})) \right)^{3.04} & Re_{p,\text{lv}} < 150 \\ 4.97Re_{p,\text{lv}}^{0.6049-1.064/\theta^{0.2}} \left(\ln((t_f/p_f)^{0.5} + 0.9) \right)^{-0.527} & 150 < Re_{p,\text{lv}} < 5,000 \end{cases} \quad (5.44)$$

$$f_2 = \begin{cases} \left(\ln((t_f/p_f)^{0.48} + 0.9) \right)^{-1.435} (D_{\text{h,air}}/p_{\text{lv}})^{-3.01} \left(\ln(0.5Re_{p,\text{lv}}) \right)^{-3.01} & Re_{p,\text{lv}} < 150 \\ \left((D_{\text{h,air}}/p_{\text{lv}}) \ln(0.3Re_{p,\text{lv}}) \right)^{-2.966} (p_f/L_f)^{-0.7931(p_f/L_f)} & 150 < Re_{p,\text{lv}} < 5,000 \end{cases} \quad (5.45)$$

$$f_3 = \begin{cases} (p_f/L_f)^{-0.308} (w_f/L_f)^{-0.308} \left(e^{-0.1167 p_f/t_f} \right) \theta^{0.35} & Re_{p,\text{lv}} < 150 \\ (p_t/t_t)^{-0.0446} \ln(1.2 + (p_{\text{lv}}/p_f)^{1.4})^{-3.553} \theta^{-0.477} & 150 < Re_{p,\text{lv}} < 5,000 \end{cases} \quad (5.46)$$

The hydraulic diameter for the air passage through the fins was found as follows:

$$D_{\text{h,air}} = \frac{4A_x}{Pe_{\text{wet}}} = \frac{2L_f(p_f - t_f)}{p_f - t_f + L_f} \quad (5.47)$$

From Table 5-9, the fin length (L_f) is 10 mm, the fin pitch (p_f) is 1 mm, and the fin thickness (t_f) is 0.1 mm. The hydraulic diameter for air ($D_{\text{h,air}}$) is found to be 1.65 mm. Using this diameter and the values in Table 5-10, the three correlation parameters (f_1 , f_2 , f_3) for the representative model are 15.5, 0.03, and 0.44, respectively. The friction factor for the air side is the product of these

parameters multiplied by a factor of four to convert to a Darcy friction factor, with the result of 0.80. Using equation (5.42), the pressure drop per unit length for the representative model is 2.11 kPa m⁻¹, for a total pressure drop of 95.7 Pa. As mentioned above, SPAL sells an axial fan (SPAL, VA18-AP51/C-41S) that can move air at 1640 m³ h⁻¹ with a static pressure of 99 Pa, so the estimated pressure drop is reasonable.

For the first section of the condenser, the coolant side heat transfer coefficient is found using a standard Nusselt number correlation for round tubes with uniform surface temperatures and the definition of the dimensionless Nusselt number [49]:

$$Nu_D = 3.66 \quad (5.48)$$

$$Nu_D = \frac{hD_h}{k} \quad (5.49)$$

From Table 5-10, the thermal conductivity of ethanol vapor (k_{eth}) at the average of the inlet and outlet temperatures of the first condenser section is 0.023 W m⁻¹ K⁻¹. The hydraulic diameter of the ethanol channels (D_h) is 0.761 mm. Therefore, the heat transfer coefficient for the representative model is estimated to be 110 W m⁻² K⁻¹.

The ethanol pressure drop through the single-phase section of condenser was found using equation (5.42) and the Churchill correlation for the Darcy friction factor [52]:

$$f_{church} = 8 \left[\left(\frac{8}{Re_{D,eth}} \right)^{12} + \left(\left(-2.457 \ln \left(\left(\frac{7}{Re_{D,eth}} \right)^{0.9} + 0.27 \frac{e}{D_h} \right) \right)^{16} + \left(\frac{37,530}{Re_{D,eth}} \right)^{16} \right)^{-1.5} \right]^{1/12} \quad (5.50)$$

The Reynolds number is based on the hydraulic diameter of the ethanol channels, and is defined as follows:

$$Re_D = \frac{G_{ch} D_h}{\mu} \quad (5.51)$$

Referring to Tables 5-7 and 5-8, the Reynolds number for ethanol vapor flow ($Re_{D,eth,v}$) through the channels is 2,130, the absolute roughness of the channel surface (e) is estimated to be 1.5 μm , and the hydraulic diameter of the channels (D_h) is 0.761 mm. The Churchill friction factor (f_{church}) is therefore found to be 0.03. With an ethanol mass flux of $30.9 \text{ kg m}^{-2} \text{ s}^{-1}$, an ethanol density of 2.43 kg m^{-3} , and a hydraulic diameter of 0.761 mm, the pressure drop per unit length for ethanol through the single-phase portion of the condenser is 7.86 kPa m^{-1} . The required length of the first section of the condenser is found using the formulas for each area in equation (5.28):

$$A_{s,in} = N_{ch} N_t N_{row} \pi D_h L_{\text{cond,sp}} \quad (5.52)$$

$$A_{s,tube} = 2 N_t N_{row} (w_t + t_t) L_{\text{cond,sp}} \quad (5.53)$$

From Table 5-9, the number of channels per tube (N_{ch}) is 17, the number of tubes per row (N_t) is 30, and the number of rows (N_{row}) is 2. With a tube width of 20.4 mm and a tube thickness of 1.5 mm, the required inner tube surface area is 0.088 m^2 and the required outer tube surface area is 0.095 m^2 . Therefore, the required length of the single-phase section of the condenser is 0.037 m. Note that the fin efficiency of the areas between the microchannels has been neglected here. This can be justified by calculating the fin efficiency (equation (5.33) and equation (5.34)) and treating the area between the microchannels as a rectangular fin with thickness equal to 0.41 mm (minimum distance between microchannels) and fin height equal to the hydraulic radius of 0.38 mm. Taking the thermal conductivity of the fin as $240 \text{ W m}^{-1} \text{ K}^{-1}$ and using the single-phase ethanol heat transfer coefficient of $110 \text{ W m}^{-2} \text{ K}^{-1}$, the fin efficiency is 99.99%. For the two-phase section of the condenser, the ethanol heat transfer coefficient is higher at $3,650 \text{ W m}^{-2} \text{ K}^{-1}$ which gives a fin efficiency of 99.64%. The fin efficiencies are very close to 100% and can therefore be neglected without significantly affecting the results.

Unlike the single-phase portion of the condenser, the two-phase section was solved by iterating over the quality of the ethanol from 1 to 0 in steps of 0.05. A similar series of equations as those outlined for the single-phase section were solved at each iteration, with the quality taken to be the average of the inlet and outlet qualities for each slice. Therefore, the length of each condenser slice was found and, along with the length of the single-phase section, were summed to arrive at the overall length. The two-phase representative point is the first quality step from a quality of 1.00 to a quality of 0.95 (Table 5-10). For this two-phase representative point, the hot side inlet temperature is 90.0°C, the cold side inlet temperature is 25°C, and the minimum heat capacity rate is 10.4 J s⁻¹ K⁻¹, giving a maximum heat transfer rate of 0.68 kW (equation (5.23)). The actual heat transfer rate is 0.60 kW, yielding a heat exchanger effectiveness of 87.4%. The relationship between effectiveness and NTUs of the two-phase section differs from that of the single-phase due to the large difference in heat capacity rates between the two-phase ethanol and air, resulting in a heat capacity ratio of essentially zero. The corresponding heat exchanger effectiveness/NTU relation becomes [49]:

$$\varepsilon_{\text{tp}} = 1 - \exp(-NTU) \quad (5.54)$$

The representative point for the two-phase slice of the condenser (for one quality step) has an effectiveness of 87.4% which yields an NTU of 2.07 and a total thermal resistance of 0.046 K W⁻¹.

The same thermal resistances described by equation (5.28) also exists in the two-phase section of the condenser. The two-phase ethanol flow required an appropriate heat transfer coefficient correlation based on the quality of the fluid. The Shah correlation was chosen because of the broad data set used to formulate the correlation, which included data using ethanol [53]. The correlation is represented by the following formulae:

$$h_{\text{eth,tp}} = h_{\text{eth,lo}} \left[(1-x)^{0.8} + \frac{3.8x^{0.76}(1-x)^{0.04}}{P_r^{0.38}} \right] \quad (5.55)$$

$$h_{\text{eth,lo}} = 0.023 Re_{D,\text{eth,lo}}^{0.8} Pr_1^{0.4} k_1 / D_{\text{h,eth}} \quad (5.56)$$

The correlation is based on the heat transfer coefficient for an entirely liquid flow ($h_{\text{eth,lo}}$), with the same flow rate as the total flow rate. Similarly, the Reynolds number is calculated as if all the flow were liquid. Shah did caution that the accuracy of the correlation tends to decrease as the Reynolds numbers drop and the Reynolds numbers were in the range of 14-62 for all systems. This fact coupled with the fact that the correlation's deviation from the mean for the data it was derived from was near 15% suggests caution should be used in relying on the absolute results. Additionally, this model applies the correlation to smaller channel diameters than the cases used for creation of the correlation. The accuracy may therefore be lower than Shah estimated, but all models (for each coolant temperature) use the same correlation so even if the heat transfer correlation is not highly accurate, the model results will be useful in comparison to one another. The liquid only Reynolds number is defined as:

$$Re_{D,\text{eth,lo}} = \frac{G_{\text{eth}} D_{\text{h,eth}}}{\mu_1} \quad (5.57)$$

The non-dimensional Prandtl number (Pr_1) for liquid ethanol in equation (5.56) is defined as:

$$Pr_1 = \frac{c_{p,\text{eth,l}} \mu_{\text{eth,l}}}{k_{\text{eth,l}}} \quad (5.58)$$

Note that this is different from the pressure ratio (P_r) from equation (5.55) which is given by:

$$P_r = \frac{P_{\text{eth}}}{P_{\text{crit,eth}}} \quad (5.59)$$

For the representative point, the ethanol mass flux is $30.9 \text{ kg m}^{-2} \text{ s}^{-1}$, the hydraulic diameter is 0.761 mm and the liquid ethanol dynamic viscosity is $0.381 \text{ mPa}\cdot\text{s}$, giving a Reynolds number of 61.8 . The ethanol thermal conductivity is $0.150 \text{ W m}^{-1} \text{ K}^{-1}$, and the hydraulic diameter is 0.761

mm, yielding a Prantdl number of 7.75 and a liquid only heat transfer coefficient ($h_{\text{eth,lo}}$) of 0.28 kW m⁻² K⁻¹. Using this value along with the average quality of 0.975 and the pressure ratio of 0.025, equation (5.55) yields a two-phase ethanol heat transfer coefficient of 3.65 kW m⁻² K⁻¹. Figure 5-9 shows the ethanol heat transfer coefficient plotted against the cumulative heat duty in the condenser. The ethanol heat transfer coefficient is very low for the single-phase vapor in the first section of the condenser, but jumps to 3.65 kW m⁻² K⁻¹ in the first two-phase section (the representative point). The two-phase ethanol heat transfer coefficient then steadily declines as the quality approaches zero at the condenser outlet.

The pressure drop calculation was also modified for the two-phase section. Note that, for the sake of simplicity, the pressure drop analysis shown here was not included in the thermodynamic analysis since calculations showed an insignificant effect on the saturation temperatures. However, this analysis was still performed to ensure that pressure drops were not excessive. A correlation proposed by Zhang et al. [54] was applied using the following equations [55]:

$$dP_{\text{eth,tp}} = L\Phi_1^2 \left(\frac{dP}{dL} \right)_1 \quad (5.60)$$

$$\Phi_1^2 = 1 + \frac{Ch}{\chi} + \frac{1}{\chi^2} \quad (5.61)$$

$$\chi^2 = \frac{\left(\frac{dP}{dL} \right)_1}{\left(\frac{dP}{dL} \right)_g} \quad (5.62)$$

The pressure drops per unit length for the liquid and vapor portions of the two-phase flow are as follows [55]:

$$\left(\frac{dP}{dL}\right)_l = f_l \frac{G^2 (1-x)^2}{2D_h \rho_l} \quad (5.63)$$

$$\left(\frac{dP}{dL}\right)_g = f_g \frac{G^2 x^2 \rho_g}{2D_h} \quad (5.64)$$

The Churchill correlation (equation (5.50)) was used to estimate the friction factors of 41.4 and 0.030 for the liquid and gas phases, respectively. The pressure drops per unit length are 22.4 Pa m⁻¹ and 7,250 Pa m⁻¹ for the liquid fraction and vapor fraction, respectively. From equation (5.62), the value of the Martinelli parameter (χ) for the representative point is 0.056. The Chisolm number correlation from Zhang et al. for two-phase flow is [54]:

$$Ch = 21 \left(1 - \exp\left(\frac{-0.142}{La}\right) \right) \quad (5.65)$$

The Chisolm number correlation is based on the Laplace number, given by:

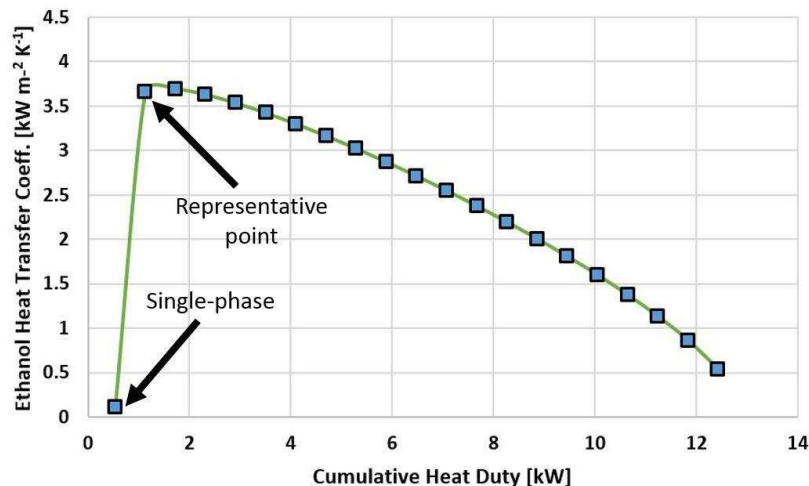


Figure 5-9. Plot of ethanol heat transfer coefficient in the condenser vs. the cumulative heat duty. The plot starts with the single-phase section (first point) and proceeds through the two-phase section as the cumulative heat duty increases. The representative point is the first point in the two-phase section.

$$La = \frac{\left[\frac{\sigma}{g(\rho_l - \rho_g)} \right]^{0.5}}{D_h} \quad (5.66)$$

The Laplace number (La) for the ethanol at the representative point is 2.01, yielding a Chisolm number (Ch) of 1.43. Thus, the value of the square of the friction multiplier (Φ_f) is 350.1. Therefore, the two-phase pressure drop per unit length is 7.84 kPa m^{-1} .

Similar to the single-phase section, the required length of each two-phase slice was found from the area formulae in equations (5.30), (5.31), (5.52), and (5.53) as well as the thermal resistance formula in equation (5.28). For the representative point, the required inner tube surface area is 0.031 m^2 and the required outer tube surface area is 0.034 m^2 , yielding a required length of 0.013 m . To fully condense the ethanol from vapor at 90°C to liquid at 90° requires a two-phase condenser section of 0.271 m . The single-phase section of the representative condenser required 0.036 m to cool the ethanol to the saturation temperature for a total condenser length of 0.307 m . Figure 5-10 plots the cumulative condenser length against the cumulative condenser heat duty,

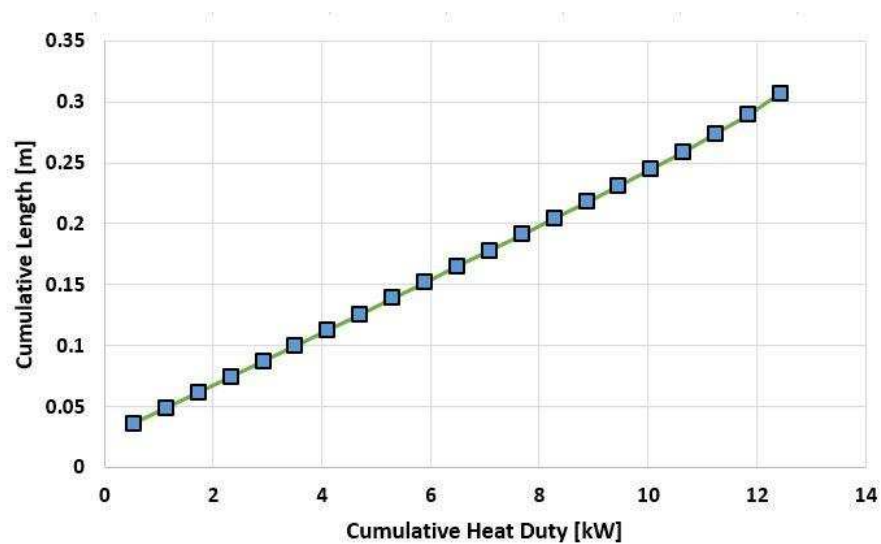


Figure 5-10. Cumulative condenser length vs. cumulative heat duty starting with vapor inlet and ending with 100% liquid ethanol.

starting with the superheated vapor at the inlet. The relationship appears to be nearly linear in the two-phase section with each slice requiring the same length to achieve a quality change of 0.05. The total pressure drop for ethanol is 1.76 kPa and the total air side pressure drop is 95.7 Pa. The ethanol pressure drop results in a decrease of the saturation temperature from 90°C to 89.7°C. The next section will describe the model used for the exhaust evaporator.

5.3.2 Evaporator Model

The evaporator design differed significantly from that of the condenser, with a counter-flow configuration and rectangular channels (Figure 5-11). The counter-flow design was chosen to keep the size reasonable while trying to extract the maximum heat from the exhaust gases. Because the exhaust approaches the temperature of the ethanol near its liquid saturation point, this design will allow a much smaller heat exchanger and higher effectiveness than for a cross-flow configuration. The exhaust enters the evaporator at one end and runs through the center channels. The liquid ethanol enters at the opposite end of the evaporator and flows in the outside channels in the opposite direction of the exhaust, becoming 100% vapor at the outlet. The details and dimensions of the evaporator model are shown in Table 5-11, and the inputs for the representative

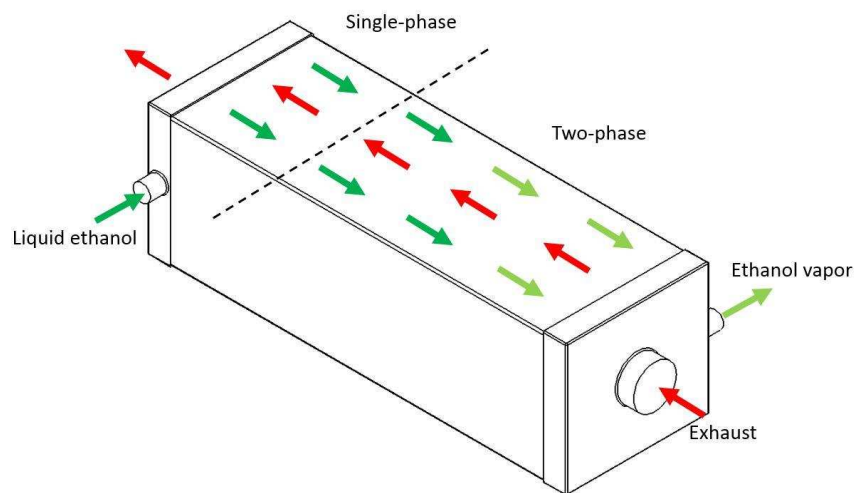


Figure 5-11. Diagram showing the counter-flow evaporator configuration.

point are given in Table 5-12. The channel configuration is shown in the evaporator cross-section in Figure 5-12. The evaporator material is 316 stainless steel due to the high temperatures and pressures present. The rectangular channels were 1.45 mm wide for the exhaust rows and 2.29 mm wide for the ethanol rows, with both channels having a height of 13 mm (Figure 5-13). The overall evaporator width was set at 0.175 m, with the length varied to meet the required heat duty for each coolant temperature model. Like the condenser models, the evaporator models were split into two sections: single-phase and two-phase. In the first section of the evaporator, the ethanol is heated to the saturation temperature as a single-phase liquid. The ethanol then begins the phase change from liquid to vapor in the second section of the evaporator, exiting with a quality of exactly one. The model details and correlations used for heat transfer coefficients and friction factors will now be discussed.

Like the condenser models, the NTU method was used to solve for the required evaporator length. For the single-phase section of the evaporator, the ethanol inlet temperature for the

Table 5-11. Evaporator model design and dimensions.

Parameter	Value	Units
Material	316 Stainless Steel	-
HX design	Counter-flow	-
Ethanol Rows ($N_{row,eth}$)	6	-
Exhaust Rows ($N_{row,exh}$)	5	-
Channel shape	Rectangular	-
Ethanol channel width ($w_{ch,eth}$)	2.29	mm
Exhaust channel width ($w_{ch,exh}$)	1.45	mm
Channel height/fin length (h_{ch}, L_f)	13	mm
Channel wall/fin thickness (t_w)	0.254	mm
HX width (w_{hx})	0.175	m
Fin style	Plain	-
Ethanol fin pitch ($p_{f,eth}$)	2.54	mm
Exhaust fin pitch ($p_{f,exh}$)	1.7	mm
Corrected fin length (L_c)	6.5	mm
Absolute roughness (e)	15	μm

representative point is 134.6°C, the exhaust inlet temperature is 159.5°C, and the minimum heat capacity rate ($C_{\min} = C_{\text{exh}}$ here) is 17.1 J s⁻¹ K⁻¹, giving a maximum heat transfer rate of 0.425 kW. The actual heat transfer rate for the single-phase section is 0.338 kW, yielding a heat exchanger effectiveness of 80.0%. For the single-phase portion of the evaporator, the counter-flow design requires a different relation between epsilon and the NTU value, which depends on the ratio of heat capacity rates [49]:

Table 5-12. Evaporator model inputs for the representative point of 3100 rpm, 24 N-m, 150°C coolant temperature, and 90°C condenser temperature.

All Phases:	Value	Units
Ethanol mass flux (G_{eth})	0.479	kg m ⁻² s ⁻¹
Single-phase:		
Minimum heat capacity rate ($C_{\min}=C_{\text{exh}}$)	17.1	W K ⁻¹
Maximum heat capacity rate ($C_{\max}=C_{\text{eth}}$)	22.0	W K ⁻¹
Exhaust inlet temperature ($T_{\text{in,hot}}$)	159.5	°C
Ethanol inlet temperature ($T_{\text{in,cold}}$)	134.6	°C
Actual heat transfer rate (\dot{Q})	0.338	kW
Exhaust thermal conductivity (k_{exh})	0.041	W m ⁻¹ K ⁻¹
Ethanol thermal conductivity (k_{eth})	0.132	W m ⁻¹ K ⁻¹
Tube wall thermal conductivity (k_w)	15.4	W m ⁻¹ K ⁻¹
Ethanol dynamic viscosity (μ_{eth})	0.019	mPa-s
Ethanol density (ρ_{eth})	661	kg m ⁻³
Two-phase:		
Average ethanol quality (x_{avg})	0.025	-
Minimum heat capacity rate ($C_{\min}=C_{\text{exh}}$)	17.1	W K ⁻¹
Ratio of heat capacity rates (C_r)	0	-
Exhaust inlet temperature ($T_{\text{in,hot}}$)	171.7	°C
Ethanol inlet temperature ($T_{\text{in,cold}}$)	150	°C
Actual heat transfer rate (\dot{Q})	0.20	kW
Liquid ethanol heat capacity ($c_{p,\text{eth,l}}$)	3.83	kJ kg ⁻¹ K ⁻¹
Liquid ethanol dynamic viscosity ($\mu_{\text{eth,l}}$)	0.173	mPa-s
Liquid ethanol thermal conductivity ($k_{\text{eth,l}}$)	0.130	W m ⁻¹ K ⁻¹
Liquid ethanol density ($\rho_{\text{eth,l}}$)	649.4	kg m ⁻³
Vapor ethanol density ($\rho_{\text{eth,g}}$)	15.0	kg m ⁻³
Ethanol inlet pressure ($P_{\text{eth,in}}$)	981.6	kPa
Ethanol critical pressure (P_{crit})	6,268	kPa
Ethanol surface tension (σ)	0.0102	N m ⁻¹

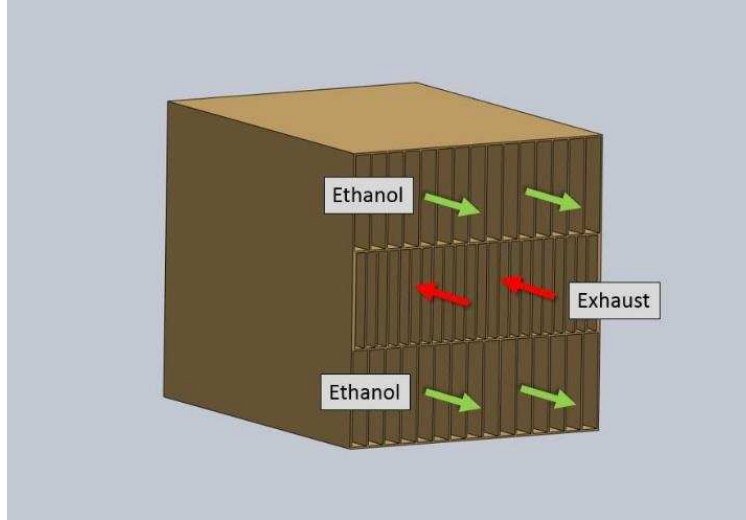


Figure 5-12. Diagram showing evaporator construction with ethanol channels on the outside and exhaust channels running in the center.

$$\varepsilon = \frac{1 - \exp[-NTU(1 - C_r)]}{1 - C_r \exp[-NTU(1 - C_r)]} \quad (C_r < 1) \quad (5.67)$$

For the representative point, the ratio of heat capacity rates for the single-phase section is 0.777 and the heat exchanger effectiveness is 80.0%, which yields an NTU value of 2.80 and a total thermal resistance of 0.021 K W^{-1} . The rectangular ducts for both the coolant and exhaust sides of the heat exchanger can be represented by finned sets of plates between which the fluids flow in alternating layers, with the cold side (ethanol) flowing through the outer layers to minimize heat loss to the environment. The total thermal resistance for the evaporator heat transfer is as follows:

$$R_{\text{evap,tot}} = \frac{1}{UA_{\text{evap}}} = \frac{1}{\eta_{\text{o,evap,eth}} h_{\text{evap,eth}} A_{\text{s,eth}}} + \frac{t_{\text{w,evap}}}{k_{\text{w,evap}} A_{\text{w,avg}}} + \frac{1}{\eta_{\text{o,evap,exh}} h_{\text{evap,exh}} A_{\text{s,exh}}} \quad (5.68)$$

The primary difference compared to the condenser model is the addition of fins on the coolant side of the heat exchanger to increase heat transfer as the ethanol becomes a vapor.

The heat transfer coefficients for both exhaust and coolant in the single-phase stage of the evaporator are found using the Nusselt number relation given in equation (5.49). The Nusselt

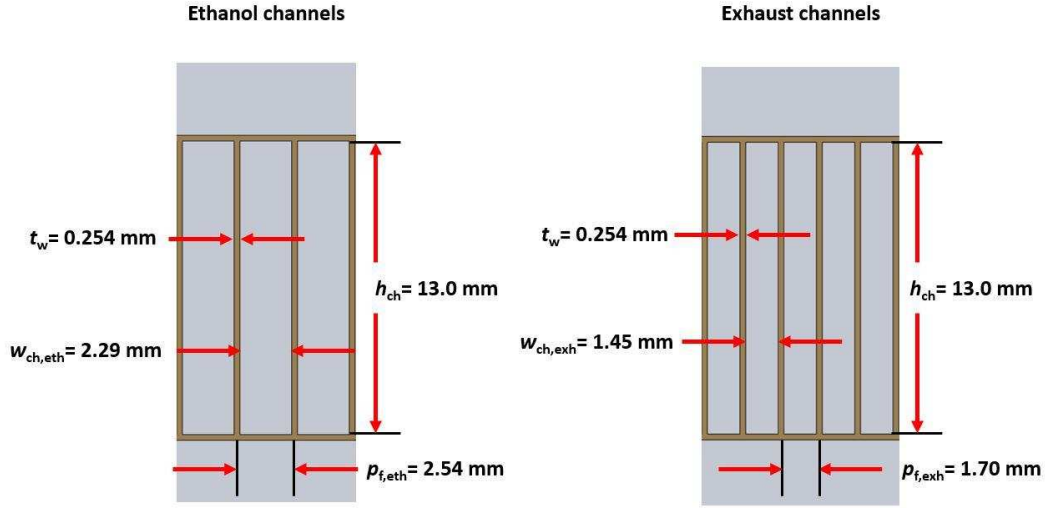


Figure 5-13. Left: Cross-section of ethanol channels in evaporator. Right: Cross-section of exhaust channels in exhaust evaporator.

number correlations were found by interpolating the values given for discrete aspect ratios in the reference material [49]. The aspect ratio (α_r) is the ratio of channel width to channel height:

$$\alpha_r = \frac{w_{ch}}{h_{ch}} \quad (5.69)$$

With a channel width of 1.45 mm and a channel height of 13 mm, the aspect ratio for the exhaust passages is 0.112. The following Nusselt number correlation for the exhaust gases applies to uniform heat flux and laminar flow in rectangular channels with an aspect ratio of 0.112:

$$Nu_{exh} = 6.78 \quad (5.70)$$

Equation (5.49) is once again used to estimate the heat transfer coefficient. The hydraulic diameter for a rectangular channel is defined as:

$$D_{h,rect} = \frac{2w_{ch}h_{ch}}{w_{ch} + h_{ch}} \quad (5.71)$$

From the channel dimensions listed above, the hydraulic diameter for the exhaust passages is 2.61 mm. With an exhaust thermal conductivity of $0.041 \text{ W m}^{-1} \text{ K}^{-1}$, the exhaust heat transfer coefficient

for the representative model is $106.3 \text{ W m}^{-2} \text{ K}^{-1}$. The heat transfer coefficient is then used to solve equations (5.29) through (5.34) for the exhaust side fin array efficiency. The heat exchanger wall thermal conductivity is $15.4 \text{ W m}^{-1} \text{ K}^{-1}$ and coupled with the heat transfer coefficient of $106.3 \text{ W m}^{-2} \text{ K}^{-1}$ and the fin dimensions in Table 5-11, the individual fin efficiency is 60.0% and the fin array efficiency is 64.0%.

The coolant channels have a greater width than the exhaust passages and therefore a larger aspect ratio. With a channel width of 2.29 mm and a channel height of 13 mm, the coolant channels have an aspect ratio of 0.176. The following Nusselt number correlation for the single-phase ethanol applies to uniform heat flux and laminar flow in rectangular channels with an aspect ratio of 0.176:

$$Nu_{\text{eth}} = 5.82 \quad (5.72)$$

With a hydraulic diameter of 3.89 mm and a thermal conductivity of $0.132 \text{ W m}^{-1} \text{ K}^{-1}$, equation (5.49) yields an ethanol heat transfer coefficient of $197.7 \text{ W m}^{-2} \text{ K}^{-1}$. The ethanol side heat transfer coefficient (h_{eth}) along with the heat exchanger material thermal conductivity (k_w) of $15.4 \text{ W m}^{-1} \text{ K}^{-1}$ and the fin thickness (t_f) of 0.254 mm can then be used to solve equation (5.34) which produces an m value of 318. The resulting fin efficiency (η_f) for the representative model is 46.9%. From equation (5.29), the efficiency for the entire fin array is 53.7%.

Pressure drop for both fluids in the single-phase section is found using the laminar flow friction factor correlation from Shah and Bhatti [56]:

$$f_{\text{SB}} = \frac{96(1 - 1.3553a_r + 1.9467a_r^2 - 1.7012a_r^3 + 0.9564a_r^4 - 0.2537a_r^5)}{Re} \quad (Re < 2300) \quad (5.73)$$

The correlation applies to laminar flow, which was verified for each evaporator model. With an aspect ratio of 0.112 and a Reynolds number of 153, the friction factor for the exhaust flow is 0.547. The exhaust pressure drop per unit length is therefore 398 Pa m^{-1} . For the ethanol flow in

the single-phase section, the aspect ratio is 0.176 and the Reynolds number is 9.76, yielding a friction factor of 8.03. The resulting pressure drop per unit length of the ethanol in the single-phase section of the condenser is 0.359 Pa m^{-1} .

The required length of the single-phase section of the evaporator is found from the area formulae given below, and the thermal resistance formula in equation (5.68).

$$A_{s,\text{eth}} = N_{\text{fin,eth}} A_{f,\text{eth}} + A_{b,\text{eth}} \quad (5.74)$$

$$A_{b,\text{eth}} = 2N_{\text{row,exh}} L_{\text{ch}} w_{\text{evap}} \quad (5.75)$$

$$A_{s,\text{exh}} = N_{\text{fin,exh}} A_{f,\text{exh}} + A_{b,\text{exh}} \quad (5.76)$$

$$A_{b,\text{exh}} = 2N_{\text{row,exh}} L_{\text{ch}} w_{\text{evap}} \quad (5.77)$$

$$A_{s,w} = 2N_{\text{row,exh}} w_{\text{evap}} L_{\text{ch}} \quad (5.78)$$

For the representative single-phase point, the required ethanol channel surface area is 1.04 m^2 and the required exhaust channel surface area is 1.25 m^2 , yielding a required length (L_{ch}) of 0.084 m for the representative single-phase evaporator section. The ethanol and exhaust pressure drops for the single-phase section are therefore 0.030 Pa and 33.5 Pa , respectively.

The two-phase section of the evaporator model was solved by incrementally stepping through the ethanol quality from 0 to 1 in steps of 0.05. For the representative point, the exhaust inlet temperature is 171.6°C , the ethanol inlet temperature is 150°C , and the minimum heat capacity rate is $17.1 \text{ J s}^{-1} \text{ K}^{-1}$, yielding a maximum heat transfer rate of 0.371 kW . The actual heat transfer rate for the representative two-phase evaporator slice is 0.203 kW , giving a heat exchanger effectiveness of 55.0% for the given evaporator slice. At each step, the required length of each slice was found using equation (5.67), equation (5.27), and equation (5.68) in the same manner demonstrated for the single-phase section. From the evaporator section effectiveness and the heat capacity ratio of 0 (during phase change), the NTU value for the representative point is 0.791 .

Therefore, the UA value is 13.5 W K^{-1} and the total thermal resistance across the heat exchanger is 0.0741 K W^{-1} .

The exhaust heat transfer coefficient and exhaust side pressure drop calculations through the two-phase section of the evaporator are the same as outlined in the description of the single-phase section. The heat transfer coefficient for the two-phase ethanol was estimated from the correlation by Bertsch et al. [57]. The two-phase flow boiling heat transfer coefficient is a combination of both nucleate boiling and convective boiling terms:

$$h_{\text{FB}} = h_{\text{NB}} (1 - x) + h_{\text{conv,tp}} \left[1 + 80(x^2 - x^6) e^{-0.6C_o} \right] \quad (5.79)$$

The nucleate boiling term is:

$$h_{\text{NB}} = 55 P_r^{0.12 - 0.2 \log_{10} R_p} (-\log_{10} P_r)^{-0.55} MW^{-0.5} (q'')^{0.67} \quad (5.80)$$

The two-phase convective term is a function of the convective heat transfer coefficients for both liquid and vapor:

$$h_{\text{conv,tp}} = h_{\text{conv,l}} (1 - x) + h_{\text{conv,v}} x \quad (5.81)$$

The correlation for both the liquid and vapor phases is:

$$h_{\text{conv}} = \left(3.66 + \frac{0.0668 \frac{D_h}{L} RePr}{1 + 0.04 \left[\frac{D_h}{L} RePr \right]^{2/3}} \right) \frac{k}{D_h} \quad (5.82)$$

Here, the Reynolds number and other properties are calculated as if the entire mass flow were saturated liquid or vapor. For the liquid phase, the Reynolds number is 10.8, the Prandtl number is 5.13, and the thermal conductivity is $0.13 \text{ W m}^{-1} \text{ K}^{-1}$. Using the same hydraulic diameter from the previous section (equation (5.71)) and the iteratively calculated length of 0.025 m, the convection heat transfer coefficient for the liquid ethanol is $138 \text{ W m}^{-2} \text{ K}^{-1}$. For the vapor phase, the Reynolds number is 147, the Prandtl number is 1.05, and the thermal conductivity is 0.03 W

$\text{m}^{-1} \text{K}^{-1}$, yielding a convection heat transfer coefficient for vapor ethanol of $37.1 \text{ W m}^{-2} \text{K}^{-1}$. From equation (5.81), the previous result plus the average quality of 0.025 yields a two-phase heat transfer coefficient of $141 \text{ W m}^{-2} \text{K}^{-1}$. Note that this ethanol heat transfer coefficient is lower than in the single-phase portion of the evaporator. However, Figure 5-14 demonstrate that the heat transfer coefficient increases to over $2 \text{ kW m}^{-2} \text{K}^{-1}$ as the cumulative heat duty rises near 3 kW , but then reduces again as the quality approaches 1.

The two-phase ethanol pressure drop was estimated using a correlation given by Friedel [58] for horizontal flow. Friedel proposed a pressure drop multiplier that is similar to the multiplier used in equation (5.60). However, Friedel's multiplier modifies the pressure drop found if the entire two-phase flow were liquid opposed to the pressure drop for the liquid fraction of the total flow:

$$\left(\frac{dP}{dL}\right)_{\text{tp}} = \Phi_{\text{lo}}^2 \left(\frac{dP}{dL}\right)_{\text{lo}} \quad (5.83)$$

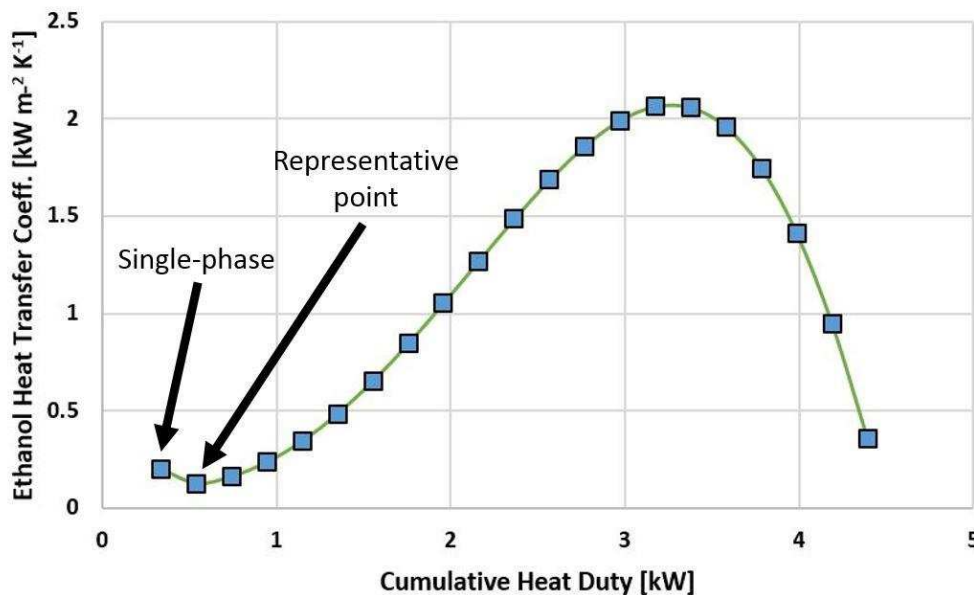


Figure 5-14. Plot of ethanol heat transfer coefficient in the evaporator vs. the cumulative heat duty. The plot starts with the single-phase section (first point) and proceeds through the two-phase section as the cumulative heat duty increases.

Here, the pressure drop per unit length if the flow were entirely liquid is:

$$\left(\frac{dP}{dL}\right)_{lo} = \frac{f_{lo}G^2}{2D_h\rho_l} \quad (5.84)$$

The friction factor for the entirely liquid flow was found using the Shah and Bhatti correlation previously outlined. For the representative point, the friction factor is 29.1, the mass flux is 479 g m⁻² s⁻¹, and the density is 649.4 kg m⁻³, yielding a liquid only pressure drop of 1.32 Pa m⁻¹. The empirically derived multiplier Friedel proposed is as follows:

$$\Phi_{lo}^2 = A + 3.21x^{0.78}(1-x)^{0.234} \left(\frac{\rho_l}{\rho_g}\right)^{0.91} \left(\frac{\mu_g}{\mu_l}\right)^{0.19} \left(1 - \frac{\mu_g}{\mu_l}\right)^{0.7} Fr^{-0.0454} We_{tp}^{-0.035} \quad (5.85)$$

Here, the value of A is found using the following relation:

$$A = (1-x)^2 + x^2\rho_l f_{go} (\rho_g f_{lo})^{-1} \quad (5.86)$$

The average quality at the representative point is 0.025, the vapor only friction factor is 0.53, and the vapor density is 15.0 kg m⁻³, resulting in an A value of 0.953. The Froude number (Fr) is found as follows:

$$Fr = \frac{G}{gD_h\rho_{tp}^2} \quad (5.87)$$

Here, the two-phase density is given by:

$$\frac{1}{\rho_{tp}} = \frac{x}{\rho_g} + \frac{1-x}{\rho_l} \quad (5.88)$$

From the quality and densities listed above, the two-phase density is calculated as 316 kg m⁻³, yielding a Froude number of 1.26×10^{-4} . The Weber number (We) for the two-phase flow is calculated as follows:

$$We_{tp} = \frac{G^2 D_h}{\rho_{tp} \sigma} \quad (5.89)$$

The surface tension for ethanol at the saturation temperature is $1.02 \times 10^{-2} \text{ N m}^{-1}$, giving a Weber number of 2.77×10^{-4} . With these values plus the liquid viscosity of 0.173 mPa-s and the vapor viscosity of 0.013 mPa-s the pressure drop modifier for the representative point is 2.71. Therefore, from equation (5.83) the two-phase ethanol pressure drop is 9.72 Pa m^{-1} for the given slice of the two-phase portion of the evaporator.

The length of each two-phase slice for the evaporator is found using the area equations given in (5.74) through (5.78). From the results described for the representative two-phase slice, the required ethanol channel surface area is 0.311 m^2 and the required exhaust channel surface area is 0.375 m^2 , requiring an evaporator slice length of 0.025 m. The overall length of the evaporator is 0.164 m and is found by summing the lengths of the single-phase section and the 20 two-phase sections. Figure 5-15 shows the cumulative evaporator length plotted against the cumulative heat duty, starting with the single-phase liquid and proceeding to 100% ethanol vapor at the outlet (left to right). This figure demonstrates that over half of the evaporator length is used to heat the liquid

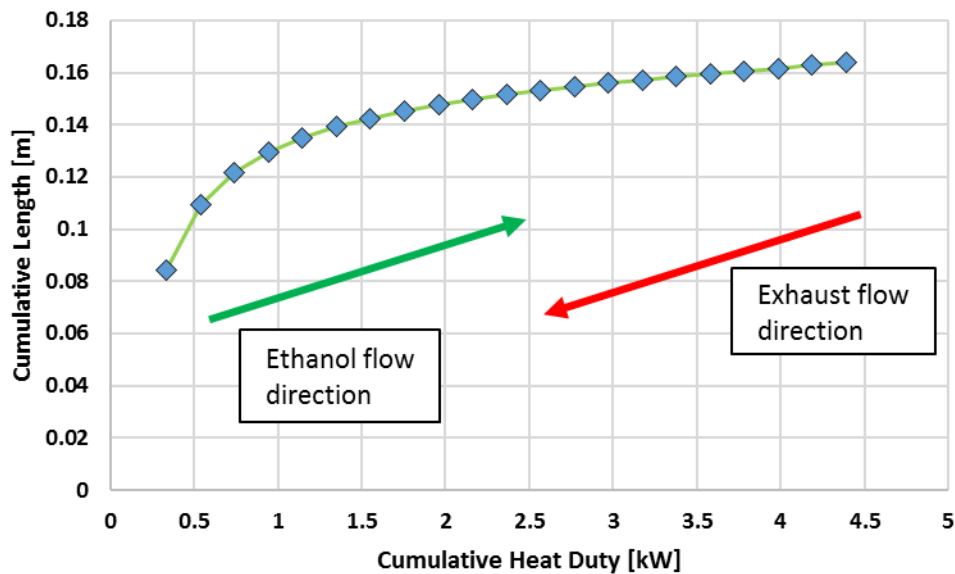


Figure 5-15. Cumulative evaporator length vs. cumulative heat duty starting with liquid inlet and ending with 100% ethanol vapor.

ethanol to the saturation temperature. The majority of the remaining length is required to reduce the quality 1 to approximately 0.75 where the heat transfer coefficient (Figure 5-14 is still relatively low. As the heat transfer coefficient rises in the latter portion of the evaporator, the evaporator length required for each quality step of 0.05 becomes relatively small (~0.012 m). The total ethanol and exhaust pressure drop for the total evaporator length are 2.38 Pa and 65.3 Pa, respectively. The next section will describe the superheater model in detail.

5.3.3 Superheater Model

The approach to the superheater models closely resembles the method used for the evaporator. The primary difference with the superheater model is that both the ethanol and exhaust gases remain single-phase throughout the entire heat exchanger. Therefore, the calculations are simplified and the entire heat exchanger can be solved at once and does not require iteration. The dimensions for the superheater models are shown in Table 5-13 along with the inputs for the representative point shown in Table 5-14. The superheater is a cross-flow design with 2 rows of exhaust channels and 3 rows of ethanol vapor channels. The large temperature difference between the exhaust gas and the ethanol allows the use of a slightly less effective cross-flow design while reducing the pressure drop in the exhaust gas compared to a counter-flow heat exchanger. The basic configuration is shown in Figure 5-16, with the exhaust channels running through the center and the ethanol channels crossing at a 90° angle. Further detail of the channel configuration is provided in Figure 5-17. The channels for both fluids are rectangular with widths of 1.45 mm and heights of 13 mm (Figure 5-18). The superheater width was set to 0.1 m and the necessary length was calculated to achieve the desired heat duty with the given inputs for each coolant temperature.

Similarly, the NTU method was utilized to solve for the required heat exchanger length. For the representative point, the exhaust inlet temperature ($T_{h,in}$) is 566°C, the ethanol inlet

temperature ($T_{c,in}$) is 150°C, and the minimum heat capacity rate is 18.0 J s⁻¹ K⁻¹ (C_{exh}), yielding a maximum heat transfer rate of 7.48 kW. The actual heat transfer rate for the evaporator is 3.00 kW, giving a heat exchanger effectiveness of 40.2%. The cross-flow design of the superheater required the use of equation (5.25) for the NTU. The effectiveness of 40.2% yields an NTU value

Table 5-13. Superheater model design and dimensions.

Parameter	Value	Units
Material	316 Stainless Steel	-
HX design	Cross-flow	-
Ethanol rows ($N_{row,eth}$)	3	-
Exhaust rows ($N_{row,exh}$)	2	-
Channel shape	Rectangular	-
Ethanol channel width ($w_{ch,eth}$)	1.45	mm
Exhaust channel width ($w_{ch,exh}$)	1.45	mm
Channel (fin) height (h_{ch}, L_f)	13	mm
Channel wall/fin thickness (t_w)	0.254	mm
HX width (w_{hx})	0.1	m
Fin style	Plain	-
Ethanol fin pitch ($p_{f,eth}$)	1.7	mm
Exhaust fin pitch ($p_{f,exh}$)	1.7	mm
Corrected fin length (L_c)	6.5	mm
Absolute roughness (e)	15	μm

Table 5-14. Superheater model inputs for the representative point of 3100 rpm, 24 N-m, 150°C coolant temperature, and 90°C condenser temperature.

Parameter	Value	Units
Minimum heat capacity rate ($C_{min}=C_{exh}$)	18.0	W K ⁻¹
Maximum heat capacity rate ($C_{max}=C_{eth}$)	33.0	W K ⁻¹
Exhaust inlet temperature ($T_{in,hot}$)	566.0	°C
Ethanol inlet temperature ($T_{in,cold}$)	150.0	°C
Actual heat transfer rate (\dot{Q})	3.00	kW
Exhaust thermal conductivity (k_{exh})	0.054	W m ⁻¹ K ⁻¹
Channel wall thermal conductivity (k_w)	18.8	W m ⁻¹ K ⁻¹
Exhaust viscosity (μ_{exh})	0.034	mPa-s
Exhaust mass flux (G_{exh})	12.2	kg m ⁻² s ⁻¹
Exhaust density (ρ_{exh})	0.482	kg m ⁻³
Ethanol thermal conductivity (k_{eth})	0.035	W m ⁻¹ K ⁻¹
Ethanol viscosity (μ_{eth})	0.014	mPa-s
Ethanol mass flux (G_{eth})	4.32	kg m ⁻² s ⁻¹
Ethanol density (ρ_{eth})	12.6	kg m ⁻³

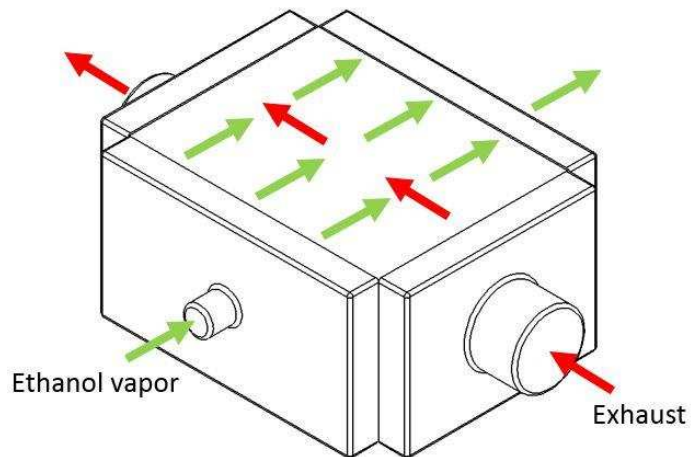


Figure 5-16. Diagram showing cross-flow superheater configuration.

of 0.514, which results in a UA value of 9.23 W K^{-1} . The rectangular ducts for both the coolant and exhaust sides of the heat exchanger were represented by finned sets of plates between which the fluids flow in alternating layers, with the cold side (coolant) flowing through the outer layers

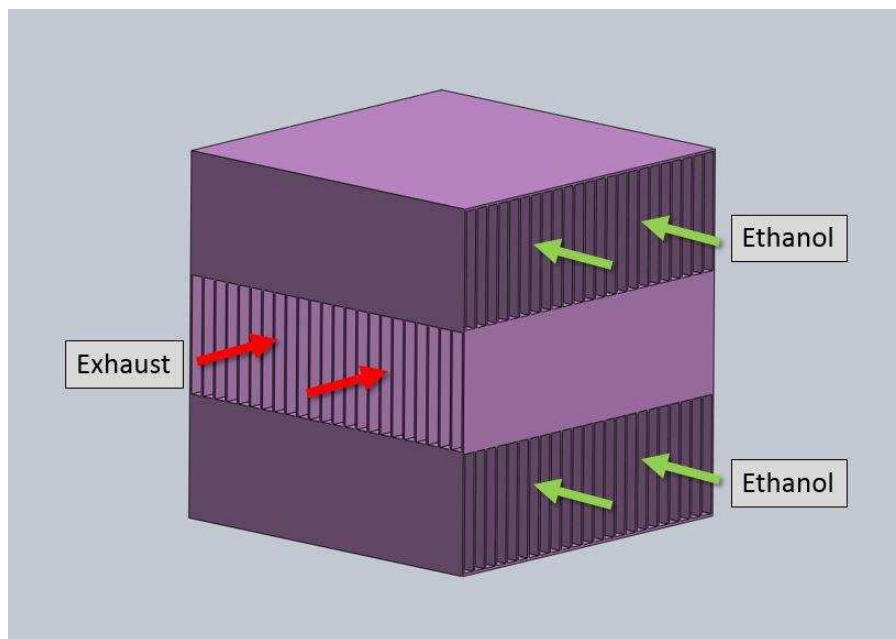


Figure 5-17. Diagram showing superheater construction with ethanol channels on the outside and exhaust channels running in the center.

to minimize heat loss to the environment. The total thermal resistance for the superheater heat transfer is as follows:

$$R_{sh,tot} = \frac{1}{UA_{sh}} = \frac{1}{\eta_{o,sh,eth} h_{sh,eth} A_{sh,eth}} + \frac{t_{w,sh}}{k_{w,sh} A_{w,sh,avg}} + \frac{1}{\eta_{o,sh,exh} h_{sh,exh} A_{sh,exh}} \quad (5.90)$$

The thermal resistances for the superheater are similar to the resistances for the evaporator because both have fins present on the exhaust and coolant sides of the heat exchanger.

The heat transfer coefficient for the exhaust side was found using the same Nusselt number correlation used in equation (5.70) for the evaporator model since the channel aspect ratios are identical. Entering the Nusselt number ($Nu_{sh,exh}$) of 6.78 into equation (5.49) along with thermal conductivity (k_{exh}) of $0.054 \text{ W m}^{-1} \text{ K}^{-1}$ from Table 5-14 and the hydraulic diameter ($D_{h,exh}$) of 2.6 mm from Table 5-15, the heat transfer coefficient for the representative point is $140 \text{ W m}^{-2} \text{ K}^{-1}$ on the exhaust side. The exhaust side heat transfer coefficient (h_{exh}) along with the heat exchanger material thermal conductivity (k_w) of $18.8 \text{ W m}^{-1} \text{ K}^{-1}$ and the fin thickness (t_f) of 0.254 mm can then be used to solve equation (5.34), which produces an m value of 242. The resulting exhaust

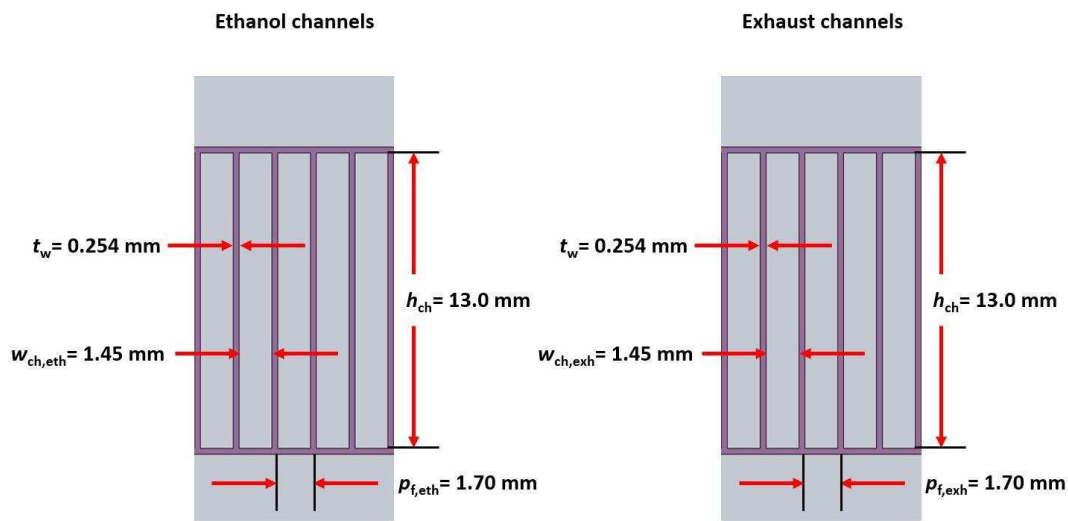


Figure 5-18. Left: Cross-section of ethanol channels in superheater. Right: Cross-section of exhaust channels in superheater.

side fin efficiency (η_f) for the representative model is 58.3%. From equation (5.29), the efficiency for the entire fin array is 65.2%.

The friction factor correlation for the exhaust pressure drop used for the evaporator (equation (5.73)) was also applicable to the superheater exhaust flow. With a Reynolds number ($Re_{sh,exh}$) of 934 and an aspect ratio ($\alpha_{sh,exh}$) of 0.112, the friction factor is 0.090. The exhaust mass flux is $12.2 \text{ kg m}^{-2} \text{ s}^{-1}$, the exhaust density is 0.482 kg m^{-3} , and the hydraulic diameter of the exhaust channel is 2.6 mm. Therefore, the pressure drop for the exhaust gases through the superheater is 9.37 kPa m^{-1} .

The coolant channels have the same dimensions and therefore the same aspect ratio as the exhaust passages. Therefore, the same Nusselt number of 6.78 is assumed. The thermal conductivity ($k_{sh,eth}$) is $0.035 \text{ W m}^{-1} \text{ K}^{-1}$ and the hydraulic diameter ($D_{h,sh,eth}$) is 2.6 mm, giving an ethanol heat transfer coefficient of $90.7 \text{ W m}^{-2} \text{ K}^{-1}$. The ethanol side heat transfer coefficient (h_{exh}) along with the heat exchanger material thermal conductivity (k_w) of $18.8 \text{ W m}^{-1} \text{ K}^{-1}$ and the fin thickness (t_f) of 0.254 mm can then be used to solve equation (5.34) which results in an m value of 195. The resulting ethanol side fin efficiency (η_f) for the representative model is 67.4%. From equation (5.29), the efficiency for the entire fin array is 70.0%.

The ethanol side pressure drop calculation uses the same set of equations as the exhaust side pressure drop. The ethanol Reynolds number ($Re_{sh,eth}$) for the representative point is 817 and the aspect ratio ($\alpha_{sh,eth}$) is 0.112, giving a friction factor of 0.0102. With an ethanol mass flux of $4.32 \text{ kg m}^{-2} \text{ s}^{-1}$, an ethanol density of 12.6 kg m^{-3} , and the hydraulic diameter of 2.6 mm, the pressure drop for the ethanol side of the superheater is 29.1 Pa m^{-1} .

Finally, the length of the superheater is found using the area equations given in (5.74) through (5.78). From the results described for the representative point, the required ethanol channel

surface area is 0.285 m^2 and the required exhaust channel surface area is 0.209 m^2 , requiring a superheater length of 0.057 m . This length yields total ethanol and exhaust pressure drop for the superheater of 1.66 Pa and 535 Pa , respectively. The ethanol in the superheater experiences a significant temperature increase inside the superheater and there is concern that using the average temperature for the ethanol properties might be a poor estimate. The superheater model for 90°C engine temperature and 60°C condenser temperature was rerun with varying ethanol temperature as the properties input to bound the problem. This case presents the largest temperature rise of all the models with the ethanol being heated from 200°C to 375°C . When the ethanol properties were found using the minimum and maximum temperatures instead of the average, the heat exchanger length only changed by 6 mm at most. Therefore, the ethanol properties at the average coolant temperature are sufficient. The next section will cover the recuperator model used to increase the efficiency of the WHR system.

5.3.4 Recuperator

The recuperator design closely resembles that of the superheater, except the recuperator is a counter-flow design instead of a cross-flow and is made of carbon steel due to the lower temperature and pressure requirements (Figure 5-19). The small temperature difference between the ethanol liquid and vapor would have required a large footprint using a less efficient cross-flow configuration. The recuperator transfers heat from the high-temperature side of the system after the turbine to the low-temperature side to pre-heat the ethanol before it enters the evaporator. The ethanol flowing through both sides of the recuperator is single-phase throughout the heat exchanger, with vapor in the high-temperature side and liquid in the low-temperature side. The details of the recuperator dimensions are shown in Table 5-15 along with the inputs for the representative point shown in Table 5-16. The recuperator has 3 rows of high-temperature vapor

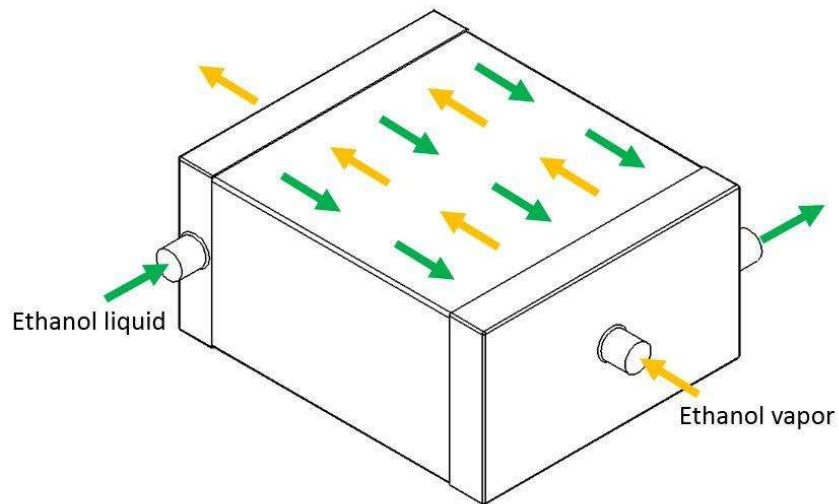


Figure 5-19. Diagram showing counter-flow recuperator configuration.

channels and 4 rows of low temperature liquid channels in the basic configuration shown in Figure 5-20. The channel dimensions are identical to those in the superheater model at 1.45 mm wide and 13 mm tall (Figure 5-21). The heat exchanger width was set to 75 mm for all recuperator models, and the heat exchanger length was found to transfer the amount of heat determined in the thermodynamic analysis.

For the given representative point, the vapor side inlet temperature is 187.4°C, the liquid inlet temperature is 90.6°C, and the minimum heat capacity rate is 27.4 W K⁻¹ (vapor side), yielding a maximum heat transfer rate of 2.65 kW. The actual heat transfer rate from the thermodynamic analysis is 2.10 kW, giving a recuperator effectiveness of 79.2%. The counter-flow design of the recuperator requires the epsilon-NTU relation previously described in equation (5.67). The effectiveness of 79.2% yields an NTU value of 2.26, which results in a UA value of 62.1 W K⁻¹. The rectangular ducts for both the vapor side and liquid side of the heat exchanger were represented by finned sets of plates between which the fluids flow in alternating layers, with

Table 5-15. Recuperator model design and dimensions.

Parameter	Value	Units
Material	Carbon Steel	-
HX design	Counter-flow	-
Vapor rows ($N_{row,v}$)	3	-
Liquid rows ($N_{row,l}$)	4	-
Channel shape	Rectangular	-
Vapor channel width ($w_{ch,v}$)	1.45	mm
Liquid channel width ($w_{ch,l}$)	1.45	mm
Channel height/fin thickness (h_{ch}, L_f)	13	mm
Channel wall/fin thickness (t_w)	0.254	mm
HX width (w_{hx})	0.075	m
Fin style	Plain	
Vapor side fin pitch ($p_{f,v}$)	1.7	mm
Liquid side fin pitch ($p_{f,l}$)	1.7	mm
Corrected fin length (L_c)	6.5	mm
Absolute roughness (e)	15	μm

the liquid side flowing through the outer layers to minimize heat loss to the environment. The thermal resistance for the recuperator heat transfer is:

Table 5-16. Recuperator model inputs for the representative point of 3100 rpm, 24 N-m, 150°C coolant temperature, and 90°C condenser temperature.

Parameter	Value	Units
Minimum heat capacity rate ($C_{min}=C_v$)	27.4	W K ⁻¹
Maximum heat capacity rate ($C_{max}=C_l$)	47.7	W K ⁻¹
Vapor inlet temperature ($T_{in,v}$)	187.4	°C
Liquid inlet temperature ($T_{in,l}$)	90.6	°C
Actual heat transfer rate (\dot{Q})	2.10	kW
Vapor thermal conductivity (k_v)	0.028	W m ⁻¹ K ⁻¹
Channel wall thermal conductivity (k_w)	47.0	W m ⁻¹ K ⁻¹
Vapor viscosity (μ_v)	0.0124	mPa-s
Vapor mass flux (G_v)	5.76	kg m ⁻² s ⁻¹
Vapor density (ρ_v)	2.11	kg m ⁻³
Liquid thermal conductivity (k_l)	0.143	W m ⁻¹ K ⁻¹
Liquid viscosity (μ_l)	0.281	mPa-s
Liquid mass flux (G_l)	4.32	kg m ⁻² s ⁻¹
Liquid density (ρ_l)	701	kg m ⁻³

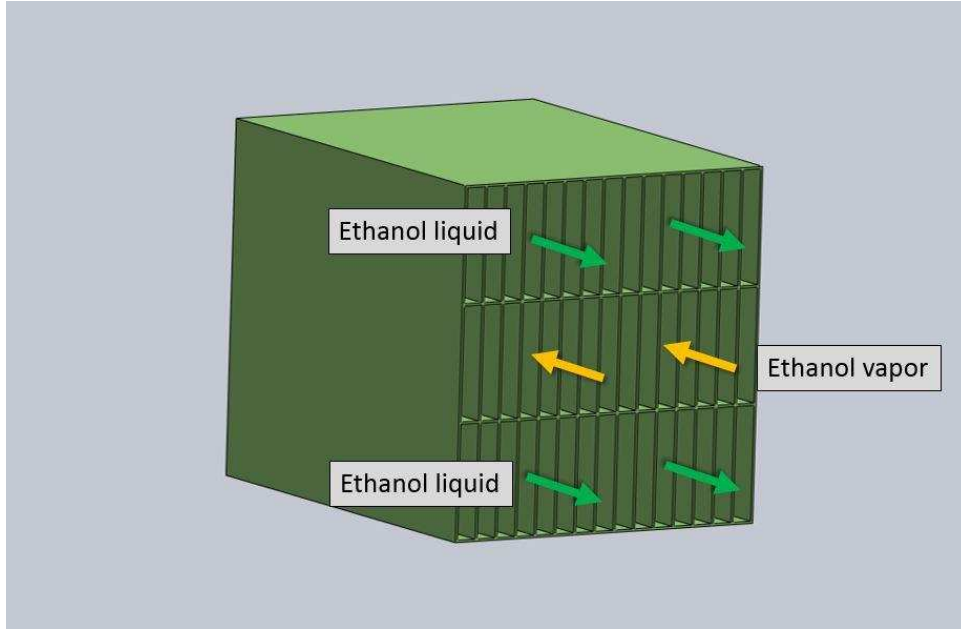


Figure 5-20. Diagram showing recuperator construction with liquid channels on the outside and vapor channels running in the center.

$$R_{\text{rec,tot}} = \frac{1}{UA} = \frac{1}{\eta_{\text{o,rec,l}} h_{\text{rec,l}} A_{\text{rec,l}}} + \frac{t_{\text{w,rec}}}{k_{\text{w,rec}} A_{\text{w,rec,avg}}} + \frac{1}{\eta_{\text{o,rec,v}} h_{\text{rec,v}} A_{\text{rec,v}}} \quad (5.91)$$

The thermal resistances for the recuperator are similar to the resistances for the evaporator and superheater because all have fins present on both sides of the heat exchanger.

The heat transfer coefficient for the vapor side of the recuperator was found using the same Nusselt number correlation from equation (5.70) used in the evaporator model since the channel aspect ratios are identical. Entering the Nusselt number ($Nu_{\text{sh,exh}}$) of 6.78 into equation (5.49) along with thermal conductivity (k_v) of $28.2 \times 10^{-3} \text{ W m}^{-1} \text{ K}^{-1}$ from Table 5-16 and the hydraulic diameter (D_h) of 2.6 mm from Table 5-15, the vapor heat transfer coefficient for the representative point is $73.6 \text{ W m}^{-2} \text{ K}^{-1}$. The vapor side heat transfer coefficient (h_v) along with the heat exchanger material thermal conductivity (k_w) of $47.0 \text{ W m}^{-1} \text{ K}^{-1}$ and the fin thickness (t_f) of 0.254 mm can then be used to solve equation (5.34) which results in a vapor side m value of 78.5. The resulting vapor side fin efficiency (η_f) for the representative model is 92.1%. From equation (5.29), the

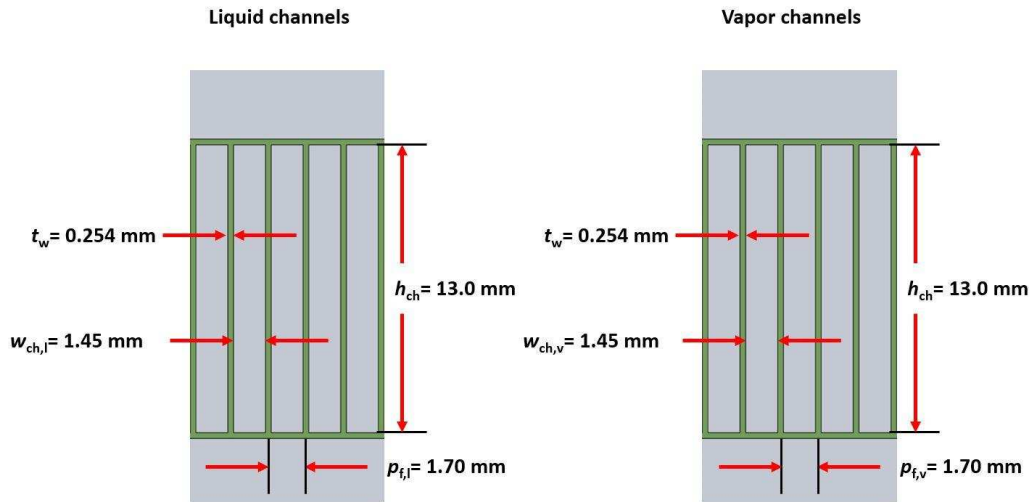


Figure 5-21. Left: Cross-section of liquid channels in recuperator. Right: Cross-section of vapor channels in recuperator.

efficiency for the entire fin array is 93.2%. The friction factor correlation for the exhaust pressure drop used for the evaporator (equation (5.73)) was also applicable to both ethanol streams through the recuperator. With a Reynolds number (Re_v) of 1,213 and an aspect ratio (α_{low}) of 0.112, the friction factor for the vapor side is 68.9×10^{-3} . The vapor side ethanol mass flux is $5.76 \text{ kg m}^{-2} \text{ s}^{-1}$, the ethanol density is 2.11 kg m^{-3} , and the hydraulic diameter of the exhaust channel is 2.6 mm, yielding a pressure drop of 208 Pa m^{-1} .

The calculations for the liquid side are identical to the vapor side calculations. The thermal conductivity (k_l) is $0.143 \text{ W m}^{-1} \text{ K}^{-1}$ and the hydraulic diameter (D_h) is 2.6 mm, giving a liquid ethanol heat transfer coefficient of $372 \text{ W m}^{-2} \text{ K}^{-1}$. The liquid side heat transfer coefficient (h_l) along with the heat exchanger material thermal conductivity (k_w) of $47.0 \text{ W m}^{-1} \text{ K}^{-1}$ and the fin thickness (t_f) of 0.254 mm can then be used to solve equation (5.34), which results in an m value of 177. The resulting liquid side fin efficiency (η_f) for the representative model is 71.2%. From equation (5.29), the efficiency for the entire fin array is 73.7%. The liquid side ethanol Reynolds number (Re_l) for the representative point is 40.1 and the aspect ratio (α_v) is 0.112, giving a friction

factor of 2.09. With a liquid side ethanol mass flux of $4.32 \text{ kg m}^{-2} \text{ s}^{-1}$, a density of 701 kg m^{-3} , the hydraulic diameter of 2.6 mm, the pressure drop per unit length is 10.7 Pa m^{-1} .

Finally, the heat exchanger surface area formulae (equations (5.74) through (5.78)) are solved to determine the required recuperator length. From the results described for the representative point, the required vapor side channel surface area is 1.09 m^2 and the required liquid side channel surface area is 1.36 m^2 , requiring a recuperator length of 0.269 m. The resulting total vapor and liquid pressure drops are 56.1 Pa and 2.88 Pa, respectively. The final section of this chapter will provide details on the oil cooler models.

5.3.5 Oil Cooler

As the engine coolant temperature increases, there will be greater heat rejection to the engine oil due to its lower temperature. This additional heat must then be rejected to the ambient air to maintain reasonable oil temperatures, which will require an oil cooler. The oil cooler dimensions scale with the magnitude of the required heat rejection and therefore may have a significant impact on packaging. Therefore, oil coolers were modeled for each engine coolant temperature. The construction and dimensions of the oil cooler models are shown in Table 5-17, with the representative point inputs presented in Table 5-18. The oil cooler construction is like the condenser described in sub-section 5.3.1 with a compact aluminum cross-flow heat exchanger design (Figure 5-22). Like the condenser, the oil cooler air-side uses louvered fins to increase heat transfer (Figure 5-23). The primary difference between the oil cooler and the condenser is the channel design. Instead of microchannels used in the condenser, the oil cooler uses rectangular tubes with fins separating the tube into individual channels to increase heat transfer, but with less pressure drop than the microchannels used in the condenser (Figure 5-24). The oil channels have a width of 2.5 mm and a height of 11.7 mm, giving a hydraulic diameter of 4.15 mm. The oil cooler

has a single row of 15 tubes separated by louvered fins of same dimension as the fins on the condenser (10 mm fin length and 8.5 mm louver length). It should be noted that the actual oil temperatures from the experiment are used as inputs for the oil cooler models. As previously mentioned, the engine oil temperature was maintained at abnormally low temperatures during the experiment compared to normal operating conditions. Therefore, the oil cooler dimensions will likely be larger because of the increased surface area required to provide the required heat duty with a smaller entering temperature difference between the oil and the ambient air. Therefore, the models provide a worst-case scenario for oil cooler footprint as well as a useful comparison of the difference in size between the different engine temperature cases.

Table 5-17. Oil cooler model design and dimensions.

Parameter	Value	Units
Material	Aluminum	-
HX design	Cross-flow compact	-
Rows (N_{row})	1	-
Tubes per row (N_t)	15	-
Tube width (w_t)	42.5	mm
Tube thickness (t_t)	12.7	mm
Tube pitch (p_t)	22.7	mm
Tube wall thickness	0.5	mm
Channel shape	Rectangular	-
Channel width (w_{ch})	2.5	mm
Channel height (h_{ch})	11.7	mm
HX width (w_{hx})	42.5	mm
Air side fin style	Louvered	-
Louver angle (θ)	27	°
Louver length (L_l)	8.5	mm
Louver pitch (p_{lv})	1	mm
Air side fin pitch ($p_{f,air}$)	3	mm
Fin thickness (t_f)	0.1	mm
Fin width (w_f)	42.5	mm
Fin length (L_f)	10.0	mm
Corrected fin length (L_c)	5.0	mm
Absolute roughness (e)	1.5	μm

Table 5-18. Oil cooler model inputs for the representative point of 3100 rpm, 24 N-m, 150°C coolant temperature, and 90°C condenser temperature.

Parameter	Value	Units
Minimum heat capacity rate ($C_{\min}=C_{\text{air}}$)	170	W K ⁻¹
Maximum heat capacity rate ($C_{\max}=C_{\text{oil}}$)	172	W K ⁻¹
Oil inlet temperature ($T_{\text{in,hot}}$)	89.43	°C
Air inlet temperature ($T_{\text{in,cold}}$)	25	°C
Actual heat transfer rate (\dot{Q})	2.36	kW
Oil thermal conductivity (k_{oil})	0.137	W m ⁻¹ K ⁻¹
Channel wall thermal conductivity (k_w)	240	W m ⁻¹ K ⁻¹
Oil viscosity (μ_{oil})	31.1	mPa-s
Oil mass flux (G_{oil})	12.2	kg m ⁻² s ⁻¹
Oil density (ρ_{oil})	834.4	kg m ⁻³
Air thermal conductivity (k_{air})	26.2	W m ⁻¹ K ⁻¹
Air dynamic viscosity (μ_{air})	0.019	mPa-s
Air mass flux (G_{air})	5.12	kg m ⁻² s ⁻¹
Air density (ρ_{air})	0.994	kg m ⁻³
Air heat capacity ($c_{p,\text{air}}$)	1.01	kJ kg ⁻¹ K ⁻¹

The oil cooler model resembles all models presented previously. The air flow was defined by setting air velocity at 2.2 m s⁻¹ for all oil coolers. To ensure that this air speed is reasonable, the SPAL catalog was again referenced. The highest demand oil cooler (200°C coolant temperature) has an air side pressure drop of 102 Pa and an air flow rate requirement of 765 m³ h⁻¹. The SPAL fan that was found for the condenser (SPAL, VA18-AP51/C-41S) would easily meet these requirements, so the air speed is deemed reasonable. For the representative point, the oil inlet temperature is 89.43°C, the air inlet temperature is assumed to be 25°C, and the minimum heat capacity rate is 170 W K⁻¹ ($C_{\min}=C_{\text{air}}$), giving a maximum heat transfer rate of 11.0 kW. The actual heat transfer rate found measured in the experiment is 2.36 kW, yielding an oil cooler effectiveness of 21.5%. The single-pass cross-flow design of the oil cooler requires the use of the NTU-epsilon relation given in equation (5.25). The effectiveness of 21.5% and the heat capacity ratio of 0.992

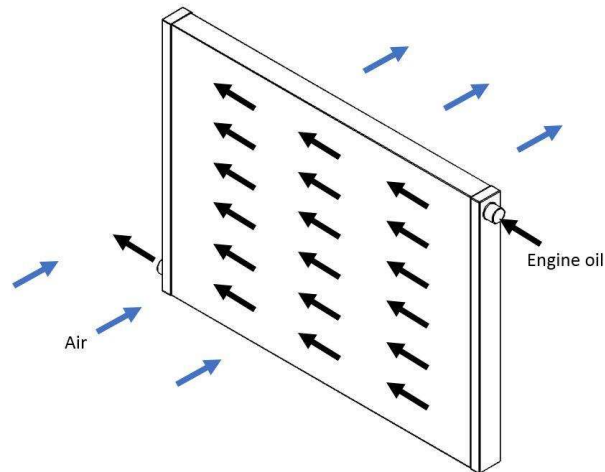


Figure 5-22. Diagram showing cross-flow engine oil cooler configuration.

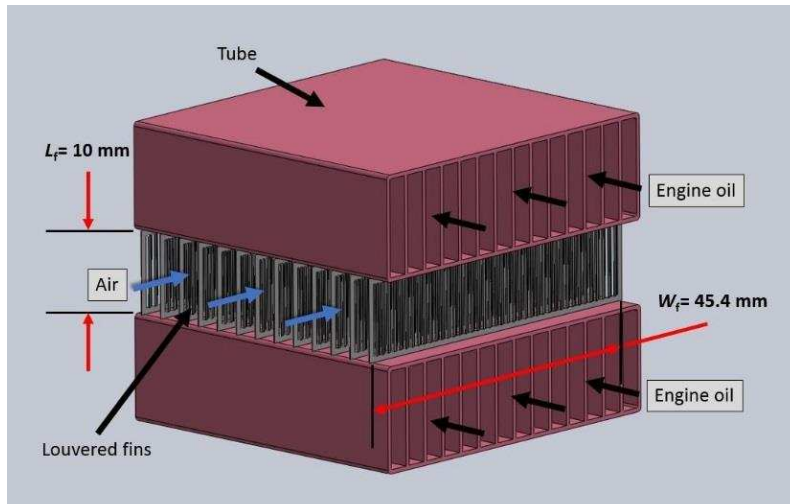


Figure 5-23. Diagram showing oil cooler construction with one row of tubes separated by louvered fins.

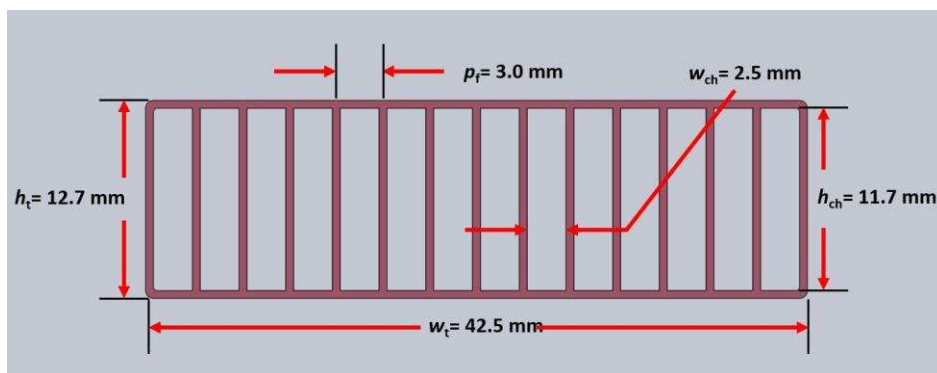


Figure 5-24. Oil cooler tube configuration and dimensions in mm.

give an NTU value of 0.291, which results in a UA value of 49.5 W K⁻¹. The thermal resistance for heat transfer across the oil cooler resembles that of the evaporator, superheater, and recuperator:

$$R_{oc,tot} = \frac{1}{UA} = \frac{1}{\eta_{o,oc,oil} h_{oc,oil} A_{oc,oil}} + \frac{t_{w,oc}}{k_{w,oc} A_{w,oc,avg}} + \frac{1}{\eta_{o,oc,air} h_{oc,air} A_{oc,air}} \quad (5.92)$$

The calculation of the individual thermal resistances differs slightly due to the channel aspect ratio that is unique to the heat exchanger models described so far.

Similar to the previous models, the Nusselt number relation given in equation (5.49) was used to estimate the heat transfer coefficient for the oil side heat transfer. The oil channels have an aspect ratio of 0.22, which translates to a Nusselt number of 5.53. With a hydraulic diameter of 4.15 mm and a thermal conductivity of 0.137 W m⁻¹ K⁻¹, the oil side heat transfer coefficient for the representative point is 182.6 W m⁻² K⁻¹. The oil side heat transfer coefficient (h_{oil}) along with the channel wall thermal conductivity (k_w) of 240 W m⁻¹ K⁻¹ and the fin thickness (t_f) of 0.5 mm can then be used to solve equation (5.34), which results in an m value of 55.2. The resulting oil side fin efficiency (η_f) for the representative model is 96.4%. From equation (5.29), the efficiency for the entire fin array is 99.4%. Oil side pressure drop is once again found using the Darcy-Weisbach formula (equation (5.42)). The friction factor is estimated using the Shah and Bhatti correlation (equation (5.73)), with inputs of 1.63 and 0.22 for the Reynolds number and oil channel aspect ratio, respectively. The friction factor is 46.6, the mass flux is 12.2 kg m⁻² s⁻¹, the oil density is 834.4 kg m⁻³, and the hydraulic diameter is 4.15 mm, yielding a pressure drop of 1.01 kPa m⁻¹.

The air side heat transfer calculations mimic the process outlined for the louvered finned air passages in the condenser model. Equations (5.36) through (5.41) are used to estimate the heat transfer coefficient for the air side of the oil cooler using the values supplied in Table 5-17 and 5-16. The air side heat transfer coefficient is found to be 111 W m⁻² K⁻¹ for the representative point. The air side heat transfer coefficient (h_{air}) along with the heat exchanger aluminum wall thermal

conductivity (k_w) of $240 \text{ W m}^{-1} \text{ K}^{-1}$ and the fin thickness (t_f) of 0.1 mm can then be used to solve equation (5.34) which results in an m value of 136. The resulting air side fin efficiency (η_f) for the representative model is 87.0%. From equation (5.29), the efficiency for the entire fin array is 90.8%. The equations for pressure drop given in the condenser section (equations (5.42) through (5.47)) are also utilized for the oil cooler due to the identical fin configuration. The air side louver Reynolds number is 277, and coupled with the fin dimensions in Table 5-17, the friction factor is 0.205. For the representative point, the air mass flux is $5.12 \text{ kg m}^{-2} \text{ s}^{-2}$, the air density is 0.994 kg m^{-3} , and the hydraulic diameter is 4.50 mm , yielding an air side pressure drop of 449 Pa m^{-1} .

Finally, the heat exchanger surface area formulae (equations (5.74) through (5.78)) are solved to determine the required oil cooler length. From the results described for the representative point, the required oil channel surface area is 0.448 m^2 and the required air channel surface area is 1.28 m^2 , requiring an oil cooler length of 0.228 m . This length results in total oil and air pressure drops of 229 Pa and 102 Pa , respectively.

5.3.6 Radiator

The 90°C engine coolant temperature systems do not recover waste heat from the engine coolant and, therefore, the engine still requires a radiator to reject the heat necessary to keep the engine at the proper operating temperature. Since the radiator is displaced in the high-temperature systems, it is important to consider the size of the radiator in the analysis of WHR footprint. The radiator design is identical to the oil cooler design, with a cross-flow, compact heat exchanger configuration chosen to maximize air side heat transfer and keep air side pressure drop low (Figure 5-25). The engine coolant was assumed to be a 50/50 mix of water and EG, which flows through the tubes with rectangular channel cross-section. In between the tubes, louvered fins increase heat transfer on the air-side of the heat exchanger (Figure 5-26). The channel dimensions are identical

to the oil cooler channel dimensions (Figure 5-27). The complete radiator dimensions are given in Table 5-19. The representative point for the radiator models also differs from the previous models, using the 90°C engine temperature case (Table 5-20).

The equations for the radiator model are identical to those for the oil cooler. The only change to the model is with the inputs. For the oil cooler, the oil mass flow rate is an input since this value was measured during the experiment. Since the engine coolant for the experiment was HTF and not EG, the required mass flow rate was not known for the given heat duty. Therefore, the EG temperature at the outlet of the radiator was substituted since this value was assumed to be the same as measured during the experiment. The air flow was defined by setting air velocity at 2.2 m s^{-1} as was done for all oil coolers. With an air side pressure drop of 102 Pa and an airflow of $961 \text{ m}^3 \text{ h}^{-1}$, the SPAL fan specified for the condenser (SPAL, VA18-AP51/C-41S) would be more than adequate to provide the required airflow. For the representative point, the EG inlet temperature is 96.5°C , the air inlet temperature is assumed to be 25°C , and the minimum heat

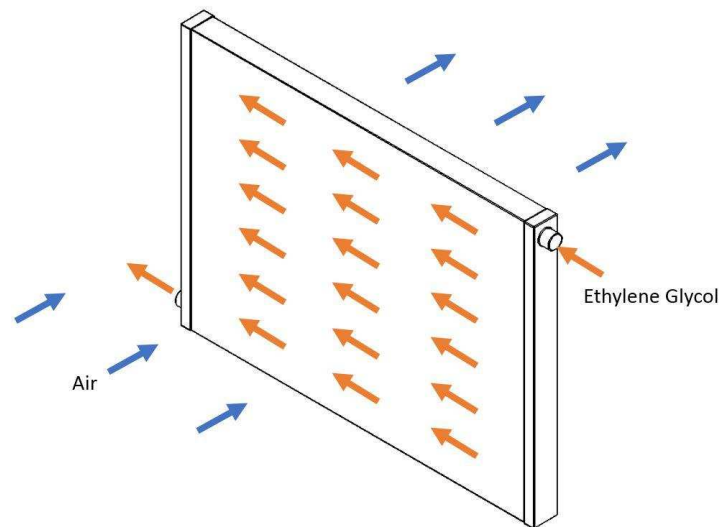


Figure 5-25. Diagram showing cross-flow radiator configuration.

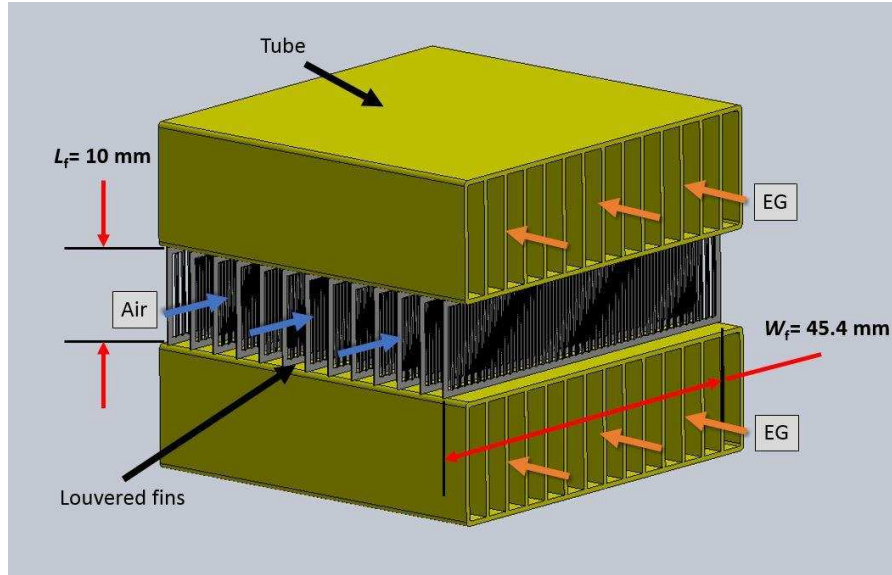


Figure 5-26. Diagram showing radiator construction with one row of tubes separated by louvered fins.

capacity rate is 295 W K^{-1} ($C_{\min}=C_{\text{air}}$), giving a maximum heat transfer rate of 21.1 kW. The actual heat transfer rate measured from the experiment is 7.23 kW, yielding a radiator effectiveness of 34.2%. The single-pass cross-flow design of the radiator requires the NTU-epsilon relation given in equation (5.25). The effectiveness of 34.2% and the heat capacity ratio of 0.592 give an NTU value of 0.495, which results in a UA value of 146 W K^{-1} .

As in the oil cooler model, the Nusselt number relation given in equation (5.49) was used to estimate the heat transfer coefficient for the EG side heat transfer. The EG channels have an aspect ratio of 0.22, which translates to a Nusselt number of 5.53. With a hydraulic diameter of 4.15 mm and a thermal conductivity of $0.431 \text{ W m}^{-1} \text{ K}^{-1}$, the EG side heat transfer coefficient for the representative point is $575 \text{ W m}^{-2} \text{ K}^{-1}$. The EG side heat transfer coefficient (h_{EG}) along with the channel wall thermal conductivity (k_w) of $240 \text{ W m}^{-1} \text{ K}^{-1}$ and the fin thickness (t_f) of 0.5 mm can then be used to solve equation (5.34), which results in an m value of 97.9. The resulting EG side fin efficiency (η_f) for the representative model is 89.6%. From equation (5.29), the efficiency

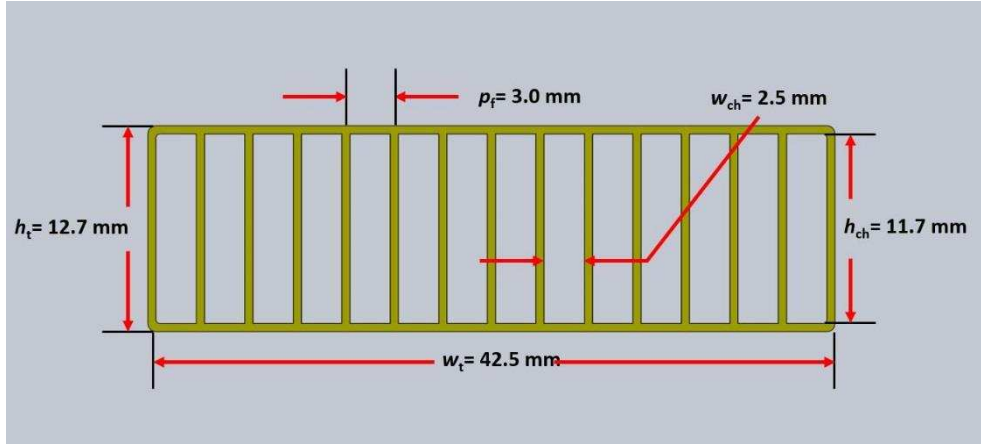


Figure 5-27. Radiator tube configuration and dimensions in mm.

for the entire fin array is 98.2%. EG side pressure drop is once again found using the Darcy-Weisbach formula (equation (5.42)). The friction factor is estimated using the Shah and Bhatti correlation (equation (5.73)), with inputs of 107.8 and 0.22 for the Reynolds number and EG channel aspect ratio, respectively. The friction factor is 0.704, the mass flux is $21.6 \text{ kg m}^{-2} \text{ s}^{-1}$, the EG density is $1,020 \text{ kg m}^{-3}$, and the hydraulic diameter is 4.15 mm, yielding a pressure drop of 38.7 Pa m^{-1} .

The air side heat transfer calculations are identical to the calculations for the oil cooler model. Equations (5.36) through (5.41) are used to estimate the heat transfer coefficient for the air side of the oil cooler using the values supplied in Table 5-19 and 5-20. The air side heat transfer coefficient is found to be $111 \text{ W m}^{-2} \text{ K}^{-1}$ for the representative point. The air side heat transfer coefficient (h_{air}) along with the heat exchanger aluminum wall thermal conductivity (k_w) of $240 \text{ W m}^{-1} \text{ K}^{-1}$ and the fin thickness (t_f) of 0.1 mm can then be used to solve equation (5.34) which results in an m value of 136. The resulting air side fin efficiency (η_f) for the representative model is 87.0%. From equation (5.29), the efficiency for the entire fin array is 90.8%. The equations for pressure drop given in the condenser section (equations (5.42) through (5.47)) are also utilized for the

Table 5-19. Radiator model design and dimensions.

Parameter	Value	Units
Material	Aluminum	-
HX design	Cross-flow compact	-
Rows (N_{row})	1	-
Tubes per row (N_t)	15	-
Tube width (w_t)	42.5	mm
Tube thickness (t_t)	12.7	mm
Tube pitch (p_t)	22.7	mm
Tube wall thickness	0.5	mm
Channel shape	Rectangular	-
Channel width (w_{ch})	2.5	mm
Channel height (h_{ch})	11.7	mm
HX width (w_{hx})	42.5	mm
Air side fin style	Louvered	-
Louver angle (θ)	27	$^{\circ}$
Louver length (L_l)	8.5	mm
Louver pitch (p_{lv})	1	mm
Air side fin pitch ($p_{f,air}$)	3	mm
Fin thickness (t_f)	0.1	mm
Fin width (w_f)	42.5	mm
Fin length (L_f)	10.0	mm
Corrected fin length (L_c)	5.0	mm
Absolute roughness (e)	1.5	μm

radiator. The air side louver Reynolds number is 277, and coupled with the fin dimensions in Table 5-19, the friction factor is 0.205. For the representative point, the air mass flux is $5.12 \text{ kg m}^{-2} \text{ s}^{-2}$, the air density is 0.994 kg m^{-3} , and the hydraulic diameter is 4.50 mm, yielding an air side pressure drop of 259 Pa m^{-1} .

Finally, the heat exchanger surface area formulae (equations (5.74) through (5.78)) are solved to determine the required radiator length. From the results described for the representative point, the required EG channel surface area is 0.778 m^2 and the required air channel surface area is 2.22 m^2 , requiring a radiator length of 0.395 m. This length results in total EG and air pressure drops of 15.3 Pa and 102 Pa, respectively.

Table 5-20. Radiator model inputs for the representative point of 3100 rpm, 24 N-m, 90°C coolant temperature.

Parameter	Value	Units
Minimum heat capacity rate ($C_{\min}=C_{\text{air}}$)	295	W K ⁻¹
Maximum heat capacity rate ($C_{\max}=C_{\text{EG}}$)	499	W K ⁻¹
EG inlet temperature ($T_{\text{in,hot}}$)	96.5	°C
Air inlet temperature ($T_{\text{in,cold}}$)	25	°C
Actual heat transfer rate (\dot{Q})	7.23	kW
EG thermal conductivity (k_{EG})	0.431	W m ⁻¹ K ⁻¹
Channel wall thermal conductivity (k_w)	240	W m ⁻¹ K ⁻¹
EG viscosity (μ_{EG})	0.830	mPa-s
EG mass flux (G_{EG})	21.6	kg m ⁻² s ⁻¹
EG density (ρ_{EG})	1020	kg m ⁻³
Air thermal conductivity (k_{air})	26.2	W m ⁻¹ K ⁻¹
Air dynamic viscosity (μ_{air})	0.019	mPa-s
Air mass flux (G_{air})	5.12	kg m ⁻² s ⁻¹
Air density (ρ_{air})	0.994	kg m ⁻³
Air heat capacity ($c_{p,\text{air}}$)	1.01	kJ kg ⁻¹ K ⁻¹

This chapter presented the thermodynamic and heat exchanger models used to estimate the WHR system output and footprint. The next chapter will explore the results of both the experimental work and the modeling described in the current chapter. The engine performance results will provide insight into the effect of high-temperature engine operation on engine efficiency and emissions. Waste heat availability and the resulting WHR models will be used to analyze the potential benefits of WHR from high-temperature engines.

CHAPTER 6. RESULTS AND DISCUSSION

The two previous chapters presented the analysis methods used for reduction of the experimental data and the heat exchanger modeling for estimating the effect of engine temperature on WHR output and system footprint. This chapter will provide the results from each analysis and discuss the implications for the viability and benefits of WHR from a high-temperature diesel engine. First, the experimental results will be covered, including the energy balance for each temperature case, engine performance, and engine emissions. Additionally, the condition of the engine during and after testing is discussed. Last, the heat exchanger model results for the high-temperature WHR systems are presented and compared with the results for the state-of-the-art WHR system that does not absorb heat from the engine.

6.1 Energy Balance

One of the primary goals of the high-temperature diesel engine experiment was to determine the energy balance for the engine at varying coolant temperature. The fuel energy leaves the engine in one of the five forms: engine output, coolant heat, exhaust heat, oil heat, and other losses. The ‘other losses’ category includes all additional losses such as pumping losses, convection and radiation heat loss to the environment, and energy lost through unburned fuel in the exhaust. Friction is not specifically listed because it is assumed that energy lost to friction is converted into heat that is either transferred to one of the fluids or to the ambient air. The uncertainty methodology for the energy balance calculations is described in Appendix B. The regression analysis method was introduced in Chapter 4. This analysis was used to determine what correlations existed between the coolant temperature and the other measured and calculated values. Figure 4-1 plots the probability that each correlation is statistically significant, found by

subtracting the p -value from 1. It is important to note that correlation does not imply causation, but simply the relationship between two values.

The quantity of waste heat present in the engine coolant, engine oil, and exhaust gases was of primary interest due to the potential effect on WHR system performance. As shown in Figure 6-1 the heat rejected to the engine coolant decreased as its temperature increased. For example, coolant waste heat decreased from $27.69 \pm 2.05\%$ to $11.97 \pm 0.62\%$ for the 3100 rpm and 18 N-m torque load point as the coolant temperature was raised from 90°C to 200°C . This trend can be explained by considering the heat transfer from the combustion gases to the cylinder wall. The heat transfer rate is proportional to the temperature difference between the combustion gases and cylinder wall, and the thermal resistance between these two items, and can be expressed as follows:

$$\dot{Q}_w = \frac{(T_g - T_w)}{R_{\text{cyl}}} \quad (6.1)$$

Here, the thermal resistance includes both radiation and convection effects [36, 49]:

$$\frac{1}{R_{\text{cyl}}} = \frac{1}{R_{\text{cyl,conv}}} + \frac{1}{R_{\text{cyl,rad}}} = (h_{\text{cyl,conv}} + h_{\text{cyl,rad}}) A_{\text{cyl}} \quad (6.2)$$

As the coolant temperature rises, the ΔT between the coolant and the combustion gases decreases and heat transfer to the coolant drops. Furthermore, the thermal resistance between the gases and the wall also changes, especially because the radiation portion of the thermal resistance increases. In addition, as the engine coolant temperature increases, the temperature of the engine structure increases, which causes increased heat rejection to the environment and the lubrication oil. The engine oil temperature was maintained near 80°C for each test, and, thus, the fraction of fuel energy transferred to the engine oil increased. For example, the oil heat fraction increased from $8.42 \pm 0.62\%$ at 90°C coolant temperature to $14.32 \pm 1.06\%$ at 200°C for data collected at 18 N-m torque (i.e., a 70% relative increase). The ambient air temperature was also below the coolant temperature,

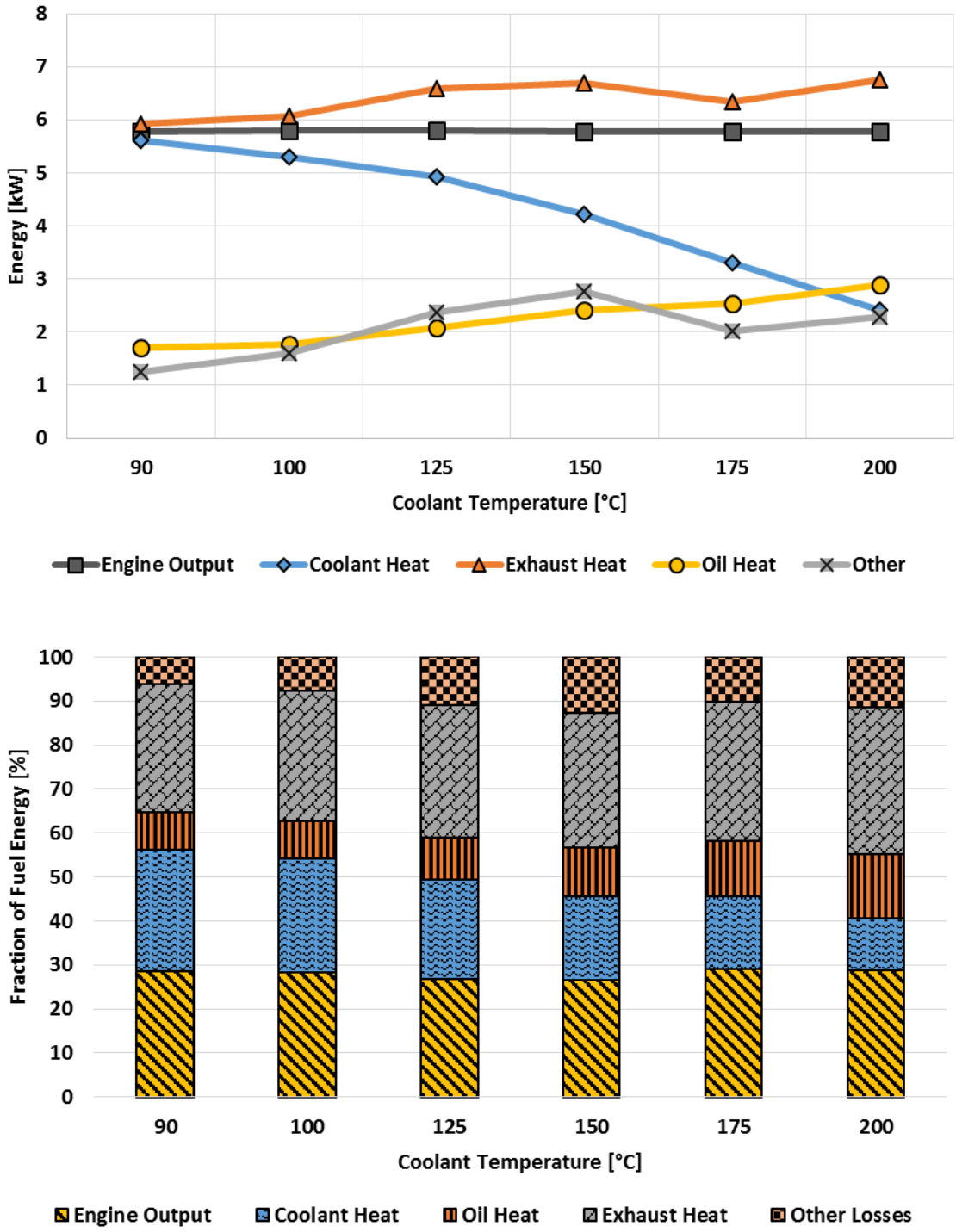


Figure 6-1. Results of energy balance on the test engine at 3100 rpm and 18 N-m of torque showing absolute values (top) and values as a percentage of fuel energy entering the engine (bottom).

which likely contributed to the increase in ‘other losses’ such as convection and radiation from the engine structure to the environment. Finally, the decrease in heat transfer from the combustion gases to the engine coolant led to an increase in exhaust heat loss as the coolant temperature rose. For example, the exhaust waste heat at 18 N-m torque increased from $29.28 \pm 1.43\%$ at 90°C to $32.13 \pm 1.66\%$ at 200°C for a 10% relative increase. The regression analysis suggests that the above correlations between the coolant temperature and the heat rejection to the coolant, oil, and exhaust are strong and statistically significant at the 95% confidence level (see Figure 4-1). Additional contributions to increased exhaust waste heat are discussed in the next section, as well as the effect of increased coolant temperature on engine brake efficiency.

Figure 6-1 also shows a noticeable change in the trends for the exhaust heat rejection and the engine oil heat rejection in the top graph, and the brake efficiency in the lower graph, when the coolant temperature rises from 150°C to 175°C . During testing, an unexpected increase in calculated engine efficiency occurred between these two coolant temperatures. After testing was completed, the data analysis revealed that the change also effected waste heat fractions, ‘other losses’, exhaust temperature, and emissions. The explanation was found after calculating the rate of oil and HTF loss throughout testing. The fluid leakage rates for the oil and HTF were found by taking the recorded quantities of fluids added and dividing by the engine run time since the last top off. As shown in Figure 6-2, the leakage rates appear to unexpectedly increase above 150°C , which is also accompanied by an increase in apparent brake efficiency. The results suggest that the cylinder head gasket was leaking engine oil, HTF, or both fluids into the combustion chambers, especially when the coolant temperature increased to 175°C and 200°C . However, the post-test engine teardown revealed that only HTF was leaking into the combustion chamber and that engine oil was exclusively leaking externally (see section 6.3). Unfortunately, this occurrence makes it

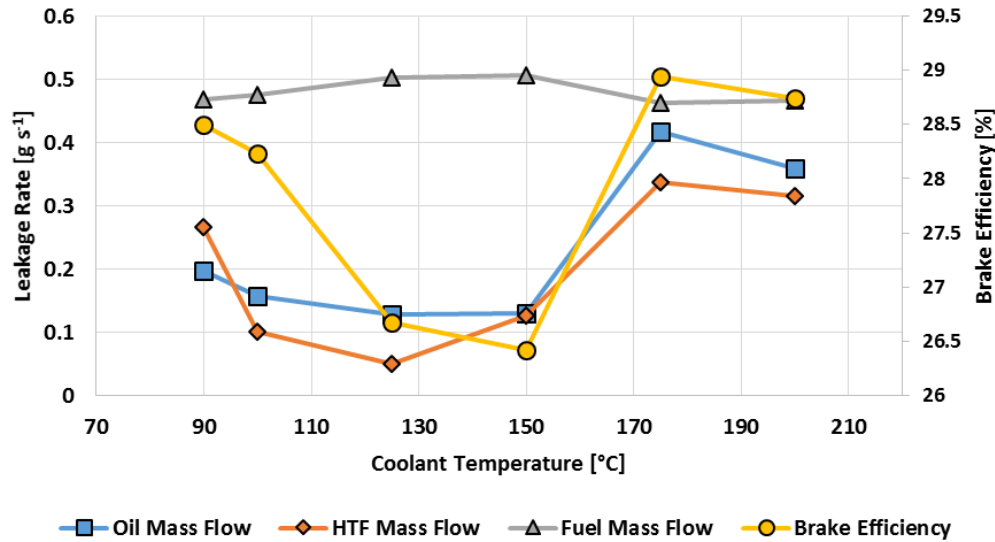


Figure 6-2. Comparison of leakage rates for engine oil and HTF with fuel flow and engine brake efficiency for 3100 rpm and 18 N-m of torque.

difficult to establish trends for some of the parameters of interest vs. coolant temperature. It also skews the energy balance percentages to some degree since unmetered fuel was entering the combustion chamber. The effects of burning the additional fuel on the waste heat availability is discussed in the next few paragraphs. Further discussion of the how the unmetered fuel may have altered engine efficiency and emissions is provided in Section 6.2.

Prior work shows that the quality of waste heat is as important as the quantity of that waste heat. The availability of each waste heat stream was evaluated to estimate the quantity of usable heat through the calculation of the rate of exergy exchanged in the heat transfer process. For heat transfer, the rate of exergy exchanged is defined as follows:

$$\dot{B} = \dot{Q} \left(1 - \frac{T_L}{\bar{T}_H} \right) \quad (6.3)$$

The rate of exergy exchanged is based on the Carnot efficiency (equation (1.1)) and therefore represents the upper limit of usable energy. From equation (6.3) it can be deduced that, to increase

the output of a heat engine such as a WHR system, either the heat input can be increased or the temperature of the source can be raised. For this analysis, the temperature of the sink was set to 25°C (i.e., 298.15 K) for all points to ensure consistency in the evaluation of exergy. The temperature of the heat source was taken to be the average temperature of the coolant inside the engine or the average exhaust temperature in the manifold. The heat loss to the exhaust was found by taking the difference in the enthalpy for each exhaust gas component (CO, CO₂, H₂O, and N₂) at the average exhaust temperature leaving the engine and at 25°C.

Figure 6-3 shows the waste heat and total exergy for the coolant and exhaust over the measured coolant temperature range for 3100 rpm at 18 N-m and 24 N-m of engine torque. This figure demonstrates that, even though the coolant waste heat flow decreases for each load point as the coolant temperature rises, the total exergy generally increases due to higher coolant and exhaust temperatures. Despite the decrease in coolant waste heat between 10% and 27%, the coolant exergy increases between 20% and 45% from 90°C to 150°C coolant temperature. For example, at the 18 N-m (56% load), the coolant waste heat drops from 5.60±0.40 kW to 4.23±0.30 kW, whereas the coolant exergy rises from 1.00±0.08 kW to 1.25±0.10 kW for the same interval. Simultaneously, the exhaust waste heat rises from 5.92±0.26 kW to 6.37±0.30 kW, which is reflected in a temperature increase of the exhaust gases: from 373.9°C at 90°C to 429.2°C at 150°C (Figure 6-4). Thus, the total exergy from the engine increases from 4.19±0.13 kW to 5.10±0.17 kW over the interval for a 22% increase. Above 150°C, coolant exergy declines for the 18 N-m torque point, which may be a result of the combustion chamber leakage. At 24 N-m of torque (74% load), the increase in exergy is even more substantial. Though coolant waste heat drops from 7.23±0.52 kW to 5.05±0.38 kW from 90°C to 200°C coolant temperature, the coolant exergy rises from 1.28±0.09 kW to 1.86±0.14 kW, a 45% increase. The exhaust heat rises from 8.45±0.27 kW to 10.05±0.35

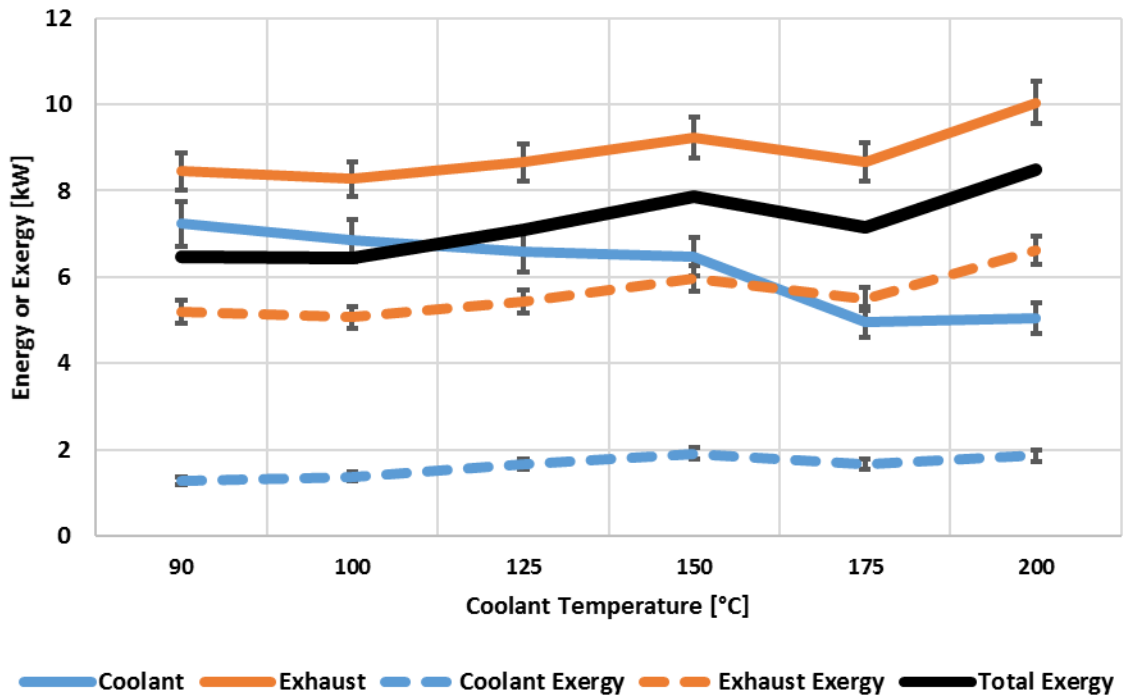
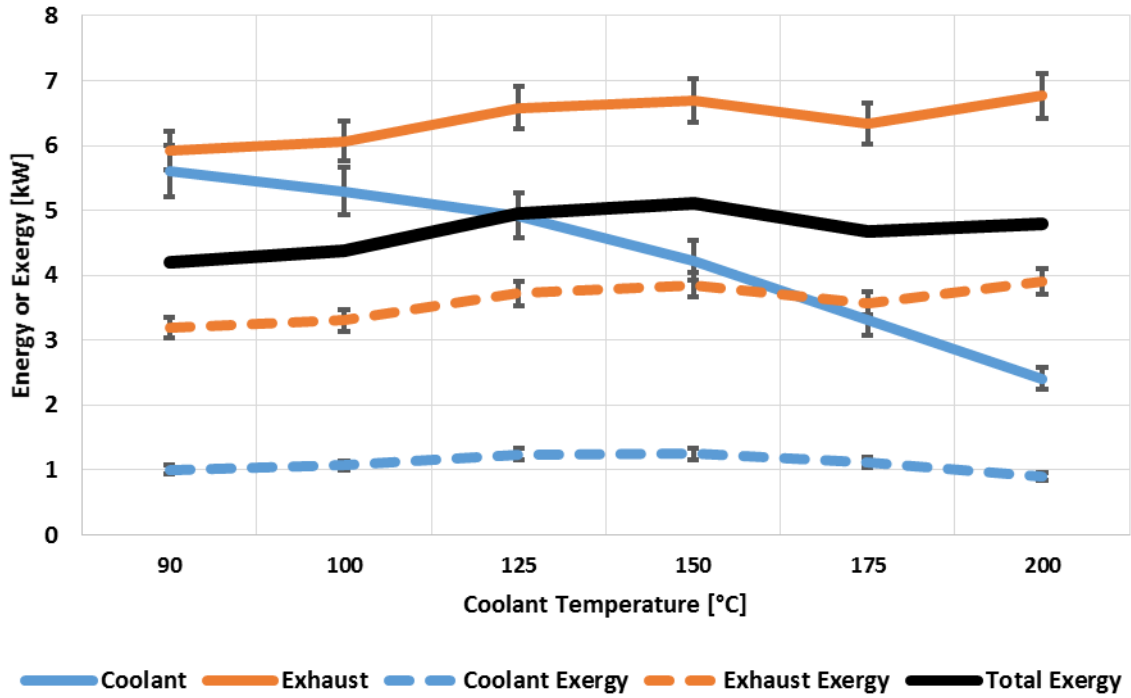


Figure 6-3. Waste heat from engine coolant and exhaust with the corresponding exergy for each source at 3100 rpm and 18 N-m of torque (top), and 3100 rpm and 24 N-m of torque (bottom).

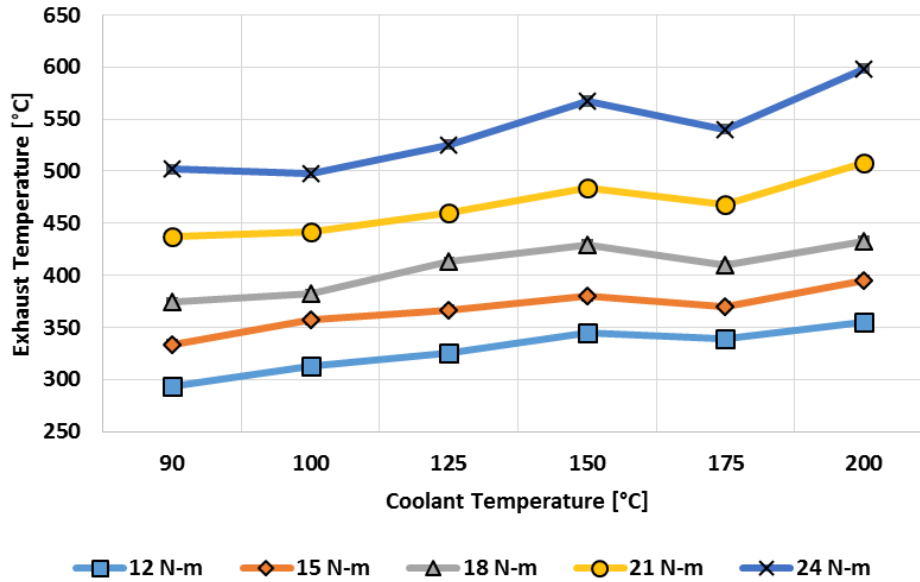


Figure 6-4. Exhaust temperatures for five load points over the measured coolant temperature range at an engine speed of 3100 rpm.

kW over the same interval, with exhaust exergy increasing from 5.20 ± 0.17 kW to 5.49 ± 0.20 kW. The total exergy rises from 6.48 ± 0.19 kW to 8.47 ± 0.27 kW, for a 31% increase. It should also be noted that the exergy of the engine oil also increases over the measured coolant temperature range. However, the availability of the engine oil heat remains very low (< 0.7 kW) due to the low engine oil temperature ($\sim 75^\circ\text{C}$), and, therefore, does not have a significant impact on the total waste heat exergy.

The exergy analysis was also affected by the increase in combustion chamber leakage seen at 175°C . There is a noticeable drop in the total waste heat exergy when the coolant temperature increases from 150°C to 175°C , which corresponded to the increase in measured engine efficiency explained previously. When the coolant temperature increases to 200°C , the total exergy continues an upward trend as exhaust waste heat rises. The increased leakage of HTF into the combustion chamber at 175°C affects both exhaust and coolant waste heat. The combination of diesel fuel and HTF may burn cooler than diesel fuel alone, lowering the exhaust temperature. Lower combustion

temperatures might also decrease heat transfer to the cylinder wall resulting in lower heat rejection to the engine coolant. The next section will cover the engine efficiency and emissions results.

6.2 Engine Efficiency and Emissions

Engine brake efficiency is the power output divided by the fuel energy entering the engine (based on the lower heating value – LHV – of 43.2 MJ kg^{-1}), and is a measure of how efficiently the engine converts the chemical energy in the fuel into usable work. The results of the brake efficiency measurements, including uncertainties, are shown in Figure 6-5 for all loads and temperatures at 3100 rpm. As previously discussed, oil and HTF leaking into the combustion chamber in varying degrees over the course of testing had a noticeable effect on brake efficiency. In fact, the brake efficiency trends shown in Figure 6-2 track so well with the leakage rates that it could be argued that any changes in efficiency were due solely to this issue. However, other possible effects and expected trends will be discussed in this section.

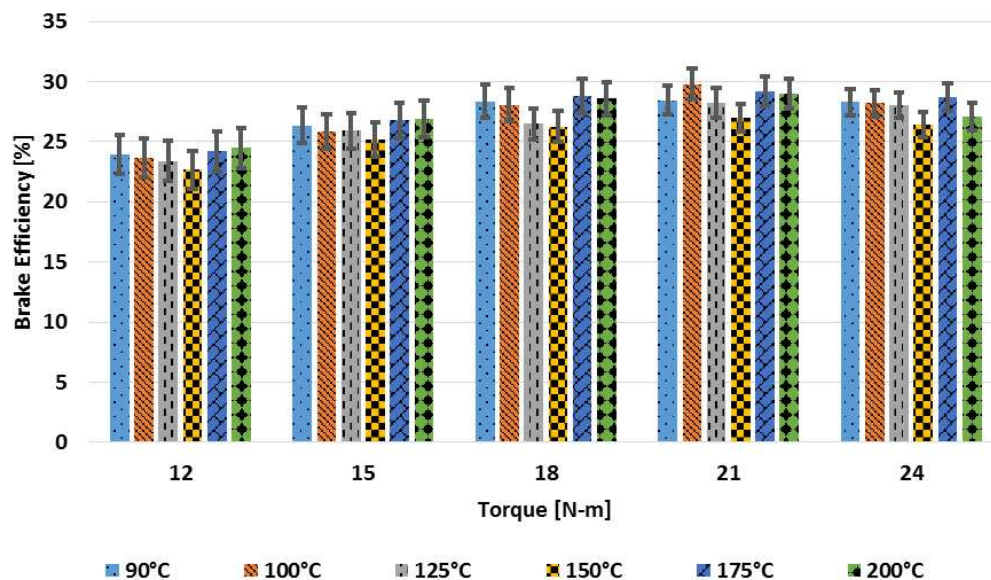


Figure 6-5. Engine efficiency for 3100 rpm at five load points over the measured coolant temperature range.

Considering only the data points between 90°C and 150°C, the negative correlation between engine efficiency and engine temperature is medium or strong for all loads and speeds, with 12 N-m through 18 N-m being statistically significant at the 95% confidence level for 3100 rpm (Figure 4-1). For example, at 18 N-m, the brake efficiency decreased from $28.50 \pm 1.38\%$ at 90°C to $26.42 \pm 1.27\%$ at 150°C (7.3% relative decline). The *p*-value for the correlation at the 24 N-m torque point was 0.052, which shows that the confidence interval of 95% was nearly met. The *p*-value at 21 N-m was 0.106 (89.4% probability of correlation). Therefore, additional data for this range of coolant temperatures is recommended to establish correlation at these two higher torques.

When the coolant temperature increases, elevated combustion chamber temperatures lead to a shorter ignition delay, smaller premixed burn, and longer diffusion combustion [36, 59, 60]. This effectively lengthens the duration of heat release to the point where some heat release occurs too late in the cycle to provide additional work, which results in a decrease in brake efficiency [36]. Prior work suggests that lost efficiency due to increased combustion chamber temperatures may be gained back with a more modern fuel injection system and additional tuning. The reduction in engine efficiency might be minimized by adjusting the injection timing to start injection earlier in the cycle to provide additional time for combustion to complete [61]. The delay in heat release also means more heat will be lost to the exhaust gases (Figure 6-3). Additionally, the temperature difference between the chamber wall and the flame is smaller at higher engine coolant temperatures, reducing the in-cylinder heat transfer, which would also contribute to the rise in exhaust waste heat.

An additional effect that may contribute to a decrease in engine efficiency is the increased losses to the ambient air from the engine block (part of ‘other losses’). As the engine surface

temperature increases, the losses due to convection and radiation from the engine structure increase. For example, at 18 N-m and 3100 RPM (Figure 6-1) other losses increase from $6.11 \pm 2.79\%$ to $14.12 \pm 2.44\%$ of the fuel energy as the coolant temperature increased from 90°C to 150°C . However, this effect was found to be statistically significant only at 12 N-m and 18 N-m engine loads. The ‘other losses’ category was also effected by the head gasket leakage that increased significantly at the 175°C coolant temperature (Figure 6-1). There is a negative correlation between other losses and the HTF leakage rates, with the other losses decreasing when the leakage increased at 175°C . However, the other losses were not directly measured, but rather derived by subtracting all measured energy flow exiting the engine from the measured fuel energy input. Therefore, the introduction of unmetered fuel into the combustion chamber resulted in both the fuel input and the other losses being underestimated. If the unmetered fuel had been measured, it is unlikely that the other losses would have been found to decrease. It should also be noted that the other losses category has a large uncertainty compared to the fractions for coolant heat and other directly measured values. The relative uncertainty for the other losses ranged from 13.41% to 52.42% and, therefore, observed changes in the other losses category could be a result of measurement uncertainty instead of actual changes in the engine operation.

During the tests, the following exhaust emissions were monitored: THC, O_2 , CO, CO_2 , and NO_x . The exhaust gas compositions were measured using a 5-gas analyzer, and representative results vs. coolant temperature are shown in Figure 6-6 (3100 rpm and 18 N-m). THC were 60-75 ppm for coolant temperatures between 90°C and 150°C . THC emissions increased at higher temperatures, reaching a maximum of 132.7 ppm at 200°C . THC concentration did increase between the 150°C and 175°C coolant temperature tests, though the concentration only partially follows the rate of leakage of HTF into the combustion chamber through the entire range of tests.

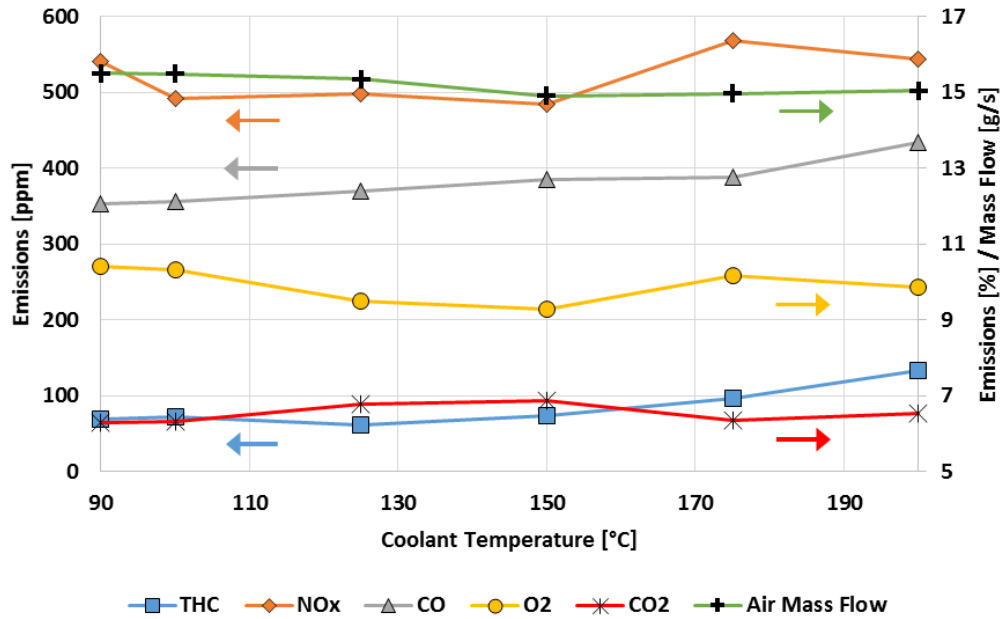


Figure 6-6. Exhaust emissions data with mass air flow rate at 3100 rpm and 18 N-m of torque.

Comparing Figure 6-2 and Figure 6-6 reveals a negative correlation between leakage rates and CO and CO₂ emissions. A decrease in CO and CO₂ from the addition of engine oil and HTF into the combustion chamber could be a result of the reduced ratio of carbon atoms to hydrogen atoms in the HTF fluid molecule, which is based on polyalkylene glycol [39, 62]. The lower ratio of carbon to hydrogen would produce less CO and CO₂ for the same energy release as diesel fuel.

THC represents the unburned diesel fuel present in the exhaust due to incomplete combustion, fuel trapped in crevices in the combustion chamber, and other potential sources such as quenching [36]. The 5-gas analyzer used to measure the THC concentration in the exhaust was calibrated for methane, which only has a single carbon atom per molecule. Using this equation, the experimental results show that energy loss from uncombusted diesel fuel is minimal and cannot be responsible for the loss in efficiency. These results show that only 0.11% to 0.21% of the fuel energy was accounted for by raw fuel present in the exhaust gases, and the increase in THC with higher coolant temperatures had little effect on the energy balance. For example, at 18 N-m and

3100 rpm, the THC energy loss increased from 0.022 kW at 90°C to 0.041 kW at 200°C. These losses are very small compared to the fuel input power of nearly 20 kW.

The emission of oxides of nitrogen is tightly regulated and must be considered when conditions for combustion are altered. NO_x production in combustion is known to be highly temperature dependent, with higher combustion temperatures generally leading to higher levels of NO_x emissions [36]. This is known as thermal NO_x production and is typically the primary production path. However, a significant increase in NO_x emissions was not seen until the coolant temperature was raised from 150°C to 175°C, with NO_x increasing from 485 ppm to 568 ppm at 18 N-m and 3100 rpm. If raised combustion chamber temperatures were the cause of the increased NO_x at 175°C, exhaust gas temperatures would also be elevated. However, the opposite effect was observed, with the average exhaust temperature decreasing from 429.22°C to 409.17°C for the 18 N-m case. This suggests that combustion temperatures did not increase in this interval. The increase in NO_x at 175°C could be explained by the presence of nitrogen in the molecular makeup of the HTF that was found to be leaking into the combustion chamber. This bound nitrogen is known as fuel nitrogen and creates an additional pathway for the formation of NO_x during combustion [63]. The Duratherm G HTF is a proprietary formula with multiple additives, so it is unknown if it does indeed contain bound nitrogen. The decrease in exhaust temperatures at 175°C may have multiple sources. The O₂ emissions increased significantly from 150°C to 175°C, rather than decreasing linearly with rising coolant temperatures and decreased intake air density. This suggests a leaner air-fuel ratio which would reduce combustion and exhaust temperatures for a diesel engine [63]. The large increase in leakage of HTF into the combustion chambers occurs at the same interval, and is likely responsible for the changes in O₂ emissions throughout testing. This can be explained by the presence of oxygen in the chemical structure of the HTF's

polyalkylene glycol base [39, 64]. Additionally, because the HTF leaking into the combustion chamber was under relatively low pressure (~70 kPa), the HTF did not atomize and, upon disassembly, was found to have coated the top of the combustion chamber. The evaporation of this coating of liquid in the combustion chamber would also serve to lower combustion chamber temperatures resulting in a reduction in exhaust temperatures.

The experiment was unable to determine the exact effect of coolant temperature on engine efficiency because of a loss of head gasket seal during testing. The changes in brake efficiency due to the unmetered fuel (engine oil and HTF) masked any direct effects from higher combustion chamber temperatures. The head gasket failure also affected the exhaust emissions, with O₂ and NO_x increasing as the leakage increased. The increased temperature of the intake air caused the air flow rate to decrease as the engine temperature rose. However, the additional oxygen provided by the HTF prevented O₂ levels from dropping at higher temperatures. The next section will describe the methods used to monitor the engine condition during testing to pinpoint problem areas during high temperature engine operation.

6.3 Engine Condition Monitoring

Engines are designed to run over a standard range of operating temperatures, usually with a maximum coolant temperature of approximately 90°C. Because the engine in the current study was operated at considerably higher temperatures, engine wear was monitored closely during testing. Prior to testing, the engine was disassembled and carefully inspected. All key components and clearances were found to be within manufacturer specifications, and photos were taken to document the initial engine condition. The engine was torn down again after all testing was completed and the condition was again evaluated for comparison with the baseline. However,

cylinder compression and oil particulate concentration were monitored throughout the experiment as a proxy for engine wear.

To monitor the condition of the engine during testing, the cylinder compression was checked between each coolant temperature interval with the engine at room temperature. The compression test results are shown in Figure 6-7 for each cylinder. The tests were performed with the engine cold because the first test was done before the engine had been run and consistency was desired. The cold tests may partially explain why the compression pressure was found to be below the manufacturer specification of 3.0 MPa with a warm engine. The larger piston ring end gaps could also have contributed to a slightly lower compression pressure than expected. The initial compression test produced nearly equal measurements for the three cylinders with an average of 2.60 MPa and a maximum difference of 1.66%. Peak compression occurred after the 90°C tests with an average of 2.73 MPa. Compression then declined to a minimum average of 2.50 MPa after the 125°C tests, which also corresponded to the maximum variation among the 3 cylinders (19.50%). The decline in compression was most likely due to sealing issues with the head gasket and piston rings. The custom copper head gasket proved to be difficult to seal sufficiently to prevent coolant and oil leakage external to the engine as well as into the combustion chamber. Conversely, this leakage path could allow combustion chamber gases to escape into the oil and cooling system and thereby reducing engine compression. Multiple gaskets and sealing methods were attempted before a combination that was thought to be adequate was found. Some external seepage of the oil and coolant was still observed throughout the tests, and the cylinder head bolts were re-torqued after each temperature run to try to maintain cylinder integrity. The compression test results in Figure 6-7 show that average compression improved after the 125°C tests, which does not agree with the increase in leakage into the combustion chamber that occurred after the

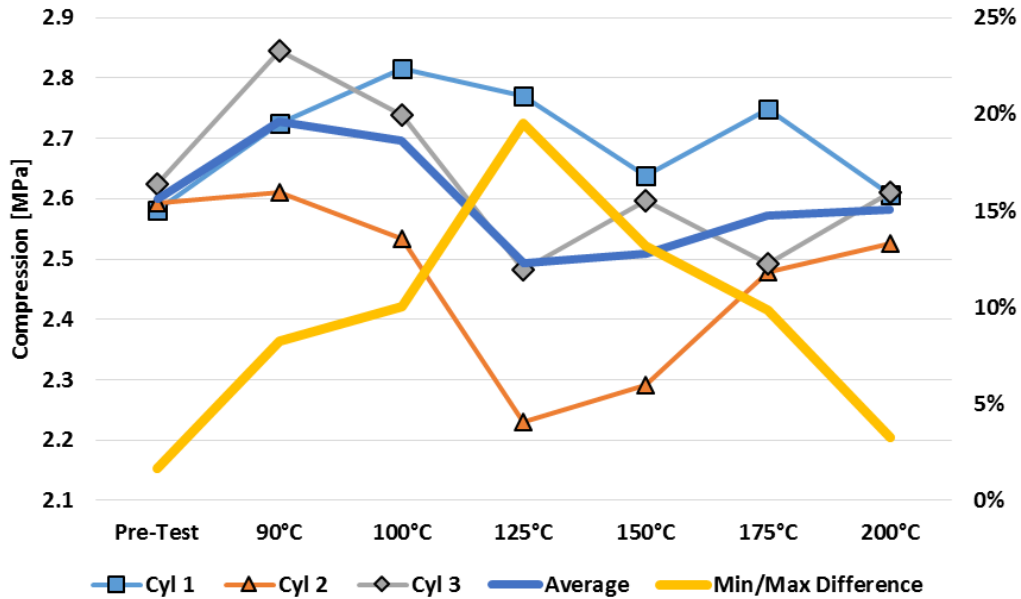


Figure 6-7. Cylinder compression test results over the course of testing. Compression tests were performed with the engine cold after completion of testing for the given temperature.

150°C tests. One possible explanation is that the engine compression was done on a cold engine, and the integrity of the head gasket seal may have changed at operating temperatures due to cylinder heat expansion and warpage. Alternatively, this improvement after the 125°C test may suggest that leaking piston rings are the more likely culprit. The piston ring condition will be discussed further later in this section.

After the engine teardown, visual inspection of the head gasket and sealing surfaces on the engine block and cylinder head revealed obvious leakage paths. Figure 6-8 shows the engine block surface photographed after testing. The image identifies the coolant passages that connect the cooling system from the cylinder head to the engine block. Stains left on the block surface indicated by the arrows indicate leakage from the cooling passages to the combustion chambers. A similar pattern is seen on the copper head gasket (Figure 6-9) where it mated with the block at the shown location. The single pressurized oil passage through the head gasket is shown in Figure

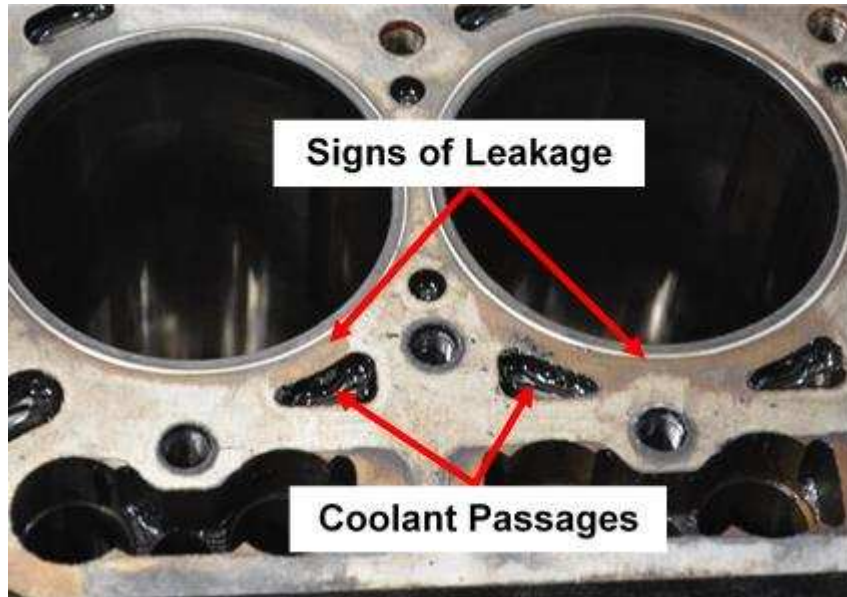


Figure 6-8. Image of engine block to head gasket mating surface with coolant passages and signs of leakage noted.

6-10. However, unlike the stains from the coolant leakage, the blackened trail from the oil passage appears to lead to the outside edge of the gasket instead of inward towards the cylinder bore. This evidence suggests that the fluid leaking into the combustion chamber was primarily HTF. Upon further inspection, evidence pointed to uneven leakage between the three cylinders. Images of the cylinder head surface creating the top of the combustion chamber for each cylinder show a large variation in HTF residue present on surfaces (Figure 6-11). Cylinder 2 appears to have suffered the most severe leak, with a thick liquid film covering the entirety of the combustion chamber. The cylinder 1 combustion chamber also appears wet, but only has thin layers of fluid covering a fraction of the surface. Finally, the cylinder 3 combustion chamber appears relatively dry, suggesting minimal leakage of HTF into the combustion chamber.

In addition to cylinder compression, the concentration of metal particulates present in the engine oil was monitored after each set of tests at a given coolant temperature. The results of the oil analysis are shown in Figure 6-12. Because the duration of each set of tests was different, the

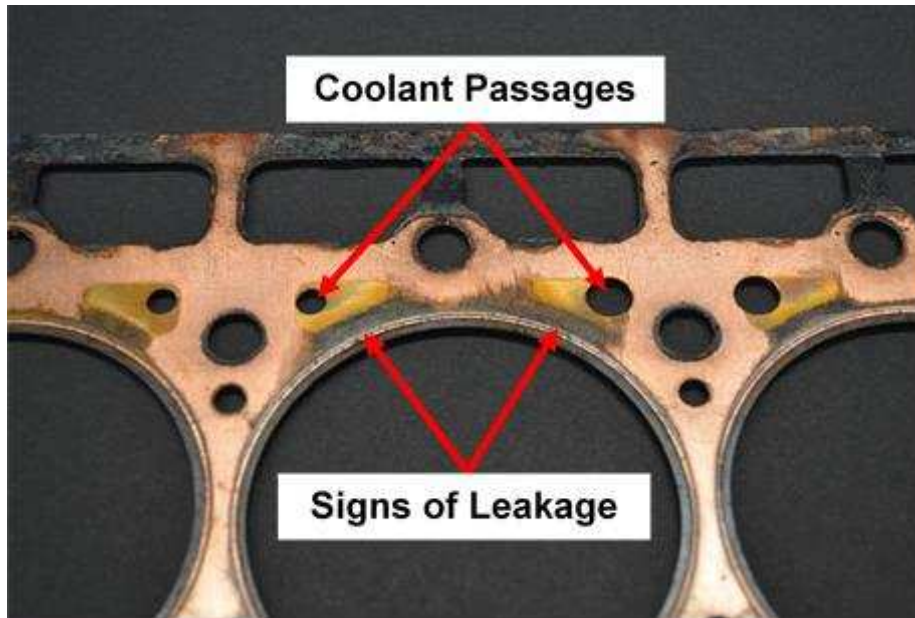


Figure 6-9. Image of copper head gasket after testing was completed. Arrows indicate coolant passages and discoloration from HTF leaking into combustion chamber.

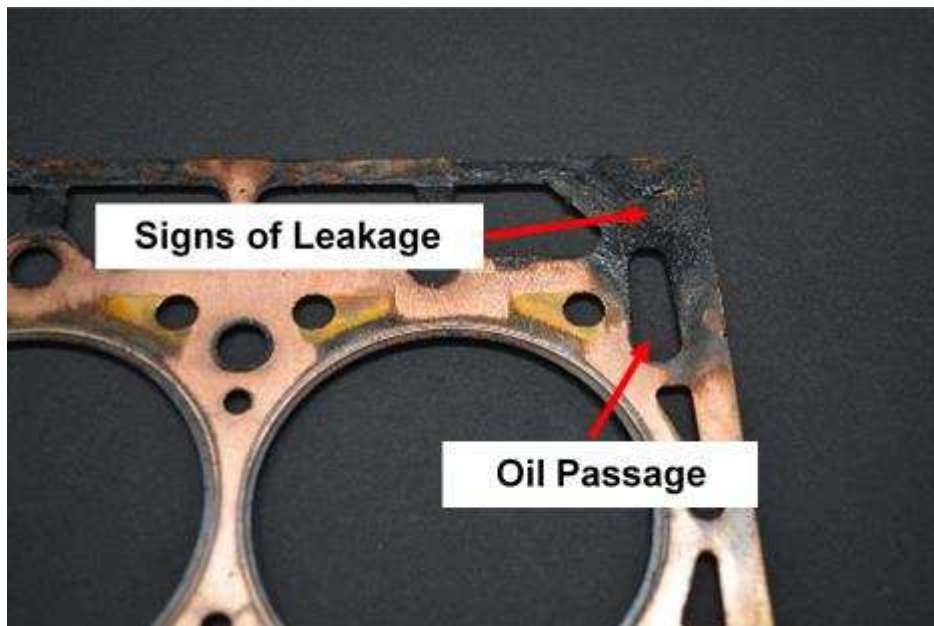


Figure 6-10. Image of copper cylinder head gasket showing pressurized oil passage and external leakage path.



Figure 6-11. Cylinder head surface above the combustion chamber for each of the three cylinders. The liquid present on the combustion chamber surfaces suggests HTF leakage was most severe in cylinder 2 and negligible in cylinder 3.

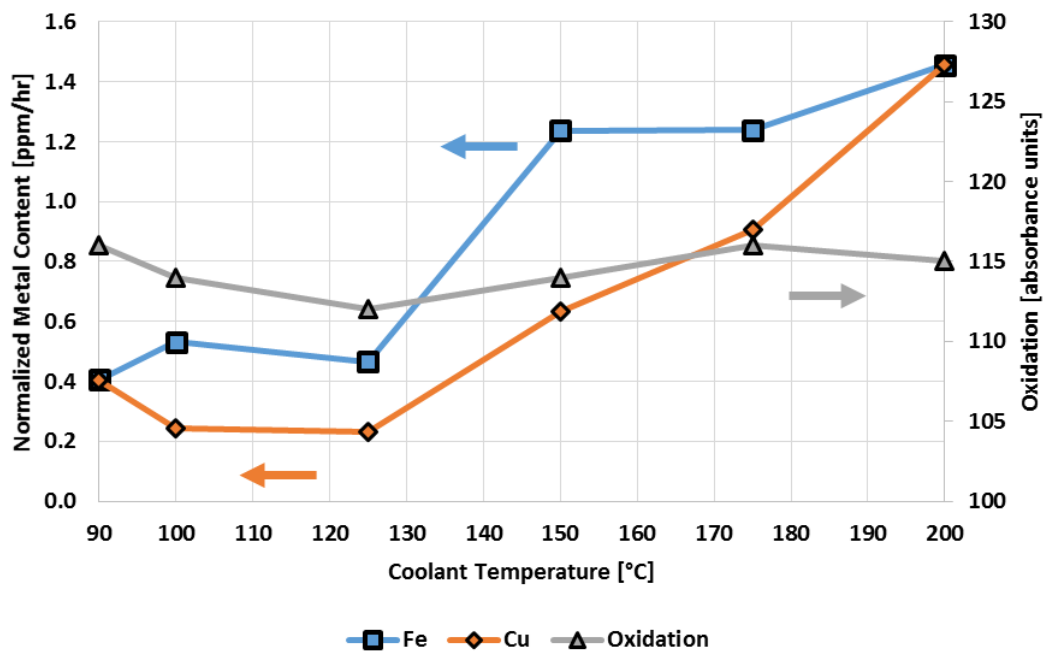


Figure 6-12. Oil analysis results including metal content in parts per million per hour and oxidation in spectral absorbance units.

metal content was normalized by the number of hours the engine operated at each temperature. The concentration of metals present in used engine oil signals wear of bearings or other internal engine components. The contamination rate for copper and iron was nominally 0.20 ppm hr⁻¹ and 0.45 ppm hr⁻¹ between 90°C and 125°C engine coolant temperature, respectively. Particulate values increased to 0.63 ppm hr⁻¹ and 1.24 ppm hr⁻¹ for copper and iron, respectively, at 150°C, and they both increased to 1.45 ppm hr⁻¹ at 200°C. This is an increase of over 200% for iron and over 500% for copper, which suggests that internal engine component wear accelerated significantly above 125°C. Figure 6-12 also shows the oxidation level of the engine oil, which is a good indicator of the level of degradation of the oil [65]. Oxidation can occur rapidly under high temperature operation, but Figure 6-12 demonstrates that oxidation levels remained essentially flat during testing. The minimal oxidation is likely due to the low average engine oil temperatures maintained, as well as the relatively small quantity of oil being exposed to extreme temperatures near the combustion chamber.

Measurements of the key component dimensions and clearances were repeated once the engine was disassembled after testing, and minimal changes were found for most the components. See Table C-1 in Appendix C for a complete list of measurements performed and the results before and after testing. The minimal changes were most likely due to the short overall run time of the tests. However, signs of internal engine component wear were evident in a few specific areas. The most obvious damage was found at the pistons (Figure 6-13). The scuffing of the aluminum alloy piston skirts shown in the bottom of Figure 6-13 could have been caused by overexpansion of the pistons due to high piston temperatures, as well as a lack of sufficient oil film thickness from excessive local oil temperatures. Additional evidence of contact between the pistons and the cylinder walls can be seen in the images of the cylinder bore surface after testing (Figure 6-14).

The damage was primarily seen on the thrust side of the piston and cylinder wall. The thrust side of the piston is the side that is loaded against the cylinder wall during expansion due to the angle of the connecting rod. If the piston expanded to the point where it was always contacting the cylinder wall, it is likely that both sides of the piston would show evidence of significant contact. Therefore, the damage to the piston and cylinder walls suggests that lack of proper lubrication was primarily at fault. Further problems were found with carbon deposits on the ring land areas due to the breakdown of the engine oil. These deposits are evident in the lower images of Figure 6-13, where a black coating is seen near the top of the pistons. The second compression rings were completely frozen in the ring grooves on cylinders 2 and 3, and the remaining compression rings on these cylinders were close to being immobilized as well. As mentioned previously, this



Figure 6-13. Documentation of piston condition showing piston from cylinder 1 before (top) and after (bottom) testing.

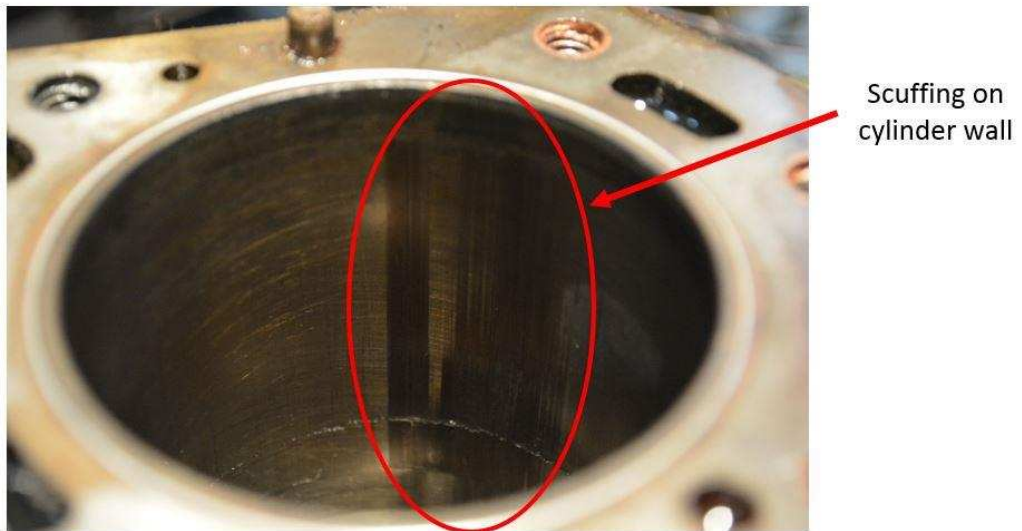


Figure 6-14. Example of scuffing of cylinder surface on thrust side of cylinder 1 bore.

condition could have contributed to the changes in compression seen over the testing period. A piston ring stuck in its groove will not expand out against the cylinder wall properly and could result in combustion gases leaking past the rings into the crankcase and excessive engine oil travelling past the rings into the combustion chamber. It is also possible that the rings may have been stuck at some times and released at others, which might explain the fluctuations in measured engine compression. Referring to Figure 6-7, the cylinders with stuck rings (cylinders 2 and 3) were also seen to have lower compression through much of the testing period.

Lubrication issues were also discovered upon removal of the pistons from the connecting rods. The pistons attach to the small ends of the connecting rods with a steel pin (Figure 6-15b). The pin is a slip fit in both the piston and rod end and is secured using two snap rings. The pin rides in a brass bushing pressed into the small end of the rod (Figure 6-15c). At disassembly, two out of the three piston pins were found to be frozen in the rod bushing and had to be pressed out to separate the pistons from the rods. The piston pins were free to rotate in the piston pin bores so that the pistons could still swivel atop the connecting rods and no further damage was caused. This



Figure 6-15. Photos of a) piston pin bore, b) piston pin, c) connecting rod pin bushing before testing, and d) connecting rod pin bushing after testing.

was despite the dark deposits seen in Figure 6-15a, caused by overheated engine oil. Similar deposits were found on the piston pin (6-15b), and on the surface of the piston pin bushing at the small end of the connecting rod (Figure 6-15d). Though no catastrophic failure occurred from the breakdown of the engine oil at the piston pin, further run time may have seen the pins seize inside the piston pin bores as well which would have led to increased contact between the pistons and the cylinder walls and further damage.

The final area where lubrication appeared to be problematic is at the lifters for the valve train. The Daihatsu diesel engine uses a cam-in-block design where solid lifters ride on the camshaft lobes and actuate the valves via pushrods and rocker arms. The lifters sit in the block directly adjacent to the top of the combustion chambers with the exhaust ports passing overhead. Therefore, the temperatures in this area are expected to be on par with the engine coolant

temperature. The inspection of the lifters after testing agrees with this prediction. Figure 6-16 shows the lifter for the cylinder 2 exhaust valve before (image a) and after testing (image b), with the latter displaying discoloration from the overheated engine oil. Signs of scuffing are evident on the lower half of the lifter on both sides as well. The lifters were still moving freely in their bores upon disassembly, but over time significant wear and seizing may have occurred. Additional signs of improper lubrication were found at the camshaft lobes themselves (Figure 6-17). With no roller element to reduce friction at the interface between the camshaft and lifter, the sliding contact

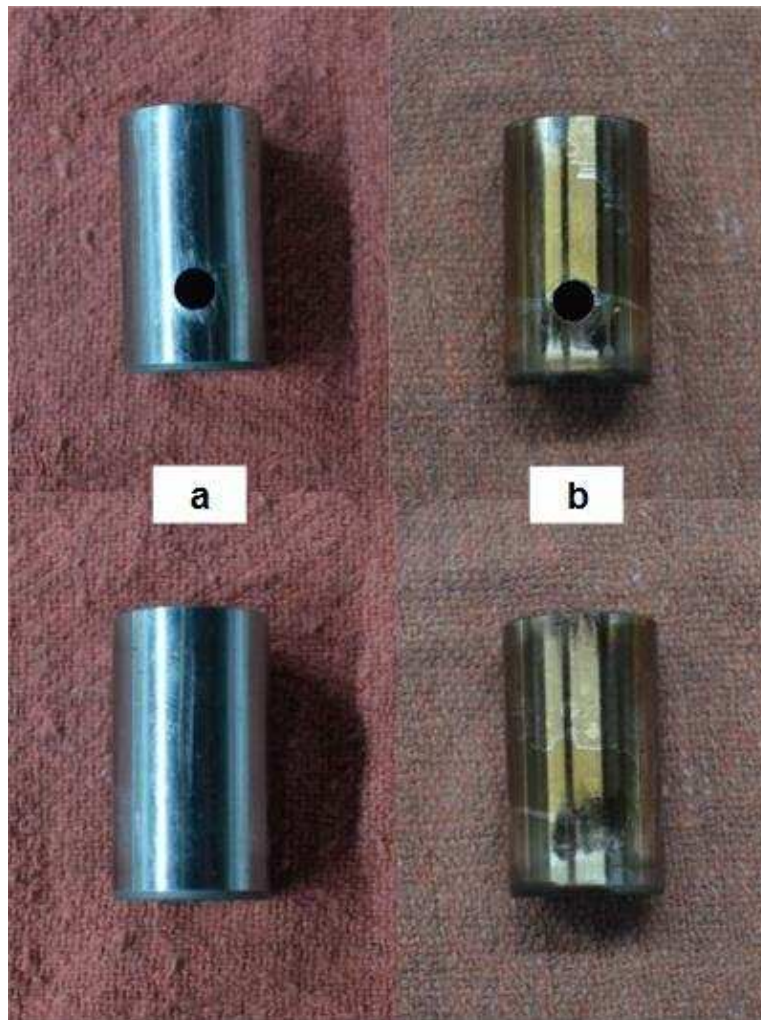


Figure 6-16. Photos cylinder 2 exhaust valve lifter, a) before testing and b) after testing.



Figure 6-17. Photos of camshaft before (a) and after (b) testing with arrow indicating slight wear from insufficient lubrication at sliding contact between lobe and lifter.

requires adequate lubrication to prevent wear of the camshaft lobe over time. No significant wear to the lobes was found after testing, but the arrow in Figure 6-17 indicates polished areas on the lobes indicating metal-on-metal contact. If the engine run time had been significantly longer, cam lobe wear might have affected valve lift profiles and engine operation. The next section will cover the results of the thermodynamic and heat exchanger modeling.

6.4 Modeling Results

The experimental results were used as the basis for the thermodynamic modeling and individual heat exchanger modeling described in Chapter 5. The purpose for the modeling effort was to estimate the theoretical WHR system output and the resulting combined efficiency of the engine and WHR system. Additionally, the individual heat exchanger models were used to

estimate the required footprint for the WHR system for each coolant temperature. As previously discussed, modeling was performed for an engine speed of 3100 rpm and torque of 24 N-m at coolant temperatures of 90°C, 150°C, 175°C, and 200°C. Each system was modeled with a condenser temperature of 60°C and 90°C for comparison.

6.4.1 Thermodynamic Modeling Results

Figures 6-18 through 6-33 show the results of the thermodynamic analysis for the four coolant temperatures and two condenser temperatures that were modeled. The efficiency gain for the eight systems is summarized in Table 6-1. For each model, a figure shows the system diagram detailing the results of the analysis including temperatures, flow rates, and power in and out of the system. The results shown in these eight figures were the basis for the individual heat exchanger models that will be described in the next section. In addition to the system diagram, a T-s diagram is included for each model to provide a visual representation of each cycle along with the temperature drop of the exhaust as the working fluid is heated in the superheater and the exhaust evaporator. The remainder of this section will be devoted to describing the results of the analysis for each of the eight systems.

The first system modeled was the state-of-the-art system with 90°C engine coolant and a 60°C condenser temperature (Figure 6-18). Starting at the bottom of the diagram, the ethanol leaves the condenser at 60°C with a quality of exactly zero and a mass flow rate of 5.06 g s⁻¹. The liquid ethanol is then pressurized by the pump, which uses 0.04 kW of power and raises the ethanol temperature to 62.0°C. The ethanol then passes through the recuperator, where it is heated to 153.7°C by the hot ethanol from the turbine outlet. Inside the exhaust evaporator, the ethanol is heated up to the 200°C saturation temperature where it is subsequently boiled so that the ethanol leaves the evaporator with a quality of unity. The evaporation of the ethanol can also be seen in

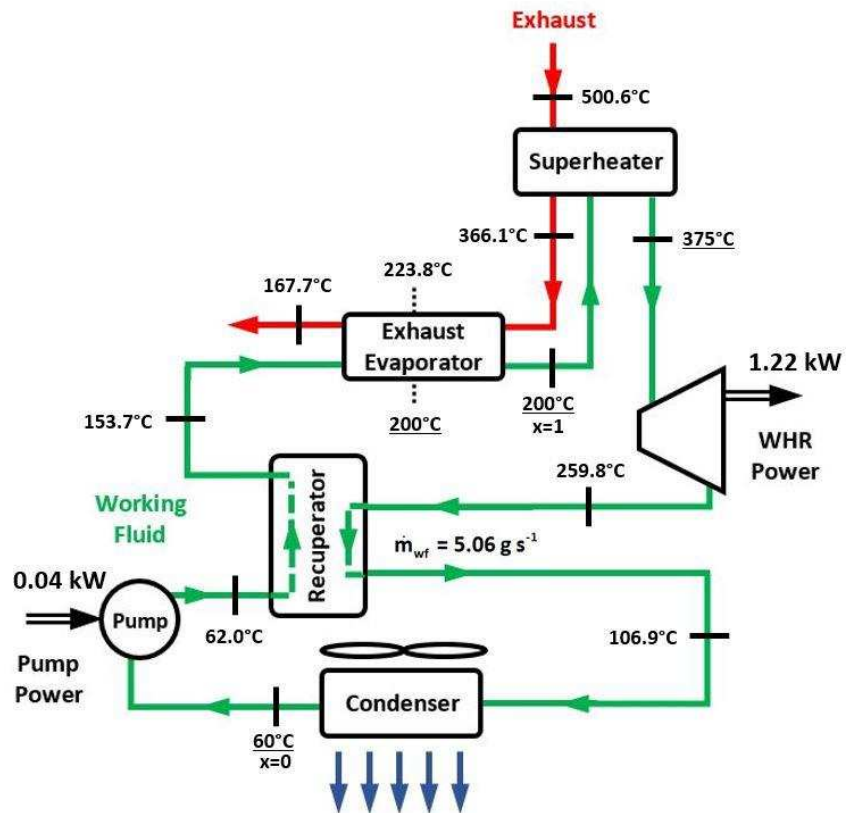


Figure 6-18. WHR system diagram for 90°C coolant and 60°C condenser temperature with results from the thermodynamic analysis. Note that underlined temperatures are predetermined values entered into the model as constants.

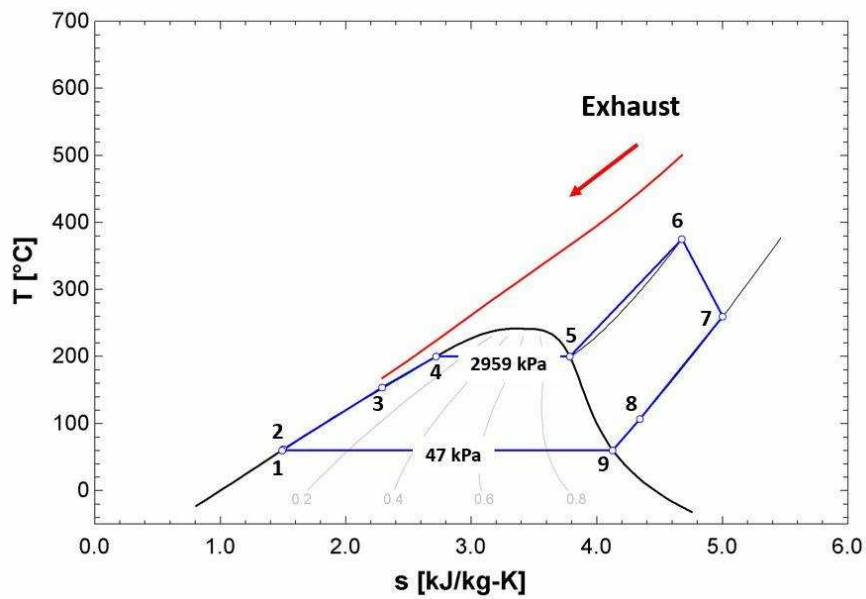


Figure 6-19. T-s diagram for 90°C coolant and 60°C condenser temperature WHR system. The exhaust temperature is shown in red and the working fluid shown in blue.

the T-s diagram (Figure 6-19), where the blue line becomes horizontal under the vapor dome at 2,959 kPa pressure. The ethanol then travels through the superheater where the temperature of the ethanol vapors is raised to 375°C before it enters the turbine expander. Through the heating of the working fluid in the superheater and the evaporator, the exhaust temperature drops from 500.6°C to 167.7°C. This can also be seen in Figure 6-19, where the exhaust temperature is represented by the red line above the cycle. The temperature of the ethanol drops from 375°C to 259.8°C across the turbine as 1.22 kW of power is produced. Subtracting the 0.04 kW required to power the pump, a net power output of 1.18 kW is attained. Combining this output with the engine output of 7.70 kW, and dividing by the fuel power input of 27.06 kW yields a combined efficiency of 32.83%. Comparing this value to the baseline efficiency of 28.47% gives a relative efficiency increase of 15.3%. Through the hot side of the recuperator, the ethanol temperature drops to 106.9°C as heat is transferred back to the beginning of the system to increase efficiency. Finally, the condenser cools the ethanol down to the saturation temperature of 60°C and the ethanol is condensed back to the liquid state.

The second WHR system is identical to the first, except for an increase in condenser temperature from 60°C to 90°C (Figure 6-20). Visual inspection of the two T-s diagrams in Figures 6-19 and 6-21 shows the reduction in system output indicated by the decreased area encompassed by the cycle. This reduction in area is due to the increase in condenser temperature and subsequent increase in condenser saturation pressure from 46.77 kPa to 157.60 kPa. This increase in low side pressure reduces the pressure difference across the turbine, resulting in lower output. The effect can be seen in Figure 6-20, where the net WHR output for the 90°C coolant temperature drops from 1.18 kW to 0.90 kW. The WHR output is added to the measured engine power output of 7.70 kW to reach a total power output of 8.60 kW. The 90°C condenser temperature system output

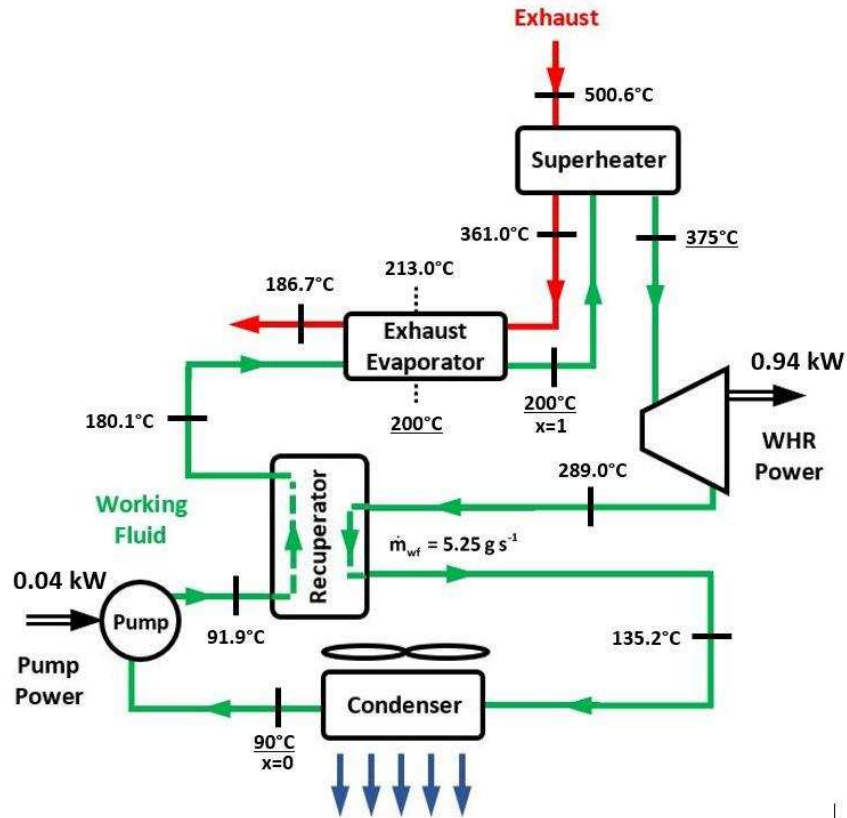


Figure 6-20. WHR system diagram for 90°C coolant and 90°C condenser temperature with results from the thermodynamic analysis.

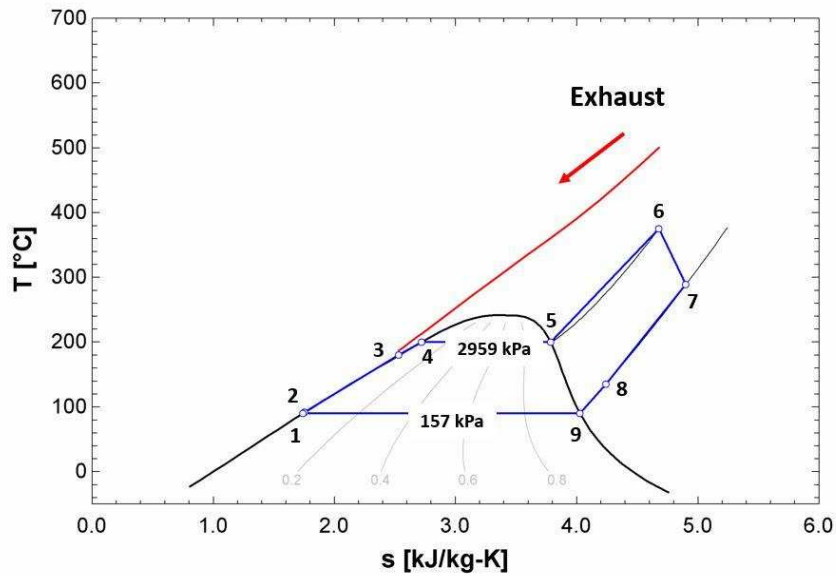


Figure 6-21. T-s diagram for 90°C coolant and 90°C condenser temperature WHR system. The exhaust temperature is shown in red and the working fluid shown in blue.

results in a total efficiency of 31.80% and a relative efficiency increase of 11.7%, which is down 24% over the same system with a 60°C condenser temperature.

The system diagram for the 150°C coolant temperature and 60°C condenser temperature model is shown in Figure 6-22. As previously mentioned, the high-temperature systems have a split path for the ethanol to travel, with one leg running through the engine as coolant and one leg running through the exhaust evaporator (same as the 90°C coolant temperature systems). The ethanol mass flow rates through the two legs are not equal and the model solves for the split depending on the given constraints. For the 150°C system, the mass flow rate through the engine block is 8.25 g s^{-1} and the mass flow rate through the exhaust evaporator is 4.39 g s^{-1} . With the additional heat source of the engine block, the total mass flow rate rises to 12.64 g s^{-1} , which is over twice the flow rate of the 90°C coolant temperature system. The net WHR system power output of 2.00 kW is added to the measured engine output of 7.65 kW for a combined total power output of 9.65 kW. Using the measured fuel energy flow of 28.80 kW results in a combined efficiency of 35.64%. Comparing this value to the baseline efficiency of 28.47% yields a relative efficiency gain of 25.20%. The T-s diagram in Figure 6-23 shows a decrease in encompassed area of the cycle compared to the 90°C coolant temperature case at the same condenser temperature. This is partly the result of reducing the evaporator temperature from 200°C to the 150°C coolant temperature, with the subsequent reduction in high-side pressure from 2,959.00 kPa to 981.60 kPa. Additionally, the superheat temperature had to be reduced from 375°C to 290°C to keep the exhaust temperature at the outlet of the exhaust evaporator at least 5°C above the ethanol inlet temperature. However, the 150°C system still makes considerably more power due to the increase in mass flow rate, which takes advantage of the additional heat supplied by the engine structure. The modeling results for the 150°C coolant temperature system with a 90°C condenser temperature

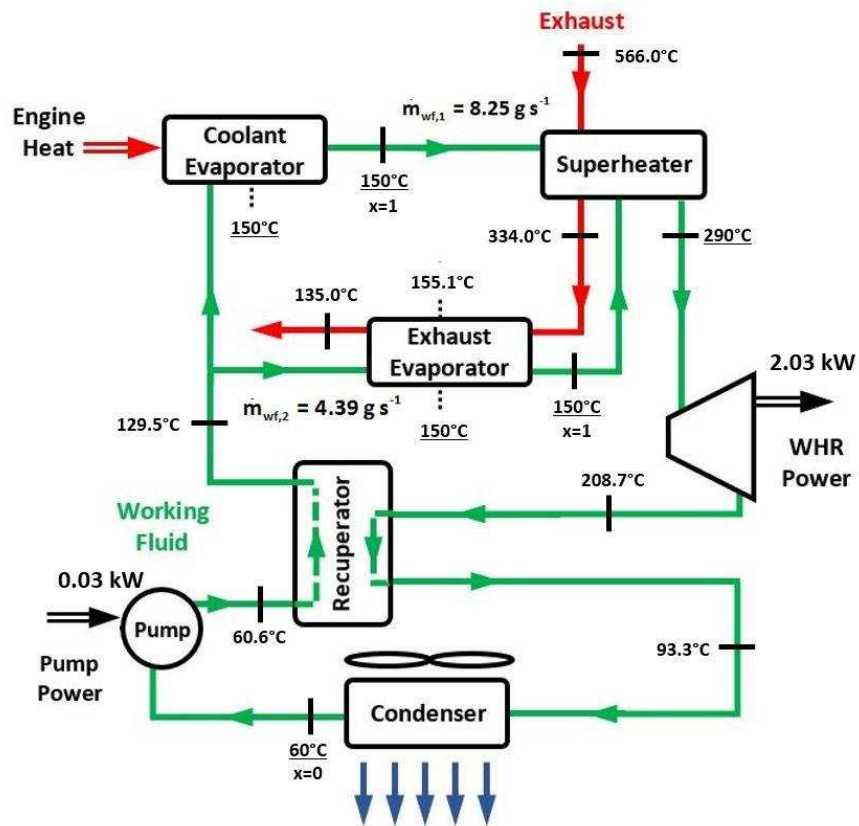


Figure 6-22. WHR system diagram for 150°C coolant and 60°C condenser temperature with results from the thermodynamic analysis.

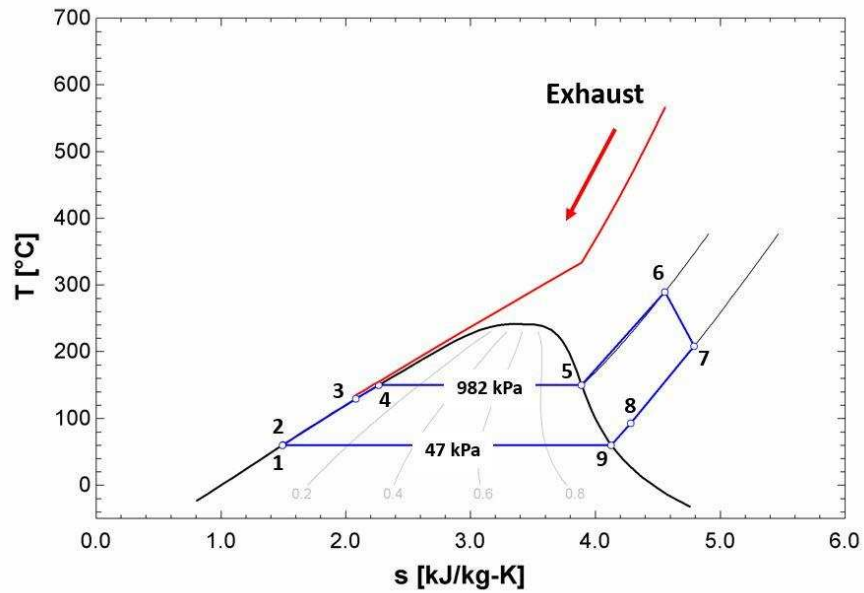


Figure 6-23. T-s diagram for 150°C coolant and 60°C condenser temperature WHR system. The exhaust temperature is shown in red and the working fluid shown in blue.

are outlined in Figure 6-24. The major difference over the 60°C model other than the increase in condenser temperature, was the reduction of the superheat temperature from 290°C to 240°C. As before, this value was reduced to keep the exhaust temperature at the exhaust evaporator outlet above the ethanol inlet temperature by at least 5°C. The T-s diagram shown in Figure 6-25 illustrates the decrease in cycle area due to the increased condenser temperature and pressure, as well as the reduction in superheat temperature. The resulting net power output for the 90°C condenser temperature model was 1.27 kW, or a total of 8.92 kW. This translates to a total efficiency of 32.94%, or an 15.71% relative efficiency increase over the baseline case.

The 175°C WHR system diagram with the 60°C condenser temperature is shown in Figure 6-26. The increase in evaporation temperature to 175°C results in decreased ethanol mass flow through the engine since the heat rejection to the coolant is a fixed value, and the temperature increase before boiling is greater than the system with 150°C coolant temperature. However, the superheat temperature was increased to 350°C to better utilize the exhaust waste heat available. This can be seen in the T-s diagram in Figure 6-27, where the exhaust temperature drops steeply in the superheater and the Rankine cycle area is increased due to the higher superheat temperature. It is important to note that the exhaust temperature decreased between the 150°C and 175°C cases, due to the change in engine operation mentioned in a previous section. This reduction in exhaust temperature leads to a slight decrease in net WHR system output for the 175°C system versus the 150°C system, dropping from 2.01 kW to 1.99 kW. The fuel energy input for the 175°C test was found to be 26.46 kW. With a fuel energy flow rate of 26.46 kW, the total power output was 9.63 kW for a combined efficiency of 35.61%, or a 25.10% relative increase over the baseline efficiency of 28.47%. However, this increase in efficiency was partly due to the apparent increase in engine efficiency seen at this operating temperature. Due to the cylinder leakage issues discussed in

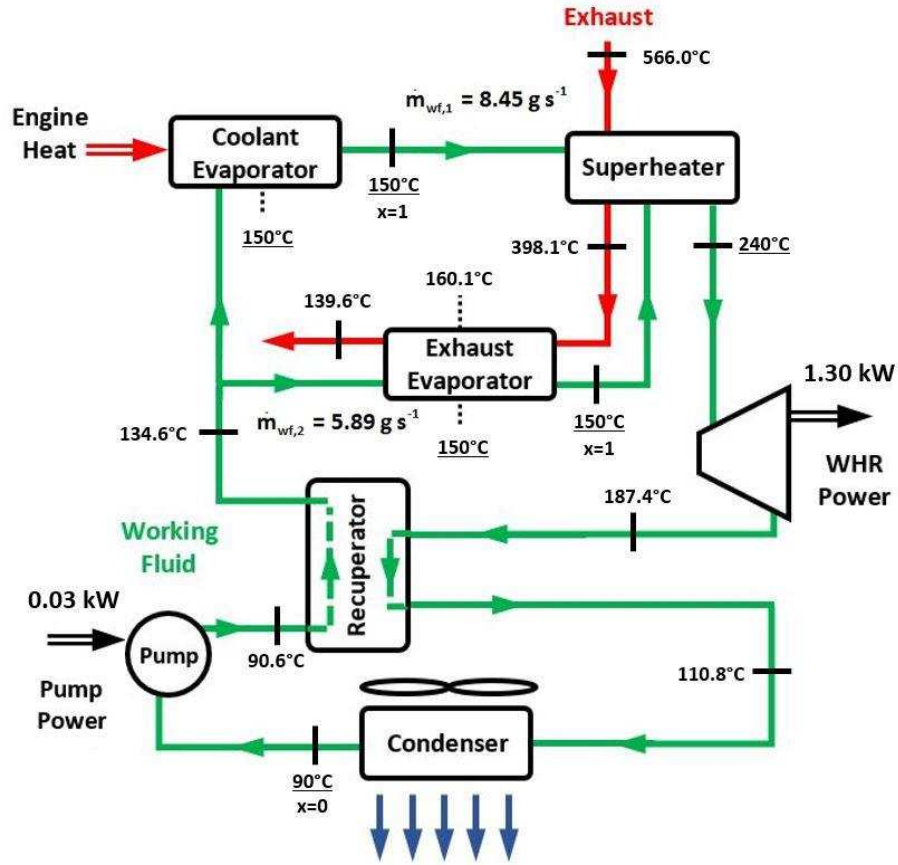


Figure 6-24. WHR system diagram for 150°C coolant and 90°C condenser temperature with results from the thermodynamic analysis.

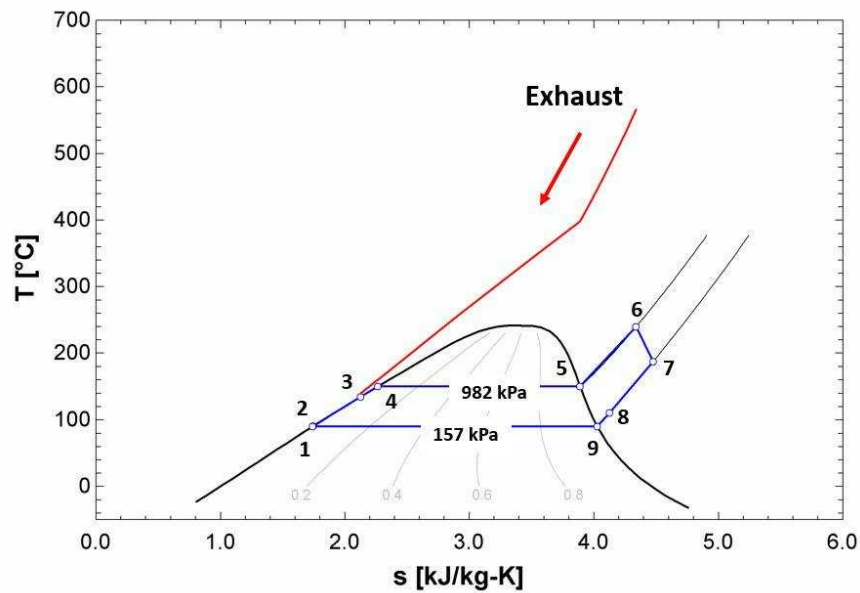


Figure 6-25. T-s diagram for 150°C coolant and 90°C condenser temperature WHR system. The exhaust temperature is shown in red and the working fluid shown in blue.

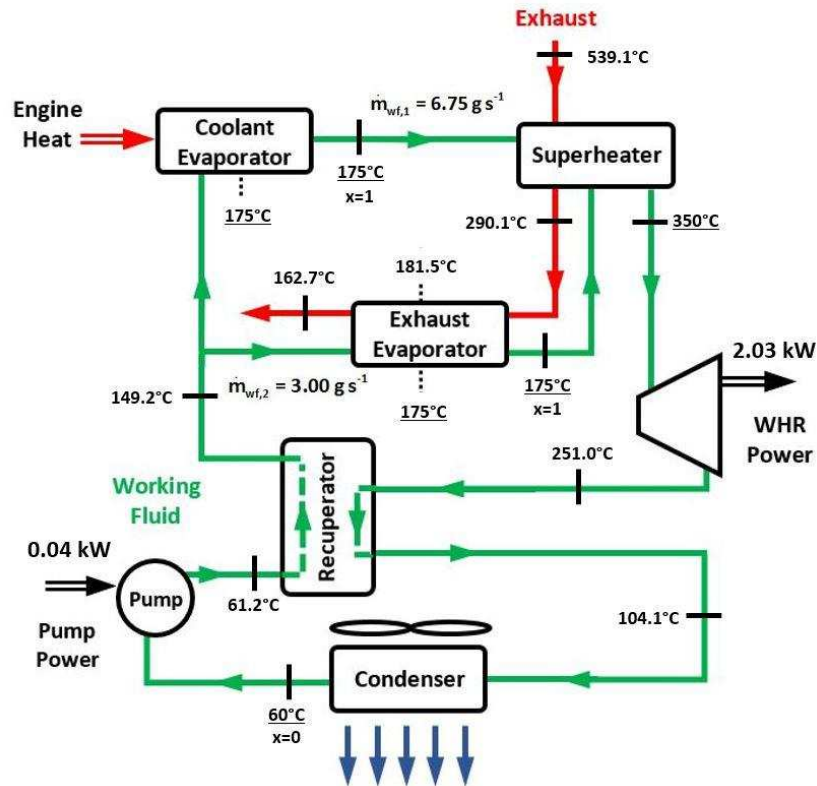


Figure 6-26. WHR system diagram for 175°C coolant and 60°C condenser temperature with results from the thermodynamic analysis.

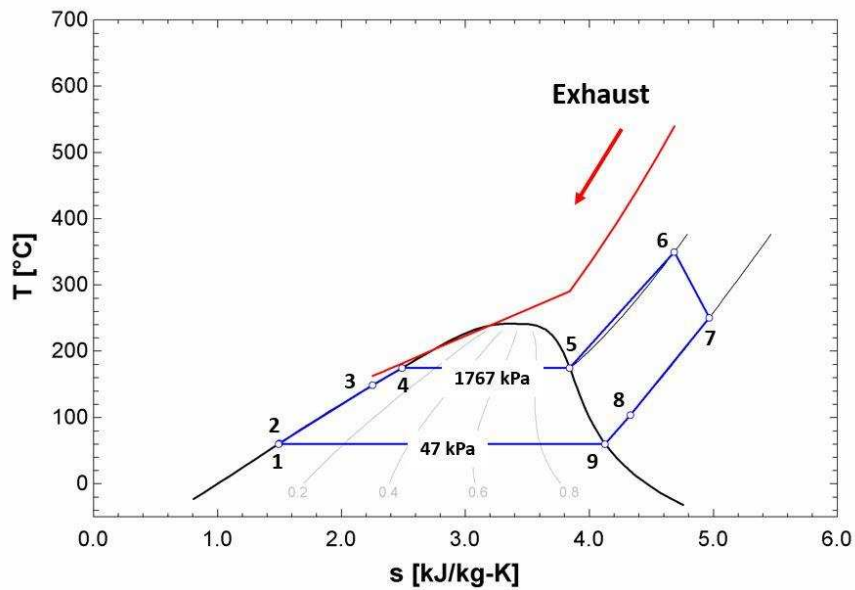


Figure 6-27. T-s diagram for 175°C coolant and 60°C condenser temperature WHR system. The exhaust temperature is shown in red and the working fluid shown in blue.

sections 6.1 and 6.2, the measured fuel flow rate may not reflect the true fuel usage. Therefore, the fuel energy flow rate may be slightly underestimated. The 90°C condenser temperature version of the 175°C WHR system is shown in Figure 6-28. Increasing the condenser temperature from 60°C to 90°C resulted in the expected decrease in cycle area shown in the T-s diagram in Figure 6-29. The superheat temperature for the 90°C condenser temperature system was reduced to 300°C to prevent boiling in the recuperator. (This is not an absolute requirement, but eliminating boiling in the recuperator may be advantageous for ensuring flow distribution in the evaporator. Further studies can explore allowing boiling the recuperator.) Thus, the net power output declined, dropping from 1.99 kW for the 60°C condenser temperature system to 1.42 kW for the 90°C condenser temperature system. With a total power output of 9.06 kW, efficiency was found to be 33.50%, which is a 17.70% relative increase in efficiency over the baseline.

The diagram for the final coolant temperature of 200°C is shown in Figure 6-30, with a condenser temperature of 60°C. The exhaust temperature increased over the 175°C case from 539.1°C to 597.3°C, raising the available exhaust energy and allowing the superheat temperature to be increased to 375°C. Figure 6-31 shows the T-s diagram for this system with the increased cycle area from the raised saturation pressure and superheat temperature. The ultimate result of the increased coolant and exhaust temperatures was a net power output of 2.45 kW, for a combined output of 10.09 kW (with 7.64 kW engine output). The fuel energy input was measured at 28.02 kW, giving a combined efficiency of 37.31%. This represents a relative efficiency increase of 31.04% over the baseline engine efficiency of 28.47%. The diagram for the 200°C system with 90°C condenser temperature is shown in Figure 6-32. Increasing the condenser temperature resulted in an increase in post-recuperator ethanol temperature to over 180°C and a consequent increase in mass flow through the engine to maintain the required heat rejection. The expected

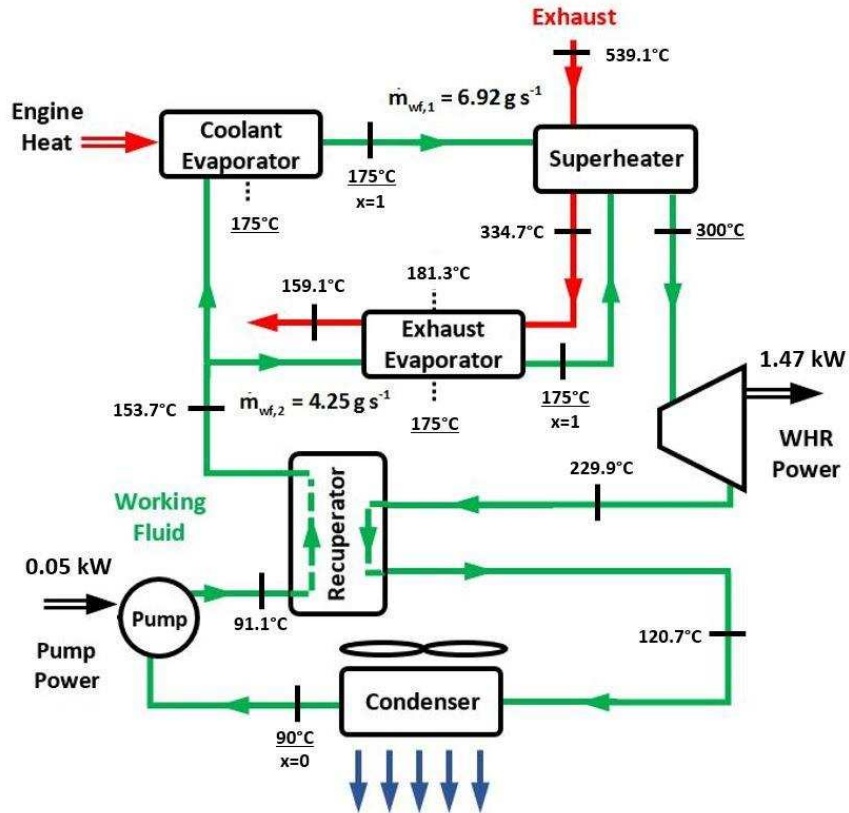


Figure 6-28. WHR system diagram for 175°C coolant and 90°C condenser temperature with results from the thermodynamic analysis.

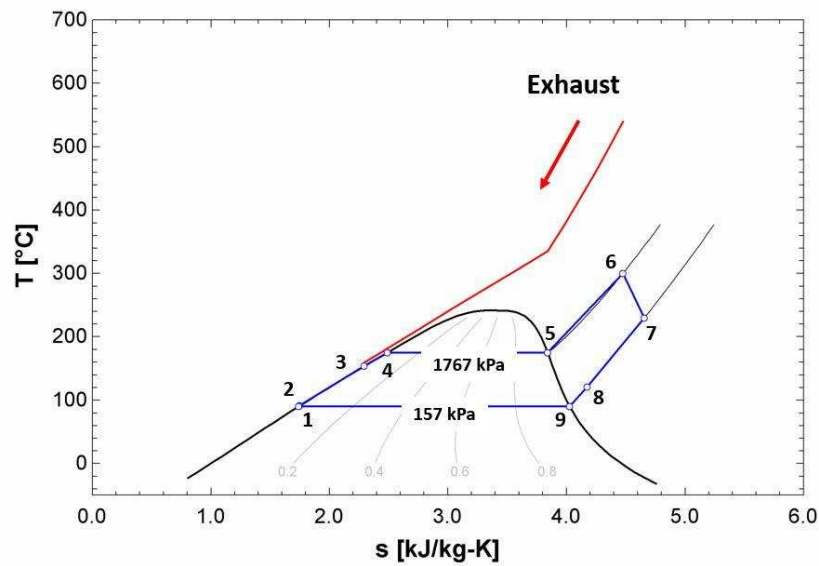


Figure 6-29. T-s diagram for 175°C coolant and 90°C condenser temperature WHR system. The exhaust temperature is shown in red and the working fluid shown in blue.

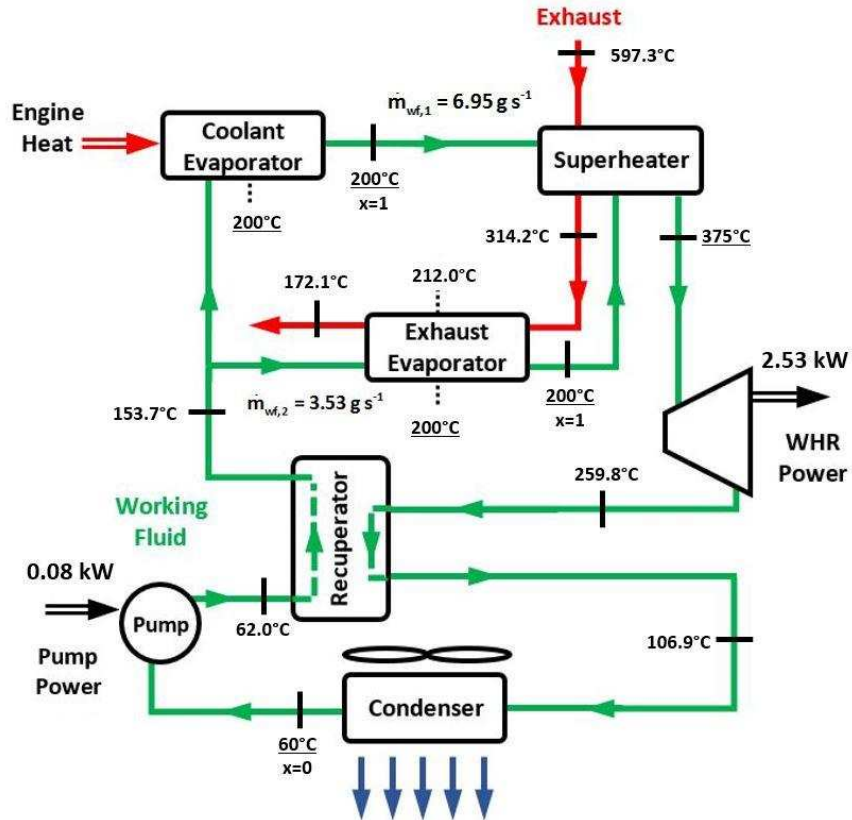


Figure 6-30. WHR system diagram for 200°C coolant and 60°C condenser temperature with results from the thermodynamic analysis.

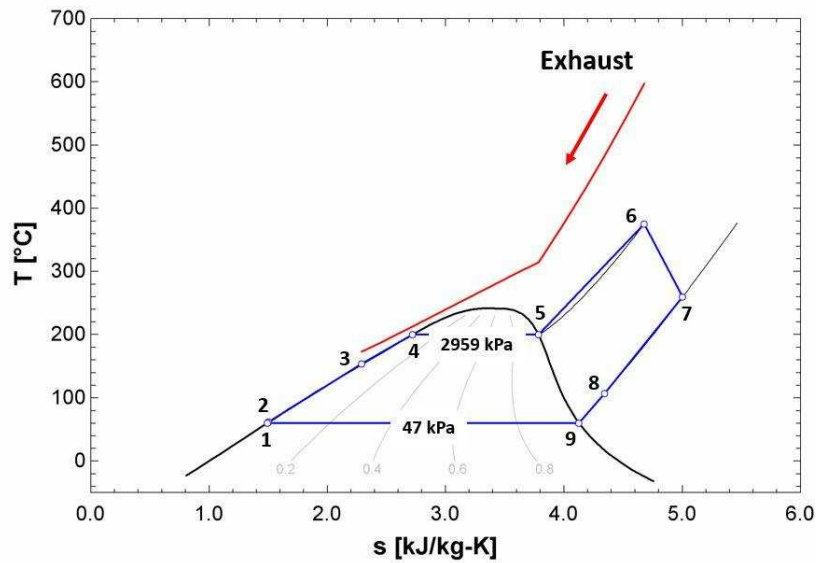


Figure 6-31. T-s diagram for 200°C coolant and 60°C condenser temperature WHR system. The exhaust temperature is shown in red and the working fluid shown in blue.

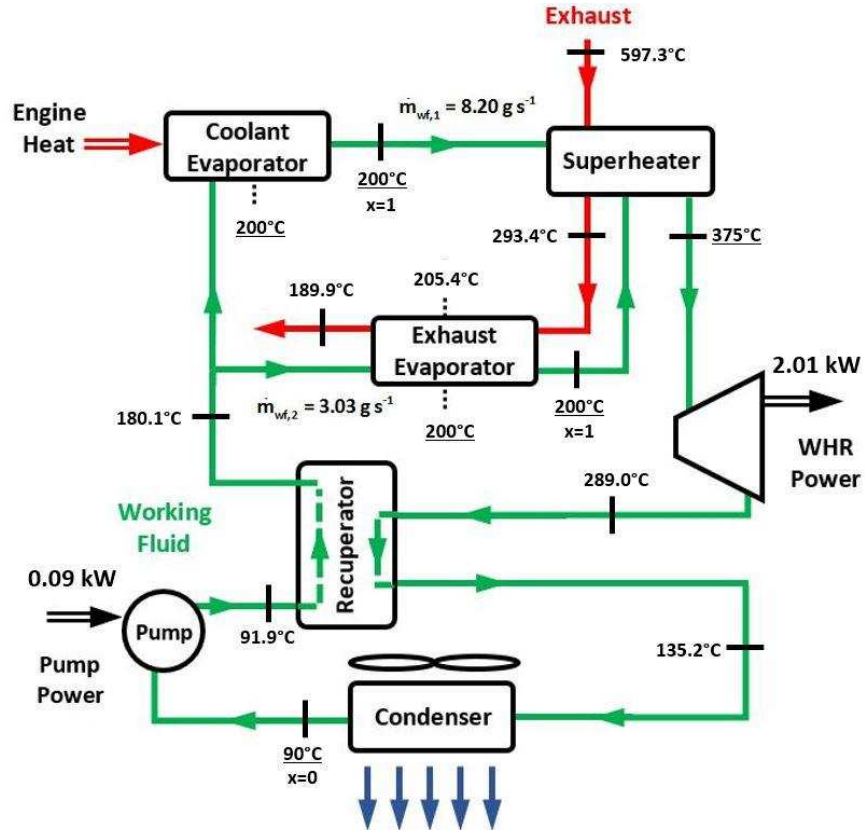


Figure 6-32. WHR system diagram for 200°C coolant and 90°C condenser temperature with results from the thermodynamic analysis.

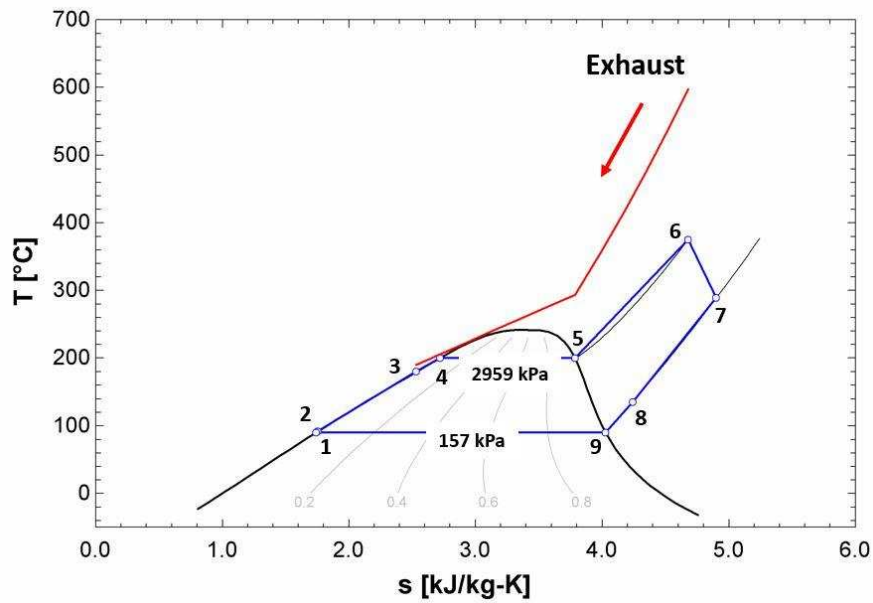


Figure 6-33. T-s diagram for 200°C coolant and 90°C condenser temperature WHR system. The exhaust temperature is shown in red and the working fluid shown in blue.

reduction in cycle area can be seen in the T-s diagram in Figure 6-33. The superheat temperature was maintained at 375°C and the net WHR output was calculated as 1.92 kW, for a combined output of 9.56 kW. With a fuel energy input of 28.02 kW, the 90°C condenser temperature system gave a combined efficiency of 35.35%, or a 24.16% relative efficiency increase over the baseline engine test.

Table 6-1. Relative efficiency gain for eight WHR system models.

Coolant Temperature	Relative Efficiency Gain	
	60°C Condenser	90°C Condenser
90	15.3%	11.7%
150	25.2%	15.7%
175	25.1%	17.7%
200	31.0%	24.2%

6.4.2 WHR System Output and Efficiency Gain

The goal of WHR is to increase overall thermal efficiency by harnessing wasted energy and converting it to additional power. The thermodynamic modeling described in Chapter 5 provided the input values for the individual heat exchanger models, but also provided estimates of the power output of the WHR systems at each coolant temperature. The WHR system power output results are shown in Figure 6-34 for 3100 rpm and 24 N-m of torque and each condenser temperature evaluated (60°C and 90°C). As hypothesized, the WHR system power output is shown to increase overall as coolant temperature is raised. For the 90°C condenser temperature, the output increases from 0.89 kW for the state-of-the-art 90°C coolant temperature system to 1.92 kW at 200°C coolant temperature, or a 116% rise. At a condenser temperature of 60°C, the WHR system output rises from 1.17 kW for the state-of-the-art system at 90°C coolant temperature to 2.45 kW at 200°C, giving an increase of 109%. The WHR system output does decrease from 150°C to 175°C coolant temperature for the 60°C condenser temperature. Here, the estimated WHR system

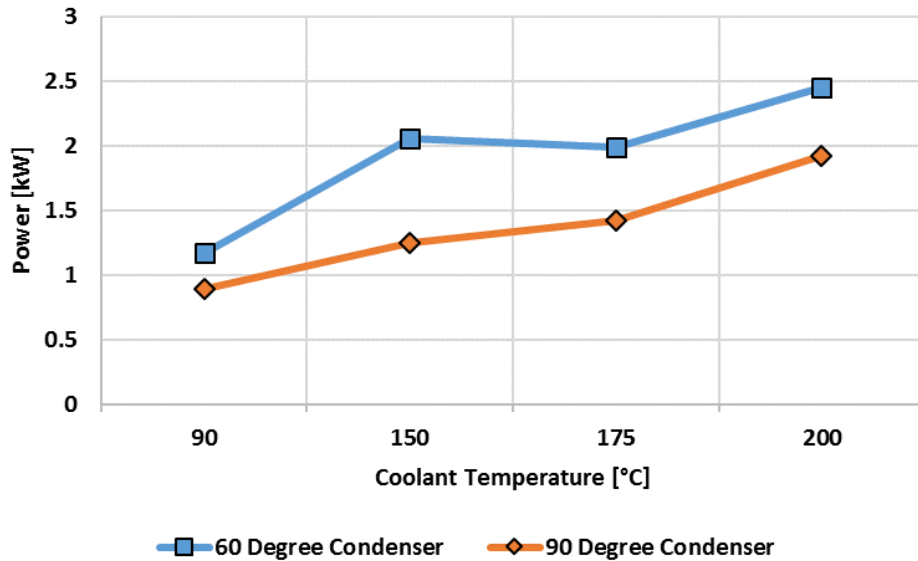


Figure 6-34. Waste heat recovery model power output results for 3100 rpm and 24 N-m of torque.

power decreases from 2.06 kW to 1.99 kW (a 3.4% drop). This unexpected decrease in WHR system output can be explained by the reduction in exhaust temperature seen to occur from 150°C to 175°C coolant temperature resulting in reduced exhaust waste heat availability. As previously discussed, the decrease in exhaust temperature at 175°C coincided with an increase in leakage of HTF into the combustion chamber. Therefore, the power output of the WHR systems at 175°C and 200°C may be underestimated here since the exhaust temperature would have likely continued to rise along with the WHR output had it not been for the head gasket failure. This effect is seen to a lesser degree for the 90°C condenser models, with a decrease in slope from 150°C to 175°C.

The ultimate metric for evaluating the WHR systems presented here is the overall efficiency gain over the engine alone. The experimental work had aimed to determine the effect of higher running temperatures on the engine efficiency to understand the impact on overall gains from WHR. Unfortunately, leakage of HTF into the combustion chambers from a compromised head gasket made the engine efficiency measurements suspect, and masked any efficiency changes due solely to higher operating temperatures. The efficiency gains for each WHR system were

found by comparing the combined efficiency of each system to the baseline 90°C coolant temperature engine efficiency. When compared to the literature, the 90°C system efficiency increase of over 15% is greater than expected. One important note is that the analysis presented here is for steady state engine operation only and at a relatively high engine load (74% of maximum). In any application where transients would be common (automotive), the average gains would likely be noticeably lower than the given results. Additionally, heat loss to the environment from the heat exchangers and conduits or pipes connecting them was neglected from this analysis. Any heat lost to the environment would reduce WHR system output and lower the efficiency gains.

The gains shown in Figure 6-35 for both 60°C and 90°C condenser temperature models demonstrate the same trend observed in the WHR power output results. Despite the negative effects of the combustion chamber leakage on WHR output (from decreased exhaust temperature), the relative efficiency gain for the 60°C condenser temperature models increased from 15.2% at 90°C coolant temperature to 31.0% at 200°C, giving a relative improvement of 104%. At a

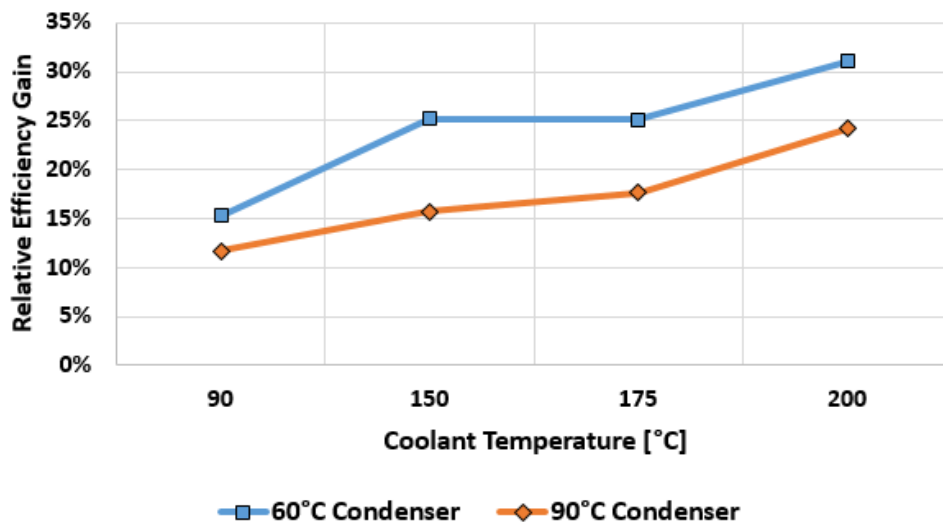


Figure 6-35. Relative efficiency gain of WHR system over 90°C engine efficiency for each temperature at 3100 rpm and 24 N-m of torque.

condenser temperature of 90°C, the efficiency gain rose from 11.6% at 90°C to 24.2% at 200°C, or a 109% relative increase. Without the decrease in exhaust temperature seen at 175°C, it is possible the gains may have been even greater above 150°C. However, the ultimate effect of increased running temperatures on actual engine efficiency is also unknown and might offset some of these gains. Regardless, the results suggest that the efficiency gains from elevated coolant temperature are likely to be significant and the concept warrants further investigation. The next section will describe the results of the individual heat exchanger modeling and present the footprint differences between the WHR systems.

6.4.3 Heat Exchanger Footprint

The performance of a WHR system is not the only consideration in deciding whether to adopt this technology for a given application. The space required to package the system is often of primary concern and the heat exchangers account for most of the required space of a WHR system. The heat exchanger models described in the previous chapter are meant to give estimates of the footprint of the four heat exchangers for the WHR systems (condenser, evaporator, superheater, and recuperator), plus the oil coolers that will likely be necessary to keep oil temperatures at reasonable levels. The height and width of each heat exchanger was fixed for all cases with the length as the only variable to make comparison simple.

The heat exchangers were modeled in SolidWorks® to provide a visual representation of the footprint required for each heat exchanger in the different WHR systems. Drawings of the heat exchanger models are shown in Figures 6-36 through 6-43, including the major dimensions given in mm. As previously mentioned, each system was modeled with condenser temperatures of 60°C and 90°C. The lower condenser temperature proved to provide greater WHR output and increased overall efficiency. However, comparing the footprint of the 60°C condenser heat exchangers in

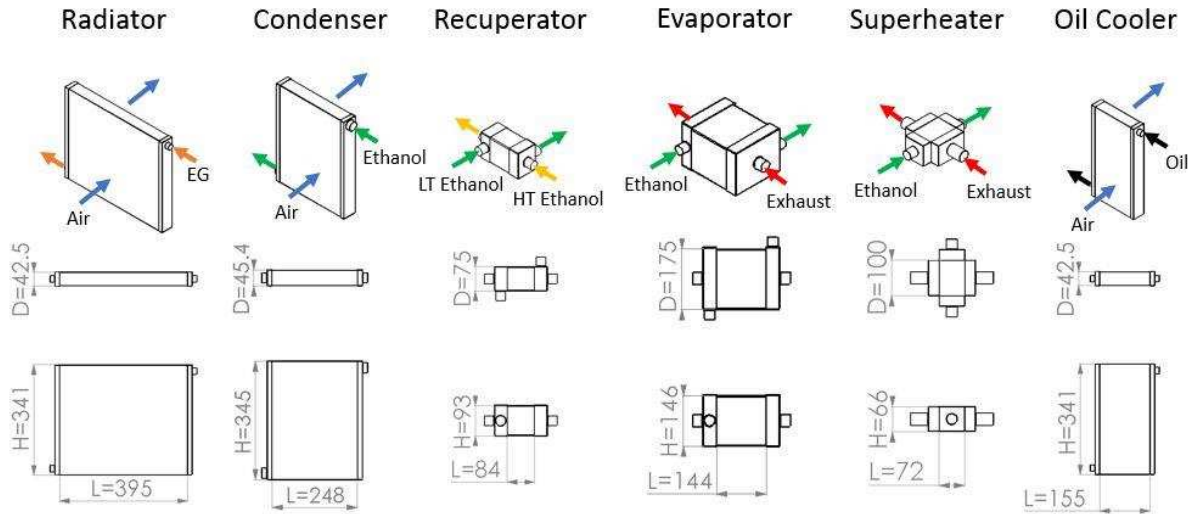


Figure 6-36. Footprint of heat exchangers for 60°C condenser temperature and 90°C coolant temperature WHR system (dimensions in mm).

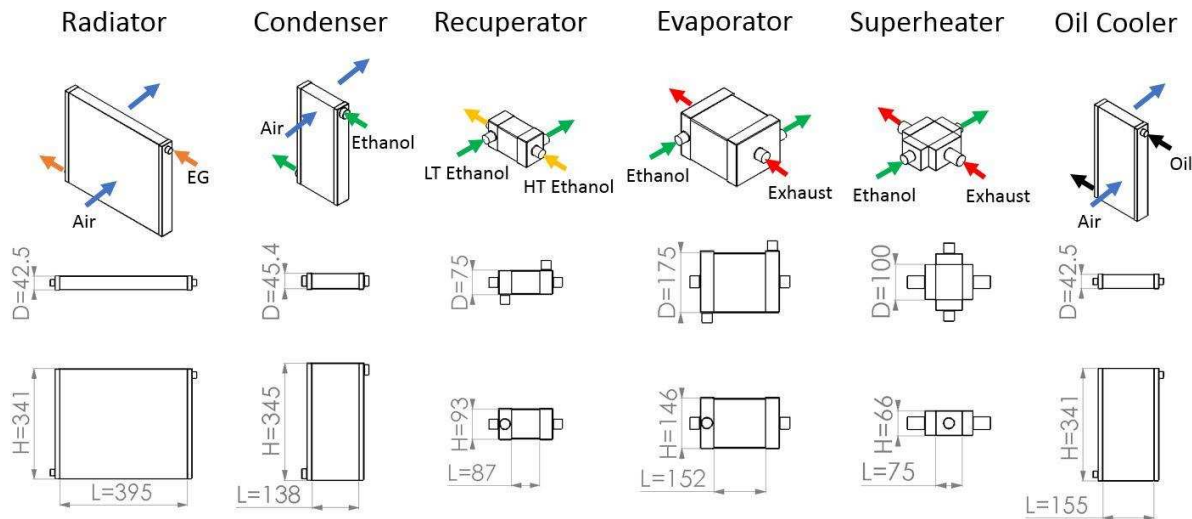


Figure 6-37. Footprint of heat exchangers for 90° condenser temperature and 90°C coolant temperature WHR system (dimensions in mm).

Figures 6-36, 6-38, 6-40, and 6-42, with the 90°C condenser temperature heat exchangers in Figures 6-37, 6-39, 6-41, and 6-43, the footprint required for the higher-performing 60°C condenser temperature systems is significantly larger. The 90°C condenser temperature systems therefore demonstrate the performance for a more compact system that might be required where

space is at a premium. The heat exchanger most affected by the condenser temperature is the condenser. The condenser size increases when the condenser temperature is closer to the ambient temperature, which lowers the entering temperature difference of the two fluids. For example, the 150°C coolant temperature system with a 60°C condenser requires a condenser 578 mm long

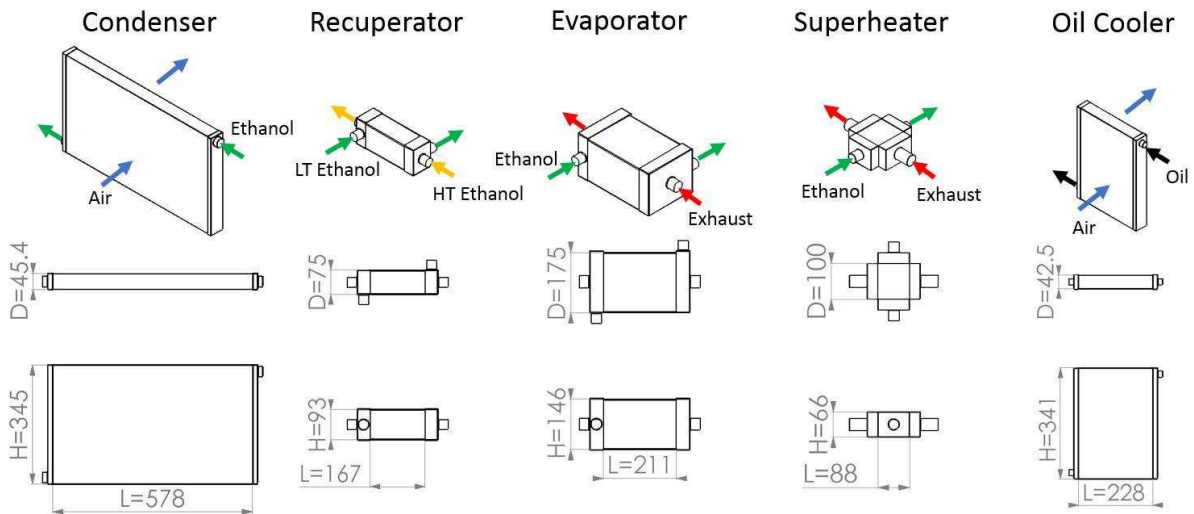


Figure 6-38. Footprint of heat exchangers for 60°C condenser temperature and 150°C coolant temperature WHR system (dimensions in mm).

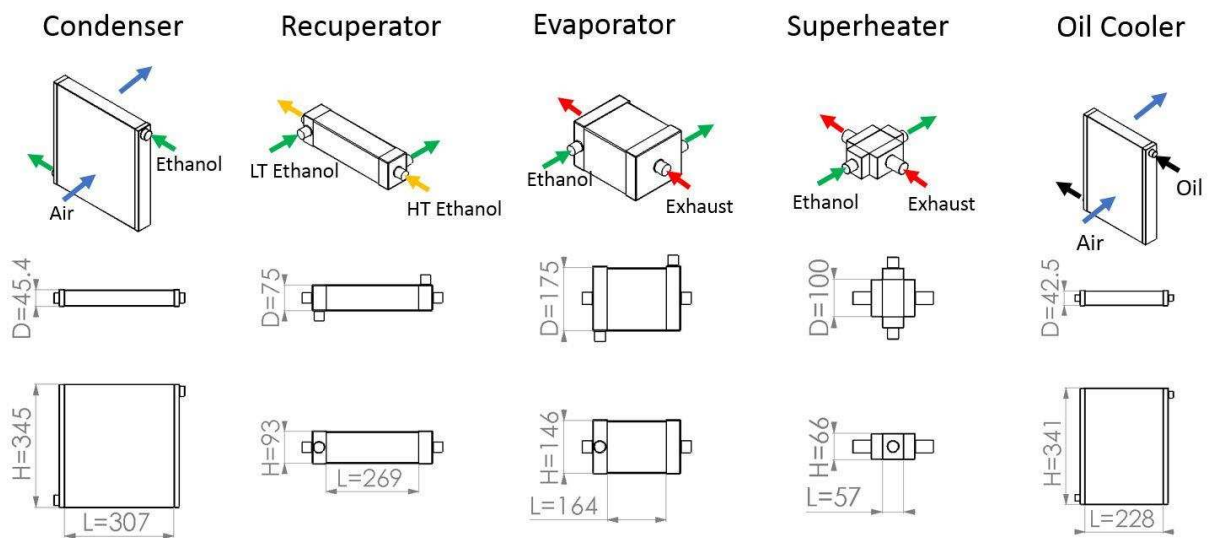


Figure 6-39. Footprint of heat exchangers for 90°C condenser temperature and 150°C coolant temperature WHR system (dimensions in mm).

(Figure 6-38) and a total heat exchanger volume of $19.5 \times 10^3 \text{ cm}^3$. The same system with a 90°C condenser only requires a condenser length of 307 mm (Figure 6-39) and a total heat exchanger volume of $14.6 \times 10^3 \text{ cm}^3$.

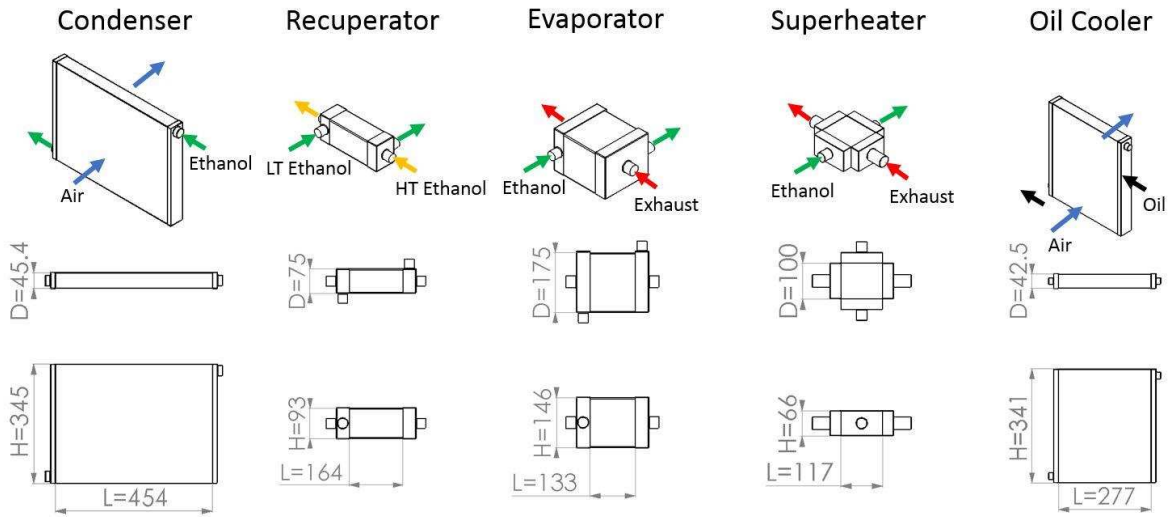


Figure 6-40. Footprint of heat exchangers for 60°C condenser temperature and 175°C coolant temperature WHR system (dimensions in mm).

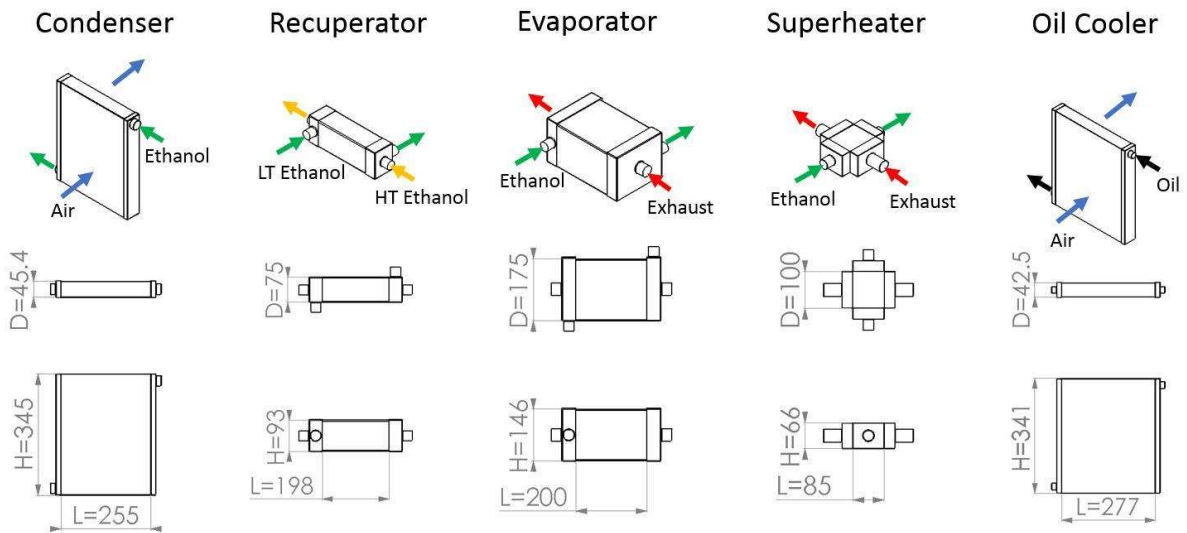


Figure 6-41. Footprint of heat exchangers for 90°C condenser temperature and 175°C coolant temperature WHR system (dimensions in mm).

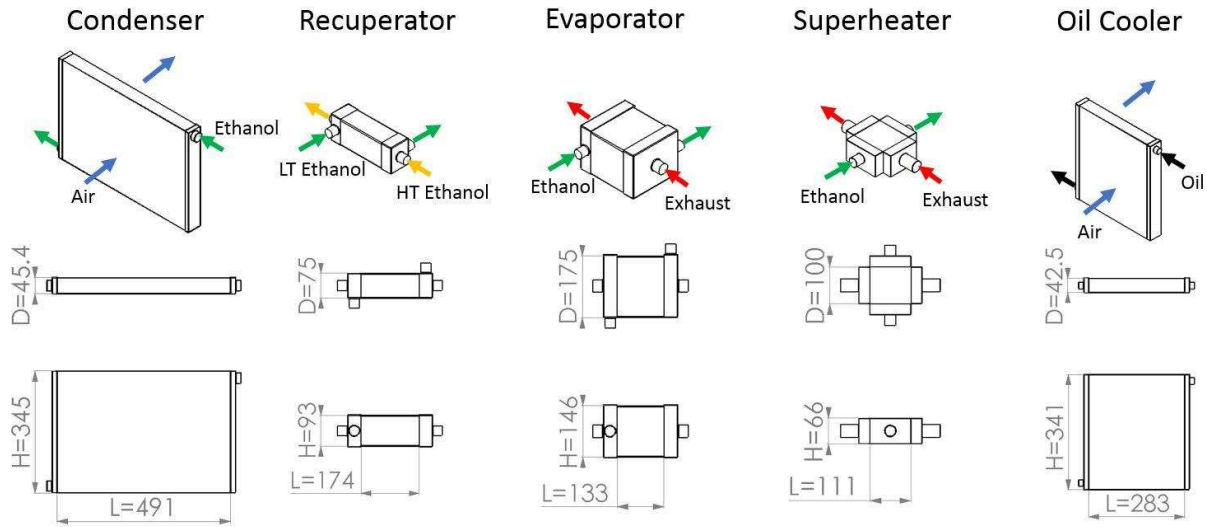


Figure 6-42. Footprint of heat exchangers for 60°C condenser temperature and 200°C coolant temperature WHR system (dimensions in mm).

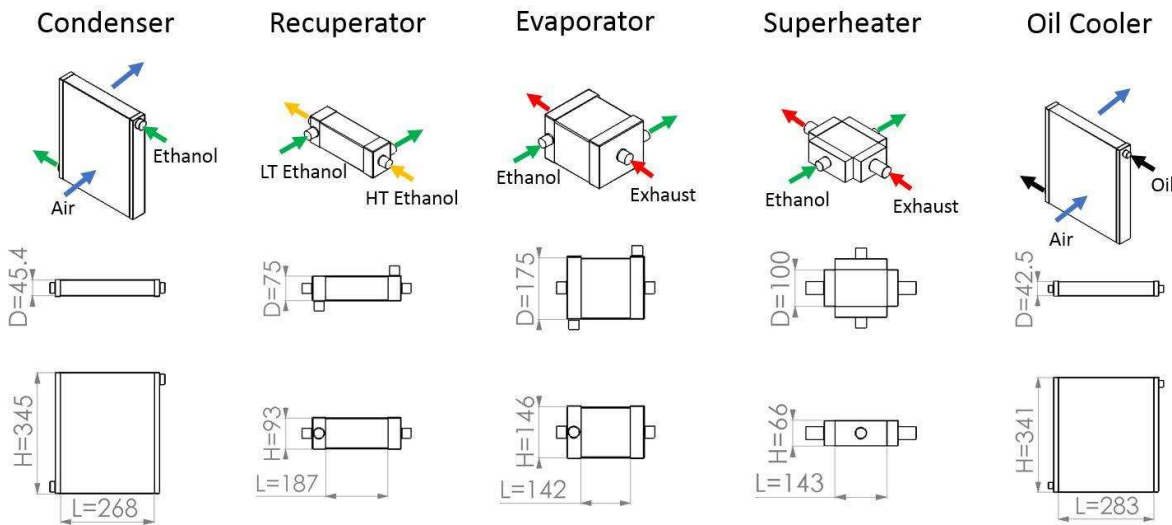


Figure 6-43. Footprint of heat exchangers for 90°C condenser temperature and 200°C coolant temperature WHR system (dimensions in mm).

The total heat exchanger volume for each of the eight systems that were modeled is shown in Figure 6-44. The figure demonstrates that total heat exchanger volume is always greater for the lower condenser temperature (60°C) systems as expected. The trends of the heat exchanger volumes for the 60°C condenser temperature and 90°C condenser temperature systems appear to be different. Overall, the heat exchanger volume for the 90°C condenser systems show little

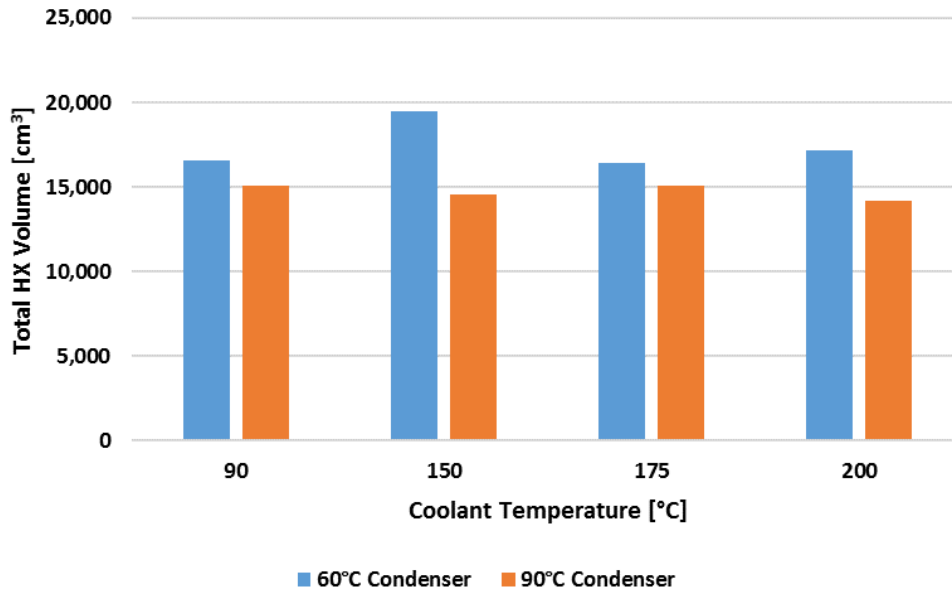


Figure 6-44. Total heat exchanger volume for all modeled system.

sensitivity to engine coolant temperature. For the 60°C condenser systems, there is a large volume increase when coolant temperature is increased from 90°C to 150°C. This increase in heat exchanger volume is accompanied by a proportional rise in WHR system power output (1.18 kW to 2.00 kW). As shown in Figure 6-45, the greater volume at 150°C coolant temperature with the 60°C condenser is primarily due to increased condenser and evaporator volume over the 90°C coolant temperature case. This is because the radiator heat is rejected at a temperature of 90°C and the same heat in the high-temperature 60°C condenser temperature system is rejected at 60°C instead. The smaller entering temperature difference between the ambient air and the ethanol results in a larger condenser volume. The trend of condenser volume for the 60°C condenser models resembles the patterns in engine efficiency (as well as waste heat exergy) seen in sections 6.1 and 6.2. The decrease in energy recovered from 150°C to 175°C results in reduced heat duty for the condenser, and in turn a smaller condenser volume. A similar pattern in condenser size is present for the 90°C condenser systems (Figure 6-46).

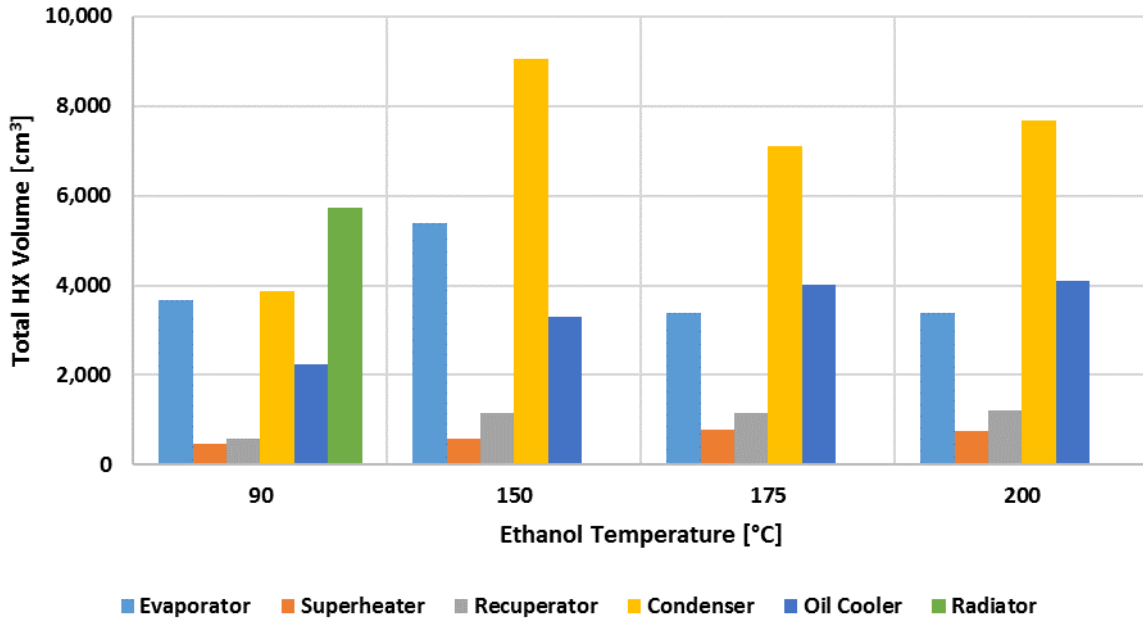


Figure 6-45. Volume of each heat exchanger for 60°C condenser temperature systems.

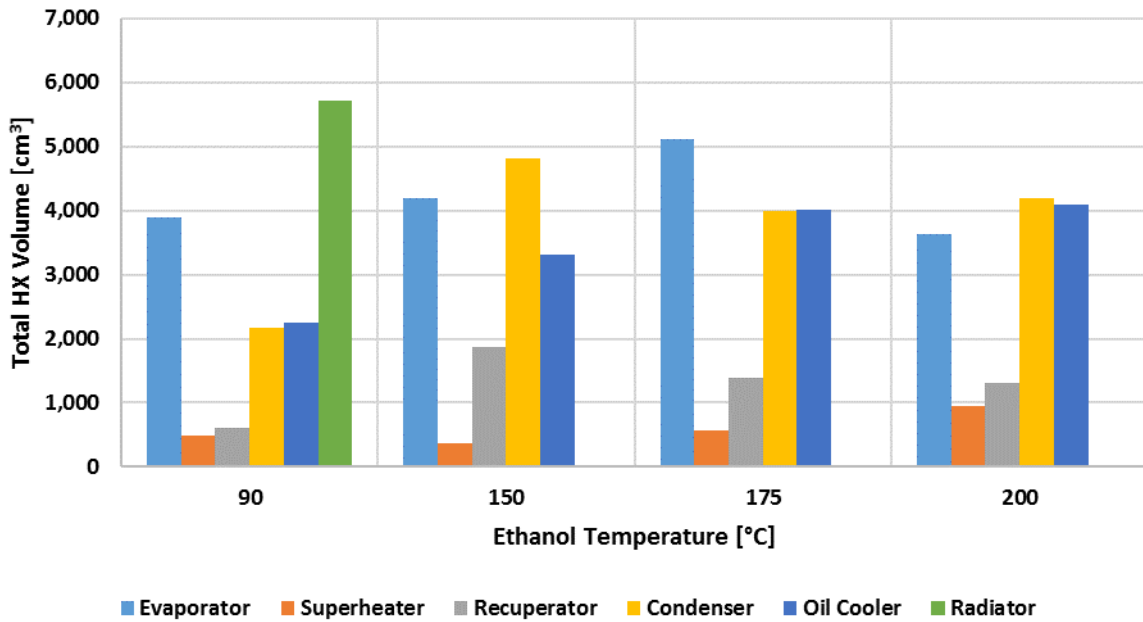


Figure 6-46. Volume of each heat exchanger for 90°C condenser temperature systems.

The plotting of total heat exchanger volume versus the range of coolant temperatures modeled generally implies a small size tradeoff for the additional efficiency with a 60°C condenser

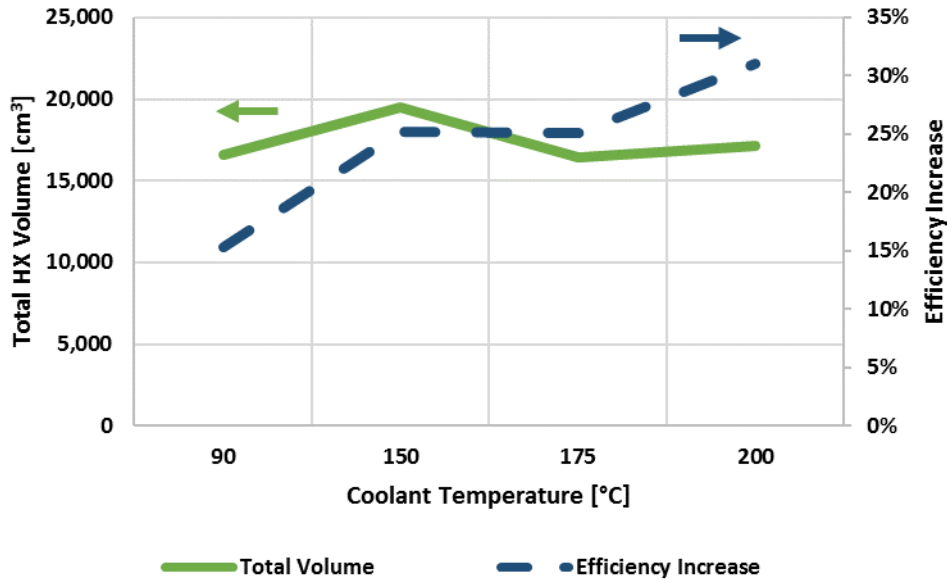


Figure 6-47. Total heat exchanger volume and efficiency increase for 60°C condenser temperature systems.

temperature (Figures 6-47). For example, the total heat exchanger volume for the 60°C condenser and 90°C coolant model is $16.6 \times 10^3 \text{ cm}^3$, which increases to $17.1 \times 10^3 \text{ cm}^3$ at a coolant temperature of 200°C (a 3% relative increase). This increase in heat exchanger size is accompanied by an increase in relative efficiency gain from 15.3% at 90°C to 31.0% at 200°C, or a 103% increase. However, the trend for the 90°C condenser systems showed very little change with coolant temperature (Figure 6-48). For the 90°C condenser models, the total heat exchanger volume actually decreased from $15.1 \times 10^3 \text{ cm}^3$ at 90°C coolant temperature to $14.2 \times 10^3 \text{ cm}^3$ at 200 °C (a 6% decrease). The 90°C condenser models estimated an efficiency increase from 11.7% at 90°C coolant temperature to 24.2% at 200°C (a 107% rise). As with the other results described in previous sections, the results when the coolant temperature is raised to 175°C do not follow the trend seen for the other test points. Here, the reduction in exhaust temperature that accompanied the increased head gasket leakage at 175°C tended to reduce, or partially offset, the increase for both efficiency gain and total heat exchanger volume. Another way to evaluate the efficiency and

size tradeoff is to consider the efficiency gain per total heat exchanger volume (Figure 6-49). This figure demonstrates that, with increasing coolant temperature (up to 200°C), the efficiency gains outweigh any increase in heat exchanger volume. For example, at the 60°C condenser temperature and 90°C coolant temperature, the WHR system provides a 9.2% relative efficiency gain for each cubic meter of heat exchanger volume. At 200°C, the WHR system gives an 18.1% relative efficiency gain for each cubic meter of heat exchanger volume, or a 96% increase. For the 90°C condenser temperature and 90°C coolant temperature system, a 7.7% relative efficiency gain is realized for each cubic meter of heat exchanger volume. A 200°C, a 17.0% relative efficiency gain is realized for each cubic meter of heat exchanger volume (a 121% increase). Again, accurate measurement of the changes in actual engine efficiency over the coolant temperature range may alter this relationship to some degree.

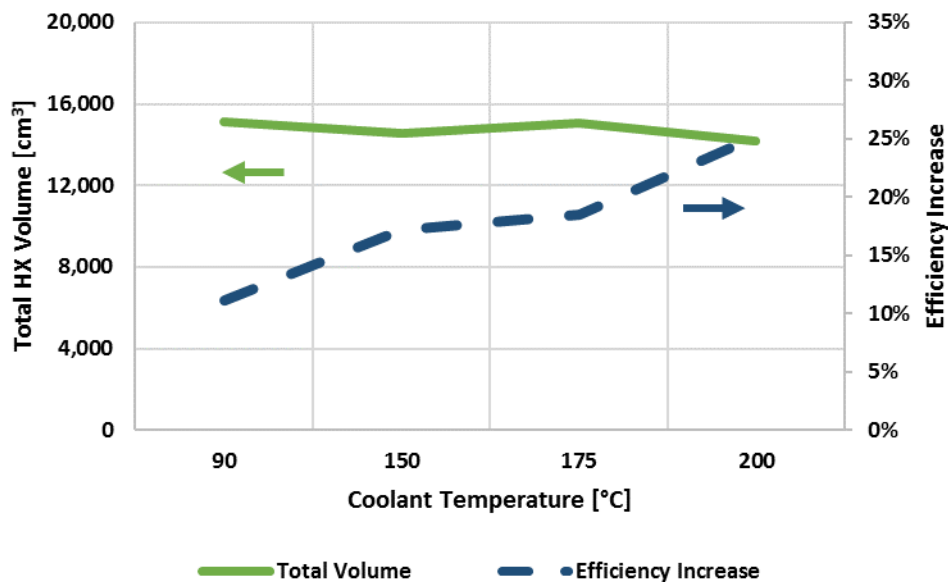


Figure 6-48. Total heat exchanger volume and efficiency increase for 90°C condenser temperature systems.

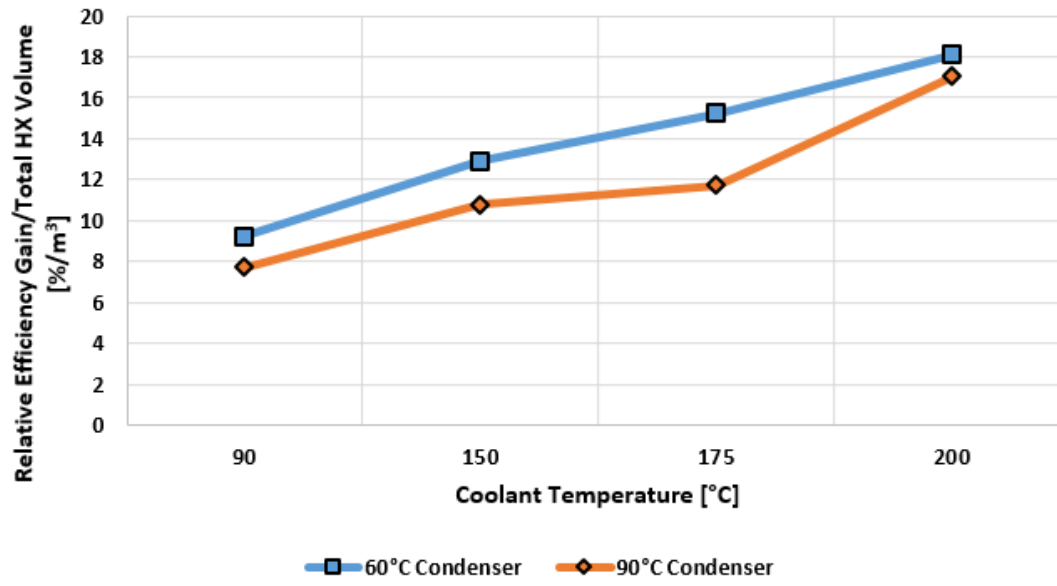


Figure 6-49. Efficiency benefit per total heat exchanger volume for condenser temperatures of 60°C and 90°C.

CHAPTER 7. CONCLUSIONS AND RECOMMENDATIONS

The present study explores a way to improve diesel engine efficiency through improved WHR. Historically, WHR from combustion engines is fundamentally limited by the low heat capacity rate of the exhaust gases and the low temperature of the engine coolant. The result is underutilization of the available waste heat and relatively small efficiency gains with respect to the energy present in the waste heat sources (i.e., <10% relative increase). Raising the coolant temperature and directly heating the WHR system working fluid in the engine block greatly increases the availability of the heat lost to the engine coolant and improves the utilization of this waste heat. This idea has been demonstrated using modeling to estimate the potential WHR gains, which can be >30% in some circumstances. However, no experimental investigations exist where experimental data from an engine running at elevated temperatures is collected, and is then used to determine the energy balance to supply realistic WHR model inputs.

The current study is the only known investigation where an engine was operated at elevated coolant temperatures to evaluate the potential of WHR from a high-temperature engine. A small 3-cylinder diesel engine was operated at coolant temperatures between 90°C and 200°C. To accomplish this, the engine was modified to improve durability under high temperature operation. The cylinder head gasket was replaced with a solid copper gasket and stainless steel O-rings were added to the engine block to seal the combustion chambers. Oil seals were replaced with high-temperature Viton™ alternatives to better withstand high temperatures. A heat shield was fabricated to protect the high-pressure fuel pump from additional heat radiating from the engine block. The waste heat in the exhaust, coolant, and engine oil was measured and the exergy in each waste heat stream was calculated. Custom cooling and engine oil systems were designed and

fabricated to provide sufficient control and facilitate measurement of fluid temperature and flow rates. Exhaust heat losses were found using the measured exhaust temperature and the combined air and fuel flow measurements. Emissions were recorded using a five-gas analyzer to measure the levels of O₂, CO₂, CO, THC, and NO_x present in the exhaust gases. An eddy current dynamometer provided engine load and power measurements. The engine was operated at three different engine speeds (2800, 3100, and 3400 rpm) and five different torque levels (12, 15, 18, 21, and 24 N-m), providing fifteen unique load points.

The results of the experiment showed that total waste heat exergy increased between 20% and 40% (depending on load condition) between the 90°C baseline coolant temperature and the 200°C coolant temperature. The rise in exergy suggested that substantial increases in WHR system output are possible when engine coolant temperature is increased. Thermodynamic models were then created for eight different WHR systems with coolant temperatures of 90°C, 150°C, 175°C, and 200°C and condenser temperatures of 60°C and 90°C. The models estimated that WHR output for both condenser temperatures would improve by over 100% when the coolant temperature was increased from 90°C to 200°C. This increased WHR output translates to relative efficiency gains as high as 31.0% for the 60°C condenser temperature and 24.2% for the 90°C condenser temperature. Individual heat exchanger models were also developed to estimate the footprint required for each WHR system. When the coolant temperature increased from 90°C to 200°C, the total heat exchanger volume increased from $16.6 \times 10^3 \text{ cm}^3$ to $17.1 \times 10^3 \text{ cm}^3$ with a 60°C condenser temperature, and decreased from $15.1 \times 10^3 \text{ cm}^3$ to $14.2 \times 10^3 \text{ cm}^3$ with a 90°C condenser temperature. Efficiency gain per total heat exchanger volume increased as the coolant temperature rose indicating that the tradeoff between efficiency gain and footprint improves at higher temperatures. However, the higher temperature systems are penalized on oil cooler size due

to the low oil temperatures maintained on the test engine. The low oil temperatures increase heat loss to the engine oil which then must be rejected via the oil cooler. Increasing the oil temperature to 100°C would likely improve waste heat exergy for the exhaust and coolant streams, increase WHR system output and reduce oil cooler volume.

The performance and condition of the engine were monitored over the course of testing. Fluctuations in engine compression were recorded during testing and metal particles in the engine oil increased as temperatures rose. Some fluctuations in apparent efficiency were also discovered. Post testing analysis revealed that HTF had leaked into the combustion chambers and that the measured leakage rates corresponded to fluctuations in the measured engine efficiency as well as other values such as exhaust temperature. The unmetered fuel entering the combustion chamber increased significantly between the 150°C coolant temperature and 175°C coolant temperature tests, making trends in engine efficiency difficult to determine at higher temperatures. Additionally, engine tear down after the experiment revealed damage to the pistons and cylinder bores from overexpansion and improper lubrication. Engine oil breakdown at the top of the piston caused the piston rings to seize in the ring grooves, possibly effecting engine compression. Scuffing and discoloration was also observed on the lifters and lifter bores.

In summary, the work presented here has demonstrated that waste heat availability can be increased by as much as 40% for a diesel engine by raising the coolant temperature. Increased waste heat availability translates into better waste heat utilization in a WHR system and improvements in overall system efficiency of over 30%. However, at higher coolant temperatures increased heat exchanger footprints are required for the WHR systems. Further work is required to understand the exact effects of raised coolant temperature on combustion and engine efficiency

to provide a complete picture of the overall benefits of WHR from a high-temperature diesel engine.

7.1 Recommendations for Future Work

Future research on this topic should include items listed below. However, some prioritization of these items is required. The validity of this concept will ultimately depend on the tradeoff between efficiency benefit and cost. This work provides an estimate of the first component, but raises some questions about what may be required to implement this concept while maintaining engine reliability. Therefore, the first step in understanding if WHR from a high-temperature diesel engine is viable is better understanding of the potential costs involved in the implementation of the concept. Estimates on WHR system component costs would be relatively easy to attain, but understand the engineering required to make the engine survive under high-temperature operation may require more effort. However, until this work is done it will be difficult to complete cost-benefit analysis to understand if the concept is marketable, and this should be the priority for future research on the subject (see the first four bullet points below).

- Head gasket integrity was the primary issue with the experiment. It is recommended that different head gasket materials and sealing techniques be explored. Different engine block and head materials may need consideration as well.
- At higher engine temperatures, the stock aluminum alloy pistons over-expand and contact the cylinder walls. Engine pistons need to be redesigned and alternative materials considered to allow operation over a wider temperature range without seizure.
- Engine oil breakdown at the top of the pistons causes the piston rings to seize affecting cylinder compression and the resulting lack of lubrication leads to piston damage from

contact with the cylinder bore. It is suggested that alternate high-temperature lubricants and additives be tested to reduce oil breakdown and coking of the piston ring grooves. Piston cooling may also aid in preventing oil breakdown.

- Solid lubricants may aid in reducing wear at locations where the engine oil film becomes too thin for adequate lubrication. Diamond-like carbon (DLC) coatings should be tested along with other solid lubricants that can withstand high-temperature environments.
- Heat lost to the environment is wasted heat with no chance for recovery. Insulating the engine structure might result in increased exergy in the engine coolant and exhaust gases.
- Increase oil temperature to reduce oil cooler size and increase exergy of exhaust and coolant streams.
- Further testing is recommended with optimization of the fuel injection timing and use of a more modern high-pressure fuel system to attempt to minimize losses in engine efficiency at higher operating temperatures [61].
- Investigate alternate working fluids and more aggressive heat exchanger surfaces to decrease WHR system volume.

REFERENCES

- [1] Arias, D. A., Shedd, T. A., and Jester, R. K., 2006, "Theoretical Analysis of Waste Heat Recovery from an Internal Combustion Engine in a Hybrid Vehicle," SAE International.
- [2] Park, T., Teng, H., Hunter, G. L., van der Velde, B., and Klaver, J., 2011, "A Rankine Cycle System for Recovering Waste Heat from HD Diesel Engines - Experimental Results," SAE International.
- [3] Kamo, R., 1987, "Adiabatic diesel-engine technology in future transportation," *Energy*, 12(10–11), pp. 1073-1080.
- [4] Modi, A. J., 2012, "Experimental Study of Energy Balance in Thermal Barrier Coated Diesel Engine," SAE International.
- [5] Taymaz, I., 2007, "The effect of thermal barrier coatings on diesel engine performance," *Surface and Coatings Technology*, 201(9–11), pp. 5249-5252.
- [6] Greene, D. L., 2008, "Assessment of Fuel Economy Technologies for Light-Duty Vehicles," *Transportation Research Record*, 2058(1).
- [7] Bento, A. M., Roth, K. D., and Wang, Y., "The Impact of CAFE Standards on Innovation in the US Automobile Industry," Proc. 2015 AAEA & WAEA Joint Annual Meeting, July 26-28, San Francisco, California, Agricultural and Applied Economics Association & Western Agricultural Economics Association.
- [8] Bergek, A., Berggren, C., and Group, K. R., 2014, "The impact of environmental policy instruments on innovation: A review of energy and automotive industry studies," *Ecological Economics*, 106, pp. 112-123.
- [9] Middleton, R. J., Harihara Gupta, O. G., Chang, H.-Y., Lavoie, G., and Martz, J., 2016, "Fuel Efficiency Estimates for Future Light Duty Vehicles, Part A: Engine Technology and Efficiency," SAE International.
- [10] Middleton, R. J., Harihara Gupta, O. G., Chang, H.-Y., Lavoie, G., and Martz, J., 2016, "Fuel Efficiency Estimates for Future Light Duty Vehicles, Part B: Powertrain Technology and Drive Cycle Fuel Economy," SAE International.
- [11] Berggren, C., and Magnusson, T., 2012, "Reducing automotive emissions—The potentials of combustion engine technologies and the power of policy," *Energy Policy*, 41, pp. 636-643.
- [12] Ickes, A., Bohac, S., and Assanis, D., 2009, "Effect of fuel cetane number on a premixed diesel combustion mode," *International Journal of Engine Research*, 10(4), pp. 251-263.
- [13] Armstead, J. R., and Miers, S. A., 2013, "Review of Waste Heat Recovery Mechanisms for Internal Combustion Engines," *Journal of Thermal Science and Engineering Applications*, 6(1), pp. 014001-014001.
- [14] Will, F., 2012, "Fuel conservation and emission reduction through novel waste heat recovery for internal combustion engines," *Fuel*, 102(0), pp. 247-255.
- [15] Wenzhi, G., Junmeng, Z., Guanghua, L., Qiang, B., and Liming, F., 2013, "Performance evaluation and experiment system for waste heat recovery of diesel engine," *Energy*, 55(0), pp. 226-235.

- [16] Valentino, R., Hall, M. J., and Briggs, T., 2013, "Simulation of Organic Rankine Cycle Electric Power Generation from Light-Duty Spark Ignition and Diesel Engine Exhaust Flows," *SAE Int. J. Engines*, 6(2), pp. 1299-1310.
- [17] Vaja, I., and Gambarotta, A., 2010, "Internal Combustion Engine (ICE) bottoming with Organic Rankine Cycles (ORCs)," *Energy*, 35(2), pp. 1084-1093.
- [18] Srinivasan, K. K., Mago, P. J., and Krishnan, S. R., 2010, "Analysis of exhaust waste heat recovery from a dual fuel low temperature combustion engine using an Organic Rankine Cycle," *Energy*, 35(6), pp. 2387-2399.
- [19] Schmid, H., "Less emissions through waste heat recovery," *Proc. Green Ship Technology Conference*, London, p. 29.
- [20] Johnson, K. G., Mollenhauer, K., and Tschöke, H., 2010, *Handbook of diesel engines*, Springer Science & Business Media.
- [21] Teng, H., Regner, G., and Cowland, C., 2006, "Achieving High Engine Efficiency for Heavy-Duty Diesel Engines by Waste Heat Recovery Using Supercritical Organic-Fluid Rankine Cycle," *SAE International*.
- [22] Katta, K. K., Kim, M., and Taggett, M., 2008, "Exhaust Heat Co-Generation System Using Phase Change Cooling for Heavy Duty Vehicles," *SAE International*.
- [23] Robinson, K., Hawley, J., and Campbell, N., 2003, "Experimental and modelling aspects of flow boiling heat transfer for application to internal combustion engines," *Proceedings of the Institution of Mechanical Engineers, Part D: Journal of Automobile Engineering*, 217(10), pp. 877-889.
- [24] Sprouse Iii, C., and Depcik, C., 2013, "Review of organic Rankine cycles for internal combustion engine exhaust waste heat recovery," *Applied Thermal Engineering*, 51(1-2), pp. 711-722.
- [25] Delgado, O., and Lutsey, N., 2014, "White Paper: The U.S. SuperTruck Program," *Department of Energy*.
- [26] Fu, J., Liu, J., Xu, Z., Ren, C., and Deng, B., 2013, "A combined thermodynamic cycle based on methanol dissociation for IC (internal combustion) engine exhaust heat recovery," *Energy*, 55(0), pp. 778-786.
- [27] Kadota, M., and Yamamoto, K., 2008, "Advanced Transient Simulation on Hybrid Vehicle Using Rankine Cycle System," *SAE Int. J. Engines*, 1(1), pp. 240-247.
- [28] Boretti, A. A., 2012, "Transient operation of internal combustion engines with Rankine waste heat recovery systems," *Applied Thermal Engineering*, 48, pp. 18-23.
- [29] Fu, J., Liu, J., Yang, Y., Ren, C., and Zhu, G., 2013, "A new approach for exhaust energy recovery of internal combustion engine: Steam turbocharging," *Applied Thermal Engineering*, 52(1), pp. 150-159.
- [30] Edwards, K. D., and Wagner, R. M., "Investigating potential efficiency improvement for light-duty transportation applications through simulation of an organic Rankine cycle for waste-heat recovery," *Proc. ASME 2010 Internal Combustion Engine Division Fall Technical Conference*, American Society of Mechanical Engineers, pp. 811-822.
- [31] Ringler, J., Seifert, M., Guyotot, V., and Hübner, W., 2009, "Rankine Cycle for Waste Heat Recovery of IC Engines," *SAE International Journal of Engines*, 2(1), pp. 67-76.

- [32] Endo, T., Kawajiri, S., Kojima, Y., Takahashi, K., Baba, T., Ibaraki, S., Takahashi, T., and Shinohara, M., 2007, "Study on Maximizing Exergy in Automotive Engines," SAE International.
- [33] Nunn, P., 2009, "From 10-15 to JC08: Japan's new economy formula," http://www.jama-english.jp/europe/news/2009/no_2/peternunn.html.
- [34] Teng, H., 2010, "Waste Heat Recovery Concept to Reduce Fuel Consumption and Heat Rejection from a Diesel Engine," SAE Int. J. Commer. Veh., 3(1), pp. 60-68.
- [35] "Heavy-Duty Supplemental Emissions Test (SET)," <https://www.dieselnet.com/standards/cycles/set.php>.
- [36] Ferguson, C. R., 1985, "International combustion engines; Applied thermosciences."
- [37] 2002, "Vanguard 3/LC Repair Manual," Briggs & Stratton Corporation.
- [38] Agoston, A., Ötsch, C., and Jakoby, B., 2005, "Viscosity sensors for engine oil condition monitoring— Application and interpretation of results," Sensors and Actuators A: Physical, 121(2), pp. 327-332.
- [39] 2012, "Duratherm G," Duratherm, ed.
- [40] Gatto, V. J., Moehle, W. E., Cobb, T. W., and Schneller, E. R., 2006, "Oxidation fundamentals and its application to turbine oil testing," Journal of ASTM International, 3(4), pp. 1-20.
- [41] Kohashi, H., "Application of fatty acid esters for lubricating oil," Proc. World Conference on Oleochemicals into the 21st Century: Proceedings, pp. 243-255.
- [42] Specification, P., "US Code of Federal Regulations, 40 CFR Part 60, Appendix A," Federal Register, 60.
- [43] Plan, D. R. R., 2000, "Appendix IV Fuels Report: Appendix to the Diesel Risk Reduction Plan."
- [44] Chase, M., "NIST-JANAF thermochemical tables. 1998," Woodbury, NY: Published by the American Chemical Society and the American Institute of Physics for the National Institute of Standards and Technology, 2.
- [45] Cápek, V., 2006, Challenges to the Second Law of Thermodynamics Theory And Experiment, Dordrecht : Springer, Dordrecht.
- [46] Urdan, T. C., 2010, Statistics in plain English, Routledge.
- [47] Ahsanullah, M., Kibria, B. G., and Shakil, M., 2014, Normal and student's t distributions and their applications, Springer.
- [48] Klein, S. A., 1992-2014, "Engineering Equation Solver," F.-C. Software, ed.
- [49] Incropera, F. P., and DeWitt, D. P., 1990, Fundamentals of heat and mass transfer, Wiley.
- [50] Chang, Y.-J., and Wang, C.-C., 1997, "A generalized heat transfer correlation for louver fin geometry," International Journal of Heat and Mass Transfer, 40(3), pp. 533-544.
- [51] Chang, Y.-J., Hsu, K.-C., Lin, Y.-T., and Wang, C.-C., 2000, "A generalized friction correlation for louver fin geometry," International journal of heat and mass transfer, 43(12), pp. 2237-2243.
- [52] Churchill, S. W., 1977, "Friction-factor equation spans all fluid-flow regimes," Chemical engineering, 84(24), pp. 91-92.

- [53] Shah, M., 1979, "A general correlation for heat transfer during film condensation inside pipes," *International Journal of heat and mass transfer*, 22(4), pp. 547-556.
- [54] Zhang, W., Hibiki, T., and Mishima, K., 2010, "Correlations of two-phase frictional pressure drop and void fraction in mini-channel," *International Journal of Heat and Mass Transfer*, 53(1), pp. 453-465.
- [55] Sun, L., and Mishima, K., 2009, "Evaluation analysis of prediction methods for two-phase flow pressure drop in mini-channels," *International Journal of Multiphase Flow*, 35(1), pp. 47-54.
- [56] Bhatti, M., Shah, R., Kakaç, S., Shah, R., and Aung, W., 1987, "Handbook of single-phase convective heat transfer," New York.
- [57] Bertsch, S. S., Groll, E. A., and Garimella, S. V., 2009, "A composite heat transfer correlation for saturated flow boiling in small channels," *International Journal of Heat and Mass Transfer*, 52(7), pp. 2110-2118.
- [58] Friedel, L., "Improved friction pressure drop correlations for horizontal and vertical two-phase pipe flow," *Proc. European two-phase flow group meeting*, Paper E, p. 1979.
- [59] Schwarz, E., Reid, M., Bryzik, W., and Danielson, E., 1993, "Combustion and Performance Characteristics of a Low Heat Rejection Engine," SAE International.
- [60] Kamo, R., Mavinahally, N. S., Kamo, L., Bryzik, W., and Schwartz, E., 1999, "Injection Characteristics that Improve Performance of Ceramic Coated Diesel Engines," SAE International.
- [61] Sun, X., Wang, W. G., Lyons, D. W., and Gao, X., 1993, "Experimental Analysis and Performance Improvement of a Single Cylinder Direct Injection Turbocharged Low Heat Rejection Engine," SAE International.
- [62] Igari, S., Mori, S., and Takikawa, Y., 2000, "Effects of molecular structure of aliphatic diols and polyalkylene glycol as lubricants on the wear of aluminum," *Wear*, 244(1-2), pp. 180-184.
- [63] Turns, S. R., 2006, *An introduction to combustion concepts and applications*, McGraw-Hill, Boston.
- [64] Paredes, X., Fandiño, O., Pensado, A. S., Comuñas, M. J. P., and Fernández, J., 2012, "Pressure-Viscosity Coefficients for Polyalkylene Glycol Oils and Other Ester or Ionic Lubricants," *Tribology Letters*, 45(1), pp. 89-100.
- [65] Long, M., 2010, "Understanding Lab Test Results," Memo.
- [66] BIPM, I., IFCC, I., ISO, I., and IUPAP, O., 2008, "Evaluation of measurement data—guide to the expression of uncertainty in measurement, JCGM 100: 2008 GUM 1995 with minor corrections," Paris: Joint Committee for Guides in Metrology.
- [67] Association, A. G., and Association, G. P., 1990, *Orifice metering of natural gas and other related hydrocarbon fluids*, American Gas Association.

APPENDIX A: INSTRUMENT CALIBRATION

The instrumentation used to measure critical values was calibrated to reduce uncertainty. The procedures used for calibration are covered in this appendix. The appendix will be divided into four sections. First, the general method for deriving the uncertainty for a given calibrated instrument is described. Second, the calibration procedure for the dynamometer is discussed. Next, the process for calibrating the thermocouples is covered. Finally, the method used for pressure transducer calibration will be presented.

A.1 Uncertainty in Measurements

Understanding the uncertainty associated with a given measurement is critical to determining the relevance of a measured value. Measurement uncertainty is found by determining both the systematic and the random contributions and combining them to reach the total uncertainty. The two types of uncertainty are merged by summing in quadrature. The systematic uncertainty is found as follows:

$$u_{\text{sys}} = \sqrt{u_{\text{std}}^2 + (k_b \text{SEE})^2} \quad (\text{A.1})$$

The systematic error in a measurement stems from repeatable errors inherent in the instrument or measurement method. This type of error can be reduced by calibration of the instrument and the application of this calibration to any measurements made with the instrument. The uncertainty associated with systematic error is the uncertainty in the correction that is applied. All instruments used to measure key values were calibrated to reduce uncertainty. From equation (A.1), the uncertainty of the measurement standard is the uncertainty in the standard used to calibrate the instrument. The coverage factor (k_p) is found using the *t-value* corresponding to the desired

confidence interval (95% here) and the number of degrees of freedom. The Sum of Experimental Error (*SEE*) is defined as follows:

$$SEE = \sqrt{\frac{\sum_{i=1}^N [Y_i - (aX_i + b)]^2}{n - 2}} \quad (\text{A.2})$$

The random uncertainty is calculated from the acquired data and combined with the systematic uncertainty for error propagation. Examples are provided in the following sections.

A.2 Dynamometer

The Mid-West DynSystems 1014A DYN-LOC IV eddy current dynamometer is capable of measuring loads up to 130 kW. Because the output of the test engine was significantly below the rated load of the dynamometer, care was taken to calibrate over the relevant load range. The dynamometer measures output via a load cell attached to the torque arm. The torque from the engine rotates the torque arm and applies a force to the load cell. The force on the load cell coupled with the known torque arm length is then used to calculate the torque applied by the engine. An additional, longer arm is provided for calibration purposes. Weights are hung at the end of the calibration arm, which also has a known length. Therefore, the torque applied from the weights can be accurately calculated and compared to the torque displayed on the dyno controller. The calibration data was used to create a least squares curve fit for correction of the measured torque. The analysis outlined in the previous section was then applied to find the uncertainty of the calibrated torque values. The summary of the calibration uncertainty values is presented in Table A-1. The torque measurement accuracy was further limited by the low resolution of the display (1 N-m). Therefore, the uncertainty found from equation (A.1) was further modified to account for the lack of resolution as follows:

$$u_{\text{sys,tot}} = \sqrt{u_{\text{sys}}^2 + u_{\text{res}}^2} \quad (\text{A.3})$$

$$u_{\text{res}} = \frac{0.5 \cdot r}{\sqrt{3}} \quad (\text{A.4})$$

For the dynamometer, the standard uncertainty is a combination of the uncertainty in the length of the calibration arm (0.002 m), and the uncertainty of the calibration weights (0.002 kg). The uncertainty in the calibration weights is propagated through the force calculation which results in an uncertainty of 0.02 N. The force uncertainty is an order of magnitude larger than the length uncertainty, so the total systematic uncertainty is essentially 0.02 N-m after summing in quadrature. With 4 degrees of freedom, the *SEE* is found to be 0.278 and the coverage factor for a 95% confidence interval is 2.57, giving a combined systematic uncertainty of 0.714 N-m. The uncertainty due to the resolution of the dynamometer readout is 0.289 N-m, giving a total systematic uncertainty of 0.770 N-m.

Table A-1. Summary of dynamometer calibration results.

Slope (m)	0.962
Intercept (b)	0.165
Sum Exp. Error (SEE)	0.278
Count [-]	6
Deg. Of Freedom [-]	4
Coverage Factor	2.57
Uncertainty of Standard [N-m]	0.002
Systematic Uncertainty [N-m]	0.714
Display Resolution Uncertainty [N-m]	0.289
Total Uncertainty [N-m]	0.770

A.3 Thermocouples

A total of 14 thermocouples were calibrated to reduce systematic uncertainty in key temperature measurements. The calibrations were performed over the relevant temperature ranges expected during testing (25-200°C). To reach sufficient temperatures and maintain uniformity, a hot stir plate was filled with Duratherm G HTF and insulated to serve as a calibration bath. The thermocouple readings were compared with a Platinum Resistance Temperature Detector (RTD)

with an accuracy of 0.0012°C. The thermocouples were sorted into categories depending on the expected temperature range and calibrated in batches. The results of calibration are shown in Table A-2. Again, equations (A.1) and (A.2) are used to find the systematic uncertainty for each thermocouple. For example, thermocouple 0 has a coverage factor of 2.30 and an *SEE* of 0.07. The uncertainty of the standard is 0.0012°C for all thermocouples, giving a total systematic uncertainty of 0.15°C.

Table A-2. Summary of thermocouple calibration results.

Thermocouple ID	0	1	2	3	4	5	6
Slope (m)	1.00	1.00	1.00	1.00	1.00	1.00	1.00
Intercept (b)	-0.17	-0.20	-0.19	0.09	0.07	0.15	-0.09
Sum Exp. Error (SEE)	0.07	0.06	0.05	0.03	0.05	0.04	0.03
Count [-]	9	9	9	9	9	9	5
Deg. Of Freedom	7	7	7	7	7	7	3
Coverage Factor	2.30	2.30	2.30	2.30	2.30	2.30	
Uncertainty of Standard [°C]	0.0012	0.0012	0.0012	0.0012	0.0012	0.0012	0.0012
Systematic Uncertainty [°C]	0.15	0.13	0.11	0.06	0.12	0.10	0.10
Thermocouple ID	7	8	9	10	11	12	13
Slope (m)	1.00	1.00	1.00	0.99	1.00	1.00	1.00
Intercept (b)	-0.01	0.04	0.13	0.51	0.95	0.46	0.93
Sum Exp. Error (SEE)	0.04	0.02	0.02	0.10	0.48	0.28	0.52
Count [-]	5	5	5	5	5	5	5
Deg. Of Freedom	3	3	3	3	3	3	3
Coverage Factor	2.78	2.78	2.78	2.78	2.78	2.78	2.78
Uncertainty of Standard [°C]	0.0012	0.0012	0.0012	0.0012	0.0012	0.0012	0.0012
Systematic Uncertainty [°C]	0.12	0.05	0.05	0.28	1.33	0.78	1.45

A.4 Pressure Transducers

Two pressure transducers were required to calculate the air flow past the orifice flow meter. One differential and one absolute pressure transducers were calibrated using a meter with an accuracy of 0.02 kPa. The differential pressure transducer was calibrated by applying a pressure to one input and leaving the other input exposed to ambient pressure, creating pressure differences between 4.5 and 29 kPa. The procedure in section A.1 was then used to calculate the systematic

uncertainty for the calibrated sensors. Table A-3 shows the inputs and results of the analysis. For example, the differential pressure sensor had an *SEE* of 0.05 and 3 degrees of freedom. The uncertainty of the standard was 0.02 kPa, giving a systematic uncertainty of 0.14 kPa.

Table A-3. Summary of pressure transducer calibration results.

Pressure Transducer	Differential	Absolute
Slope (m)	2.16	6.67
Intercept (b)	-8.71	-30.03
Sum Exp. Error (SEE)	0.05	0.06
Count [-]	5	4
Deg. Of Freedom	3	2
Coverage Factor	2.78	3.18
Uncertainty of Standard [kPa]	0.02	0.02
Systematic Uncertainty [kPa]	0.14	0.18

APPENDIX B: UNCERTAINTY IN ENERGY BALANCE CALCULATIONS

The uncertainty in the calculation of each portion of the energy balance originates from the calibrated uncertainty of each instrument used for measurement as seen in Table 3-4. These calibrated uncertainties were then propagated using the standard method of error propagation to arrive at the uncertainty for the resulting calculation [66]:

$$u_{\text{comb}}(y) = \sqrt{\sum_{i=1}^N \left(\frac{\partial f}{\partial x_i} \right)^2 u^2(x_i)} \quad (\text{B.1})$$

The representative test point values in Table 4-1 will be used to demonstrate the application of the uncertainty propagation for each energy balance component. Applying equation (B.1) to the fuel energy flow calculation yields the following expression:

$$u_{\dot{E}_{\text{fuel}}} = \sqrt{\left(u_{m_{\text{fuel,st}}} \frac{\partial \dot{E}_{\text{fuel}}}{\partial m_{\text{fuel,st}}} \right)^2 + \left(u_{m_{\text{fuel,end}}} \frac{\partial \dot{E}_{\text{fuel}}}{\partial m_{\text{fuel,end}}} \right)^2 + \left(u_{\text{LHV}} \frac{\partial \dot{E}_{\text{fuel}}}{\partial \text{LHV}} \right)^2 + \left(u_{t_{\text{daq}}} \frac{\partial \dot{E}_{\text{fuel}}}{\partial t_{\text{test}}} \right)^2} \quad (\text{B.2})$$

The partial derivatives are as follows:

$$\frac{\partial \dot{E}_{\text{fuel}}}{\partial m_{\text{fuel,st}}} = \frac{\text{LHV}_{\text{fuel}}}{t_{\text{test}}} = \frac{43,200 \cdot \text{kJ} \cdot \text{kg}^{-1}}{6.000 \times 10^3 \cdot \text{s}} = 7.20 \cdot \text{kW} \cdot \text{kg}^{-1} \quad (\text{B.3})$$

$$\frac{\partial \dot{E}_{\text{fuel}}}{\partial m_{\text{fuel,end}}} = \frac{-\text{LHV}_{\text{fuel}}}{t_{\text{test}}} = \frac{-43,200 \cdot \text{kJ} \cdot \text{kg}^{-1}}{6.000 \times 10^3 \cdot \text{s}} = -7.20 \cdot \text{kW} \cdot \text{kg}^{-1} \quad (\text{B.4})$$

$$\frac{\partial \dot{E}_{\text{fuel}}}{\partial \text{LHV}_{\text{fuel}}} = \frac{m_{\text{fuel,st}} - m_{\text{fuel,end}}}{t_{\text{test}}} = \frac{22.12 \cdot \text{kg} - 19.08 \cdot \text{kg}}{6.000 \times 10^3 \cdot \text{s}} = 5.067 \times 10^{-4} \cdot \text{kg} \cdot \text{s}^{-1} \quad (\text{B.5})$$

$$\begin{aligned} \frac{\partial \dot{E}_{\text{fuel}}}{\partial t_{\text{test}}} &= \frac{-(m_{\text{fuel,st}} - m_{\text{fuel,end}}) \text{LHV}_{\text{fuel}}}{t_{\text{test}}^2} = \frac{-(22.12 \cdot \text{kg} - 19.08 \cdot \text{kg}) 43,200 \cdot \text{kJ} \cdot \text{kg}^{-1}}{(6.000 \times 10^3 \cdot \text{s})^2} \\ &= -3.65 \cdot \text{W} \cdot \text{s}^{-1} \end{aligned} \quad (\text{B.6})$$

Using the uncertainties in each component from Table 3-4, the combined uncertainty is 0.45 kW, or 2.07%.

The expression for the engine power output combined uncertainty is as follows:

$$u_{\dot{W}_{\text{out}}} = \sqrt{\left(u_n \frac{\partial \dot{W}_{\text{out}}}{\partial n}\right)^2 + \left(u_\tau \frac{\partial \dot{W}_{\text{out}}}{\partial \tau}\right)^2} \quad (\text{B.7})$$

The value of the partial derivatives from equation (B.7) for the representative test point are:

$$\frac{\partial \dot{W}_{\text{out}}}{\partial N} = \frac{2\pi\tau}{60,000} = \frac{2\pi \cdot \text{rev}^{-1} (17.8 \cdot \text{N} \cdot \text{m})}{(60 \cdot \text{s} \cdot \text{min}^{-1})(1,000 \cdot \text{N} \cdot \text{kN}^{-1})} = 1.86 \cdot \text{N} \cdot \text{m} \cdot \text{min} \cdot \text{rev}^{-1} \cdot \text{s}^{-1} \quad (\text{B.8})$$

$$\frac{\partial \dot{W}_{\text{out}}}{\partial \tau} = \frac{2\pi N}{60,000} = \frac{2\pi \cdot \text{rev}^{-1} (3101.5 \cdot \text{rev} \cdot \text{min}^{-1})}{(60 \cdot \text{s} \cdot \text{min}^{-1})(1,000 \cdot \text{N} \cdot \text{kN}^{-1})} = 324.80 \cdot \text{kN} \cdot \text{N}^{-1} \cdot \text{s}^{-1} \quad (\text{B.9})$$

From the uncertainties listed in Table 3-4, the combined uncertainty for the engine output is found to be 0.25 kW, or 4.36%.

The engine coolant and oil uncertainty calculations are similar and will be described together. For the engine coolant and oil heat rates, the expression for the combined uncertainty is:

$$u_{\dot{Q}} = \sqrt{\left(u_{\dot{V}} \frac{\partial \dot{Q}}{\partial \dot{V}}\right)^2 + \left(u_\rho \frac{\partial \dot{Q}}{\partial \rho}\right)^2 + \left(u_{c_p} \frac{\partial \dot{Q}}{\partial c_p}\right)^2 + \left(u_{T_{\text{out}}} \frac{\partial \dot{Q}}{\partial T_{\text{out}}}\right)^2 + \left(u_{T_{\text{in}}} \frac{\partial \dot{Q}}{\partial T_{\text{in}}}\right)^2} \quad (\text{B.10})$$

For the engine coolant, the partial derivatives for the representative test point are as follows:

$$\begin{aligned} \frac{\partial \dot{Q}_{\text{HTF}}}{\partial \dot{V}_{\text{HTF}}} &= \rho_{\text{HTF}} c_{p,\text{HTF}} (T_{\text{HTF,out}} - T_{\text{HTF,in}}) \\ &= (860.29 \cdot \text{kg} \cdot \text{m}^{-3}) (2.194 \cdot \text{kJ} \cdot \text{kg}^{-1} \cdot \text{K}^{-1}) (428.82 \cdot \text{K} - 417.92 \cdot \text{K}) \\ &= 20,570 \cdot \text{kJ} \cdot \text{m}^{-3} \end{aligned} \quad (\text{B.11})$$

$$\begin{aligned} \frac{\partial \dot{Q}_{\text{HTF}}}{\partial \rho_{\text{HTF}}} &= \dot{V}_{\text{HTF}} c_{p,\text{HTF}} (T_{\text{HTF,out}} - T_{\text{HTF,in}}) \\ &= (0.000206 \cdot \text{m}^3 \cdot \text{s}^{-1}) (2.194 \cdot \text{kJ} \cdot \text{kg}^{-1} \cdot \text{K}^{-1}) (428.82 \cdot \text{K} - 417.92 \cdot \text{K}) \\ &= 0.00492 \cdot \text{kW} \cdot \text{m}^3 \cdot \text{kg}^{-1} \end{aligned} \quad (\text{B.12})$$

$$\begin{aligned}
\frac{\partial \dot{Q}_{\text{HTF}}}{\partial c_{p,\text{HTF}}} &= \dot{V}_{\text{HTF}} \rho_{\text{HTF}} (T_{\text{HTF,out}} - T_{\text{HTF,in}}) \\
&= (0.000206 \cdot \text{m}^3 \cdot \text{s}^{-1}) (860.29 \cdot \text{kg} \cdot \text{m}^{-3}) (428.82 \cdot \text{K} - 417.92 \cdot \text{K}) \\
&= 1.93 \cdot \text{kg} \cdot \text{K} \cdot \text{s}^{-1}
\end{aligned} \tag{B.13}$$

$$\begin{aligned}
\frac{\partial \dot{Q}_{\text{HTF}}}{\partial T_{\text{HTF,out}}} &= \dot{V}_{\text{HTF}} \rho_{\text{HTF}} c_{p,\text{HTF}} \\
&= (0.000206 \cdot \text{m}^3 \cdot \text{s}^{-1}) (860.29 \cdot \text{kg} \cdot \text{m}^{-3}) (2.194 \cdot \text{kJ} \cdot \text{kg}^{-1} \cdot \text{K}^{-1}) \\
&= 0.389 \cdot \text{kW} \cdot \text{K}^{-1}
\end{aligned} \tag{B.14}$$

$$\begin{aligned}
\frac{\partial \dot{Q}_{\text{HTF}}}{\partial T_{\text{HTF,in}}} &= -\dot{V}_{\text{HTF}} \rho_{\text{HTF}} c_{p,\text{HTF}} \\
&= (0.000206 \cdot \text{m}^3 \cdot \text{s}^{-1}) (860.29 \cdot \text{kg} \cdot \text{m}^{-3}) (2.194 \cdot \text{kJ} \cdot \text{kg}^{-1} \cdot \text{K}^{-1}) \\
&= -0.389 \cdot \text{kW} \cdot \text{K}^{-1}
\end{aligned} \tag{B.15}$$

Using the measurement uncertainties from Table 3-4, the combined uncertainty for the HTF is 0.30 kW, or 7.16%.

The procedure for finding the combined uncertainty for the engine oil waste heat flow is the same. The partial derivatives for the oil waste heat flow can be written as:

$$\begin{aligned}
\frac{\partial \dot{Q}_{\text{oil}}}{\partial \dot{V}_{\text{oil}}} &= \rho_{\text{oil}} c_{p,\text{oil}} (T_{\text{oil,out}} - T_{\text{oil,in}}) \\
&= (838.41 \cdot \text{kg} \cdot \text{m}^{-3}) (2.183 \cdot \text{kJ} \cdot \text{kg}^{-1} \cdot \text{K}^{-1}) (356.55 \cdot \text{K} - 343.45 \cdot \text{K}) \\
&= 23,980 \cdot \text{kJ} \cdot \text{m}^{-3}
\end{aligned} \tag{B.16}$$

$$\begin{aligned}
\frac{\partial \dot{Q}_{\text{oil}}}{\partial \rho_{\text{oil}}} &= \dot{V}_{\text{oil}} c_{p,\text{oil}} (T_{\text{oil,out}} - T_{\text{oil,in}}) \\
&= (0.000101 \cdot \text{m}^3 \cdot \text{s}^{-1}) (2.183 \cdot \text{kJ} \cdot \text{kg}^{-1} \cdot \text{K}^{-1}) (356.55 \cdot \text{K} - 343.45 \cdot \text{K}) \\
&= 0.00286 \cdot \text{kW} \cdot \text{m}^3 \cdot \text{kg}^{-1}
\end{aligned} \tag{B.17}$$

$$\begin{aligned}
\frac{\partial \dot{Q}_{\text{oil}}}{\partial c_{p,\text{oil}}} &= \dot{V}_{\text{oil}} \rho_{\text{oil}} (T_{\text{oil,out}} - T_{\text{oil,in}}) \\
&= (0.000101 \cdot \text{m}^3 \cdot \text{s}^{-1}) (838.41 \cdot \text{kg} \cdot \text{m}^{-3}) (356.55 \cdot \text{K} - 343.45 \cdot \text{K}) \\
&= 1.11 \cdot \text{kg} \cdot \text{K} \cdot \text{s}^{-1}
\end{aligned} \tag{B.18}$$

$$\begin{aligned}
\frac{\partial \dot{Q}_{\text{oil}}}{\partial T_{\text{oil,out}}} &= \dot{V}_{\text{oil}} \rho_{\text{oil}} c_{p,\text{oil}} \\
&= (0.000101 \cdot \text{m}^3 \cdot \text{s}^{-1}) (838.41 \cdot \text{kg} \cdot \text{m}^{-3}) (2.183 \cdot \text{kJ} \cdot \text{kg}^{-1} \cdot \text{K}^{-1}) \\
&= 0.185 \cdot \text{kW} \cdot \text{K}^{-1}
\end{aligned} \tag{B.19}$$

$$\begin{aligned}
\frac{\partial \dot{Q}_{\text{oil}}}{\partial T_{\text{oil,in}}} &= -\dot{V}_{\text{oil}} \rho_{\text{oil}} c_{p,\text{oil}} \\
&= -(0.000101 \cdot \text{m}^3 \cdot \text{s}^{-1}) (838.41 \cdot \text{kg} \cdot \text{m}^{-3}) (2.183 \cdot \text{kJ} \cdot \text{kg}^{-1} \cdot \text{K}^{-1}) \\
&= -0.185 \cdot \text{kW} \cdot \text{K}^{-1}
\end{aligned} \tag{B.20}$$

Using equation (B.10) and the uncertainties in the measurements from Table 3-4, the combined uncertainty for the oil waste heat flow is 0.18 kW, or 7.23%.

The uncertainty for the exhaust waste heat flow calculation can be represented by:

$$u_{\dot{Q}_{\text{exh}}} = \sqrt{\left(u_{\dot{m}_{\text{fuel}}} \frac{\partial \dot{Q}_{\text{exh}}}{\partial \dot{m}_{\text{fuel}}} \right)^2 + \left(u_{\dot{m}_{\text{air}}} \frac{\partial \dot{Q}_{\text{exh}}}{\partial \dot{m}_{\text{air}}} \right)^2 + \left(u_{\Delta h_{\text{CO}_2}} \frac{\partial \dot{Q}_{\text{exh}}}{\partial \Delta h_{\text{CO}_2}} \right)^2 + \left(u_{\Delta h_{\text{H}_2\text{O}}} \frac{\partial \dot{Q}_{\text{exh}}}{\partial \Delta h_{\text{H}_2\text{O}}} \right)^2 + \left(u_{\Delta h_{\text{N}_2}} \frac{\partial \dot{Q}_{\text{exh}}}{\partial \Delta h_{\text{N}_2}} \right)^2 + \left(u_{\Delta h_{\text{O}_2}} \frac{\partial \dot{Q}_{\text{exh}}}{\partial \Delta h_{\text{O}_2}} \right)^2 + \left(u_{MF_{\text{CO}_2}} \frac{\partial \dot{Q}_{\text{exh}}}{\partial MF_{\text{CO}_2}} \right)^2 + \left(u_{MF_{\text{H}_2\text{O}}} \frac{\partial \dot{Q}_{\text{exh}}}{\partial MF_{\text{H}_2\text{O}}} \right)^2 + \left(u_{MF_{\text{N}_2}} \frac{\partial \dot{Q}_{\text{exh}}}{\partial MF_{\text{N}_2}} \right)^2 + \left(u_{MF_{\text{O}_2}} \frac{\partial \dot{Q}_{\text{exh}}}{\partial MF_{\text{O}_2}} \right)^2} \tag{B.21}$$

The partial derivatives for the representative case can be found as follows:

$$\begin{aligned}
\frac{\partial \dot{Q}_{\text{exh}}}{\partial \dot{m}_{\text{fuel}}} &= MF_{\text{CO}_2} \times \Delta h_{\text{CO}_2} + MF_{\text{H}_2\text{O}} \times \Delta h_{\text{H}_2\text{O}} + MF_{\text{N}_2} \times \Delta h_{\text{N}_2} + MF_{\text{O}_2} \times \Delta h_{\text{O}_2} \\
&= (0.1038)(398.74 \cdot \text{kJ} \cdot \text{kg}^{-1}) + (0.04070)(787.34 \cdot \text{kJ} \cdot \text{kg}^{-1}) \\
&\quad + (0.7417)(427.39 \cdot \text{kJ} \cdot \text{kg}^{-1}) + (0.1133)(388.13 \cdot \text{kJ} \cdot \text{kg}^{-1}) \\
&= 434.4 \cdot \text{kJ} \cdot \text{kg}^{-1}
\end{aligned} \tag{B.22}$$

$$\begin{aligned}
\frac{\partial \dot{Q}_{\text{exh}}}{\partial \dot{m}_{\text{air}}} &= MF_{\text{CO}_2} \times \Delta h_{\text{CO}_2} + MF_{\text{H}_2\text{O}} \times \Delta h_{\text{H}_2\text{O}} + MF_{\text{N}_2} \times \Delta h_{\text{N}_2} + MF_{\text{O}_2} \times \Delta h_{\text{O}_2} \\
&= (0.1038)(398.74 \cdot \text{kJ} \cdot \text{kg}^{-1}) + (0.04070)(787.34 \cdot \text{kJ} \cdot \text{kg}^{-1}) \\
&\quad + (0.7417)(427.39 \cdot \text{kJ} \cdot \text{kg}^{-1}) + (0.1133)(388.13 \cdot \text{kJ} \cdot \text{kg}^{-1}) \\
&= 434.4 \cdot \text{kJ} \cdot \text{kg}^{-1}
\end{aligned} \tag{B.23}$$

$$\begin{aligned}\frac{\partial \dot{Q}_{\text{exh}}}{\partial \Delta h_{\text{CO}_2}} &= MF_{\text{CO}_2} (\dot{m}_{\text{fuel}} + \dot{m}_{\text{air}}) = (0.1038)(0.0005067 \cdot \text{kg} \cdot \text{s}^{-1} + 0.0149 \cdot \text{kg} \cdot \text{s}^{-1}) \\ &= 0.00160 \cdot \text{kg} \cdot \text{s}^{-1}\end{aligned}\quad (\text{B.24})$$

$$\begin{aligned}\frac{\partial \dot{Q}_{\text{exh}}}{\partial \Delta h_{\text{H}_2\text{O}}} &= MF_{\text{H}_2\text{O}} (\dot{m}_{\text{fuel}} + \dot{m}_{\text{air}}) = (0.04070)(0.0005067 \cdot \text{kg} \cdot \text{s}^{-1} + 0.0149 \cdot \text{kg} \cdot \text{s}^{-1}) \\ &= 0.000627 \cdot \text{kg} \cdot \text{s}^{-1}\end{aligned}\quad (\text{B.25})$$

$$\begin{aligned}\frac{\partial \dot{Q}_{\text{exh}}}{\partial \Delta h_{\text{N}_2}} &= MF_{\text{N}_2} (\dot{m}_{\text{fuel}} + \dot{m}_{\text{air}}) = (0.7417)(0.0005067 \cdot \text{kg} \cdot \text{s}^{-1} + 0.0149 \cdot \text{kg} \cdot \text{s}^{-1}) \\ &= 0.0114 \cdot \text{kg} \cdot \text{s}^{-1}\end{aligned}\quad (\text{B.26})$$

$$\begin{aligned}\frac{\partial \dot{Q}_{\text{exh}}}{\partial \Delta h_{\text{O}_2}} &= MF_{\text{O}_2} (\dot{m}_{\text{fuel}} + \dot{m}_{\text{air}}) = (0.1133)(0.0005067 \cdot \text{kg} \cdot \text{s}^{-1} + 0.0149 \cdot \text{kg} \cdot \text{s}^{-1}) \\ &= 0.00175 \cdot \text{kg} \cdot \text{s}^{-1}\end{aligned}\quad (\text{B.27})$$

$$\begin{aligned}\frac{\partial \dot{Q}_{\text{exh}}}{\partial MF_{\text{CO}_2}} &= \Delta h_{\text{CO}_2} (\dot{m}_{\text{fuel}} + \dot{m}_{\text{air}}) \\ &= (398.74 \cdot \text{kJ} \cdot \text{kg}^{-1})(0.0005067 \cdot \text{kg} \cdot \text{s}^{-1} + 0.0149 \cdot \text{kg} \cdot \text{s}^{-1}) \\ &= 6.14 \cdot \text{kg} \cdot \text{s}^{-1}\end{aligned}\quad (\text{B.28})$$

$$\begin{aligned}\frac{\partial \dot{Q}_{\text{exh}}}{\partial MF_{\text{H}_2\text{O}}} &= \Delta h_{\text{H}_2\text{O}} (\dot{m}_{\text{fuel}} + \dot{m}_{\text{air}}) \\ &= (787.34 \cdot \text{kJ} \cdot \text{kg}^{-1})(0.0005067 \cdot \text{kg} \cdot \text{s}^{-1} + 0.0149 \cdot \text{kg} \cdot \text{s}^{-1}) \\ &= 12.1 \cdot \text{kg} \cdot \text{s}^{-1}\end{aligned}\quad (\text{B.29})$$

$$\begin{aligned}\frac{\partial \dot{Q}_{\text{exh}}}{\partial MF_{\text{N}_2}} &= \Delta h_{\text{N}_2} (\dot{m}_{\text{fuel}} + \dot{m}_{\text{air}}) \\ &= (427.39 \cdot \text{kJ} \cdot \text{kg}^{-1})(0.0005067 \cdot \text{kg} \cdot \text{s}^{-1} + 0.0149 \cdot \text{kg} \cdot \text{s}^{-1}) \\ &= 6.58 \cdot \text{kg} \cdot \text{s}^{-1}\end{aligned}\quad (\text{B.30})$$

$$\begin{aligned}\frac{\partial \dot{Q}_{\text{exh}}}{\partial MF_{\text{O}_2}} &= \Delta h_{\text{O}_2} (\dot{m}_{\text{fuel}} + \dot{m}_{\text{air}}) \\ &= (388.13 \cdot \text{kJ} \cdot \text{kg}^{-1})(0.0005067 \cdot \text{kg} \cdot \text{s}^{-1} + 0.0149 \cdot \text{kg} \cdot \text{s}^{-1}) \\ &= 5.98 \cdot \text{kg} \cdot \text{s}^{-1}\end{aligned}\quad (\text{B.31})$$

The uncertainties in equation (B.21) require further analysis and the necessary calculations will now be discussed. The uncertainty in the fuel mass flow rate is:

$$u_{\dot{m}_{\text{fuel}}} = \sqrt{\left(u_{m_{\text{fuel,st}}} \frac{\partial \dot{m}_{\text{fuel}}}{\partial m_{\text{fuel,st}}}\right)^2 + \left(u_{m_{\text{fuel,end}}} \frac{\partial \dot{m}_{\text{fuel}}}{\partial m_{\text{fuel,end}}}\right)^2 + \left(u_{t_{\text{test}}} \frac{\partial \dot{m}_{\text{fuel}}}{\partial t_{\text{test}}}\right)^2} \quad (\text{B.32})$$

The partial derivatives are:

$$\frac{\partial \dot{m}_{\text{fuel}}}{\partial m_{\text{fuel,st}}} = \frac{1}{t_{\text{test}}} = \frac{1}{6.000 \times 10^3 \cdot \text{s}} = 1.667 \times 10^{-4} \cdot \text{s}^{-1} \quad (\text{B.33})$$

$$\frac{\partial \dot{m}_{\text{fuel}}}{\partial m_{\text{fuel,end}}} = -\frac{1}{t_{\text{test}}} = -\frac{1}{6.000 \times 10^3 \cdot \text{s}} = -1.667 \times 10^{-4} \cdot \text{s}^{-1} \quad (\text{B.34})$$

$$\frac{\partial \dot{m}_{\text{fuel}}}{\partial t_{\text{test}}} = -\frac{m_{\text{fuel,st}} - m_{\text{fuel,end}}}{t_{\text{test}}^2} = -\frac{22.12 \cdot \text{kg} - 19.08 \cdot \text{kg}}{(6.000 \times 10^3 \cdot \text{s})^2} = 8.444 \times 10^{-8} \cdot \text{kg} \cdot \text{s}^{-2} \quad (\text{B.35})$$

Using these three equations and the systematic uncertainties from Table 4-1, the uncertainty for the fuel mass flow calculation is 0.28 g min^{-1} , or 0.93%.

The air mass flow was measured using an orifice flow meter and the calculation method put forth by the American Gas Association [67]. The method of calculation is derived from the principles of conservation equations, fluid dynamics, and various state equations. The result is the following set of expressions:

$$\dot{m}_{\text{air}} = N_1 C_d E_v Y d^2 \sqrt{\rho_{\text{tp}} \Delta P} \quad (\text{B.36})$$

$$N_1 = 1.11072 \quad (\text{B.37})$$

$$C_d = C_i (FT) + 0.000511 \left(\frac{10^6 \beta}{Re_D}\right)^{0.7} + (0.0210 + 0.0049) \beta^4 C \quad (\text{B.38})$$

$$C_i (FT) = C_i (CT) + TapTerm \quad (\text{B.39})$$

$$C_i (CT) = 0.5961 + 0.0291 \beta^2 - 0.2290 \beta^8 + 0.003(1 - \beta) M_1 \quad (\text{B.40})$$

$$TapTerm = Upstrm + Dnstrm \quad (\text{B.41})$$

$$Upstrm = (0.0433 + 0.0712e^{-8.5L_1} - 0.1145e^{-6.0L_1})(1 - 0.23A)B \quad (B.42)$$

$$Dnstrm = -0.0116(M_2 - 0.52M_2^{1.3})\beta^{1.1}(1 - 0.14A) \quad (B.43)$$

$$B = \frac{\beta^4}{1 - \beta^4} \quad (B.44)$$

$$M_1 = \max\left(2.8 - \frac{D}{N_4}, 0.0\right) \quad (B.45)$$

$$M_2 = \frac{2L_2}{1 - \beta} \quad (B.46)$$

$$A = \left(\frac{19,000\beta}{Re_D}\right)^{0.8} \quad (B.47)$$

$$C = \left(\frac{10^6}{Re_D}\right)^{0.35} \quad (B.48)$$

$$\beta = \frac{d}{D} \quad (B.49)$$

$$N_4 = 25.4 \quad (B.50)$$

$$L_1 = L_2 = \frac{N_4}{D} \quad (B.51)$$

$$Re_D = \frac{N_2 \dot{m}_{air}}{\mu D} \quad (B.52)$$

$$N_2 = 1,273.24 \quad (B.53)$$

$$E_v = \frac{1}{\sqrt{1 - \beta^4}} \quad (B.54)$$

$$Y = 1 - (0.41 + 0.35\beta^4) \frac{x_1}{k} \quad (B.55)$$

$$x_1 = \frac{\Delta P}{N_3 P_{f_1}} \quad (B.56)$$

Fortunately, the AGA document provides a method for the estimation of uncertainty in the calculation of mass flow when using the above method. The following equation is used to provide the uncertainty of the mass flow rate of the intake air:

$$\frac{u_{\dot{m}_{\text{air}}}}{\dot{m}_{\text{air}}} = \left\{ \begin{aligned} &\left(\frac{u_{C_d}}{C_d} \right)^2 + \left(\frac{u_Y}{Y} \right)^2 + \left(\frac{2}{1-\beta^4} \right)^2 \left(\frac{u_d}{d} \right)^2 \\ &+ \left(\frac{-2\beta^4}{1-\beta^4} \right)^2 \left(\frac{u_D}{D} \right)^2 + \frac{1}{4} \left(\frac{u_{\rho_{t,p}}}{\rho_{t,p}} \right)^2 + \frac{1}{4} \left(\frac{u_{\Delta P}}{\Delta P} \right)^2 \end{aligned} \right\}^{0.5} \quad (\text{B.57})$$

The uncertainty in the discharge coefficient term is found by estimating the uncertainty at an infinite Reynolds number and then applying a correction factor. The equations are:

$$\frac{u_{C_{d,\infty}}}{C_d} = 0.5600 - 0.2550\beta + 1.9316\beta^8 \quad (\text{B.58})$$

$$u_{C_{d,\text{corr}}} = 1 + 1.7895 \left(\frac{4000}{Re_D} \right)^{0.8} \quad (\text{B.59})$$

The product of the results from equations (B.58) and (B.59) gives the first term for equation (B.57). From the orifice and pipe diameters given in Table B-1, beta is found to be 0.49. The uncertainty for the discharge coefficient at infinite Reynolds number is therefore 0.44%. The Reynolds number is:

$$Re_D = \frac{4\dot{m}_{\text{air}}}{\pi\mu D} = \frac{4(0.0149 \cdot \text{kg} \cdot \text{s}^{-1})}{3.14159(1.972 \times 10^{-5} \cdot \text{Pa} \cdot \text{s})(0.04127 \cdot \text{m})} = 23,300 \quad (\text{B.60})$$

Therefore, equation (B.59) gives a correction factor of 1.437. The product of the two values results in a discharge coefficient uncertainty of 0.63%. The relative uncertainty of the expansion factor is 0.5%. The uncertainties for the orifice and pipe diameters were found from the collection of measurements taken as shown in Table B-1. The measurement uncertainty was taken to be the root mean square of the precision and bias values listed in the table. The precision is the product of the standard deviation and the t-stat. The bias value represents the systematic error of the measuring

Table B-1. Measurement and uncertainty data for orifice and pipe diameters.

Parameter	Orifice	Pipe
Average Diameter [m]	0.020264	0.041266
N	5	10
Bias of Standard [m]	0.0000635	0.0000254
t-stat	2.7764	2.2622
Standard Deviation [m]	6.4758x10 ⁻⁶	6.1115x10 ⁻⁵
Precision [m]	1.798x10 ⁻⁵	1.383x10 ⁻⁴
Uncertainty [m]	6.5996x10 ⁻⁵	1.4057x10 ⁻⁴
Uncertainty [%]	0.33	0.34

instruments, namely the calibrated calipers used to measure the ID of the orifice and pipe. The air density was calculated from the measured temperature and absolute pressure of the intake air using the ideal gas equation. The combined uncertainty for the air density is:

$$\frac{u_{\rho_{t,p}}}{\rho_{t,p}} = \sqrt{\left(u_{P_{abs}} \frac{\partial \rho_{t,p}}{\partial P_{abs}}\right)^2 + \left(u_{T_{air}} \frac{\partial \rho_{t,p}}{\partial T_{air}}\right)^2} \quad (\text{B.61})$$

The partial derivatives are:

$$\frac{\partial \rho_{t,s}}{\partial P_{abs}} = \frac{1}{T_{air} R_{air}} = \frac{1}{(307.494 \cdot \text{K})(0.287 \cdot \text{kJ} \cdot \text{kg}^{-1} \cdot \text{K}^{-1})} = 0.0113 \cdot \text{kg} \cdot \text{kJ}^{-1} \quad (\text{B.62})$$

$$\frac{\partial \rho_{t,p}}{\partial T_{air}} = -\frac{P_{abs}}{T_{air}^2 R_{air}} = -\frac{84.396 \cdot \text{kPa}}{(307.494 \cdot \text{K})^2 (0.287 \cdot \text{kJ} \cdot \text{kg}^{-1} \cdot \text{K}^{-1})} = -0.00311 \cdot \text{kg} \cdot \text{m}^{-3} \cdot \text{K}^{-1} \quad (\text{B.63})$$

The results from the two partial derivatives combined with the uncertainties from Table 3-4 result in a combined air density uncertainty of 2.56 g m⁻³, or 0.27%. The uncertainty for the differential pressure across the orifice is 0.14 kPa, as shown in Table 3-4, or 4.99%. Using equation (B.57), the combined uncertainty for the air mass flow calculation at the representative test point is 2.72%.

The uncertainty in the enthalpy change for each gas was found by evaluating the applied fit of the data from the NIST-JANAF tables. The uncertainty in the JANAF data was assumed to be small compared to the uncertainty resulting from the applied fit. Therefore, the enthalpy change uncertainty is the precision of the curve fit:

$$u_{\Delta h} = \sigma t_{\text{stat}} \quad (\text{B.64})$$

The results of the uncertainty calculations for the enthalpy change for each gas are shown in Table B-2.

The uncertainties for the mass fraction of the four gases are all calculated using the same general formula:

$$u_{MF} = \sqrt{\left(u_{\dot{n}} \frac{\partial MF}{\partial \dot{n}}\right)^2 + \left(u_{\dot{m}_{\text{air}}} \frac{\partial MF}{\partial \dot{m}_{\text{air}}}\right)^2 + \left(u_{\dot{m}_{\text{fuel}}} \frac{\partial MF}{\partial \dot{m}_{\text{fuel}}}\right)^2} \quad (\text{B.65})$$

The partial derivatives for the mass fraction uncertainty of CO₂ are:

$$\frac{\partial MF_{\text{CO}_2}}{\partial \dot{n}_{\text{CO}_2}} = \frac{MW_{\text{CO}_2}}{\dot{m}_{\text{fuel}} + \dot{m}_{\text{air}}} = \frac{44.0095 \cdot \text{kg} \cdot \text{kmol}^{-1}}{0.0005067 \cdot \text{kg} \cdot \text{s}^{-1} + 0.0149 \cdot \text{kg} \cdot \text{s}^{-1}} = 2,860 \cdot \text{s} \cdot \text{kmol}^{-1} \quad (\text{B.66})$$

$$\begin{aligned} \frac{\partial MF_{\text{CO}_2}}{\partial \dot{m}_{\text{air}}} &= -\frac{\dot{n}_{\text{CO}_2} MW_{\text{CO}_2}}{(\dot{m}_{\text{fuel}} + \dot{m}_{\text{air}})^2} = -\frac{(3.64 \times 10^{-5} \cdot \text{kmol} \cdot \text{s}^{-1})(44.0095 \cdot \text{kg} \cdot \text{kmol}^{-1})}{(0.0005067 \cdot \text{kg} \cdot \text{s}^{-1} + 0.0149 \cdot \text{kg} \cdot \text{s}^{-1})^2} \\ &= -6.75 \cdot \text{s} \cdot \text{kg}^{-1} \end{aligned} \quad (\text{B.67})$$

$$\begin{aligned} \frac{\partial MF_{\text{CO}_2}}{\partial \dot{m}_{\text{fuel}}} &= -\frac{\dot{n}_{\text{CO}_2} MW_{\text{CO}_2}}{(\dot{m}_{\text{fuel}} + \dot{m}_{\text{air}})^2} = -\frac{(3.64 \times 10^{-5} \cdot \text{kmol} \cdot \text{s}^{-1})(44.0095 \cdot \text{kg} \cdot \text{kmol}^{-1})}{(0.0005067 \cdot \text{kg} \cdot \text{s}^{-1} + 0.0149 \cdot \text{kg} \cdot \text{s}^{-1})^2} \\ &= -6.75 \cdot \text{s} \cdot \text{kg}^{-1} \end{aligned} \quad (\text{B.68})$$

The uncertainty for the CO₂ molar flow rate is:

$$\begin{aligned} u_{\dot{n}_{\text{CO}_2}} &= u_{\dot{m}_{\text{fuel}}} \frac{x_{\text{C}}}{MW_{\text{fuel}}} = (4.716 \times 10^{-6} \cdot \text{kg} \cdot \text{s}^{-1}) \left(\frac{12}{167.311 \cdot \text{kg} \cdot \text{kmol}^{-1}} \right) \\ &= 3.382 \times 10^{-7} \cdot \text{kmol} \cdot \text{s}^{-1} \end{aligned} \quad (\text{B.69})$$

Table B-2. Uncertainty results for exhaust gas enthalpy calculations.

Gas	σ	t-stat	Uncertainty
CO ₂	1.070191	2.4469	2.61866
H ₂ O	0.391521	2.4469	0.95802
N ₂	0.215784	2.3646	0.51025
O ₂	0.400227	2.3646	0.94639

The uncertainties for the fuel and air mass flow rates were previously found, so the resulting combined uncertainty for the CO₂ mass fraction is 0.00284, or 2.73%.

The partial derivatives for the mass fraction uncertainty of H₂O are:

$$\frac{\partial MF_{H_2O}}{\partial \dot{n}_{H_2O}} = \frac{MW_{H_2O}}{\dot{m}_{fuel} + \dot{m}_{air}} = \frac{18.01528 \cdot \text{kg} \cdot \text{kmol}^{-1}}{0.0005067 \cdot \text{kg} \cdot \text{s}^{-1} + 0.0149 \cdot \text{kg} \cdot \text{s}^{-1}} = 1,170 \cdot \text{s} \cdot \text{kmol}^{-1} \quad (\text{B.70})$$

$$\begin{aligned} \frac{\partial MF_{H_2O}}{\partial \dot{m}_{air}} &= -\frac{\dot{n}_{H_2O} MW_{H_2O}}{(\dot{m}_{fuel} + \dot{m}_{air})^2} = -\frac{(3.48 \times 10^{-5} \cdot \text{kmol} \cdot \text{s}^{-1})(18.01528 \cdot \text{kg} \cdot \text{kmol}^{-1})}{(0.0005067 \cdot \text{kg} \cdot \text{s}^{-1} + 0.0149 \cdot \text{kg} \cdot \text{s}^{-1})^2} \\ &= -2.64 \cdot \text{s} \cdot \text{kg}^{-1} \end{aligned} \quad (\text{B.71})$$

$$\begin{aligned} \frac{\partial MF_{H_2O}}{\partial \dot{m}_{fuel}} &= -\frac{\dot{n}_{H_2O} MW_{H_2O}}{(\dot{m}_{fuel} + \dot{m}_{air})^2} = -\frac{(3.48 \times 10^{-5} \cdot \text{kmol} \cdot \text{s}^{-1})(18.01528 \cdot \text{kg} \cdot \text{kmol}^{-1})}{(0.0005067 \cdot \text{kg} \cdot \text{s}^{-1} + 0.0149 \cdot \text{kg} \cdot \text{s}^{-1})^2} \\ &= -2.64 \cdot \text{s} \cdot \text{kg}^{-1} \end{aligned} \quad (\text{B.72})$$

The uncertainty for the H₂O molar flow rate is:

$$\begin{aligned} u_{\dot{n}_{H_2O}} &= u_{\dot{m}_{fuel}} \frac{y_H}{2MW_{fuel}} = (4.716 \times 10^{-6} \cdot \text{kg} \cdot \text{s}^{-1}) \left(\frac{23}{(2)167.311 \cdot \text{kg} \cdot \text{kmol}^{-1}} \right) \\ &= 3.242 \times 10^{-7} \cdot \text{kmol} \cdot \text{s}^{-1} \end{aligned} \quad (\text{B.73})$$

Using the air and fuel flow uncertainties from before, the uncertainty for the H₂O mass fraction is 0.0011, or 2.70%.

The partial derivatives for the mass fraction uncertainty of N₂ are:

$$\frac{\partial MF_{N_2}}{\partial \dot{n}_{N_2}} = \frac{MW_{N_2}}{\dot{m}_{fuel} + \dot{m}_{air}} = \frac{28.0134 \cdot \text{kg} \cdot \text{kmol}^{-1}}{0.0005067 \cdot \text{kg} \cdot \text{s}^{-1} + 0.0149 \cdot \text{kg} \cdot \text{s}^{-1}} = 1,820 \cdot \text{s} \cdot \text{kmol}^{-1} \quad (\text{B.74})$$

$$\begin{aligned} \frac{\partial MF_{N_2}}{\partial \dot{m}_{air}} &= -\frac{\dot{n}_{N_2} MW_{N_2}}{(\dot{m}_{fuel} + \dot{m}_{air})^2} = -\frac{(4.10 \times 10^{-4} \cdot \text{kmol} \cdot \text{s}^{-1})(28.0134 \cdot \text{kg} \cdot \text{kmol}^{-1})}{(0.0005067 \cdot \text{kg} \cdot \text{s}^{-1} + 0.0149 \cdot \text{kg} \cdot \text{s}^{-1})^2} \\ &= -48.4 \cdot \text{s} \cdot \text{kg}^{-1} \end{aligned} \quad (\text{B.75})$$

$$\begin{aligned} \frac{\partial MF_{N_2}}{\partial \dot{m}_{fuel}} &= -\frac{\dot{n}_{N_2} MW_{N_2}}{(\dot{m}_{fuel} + \dot{m}_{air})^2} = -\frac{(4.10 \times 10^{-4} \cdot \text{kmol} \cdot \text{s}^{-1})(28.0134 \cdot \text{kg} \cdot \text{kmol}^{-1})}{(0.0005067 \cdot \text{kg} \cdot \text{s}^{-1} + 0.0149 \cdot \text{kg} \cdot \text{s}^{-1})^2} \\ &= -48.4 \cdot \text{s} \cdot \text{kg}^{-1} \end{aligned} \quad (\text{B.76})$$

The uncertainty for the N₂ molar flow rate is:

$$u_{\dot{n}_{N_2}} = u_{\dot{m}_{air}} \frac{3.76}{MW_{air}} = (0.000396 \cdot \text{kg} \cdot \text{s}^{-1}) \left(\frac{3.76}{137.3292 \cdot \text{kg} \cdot \text{kmol}(\text{O}_2)^{-1}} \right) \quad (\text{B.77})$$

$$= 1.08 \times 10^{-5} \cdot \text{kmol} \cdot \text{s}^{-1}$$

Using the air and fuel flow uncertainties from before, the uncertainty for the N₂ mass fraction is 0.0275, or 3.69%.

The partial derivatives for the mass fraction uncertainty of O₂ are:

$$\frac{\partial MF_{O_2}}{\partial \dot{n}_{O_2}} = \frac{MW_{O_2}}{\dot{m}_{fuel} + \dot{m}_{air}} = \frac{31.9988 \cdot \text{kg} \cdot \text{kmol}^{-1}}{0.0005067 \cdot \text{kg} \cdot \text{s}^{-1} + 0.0149 \cdot \text{kg} \cdot \text{s}^{-1}} = 2,080 \cdot \text{s} \cdot \text{kmol}^{-1} \quad (\text{B.78})$$

$$\frac{\partial MF_{O_2}}{\partial \dot{m}_{air}} = - \frac{\dot{n}_{O_2} MW_{O_2}}{(\dot{m}_{fuel} + \dot{m}_{air})^2} = - \frac{(5.52 \times 10^{-5} \cdot \text{kmol} \cdot \text{s}^{-1})(31.9988 \cdot \text{kg} \cdot \text{kmol}^{-1})}{(0.0005067 \cdot \text{kg} \cdot \text{s}^{-1} + 0.0149 \cdot \text{kg} \cdot \text{s}^{-1})^2} \quad (\text{B.79})$$

$$= -7.44 \cdot \text{s} \cdot \text{kg}^{-1}$$

$$\frac{\partial MF_{O_2}}{\partial \dot{m}_{fuel}} = - \frac{\dot{n}_{O_2} MW_{O_2}}{(\dot{m}_{fuel} + \dot{m}_{air})^2} = - \frac{(5.52 \times 10^{-5} \cdot \text{kmol} \cdot \text{s}^{-1})(31.9988 \cdot \text{kg} \cdot \text{kmol}^{-1})}{(0.0005067 \cdot \text{kg} \cdot \text{s}^{-1} + 0.0149 \cdot \text{kg} \cdot \text{s}^{-1})^2} \quad (\text{B.80})$$

$$= -7.44 \cdot \text{s} \cdot \text{kg}^{-1}$$

The uncertainty for the O₂ molar flow rate is:

$$u_{\dot{n}_{O_2}} = \sqrt{\left(u_{\dot{m}_{fuel}} \frac{\partial \dot{n}_{O_2}}{\partial \dot{m}_{fuel}} \right)^2 + \left(u_{\dot{m}_{air}} \frac{\partial \dot{n}_{O_2}}{\partial \dot{m}_{air}} \right)^2} \quad (\text{B.81})$$

The partial derivatives for equation (B.81) are:

$$\frac{\partial \dot{n}_{O_2}}{\partial \dot{m}_{fuel}} = - \frac{17.75}{MW_{fuel}} = - \frac{17.75}{167.311 \cdot \text{kg} \cdot \text{kmol}^{-1}} = -0.1061 \cdot \text{kmol} \cdot \text{kg}^{-1} \quad (\text{B.82})$$

$$\frac{\partial \dot{n}_{O_2}}{\partial \dot{m}_{air}} = \frac{1}{MW_{air}} = \frac{1}{137.3292 \cdot \text{kg} \cdot \text{kmol}(\text{O}_2)^{-1}} = 0.007282 \cdot \text{kmol}(\text{O}_2) \cdot \text{kg} \quad (\text{B.83})$$

Therefore, the uncertainty for the O₂ molar flow rate is 2.93x10⁻⁶ kmol s⁻¹. Using the air and fuel flow uncertainties from before, the uncertainty for the O₂ mass fraction is 0.00676, or 5.90%.

Finally, entering everything into equation (B.21), the exhaust waste heat uncertainty is 0.255 kW, or 3.79%.

APPENDIX C: ENGINE COMPONENT MEASUREMENTS

The test engine was disassembled and key components were measured before any testing was performed. The measurements served two purposes. First, the measurements were compared to the specifications to determine if any components required replacement. Second, the measurements served as a baseline for comparison with measurements to be repeated after testing was completed. Table C-1 summarizes the measurements before and after testing. The methods used to perform the measurements listed in the table and their interpretation will be discussed in this appendix. It should be noted that the piston and connecting rod were replaced on cylinder 3 due to a hydro-lock event while commissioning the test stand. The measurements presented here are for the new components that were installed to repair the damage.

Outside diameters (ODs) on engine components were measured using the appropriate outside micrometer (Mitutoyo, 103-922). The inside diameters (IDs) on the engine were measured using dial bore gauges of the appropriate size (Mitutoyo, 511-932). Both sets of gauges have graduations of 0.0001 in (0.00254 mm). The measurement procedure for ODs is as follows. Before measurements were performed, the contact surfaces of the micrometer were cleaned and the micrometer was calibrated against the included gauge block. After calibration, the OD was measured by using the ratchet stop to ensure consistent readings. Measurements were recorded in inches and then later converted to mm by multiplying by the 25.4 mm in⁻¹ conversion factor. For IDs, the measurement procedure is as follows. First, a calibrated micrometer was adjusted to size approximating the ID measured in the first step and the micrometer was locked to maintain the adjustment. Then, the appropriate bore gauge was placed inside the micrometer and zeroed. The ID was then measured as a difference in relation to the OD of the associated component. This

Table C-1. Engine component measurements.

Component	Specification	Pre-test Value	Post-test Value	Difference
Cylinder 1 Bore				
Height 1 Avg. [mm]	68.000-68.030	68.012	68.017	0.005
Height 2 Avg. [mm]	68.000-68.030	68.012	68.019	0.007
Height 3 Avg. [mm]	68.000-68.030	68.010	68.017	0.007
Cylinder 2 Bore				
Height 1 Avg. [mm]	68.000-68.030	68.014	68.019	0.005
Height 2 Avg. [mm]	68.000-68.030	68.014	68.019	0.005
Height 3 Avg. [mm]	68.000-68.030	68.010	68.017	0.007
Cylinder 3 Bore				
Height 1 Avg. [mm]	68.000-68.030	68.004	68.019	0.015
Height 2 Avg. [mm]	68.000-68.030	68.007	68.019	0.013
Height 3 Avg. [mm]	68.000-68.030	68.005	68.016	0.011
Rod 1 Big End Clearance (with bearings)				
Position 1 [mm]	<0.07	0.066	0.058	-0.008
Position 2 [mm]	<0.07	0.061	0.061	0.000
Rod 2 Big End Clearance (with bearings)				
Position 1 [mm]	<0.07	0.058	0.069	0.011
Position 2 [mm]	<0.07	0.061	0.066	0.005
Rod 3 Big End Clearance (with bearings)				
Position 1 [mm]	<0.07	0.048	0.051	0.003
Position 2 [mm]	<0.07	0.043	0.046	0.003
Piston 1 Pin Clearance				
Position 1 [mm]	<0.05	0.015	0.031	0.016
Position 2 [mm]	<0.05	0.011	0.006	-0.005
Position 3 [mm]	<0.05	0.018	0.026	0.008
Piston 2 Pin Clearance				
Position 1 [mm]	<0.05	0.014	0.029	0.015
Position 2 [mm]	<0.05	0.012	-0.003	-0.015
Position 3 [mm]	<0.05	0.017	0.030	0.013
Piston 3 Pin Clearance				
Position 1 [mm]	<0.05	0.017	0.033	0.016
Position 2 [mm]	<0.05	0.017	0.010	-0.007
Position 3 [mm]	<0.05	0.017	0.033	0.016
Main Bearing Clearance #1				
Position 1 [mm]	<0.07	0.058	0.056	-0.002
Position 2 [mm]	<0.07	0.056	0.053	-0.003
Main Bearing Clearance #2				
Position 1 [mm]	<0.07	0.064	0.064	0.000
Position 2 [mm]	<0.07	0.051	0.056	0.005
Main Bearing Clearance #3				
Position 1 [mm]	<0.07	0.066	0.066	0.000
Position 2 [mm]	<0.07	0.058	0.058	0.000

Main Bearing Clearance #4				
Position 1 [mm]	<0.07	0.069	0.071	0.002
Position 2 [mm]	<0.07	0.057	0.067	0.010
Lifter Clearance Cylinder 1				
Intake [mm]	<0.14	0.033	0.019	-0.014
Exhaust [mm]	<0.14	0.023	0.030	0.007
Lifter Clearance Cylinder 2				
Intake [mm]	<0.14	0.020	0.024	0.004
Exhaust [mm]	<0.14	0.022	0.024	0.002
Lifter Clearance Cylinder 3				
Intake [mm]	<0.14	0.028	0.024	-0.004
Exhaust [mm]	<0.14	0.018	0.033	0.015

method was used to reduce the uncertainty in the ID measurements. By zeroing the dial bore gauge at a known diameter, the resulting uncertainty in the clearances between the two components stems from only one of the measurement tool instead of both. Each individual measurement will now be described in detail.

The first measurements listed in Table C-1 are the cylinder bore diameters. First, an outside micrometer was calibrated and adjusted to the nominal diameter of 68 mm. The appropriate dial bore gauge was then zeroed using this micrometer and then used to measure the bore diameters at three different heights of the bore (13 mm, 32 mm, and 51 mm below deck height). At each bore height, the diameter was measured at four different circumferential positions around the bore. The values shown in Table C-1 are the averages of the four positions at each height. The cylinder bores were found to increase in diameter between 0.005 mm and 0.015 mm over the course of testing. Bore diameters did remain inside the specification provided by the manufacturer, though the quality of the bore surfaces after testing would have required re-boring.

The second set of measurements in Table C-1 is for the connecting rod big end that attaches to the rod journal on the crankshaft. The rod journals on the crankshaft were measured first using a calibrated outside micrometer at two different axial positions. At each axial position, the rod journal OD was measured at four different positions around the journal. A two-piece bearing insert

resides between the connecting rod and the rod journal. The ID of the rod end was measured with the bearing in place to determine the effective clearance with the component installed on the crankshaft. The ID of the rod end was also measured at two axial positions, with multiple measurements at each position. The measurement process was as follows. An outside micrometer was adjusted to 37 mm, and the appropriate dial bore gauge was inserted in the micrometer and zeroed. The dial bore gauge was then used to measure the ID of the big rod end with the bearing installed. The differences between the ID of the rod end and the rod journal OD were then taken and the results are shown in the table. Note that the connecting rod clearances for cylinders 1 and 2 were approaching the limit for replacement by the end of testing. Also, some rod bearing clearance measurements resulted in a decrease in clearance over the course of testing, which is unlikely. Therefore, the validity of those measurements is questionable.

Next, Table C-1 shows the clearance measurements for the piston pin and piston pin bore in both the small rod end and the piston itself. Positions 1 and 3 in the table refer to the locations where the piston pin and piston interface, where position 2 is where the pin and the small end of the connecting rod interface. At each position, four measurements were taken at different locations around the pins and bores. These four measurements were then averaged and the average pin OD was subtracted from the average pin bore at each of the three positions to arrive at the clearances shown in the table. For the ID measurements, an outside micrometer was adjusted to 18.0 mm and locked at that setting. The appropriate dial bore gauge was then inserted into the micrometer and zeroed. Measurements were then taken and the differences between the average IDs and ODs at each position were calculated to arrive at the clearances in the table. Note the decrease in clearance in position 2 (rod small end) for each cylinder. This reduction in clearance is due to the buildup of

carbon from overheated engine oil as described previously. This buildup resulted in the piston pins for cylinders one and two being frozen in the rod ends which had to be pressed out for disassembly.

The test engine has four main bearings supporting the crankshaft. The main bearing clearances are critical to crankshaft journal longevity. The main bearing journals and bearing IDs were measured at two axial position and four circumferential locations at each position. The average values at each axial position were then compared to arrive at the bearing clearances shown in the table. For the ID measurements, the bearing inserts were installed and an outside micrometer was set to 42 mm and the appropriate dial bore gauge was inserted and zeroed. The results show that the main bearings showed insignificant changes in clearance over the course of testing.

Finally, the valve lifter clearances were measured. The lifter ODs and lifter bore IDs were measured at two axial positions and then averaged and the differences taken to arrive at the clearances shown in Table C-1. For the lifter bores, a calibrated micrometer was set to 18.0 mm and the appropriate dial bore gauge was inserted and zeroed. In general, the exhaust valve lifter clearances tended to increase over the course of testing, mainly due to wear of the lifter bores. The intake valve lifter bores also experience similar wear, but the intake valve lifters tended to increase in diameter. One possible explanation is that oil breakdown may have left a layer on the surface of the lifter, slightly increasing the diameter.